First Identification of the 0_2^+ State in ^{30}Mg via its E0 Transition

Wolfgang Norbert Erik Schwerdtfeger

München 2008

First Identification of the 0_2^+ State in ^{30}Mg via its E0 Transition

Wolfgang Norbert Erik Schwerdtfeger

Dissertation
an der Fakultät für Physik
der Ludwig–Maximilians–Universität
München

vorgelegt von
Wolfgang Norbert Erik Schwerdtfeger
aus Ludwigshafen am Rhein

München, den 28.08.2008

Erstgutachter: Prof. Dr. Dietrich Habs

Zweitgutachter: Prof. Dr. Hermann Wolter

Tag der mündlichen Prüfung: 25.11.2008

Dedicated to my parents, my twin brother Matthias and all my supporting friends.

Summary

Since the discovery of the 'Island of Inversion' in 1975 by C. Thibault et al. [THI75], this mass region around the $N = 20$ shell closure in Ne, Na and Mg isotopes is still the aim of many nuclear structure experiments. In this region strongly deformed $2p - 2h$ intruder states occur as ground states, resulting from a promotion of a pair of neutrons across the $N = 20$ shell gap in contrast to the normal $0p - 0h$ configuration. Inside and at the borderline of the so called 'Island of Inversion' a shape coexistence of spherical and deformed 0^+ states is predicted especially in the ^{30,32}Mg isotopes. At present only spectroscopic information on the 0^+ ground states is available. The $B(E2, 2_1^+ \rightarrow 0_1^+)$ values in ^{30}Mg (241(31) e²fm⁴ [NIE05]) and ^{32}Mg (545(78) e²fm⁴ [SCH05]) were measured via Coulomb excitation at REX-ISOLDE using the MINIBALL γ spectrometer. The nucleus ^{32}Mg (inside the 'Island of Inversion') exhibits a highly deformed 0_1^+ ground state, while the 0_1^+ ground state in ^{30}Mg (outside the 'Island of Inversion') is expected to be much less deformed, whereas the 0_2^+ states escaped observation so far.

Within a fast timing experiment by H. Mach et al. [MAC05] the known 1789 keV level in ^{30}Mg turned out to be a candidate for the 0_2^+ state due to its long lifetime of 3.9(4) ns and the absence of a γ transition to the ground state. This triggered our search on the $0_2^+ \rightarrow 0_1^+$ E0 transition in ^{30}Mg following the β decay of ^{30}Na: β decay electrons were detected in a scintillation detector, while conversion electrons were focused onto a cooled Si(Li) detector using a Mini-Orange and detected with high resolution, which simultaneously suppresses the high background of β decay electrons.

Due to the large Q value of the β decay of ^{30}Na (17.3 MeV) the suppression of the coincident background induced by high-energy γ rays and subsequently Compton-scattered electrons turned out to be the key challenge for the success of this experiment. In order to optimise the background suppression and thus the sensitivity to weak E0 transitions, offline test measurements using an ^{90}Y and a ^{152}Eu source were performed together with GEANT4 simulations. Resulting from these test measurements a highly sensitive experimental setup was designed and built, consequently minimising the amount of high-Z material in the target chamber, reducing X-ray production. As a by-product from test measurements the database value of the half-life of the 0_2^+ state in ^{90}Zr could be corrected by more than 30 % to be $t_{1/2} = 41(1)$ ns.

Finally, in a β decay experiment at the ISOLDE facility at CERN the $0_2^+ \rightarrow 0_1^+$ E0 transition in ^{30}Mg could be identified at the expected transition energy of 1788 keV proving for the first time shape coexistence at the borderline of the 'Island of Inversion'. This identification allows to determine the electric monopole strength as $\rho^2(E0) = 26.2(7.5) \cdot 10^{-3}$, indicating a rather weak mixing between the states in two potential minima in a simplified two-level mixing model. This result allows to extract the mixing amplitude between the two 0^+ states as $a = 0.179(83)$ and has been submitted for publication in Physical Review Letters (W. Schwerdtfeger et al. 2008). This experimental finding represents the first case in light nuclei where an E0 back-decay from a strongly deformed second to the first normal deformed potential minimum has been unambiguously observed.

In order to interpret our experimental findings, calculations in the Beyond Mean Field Approach (BMFA) [ROD07] have been performed by T.R. Rodriguez and J.L. Egido [ROD08]. These calculations identify the 0_1^+ ground state in ^{30}Mg as mixture of prolate and oblate $\nu\, 1d_{3/2}$ orbits and the excited 0_2^+ state as a strongly deformed $\nu\, 1f_{7/2}$ level. Moreover, the calculated deformation parameters $\beta_1 = 0.16$ and $\beta_2 = 0.59$ locate this nucleus outside the 'Island of Inversion'.

Zusammenfassung

Seit der Entdeckung der 'Insel der Inversion' im Jahr 1975 durch C. Thibault et al. [THI75] ist die Region um den Schalenabschluss $N = 20$ in Ne-, Na- und Mg-Isotopen immer noch Gegenstand vieler Kernstrukturexperimente. In dieser Region treten stark deformierte $2p - 2h$ Intruderzustände als Grundzustände auf, die sich im Gegensatz zu normalen $0p - 0h$ Zuständen durch eine Anregung zweier Neutronen über den Schalenabschluss bei $N = 20$ hinweg auszeichnen. Innerhalb und an der Grenze zur 'Insel der Inversion' ist eine Formkoexistenz eines sphärischen und eines deformierten 0^+ Zustandes vorhergesagt, speziell in den Isotopen ^{30}Mg und ^{32}Mg. Aktuell sind nur Informationen über die 0^+ Grundzustände verfügbar. Die $B(E2, 2_1^+ \rightarrow 0_1^+)$ Werte in ^{30}Mg $(241(31)$ e^2fm^4 [NIE05]) und ^{32}Mg $(545(78)$ e^2fm^4 [SCH05]) wurden mit Coulombanregung mit REX-ISOLDE und dem MINIBALL Spektrometer gemessen. ^{32}Mg (innerhalb der 'Insel der Inversion') weist einen stark deformierten 0^+ Grundzustand auf, während in ^{30}Mg (außerhalb der 'Insel der Inversion') lediglich eine schwache Deformation des 0^+ Grundzustand erwartet wird. In beiden Fällen wurden die 0_2^+ Zustände bis jetzt noch nicht beobachtet.

Im Rahmen eines Experiments zur Messung von Lebensdauern von H. Mach et al. [MAC05] stellte sich das bekannte Niveau bei 1789 keV in ^{30}Mg als ein Kandidat für den 0_2^+ Zustand heraus auf Grund seiner langen Lebensdauer von 3.9(4) ns und dem Fehlen eines γ Grundzustandsübergangs. Dies motivierte unsere Suche nach dem $0_2^+ \rightarrow 0_1^+$ E0 Übergang in ^{30}Mg nach Population im β Zerfall aus ^{30}Na. Im Experiment werden β Zerfallselektronen in einem Szintillationsdetektor und Konversionselektronen nach Fokusierung mittels einer Mini-Orange, die zugleich den starken Elektronenuntergrund aus dem β Zerfall unterdrückt, mit einem hochauflösenden Si(Li) Detektor nachgewiesen.

Auf Grund des großen Q-Wertes aus dem β-Zerfall des ^{30}Na (17.3 MeV) ergab sich als zentrale Herausforderung für den Erfolg der Messung die Notwendigkeit einer effizienten Unterdrückung koinzidenten Untergrunds, verursacht durch hochenergetische γ-Strahlung und daraus folgend Compton-gestreuter Elektronen. Um die Untergrundunterdrückung und somit die Sensitivität für schwache E0-Übergänge zu optimieren, wurden Labormessungen mit einer ^{90}Y- und einer ^{152}Eu-Quelle und GEANT4-Simulationen durchgeführt. Resultierend aus diesen Testmessungen wurde ein hochsensitiver Experimentaufbau realisiert, bestehend aus möglichst wenig hoch-Z Materialien innerhalb der Experimentierkammer zur Reduktion von Compton-Streuung und Erzeugung von Röntgenstrahlen. Als Nebenprodukt dieser Testmessungen konnte auch der Literaturwert für die Halbwertszeit des 0_2^+ Zustands in ^{90}Zr um mehr als 30 % auf $t_{1/2} = 41(1)$ ns korrigiert werden.

Schließlich wurde mittels eines β-Zerfallexperiments an der ISOLDE-Anlage am CERN der $0_2^+ \rightarrow 0_1^+$ E0-Übergang in ^{30}Mg bei der erwarteten Übergangsenergie von 1788 keV identifiziert, was erstmalig Formkoexistenz an der Grenze zur 'Insel der Inversion' beweist. Diese Identifikation erlaubt auch den Wert für die elektrische Monopolstärke $\rho^2(E0) = 26.2(7.5) \cdot 10^{-3}$ zu bestimmen, welcher in einem einfachen Zweiniveaumo-

dell eine kleine Mischung zwischen den Zuständen in den beiden Potentialminima beschreibt. Mit diesem Resultat kann die Mischungsamplitude zwischen den beiden 0^+ Zuständen zu $a = 0.179(83)$ bestimmt werden. Dieses Ergebnis wurde bei Physical Review Letters (W. Schwerdtfeger 2008 et al.) zur Veröffentlichung eingereicht.

Um dieses experimentelle Ergebnis zu interpretieren, wurden Rechnungen im Rahmen des Beyond Mean Field Models (BMFA) von T.R. Rodriguez und J.L. Egido [ROD08] durchgeführt. Diese Rechnungen identifizieren den 0_1^+ Grundzustand in ^{30}Mg als Überlagerung prolater und oblater $\nu\, 1d_{3/2}$ Orbits und den angeregten 0_2^+ Zustand als stark deformierte $\nu\, 1f_{7/2}$ Orbitale. Auch die errechneten Deformationen $\beta_1 = 0.16$ und $\beta_2 = 0.59$ bestätigen die Lage des Kerns außerhalb der 'Insel der Inversion'.

Contents

List of Figures

List of Tables

1 Motivation

Our present knowledge on nuclear structure and nuclear reactions is mostly based on what is known about stable and long-lived nuclei. Between these nuclei and the dripline, where nuclear binding comes to an end, lies an unexplored landscape where many nuclear phenomena are anticipated. Exploring this region is expected to reveal a wealth of information about the fundamental properties of the nuclear many-body problem, about astrophysical processes and the origin of heavy elements as well as about fundamental symmetries.

The strong interaction binding nucleons together is much more complicated than the electromagnetic force binding the electrons. While it is believed that nuclei can ultimately be described using the presently fundamental theory of strongly interacting quantum chromodynamics (QCD), more empirical nuclear models have provided a framework to understand many nuclear phenomena.

In general the shape of nuclei around a shell closure is spherical in the valley of stability. One region of the nuclear chart, where the nuclear structure described by the shell model appears to be anomalous is around the neutron number $N = 20$ in neutron-rich Ne, Na and Mg isotopes. This anomaly was first discovered more than 30 years ago during measurements of the binding energies in $^{27-32}$Na isotopes [THI75]. It was found that ^{31}Na and ^{32}Na were considerably more bound than theoretically predicted, which can be interpreted as a reduction of the shell gap due to deformation. This so-called intruder state becomes the ground state. This behaviour coined the name 'Island of Inversion' for this region, as first mentioned in [WAR90]. Even after more than 30 years of experiments around this region the exact location of the borderline of the 'Island of Inversion' is still not fully settled and this region is still of interest for theoretical and experimental studies [YAM04].

This shape coexistence is a well-known phenomenon in many heavy nuclei (see Sect. 3.1). In ^{236,238}U the E0 transition of the superdeformed configuration to the deformed ground state is very weak due to the large potential barrier between the two potential minima. In light nuclei the deformation of the 0_1^+ ground state was normally determined via the $B(\text{E2}, 0_1^+ \rightarrow 2_1^+)$ transition strength, a procedure which is model dependent. In ^{30}Mg the knowledge of the monopole strength allows for the first time a consistent interpretation of nuclear deformation and $B(\text{E2})$ values.

During the last years Coulomb excitation experiments were performed in ^{30}Mg and ^{32}Mg. The large value of $B(\text{E2}; 2_1^+ \rightarrow 0_1^+) = 545(78)$ e^{2}fm^4 [SCH05] in ^{32}Mg points to a strongly deformed 0^+ ground state, while the much smaller $B(\text{E2}; 2_1^+ \rightarrow 0_1^+) =$
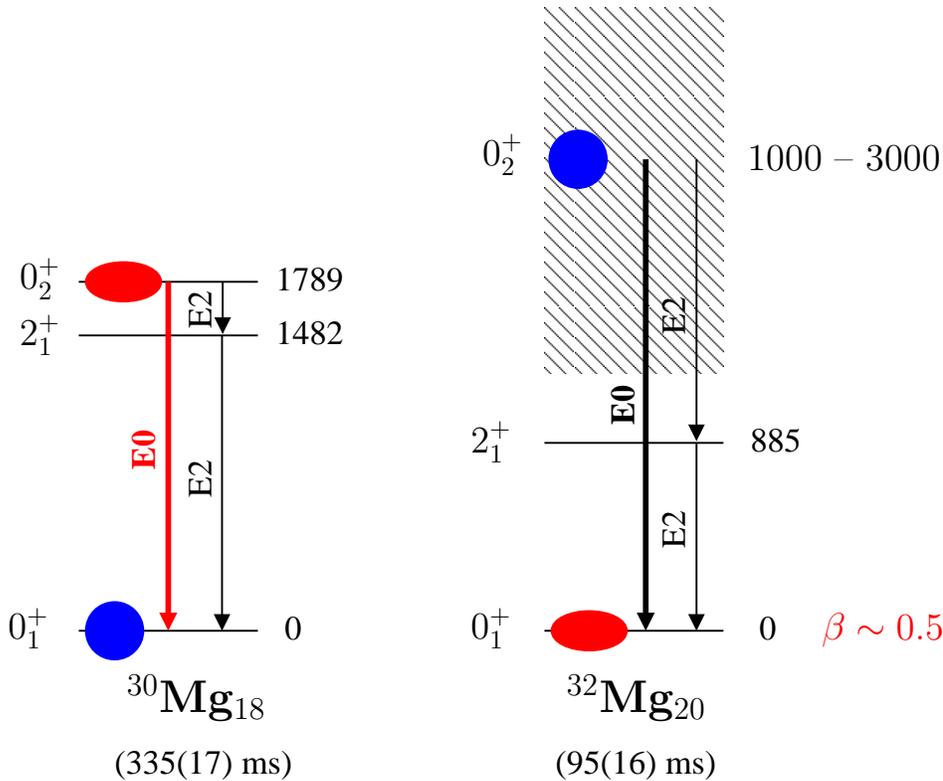
Figure 1.1: Shape coexistence of low-lying 0^+ states in Mg isotopes around $N = 20$. For ^{30}Mg a spherical 0_1^+ ground state is expected, while the 1789 keV level was considered already prior to the present work as a candidate for the deformed 0_2^+ state [MAC05]. In contrast to this, in ^{32}Mg the 0_1^+ ground state is deformed and a spherical 0_2^+ state is theoretically predicted to be located between ~ 1.4 MeV [CAU01] and ~ 3 MeV [OTS04].

241(31) e^2fm^4 value [NIE05] in ^{30}Mg could belong to a pure spherical sd configuration. Thus ^{30}Mg is located outside the 'Island of Inversion', while ^{32}Mg is located inside.

In the neutron-rich ^{30,32}Mg nuclei a coexistence of spherical and deformed 0^+ states is predicted as shown in Fig. 1.1. In ^{30}Mg the 0_1^+ ground state is expected to be almost spherical, while the 1789 keV level prior to our experimental work was discussed as a candidate for the deformed 0_2^+ state [MAC05]. In contrast to this, in ^{32}Mg the 0_1^+ ground state is strongly deformed and an excited spherical 0_2^+ state is predicted by theory between ~ 1.4 MeV [CAU01] and ~ 3 MeV [OTS04].

In Fig. 1.2 the energy difference between the deformed and spherical 0^+ states from experimental results and theoretical calculations is shown for neutron-rich Mg isotopes. This exemplifies the inversion between spherical and deformed 0^+ states occurring for ^{32}Mg ($N = 20$). In ^{26}Mg and ^{28}Mg the excited 0_2^+ state has already been identified at 3589 keV [FIR96] and 3864 keV [MAC05], respectively. For ^{30}Mg the deformed 0^+ state was predicted by theory at the beginning of the present work between 2 MeV and
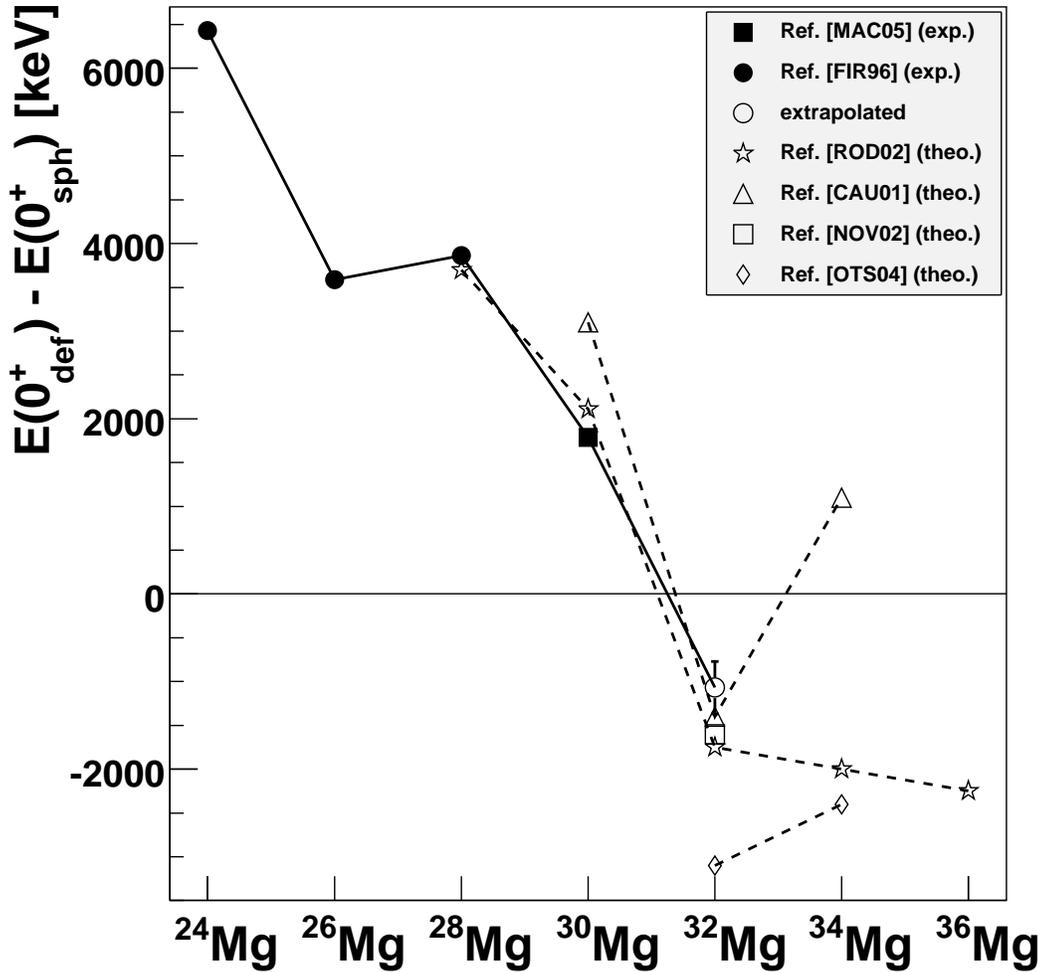
Figure 1.2: Energy difference between spherical and deformed 0^+ states in neutron rich Mg isotopes. Experimental results and theoretical predictions using different models are shown.

3 MeV [RG02a, CAU01]. The experimental result by H. Mach et al. [MAC05], which established the 1789 keV level as a candidate for the deformed 0_2^+ state, is also included in Fig. 1.2, providing the main motivation for the presented E0 studies in ^{30}Mg.

Resulting from fast timing γ spectroscopy experiments of H. Mach et al. [MAC05], the 1789 keV level in ^{30}Mg emerged as a strong candidate for the deformed excited 0_2^+ state due to its long lifetime of 3.9(4) ns and the absence of a ground state γ transition (see Sect. 5). This triggered our search for the deformed 0_2^+ state in ^{30}Mg via conversion electron spectroscopy following the β decay of ^{30}Na at the ISOLDE facility at CERN.

A large amount of experimental data on $B(E2; 2_1^+ \rightarrow 0_1^+)$ values has been acquired for isotopes in and around the 'Island of Inversion'. However, these data may only be interpreted consistently by knowing the monopole strength $\rho^2(E0)$. This quantity

allows to draw conclusions on the configuration mixing of the differently deformed 0^+ states residing in neighbouring potential minima. In a simplified two-level mixing model this configuration mixing is expressed by the mixing amplitude a, which can be extracted using the E0 transition strength $\rho^2(\text{E0})$ and the $B(\text{E2})$ values, as will be discussed in Sect. 3.

Outline of the thesis

In the next chapter the theoretical background of shell modifications leading to the 'Island of Inversion' is presented in the shell model approach. Also the Relativistic Hartree-Bogoliubov model and different Beyond Mean Field approaches are presented. Results of these calculations will be discussed and compared to experimental values in chapter 8. Chapter 3 is dedicated to shape coexistence and the spectroscopic information obtained from the monopole transition strength. In chapter 4 the properties of the Mini-Orange spectrometer, which was used for the measurement, are explained. In chapter 5 the 1789 keV level is discussed as a candidate for the 0_2^+ state and the E0 transition intensity is estimated. Chapter 6 is dedicated to the discussion of several online and offline experiments performed in order to optimise the sensitivity limit of the experimental setup with respect to background suppression, which turned out to be the key issue of the experiment. In chapter 7 the experimental results leading to the identification of the 0_2^+ state in ^{30}Mg will be presented. In chapter 8 the experimental results are interpreted within their physical context. In the last chapter an outlook to the potential of an application of this technique to the identification of the 0_2^+ state in ^{32}Mg is presented.

2 The 'Island of Inversion' around N = 20

2.1 Experimental evidence

First experimental evidence on the existence of irregularities in the binding energies of neutron-rich $A \simeq 32$ nuclei and the suggestion that this might be connected to nuclear deformation was first made by C. Thibault et al. [THI75] in measurements of the binding energies of $^{27-32}$Na isotopes. It was found that ^{31}Na and ^{32}Na were considerably more bound than predicted in calculations with spherical shapes. On the other hand it was confirmed by deformed Hartree-Fock calculations [CAM75].

Fig. 2.1 shows the two-neutron separation energy S_{2n} for F, Ne, Na, Mg, Al and Si isotopes around the 'Island of Inversion'. In such a diagram a shell closure is indicated by a sudden drop of the separation energies. It can be seen, however, that the Ne,
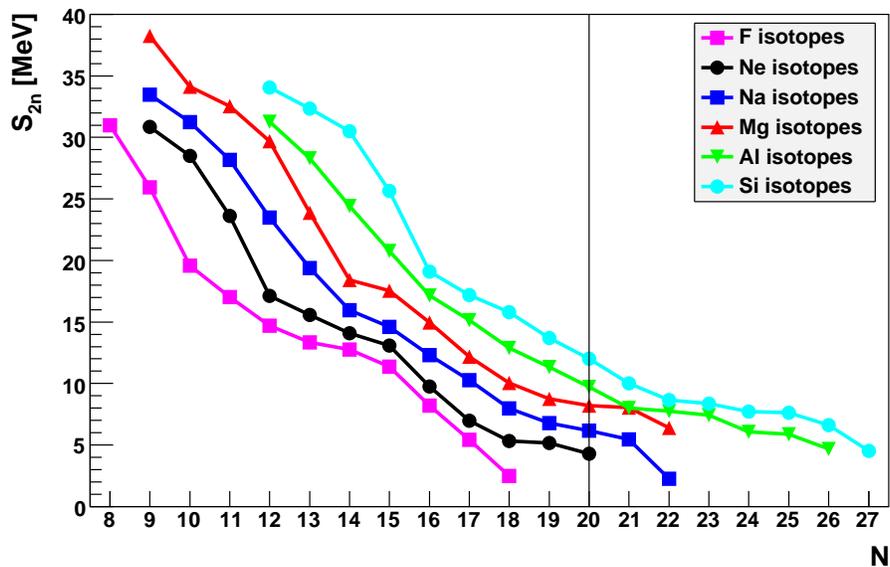
Figure 2.1: Measured two-neutron separation energies for nuclei around the 'Island of Inversion'. The $S(2n)$ values of Ne, Na and Mg isotopes around $N = 20$ exhibit a reduced slope compared to neighbouring elements, indicating a deviation from the shell closure. The data are taken from [AUD03, AUD06].
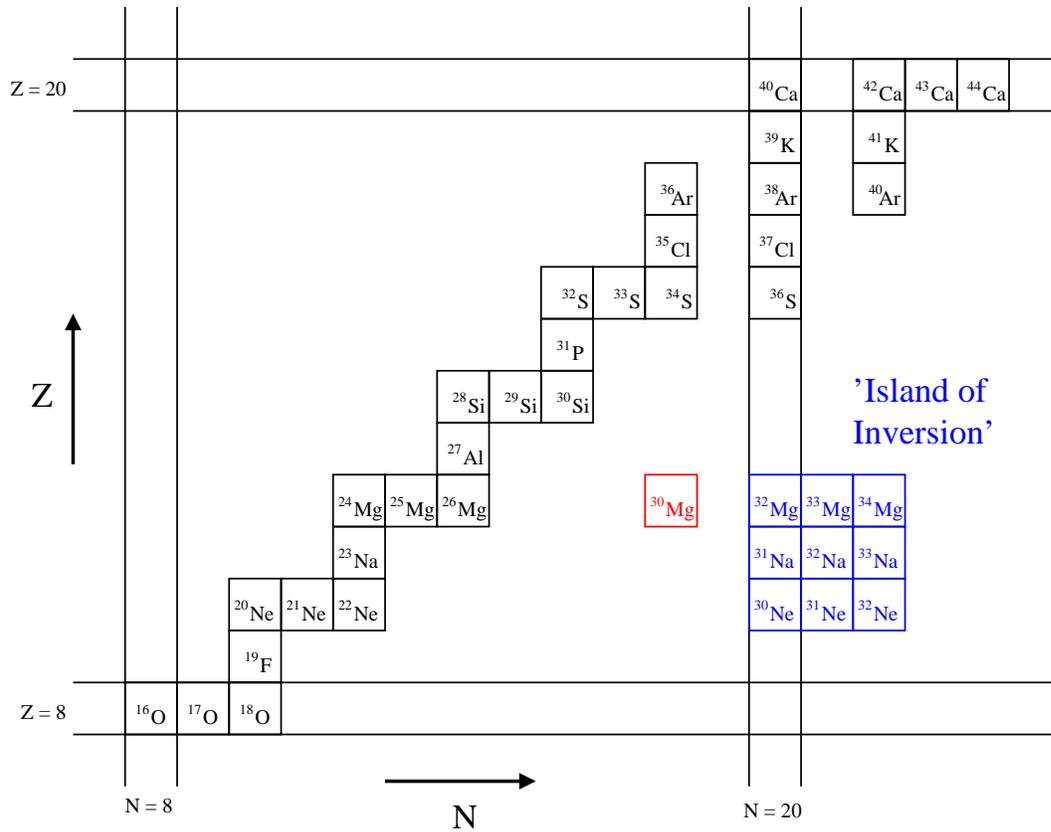
Figure 2.2: The nuclei inside the 'Island of Inversion' are marked in blue [WAR90]. These nuclei are characterised by a deformed intruder state becoming the ground state in coexistence with a spherical excited state with the same spin and parity. Also ^{30}Mg, which is the main issue of this work, is indicated. This nucleus is located outside of the 'Island of Inversion'. The magic numbers 8 and 20 correspond to a complete filling of the $(1s, 1p)$ and $(1s, 1p, 2s, 1d)$ shell, respectively.

Na and Mg isotopes rather show a reduced slope of the decreasing separation energy around $N = 20$ compared to, neighbouring elements.

Presently, the so-called 'Island of Inversion' [WAR90] is understood as a region of light neutron-rich nuclei around $N \sim 20$ with a coexistence of states with the same spin and parity but different deformations. For nuclei inside the 'Island of Inversion' the deformed state is the ground state, while this relation is reversed for isotopes outside the 'Island of Inversion'. Fig. 2.2 displays in blue the supposed location of the 'Island of Inversion' in the nuclear chart [WAR90].

The prototype of a nucleus inside the 'Island of Inversion' is ^{32}Mg, while ^{30}Mg, which is the isotope of interest of this work, is supposed to be located by one neutron pair outside the 'Island of Inversion'. ^{30}Mg consists of 18 neutrons and is expected to have a spherical 0_1^+ ground state. The half-life of the 1789 keV level was measured in a fast
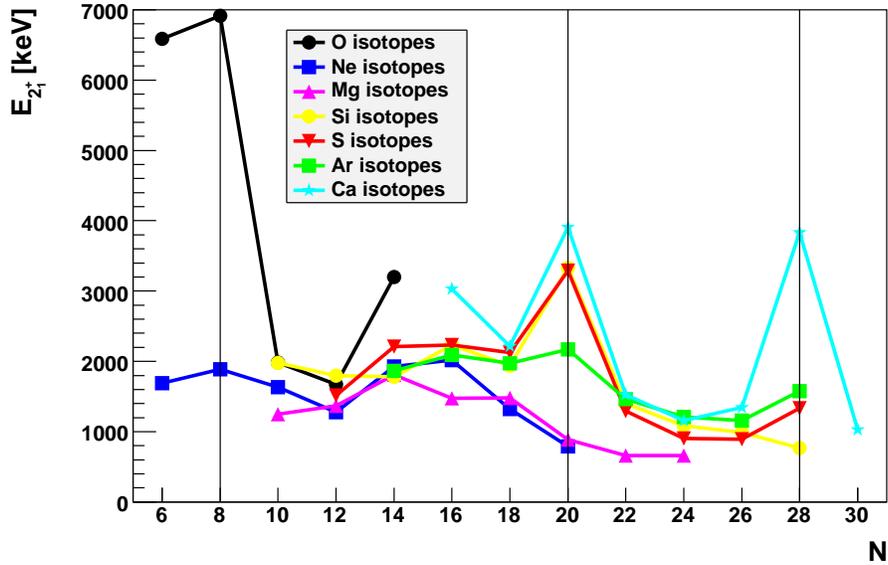
Figure 2.3: Excitation energy of the 2_1^+ state for various elements around the 'Island of Inversion'. The magic shell closures at $N = 8$, 20 and 28 are indicated. ^{34}Si, ^{36}S, ^{38}Ar and ^{40}Ca reveal the magic shell closure at $N = 20$ in contrast to ^{32}Mg and ^{30}Ne, which is also an indication for the occurrence of deformation in this mass region.

timing $\beta\gamma\gamma$ coincidence experiment by H. Mach et al. to be $t_{1/2} = 3.9(4)$ ns [MAC05], which is too long for a normal γ transition between low-spin states. Because of this result this state was discussed to be the 0_2^+ state decaying via a weak E0 transition to the 0^+ ground state, which will be discussed in Sect. 5.1. This triggered our search for the E0 transition in ^{30}Mg via measuring the conversion electron transition at 1788 keV. Another possible interpretation is, that this state is a high-spin isomeric state.

Fig. 2.3 displays the excitation energies of the 2_1^+ state in this region. The shell closure at $N = 8$ can clearly be seen in ^{16}O (and smaller in ^{18}Ne) due to the high excitation energy. Also the $N = 28$ shell closure is indicated in the ^{44}S, ^{46}Ar and ^{48}Ca isotopes. The excitation energies of the 2_1^+ state in the ^{34}Si, ^{36}S, ^{38}Ar and ^{40}Ca isotopes reveal the shell closure at $N = 20$. In the Ne and Mg isotopes the excitation energy of the 2_1^+ state is decreasing, while crossing the neutron number $N = 20$. This is a strong indication for a weakening of the $N = 20$ shell closure in the Ne and Mg isotopes.

More recently the transition probabilities of the E2 transition from the 0_{gs}^+ to the 2_1^+ state were measured. The results of measurements at different facilities (MSU [PRI99], RIKEN [YAN03, MOT95, IWA01], ISOLDE [NIE05, SCH05] and GANIL [CHI01]) in the Ne and Mg isotopes are shown in Fig. 2.4. The B(E2) values in ^{28}Ne and ^{30}Mg are smaller compared to ^{30}Ne and ^{32}Mg. Also theoretical calculations described in [NIE05] reproduce the experimental values in ^{30}Mg, consisting of a pure sd configuration, and in ^{32}Mg, consisting of a pf configuration, rather well. This is an indication of a well
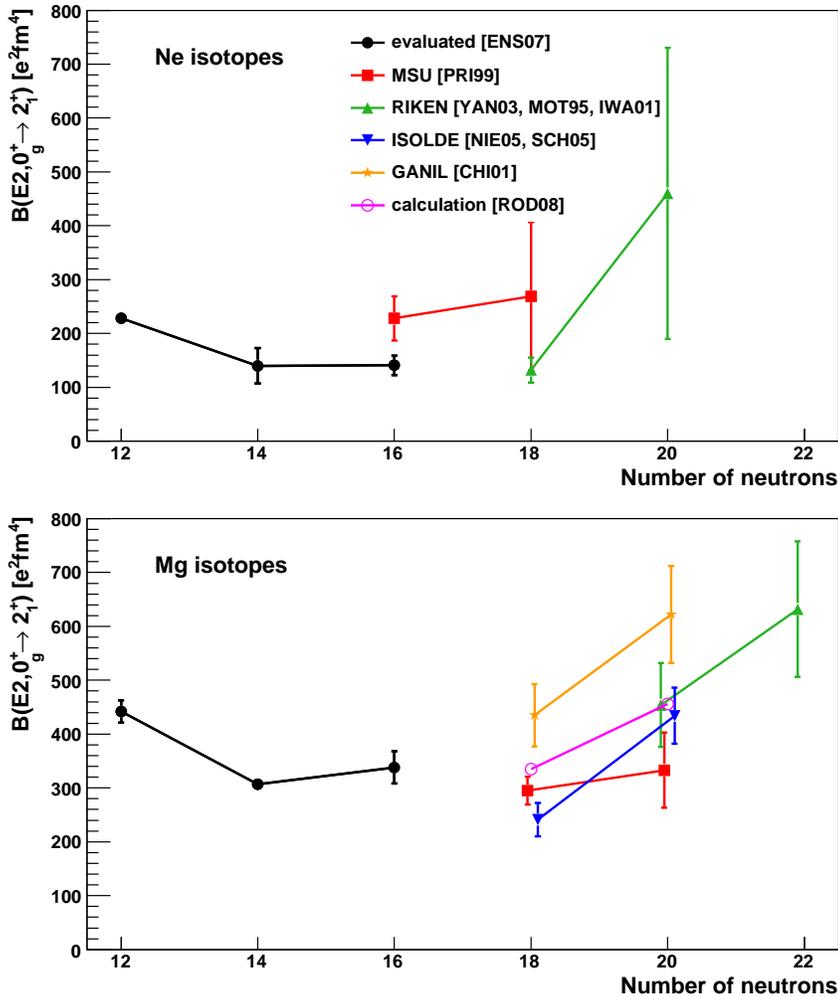
Figure 2.4: $B(\text{E2}; 0^+_{\text{gs}} \rightarrow 2^+_1)$ values in even-even Ne and Mg isotopes measured at different facilities. Also the result of a theoretical calculation [ROD08] is indicated.

deformed ground state in ^{30}Mg and a highly deformed intruder state (see Sect. 2.4.4) in ^{32}Mg. Also the results of Beyond Mean Field calculations by T.R. Rodriguez and J.L. Egido [ROD08] are shown and discussed later on in Sect. 8.2.2.

These experimental findings give evidence for a weakening of the $N = 20$ shell gap in the neutron-rich neon and magnesium isotopes.

2.2 Overview of theoretical approaches

During the last decades more and more phenomena in exotic neutron-rich nuclei were studied experimentally. Also the modern nuclear structure theory has evolved following

the experimental trend to describe phenomena in regions of exotic short-lived nuclei far from the valley of stability and astrophysical applications. The main challenge of theory is to describe nuclear properties, excitations and reactions in a consistent microscopic framework.

Thus the 'Island of Inversion' is concerned with the occurrence of deformed shapes and the coexistence with more regular spherical shapes. The theoretical description of such phenomena can be performed in various models with more or less microscopic input. Some of these models will be briefly discussed in the following sections.

The Nilsson model (Sect. 2.3) is an empirical shell model in which the nucleons move without interactions (Independent Particle Model, IPM).

In the interacting shell model (usually just called the Shell Model, SM) the nucleons in the active shells move in a spherical basic potential (usually a harmonic oscillator or Woods-Saxon potential), but they are subject to residual interactions. All possible configurations of the nucleons are generated and diagonalised with the residual interaction. Than it may occur that a configuration, which is at higher energy, without interactions is lowered and may even compete with the ground state. Such configurations are called 'intruder configurations' and represent $np - nh$ configurations relative to the unperturbed ground state. This approach and the specific features of the interactions responsible for this are discussed in Sect. 2.4.

The above shell model is usually formulated non-relativistically. Recently a relativistic field-theoretical formulation for the nuclear many body problem has been widely discussed and successfully applied. The Relativistic Mean Field model (RMF) is introduced in Sect. 2.5.

In a mean-field model the independent nuclear orbitals are calculated self-consistently in a potential, which is generated by the mean nuclear field. This is generally the Hartree-Fock method and its variants. The RMF model is basically a Hartree approach, where the exchange term is effectively parameterised in a density functional. Pairing is the most important residual interaction and can self-consistently be included in a Hartree-Fock-Bogoliubov (HFB) or, here, the relativistic Hartree-Bogoliubov (RHB) method. RMF calculations may also yield deformed results.

However, the RMF approach is still an independent particle method. To describe the shape coexistence phenomena, one has to be beyond the mean field. The interacting SM described above is one way. Another is the Generator Coordinate Method (GCM). Here a state is described as a continuous superposition of states of different deformations and the energy of such an ansatz is minimised.

This procedure, based on deformed non-relativistic HFB and relativistic HB calculations, is described finally in Sect. 2.6. This approach will finally be compared to our experimental results.

2.3 The Nilsson model

Far from closed shells the nuclei are permanently deformed. For these nuclei a deformed single-particle potential is assumed [RIN80]. The idea of the deformed shell model was first proposed by Nilsson and thus it is often called the Nilsson model. It describes the single-particle motion in a deformed mean field potential. The deformed oscillator potential can be written as

$$V_{\text{osc}} = \frac{1}{2} M \left[\omega_\perp^2 (x^2 + y^2) + \omega_z^2 z^2 \right] \tag{2.1}$$

in the shape of a spheroid [NIL69]. Introducing the deformation parameter ϵ, $\omega_\perp$ and ω_z can be defined as

$$\omega_\perp = \omega_0(\epsilon) \left(1 + \frac{1}{3}\epsilon \right) \text{ and } \omega_z = \omega_0(\epsilon) \left(1 - \frac{2}{3}\epsilon \right). \tag{2.2}$$

A single nucleon orbit in a deformed nucleus can be described by the interaction of the valence nucleon with the core. This interaction depends on the relative orientation of the orbit with respect to the time-averaged shape of the deformed core. The degeneracy of the substates in the spherical case will be lifted according to the projection of the spin j onto the symmetry axis of the deformed nucleus ($\Omega = j, j - 1, \ldots, -j$). The amount of energy splitting between the substates depends on the relative interaction of the Ω-orbits with the deformed nucleus.

The Nilsson model describes the splitting of the Ω-states as a function of deformation. Fig. 2.5 displays the splitting of the single-particle orbits as a function of the deformation parameter β_2 around the region of interest. The deformation parameter β_2 can be calculated from the quadrupole deformation ϵ used in the oscillator model according to $\epsilon_2 \approx 1.05\beta_2$ [BOH69]. The labelling of the orbits is $\Omega[N, n_z, \Lambda]$. N is the quantum number of the major oscillator shell, n_z is the number of quanta associated with the wave function moving along the z-direction and Λ is the projection of the orbital angular momentum onto the z axis. In the Nilsson model Ω is the only good quantum number of an orbital, otherwise it is a superposition of different spherical states nlj. From the correlation diagram like Fig. 2.5 one may see, however, that a deformed level originates from a spherical one. One often denotes a Nilsson orbit by the corresponding spherical one.

It is indicated in blue how in case of ^{32}Mg a strongly deformed ground state consisting of a pf intruder configuration at $\beta \approx 0.5$ (full circles) is energetically more favourable than a spherical ground state at $\beta \approx 0.1$ (open circles). In case of the deformed configuration the $1/2\,[330]$ orbit is located relatively lower than the $1/2\,[200]$ orbit with respect to the dashed black line, which results in a reduced total energy.
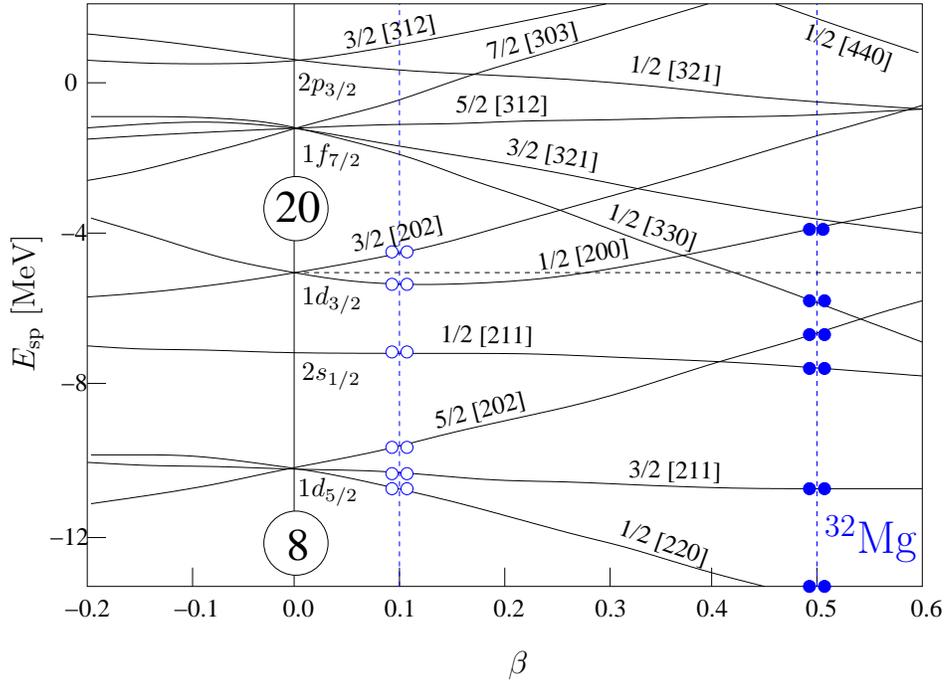
Figure 2.5: Neutron single-particles energies as a function of the deformation parameter β calculated by Nilsson et al. [NIL69]. For ^{32}Mg it is indicated in blue that a strongly deformed ground state at $\beta \approx 0.5$ (full circles) is energetically more favourable than a spherical ground state at $\beta \approx 0.1$ (open circles). In case of the deformed configuration the $1/2$ [330] orbit is located relatively lower than the $1/2$ [200] orbit with respect to the dashed black line, which results in a reduced total energy.

2.4 Shell model approach to the 'Island of Inversion'

2.4.1 Energy levels and shell closures

In the nuclear shell model [BER92, BOH69, BOH75, CAS90] the wave function of the nucleons (protons and neutrons) is described as the solution of the Schrödinger equation

$$\mathcal{H}|\Psi\rangle = E|\Psi\rangle \tag{2.3}$$

with the Hamilton operator

$$\mathcal{H} = \sum_{i=1}^{A} T_i + \sum_{\substack{i,j=1 \\ i<j}}^{A} V_{ij} + \sum_{\substack{i,j,k=1 \\ i<j<k}}^{A} V_{ijk} \tag{2.4}$$
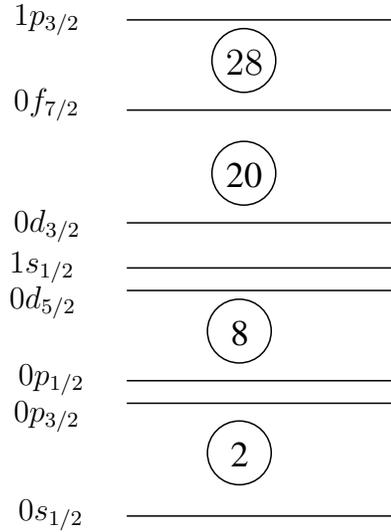
Figure 2.6: Single-particle energy levels for light nuclei with $A < 50$. The level structure is similar for protons and neutrons. The resulting shell closures known as the 'magic numbers' are indicated in circles.

where T_i is the kinetic energy of the ith particle and V_{ij} is the two-body interaction potential between the particles i and j. In modern SM calculations also three-body interactions V_{ijk} are included for precision descriptions of light nuclei [PIE01]. The wave functions of the particles are given by $|\Psi\rangle$. Since each particle interacts with all other particles, the exact many-body solution of Eq. (2.3) is very complicated. In the SM one first assumes a single particle potential

$$V_i = V_c(r_i) + V_{ls}(r_i)\mathbf{l}_i\mathbf{s}_i \qquad (2.5)$$

consisting of an attractive central potential $V_c(r_i)$ and the spin-orbit-term $V_{ls}(r_i)\mathbf{l}_i\mathbf{s}_i$. A Harmonic-Oscillator or Woods-Saxon type potential has to be assumed for the nuclear potential. The spin-orbit term depends on the relative orientation of the nucleon spin $\mathbf{s}$ and the angular momentum $\mathbf{l}$, resulting in a momentum $\mathbf{j}$ with the quantum numbers $j = l \pm s$. The nucleons in the single particle states of this potential are than subject to the residual interaction V_{ij}. The potential with its single-particle levels are chosen to correspond to the empirical single-particle level schemes for stable nuclei.

The single-particle energy levels for light nuclei with $A < 50$ with similar structure for protons and neutrons are shown in Fig. 2.6. Each level is populated by $2 \cdot (2l + 1)$ particles according to the angular momentum of the state. Large energy differences between two levels are shell closures leading to the 'magic numbers', which are the same for protons and neutrons for light nuclei. The first magic nucleon numbers are 2, 8, 20 and 28. Isotopes or isotones with closed proton or neutron shells are more stable compared to nuclei without closed shells. They are characterised by a spherical ground state and a large excitation energy of the 2_1^+ state of typically several MeV.

2.4.2 Residual interaction

The Skyrme interaction

In order to calculate the three-body interaction V_{ijk} Skyrme et al. [SKY56, SKY59] proposed an effective interaction with a three-body-term

$$V = \sum_{i<j} V(i,j) + \sum_{i<j<k} V(i,j,k). \tag{2.6}$$

For the three-body force a zero range force

$$V(1,2,3) = t_3 \delta(r_1 - r_2)\delta(r_2 - r_3) \tag{2.7}$$

was assumed.

Several sets of parameters called Skyrme I, II, etc. are existing resulting from different fits to experimentally determined binding energies and radii.

The Hamiltonian formulated as a Hartree-Fock equation is:

$$\left(-\nabla \frac{\hbar^2}{2m^\star(r)}\nabla + U(r) + W(r)\frac{1}{\imath}(\nabla \times \sigma)\right)\phi_i(r) = \epsilon_i \phi_i(r) \tag{2.8}$$

with an effective mass $m^\star(r)$, an average field $U(r)$ and a one-body spin-orbit potential $W(r)$. This equation gives the wave functions.

The Gogny interaction

Despite the great success of the Skyrme interaction, zero range forces might not be able to simulate the long range or even the intermediate range parts of the effective interaction. In detail the present versions of the Skyrme force are not able to describe pairing correlations properly. Therefore Gogny replaced parts of the Skyrme force by a sum of two Gaussians with spin-isospin exchange mixture [RIN80].

The resulting non-local Schrödinger equation is

$$\left(-\frac{\hbar^2}{2m}\Delta + \Gamma_H(r)\right)\phi_k(r) + \int dr' \Gamma_{ex}(r,r')\phi_k(r') = \epsilon_k \phi_k(r) \tag{2.9}$$

with the local Hartree potential $\Gamma_H(r)$ and the non-local or exchange potential $\Gamma_{ex}(r,r')$. This equation contains a self-consistency problem. The equations can be solved by iteration, starting with a set of phenomenological shell model wave functions to calculate $\Gamma_H(r)$ and $\Gamma_{ex}(r,r')$ as a first step.
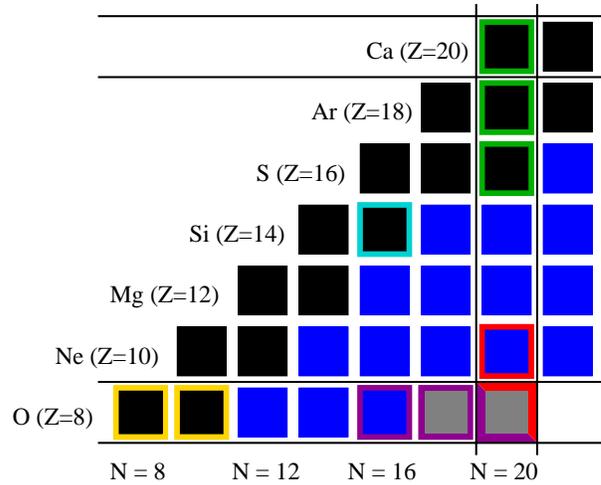
Figure 2.7: Part of the nuclear chart around the shell closure at $N = 20$. Only even-even nuclei are shown. The stable nuclei are marked in black, neutron-rich β-unstable nuclei are marked in blue and particle-unstable nuclei are marked in grey. Isotopes whose shell structure will be discussed in this section are indicated by a green, a cyan, a yellow, a magenta and a red frame.

2.4.3 Modification of shell closures in exotic neutron-rich nuclei

In this section the physical background of interactions in the shell model leading to a modification of shell closures will be explained. This background knowledge is important for the understanding of shape coexistence and deformations in exotic neutron-rich nuclei.

Fig. 2.7 shows a part of the nuclear chart in the vicinity of the 'Island of Inversion'. Only even-even nuclei around the shell closure at $N = 20$ are shown. The stable nuclei are marked in black, while the neutron-rich β-unstable bound nuclei are marked in blue and particle-unstable nuclei are marked in grey. The single-particle levels along the magic number $Z = 8$ are shown in Fig. 2.8. The stable isotopes ^{16,18}O are marked by a yellow frame and the position of the neutron-rich nuclides ^{24,26,28}O in the nuclear chart is indicated by a magenta frame. ^{24}O is bound, as indicated by the blue square in Fig. 2.7, while the isotopes ^{26,28}O are unbound, as indicated by the grey square. The stable nucleus ^{30}Si is marked by a cyan frame and will be discussed as an example of a stable nucleus with modified structure compared to ^{24}O with the same number of neutrons ($N = 16$). Also the shell structure along the magic number $N = 20$ is shown in Fig. 2.9. Here, the stable $N = 20$ nuclei ^{36}S, ^{38}Ar and ^{40}Ca are indicated by a green frame and the neutron-rich unstable isotopes ^{28}O and ^{30}Ne are marked by a red frame. The nucleus ^{30}Ne is bound, which is indicated by the blue square.

In the following results of SM calculations by T. Otsuka and his group [UTS99, OTS01, OTS02] will be discussed. In these calculations a residual interaction, named GXPF1,
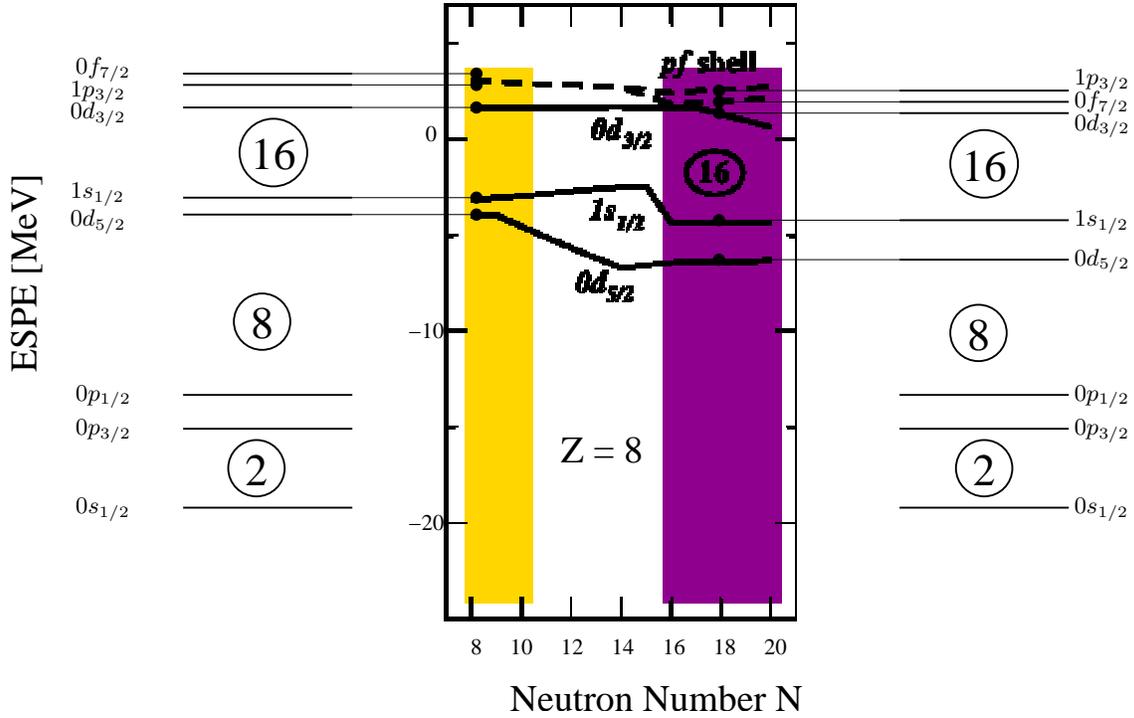
Figure 2.8: Effective neutron single-particle energies (ESPE) for oxygen isotopes from $N = 8$ to $N = 20$ [OTS02]. The stable isotopes ^{16,18}O are marked by the yellow band according to Fig. 2.7 and the neutron-rich isotopes ^{24,26,28}O are marked in magenta. Since the ESPE of the $0d_{3/2}$ shell is above zero, ^{26,28}O are unbound. Also the single-particle energy levels are indicated for ^{16,18}O (left) and for ^{24,26,28}O (right). A large shell gap between the $0d_{3/2}$ and the $1s_{1/2}$ orbits exists for oxygen isotopes in general, which becomes even wider for $N > 14$. This provides a magic nucleus ^{24}O at $N = 16$.

was determined and used successfully in many light and medium heavy nuclei. A large basic space and Monte Carlo techniques are used to solve the diagonal problem. In such calculations effective single-particle energies (ESPE) can be calculated, which are given by the monopole part of the Hamiltonian and thus reflect the angle-averaged effect of the two body interactions.

In order to understand the single-particle properties of a nucleus, effective (spherical) single-particle energies (ESPE) are discussed. The ESPE of an occupied orbit is the negative energy required to remove a nucleon from this orbit.

Fig. 2.8 shows the ESPE for oxygen isotopes ($Z = 8$) as calculated in the shell model by Otsuka et al. [OTS02]. The gap between the $0d_{3/2}$ and the $1s_{1/2}$ orbits is almost constant for $^{16-22}$O isotopes. For oxygen isotopes with $N > 14$ the shell gap increases. For $N = 16$ a significant gap of about 6 MeV is found. This represents a large energy gap comparable to the $sd - pf$ shell gap in the doubly magic nucleus ^{40}Ca. Since the $0d_{3/2}$ orbit has a positive single-particle energy, oxygen isotopes heavier than ^{24}O are
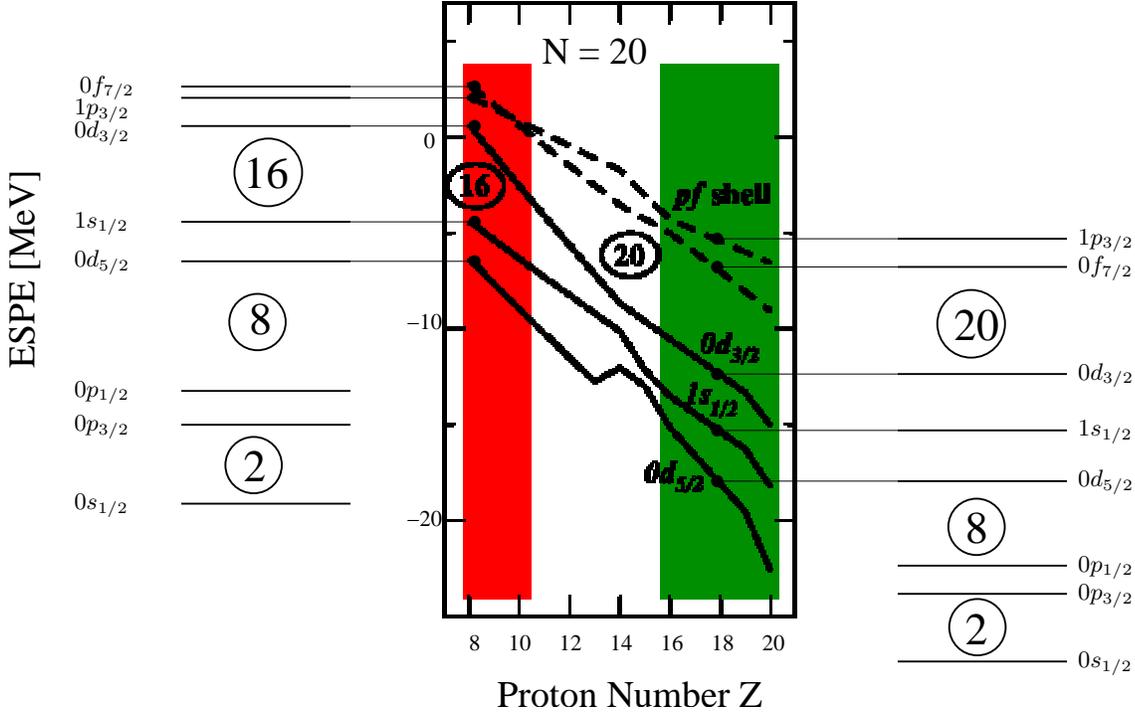
Figure 2.9: Effective single-particle energies of neutrons from $N = 20$ isotones for $Z = 8$ to 20 [UTS99, OTS02]. The stable isotones ^{36}S, ^{38}Ar and ^{40}Ca are marked in green according to Fig. 2.7, while the neutron-rich isotones ^{28}O and ^{30}Ne are marked in red. The ESPE gap between the $0d_{3/2}$ shell and the $1s_{1/2}$ orbital becomes wider for neutron-rich nuclei with $Z < 14$ and the ESPE gap between the $0d_{3/2}$ shell and the $0f_{7/2}$ shell becomes narrower. The single-particle energy levels are indicated for ^{28}O (left) and for ^{38}Ar (right). This illustrates a change of the magic shell closure along the $N = 20$ isotones from stable nuclei (magic shell closure at $N = 20$) to neutron-rich unstable nuclei (magic shell closure at $N = 16$).

unbound in agreement with experimental data [GM90]. In lighter oxygen isotopes the valence nucleons predominantly occupy the $0d_{5/2}$ orbit, and are thus not much affected by the $0d_{3/2}$ – $1s_{1/2}$ gap. The increase of the shell gap becomes more relevant for $N > 14$, providing a new magic number at $N = 16$.

Fig. 2.10 shows the calculated neutron ESPEs for the stable ^{30}Si nucleus and the exotic neutron-rich ^{24}O isotope [OTS01, OTS02]. Both nuclei have 16 neutrons. In the stable ^{30}Si nucleus a considerable gap (~ 4 MeV) exists between the $0d_{3/2}$ shell and the pf shell as expected in the valley of stability. In the neutron-rich ^{24}O nucleus the $0d_{3/2}$ orbit is found to be very close to the pf shell. Also the shell gap between the $1s_{1/2}$ and the $0d_{3/2}$ shell is even larger (~ 6 MeV) compared to the stable ^{30}Si nucleus (~ 2 MeV).

This interaction process between the neutrons and the protons is described with the two-body interaction
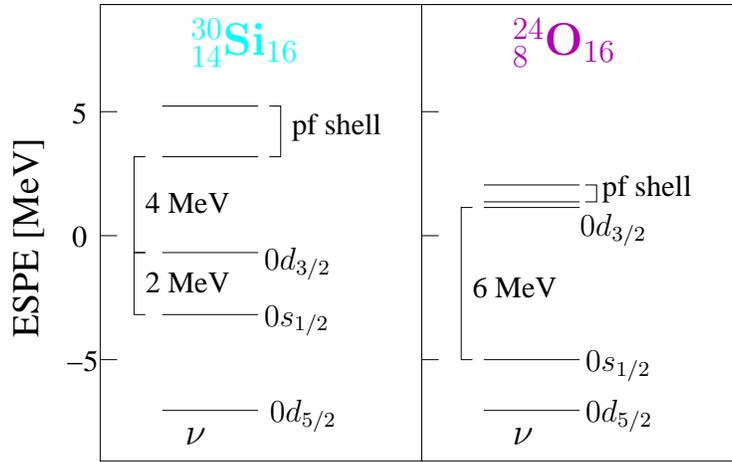
Figure 2.10: Effective neutron single-particle energies for ^{30}Si and ^{24}O [OTS01, OTS02].
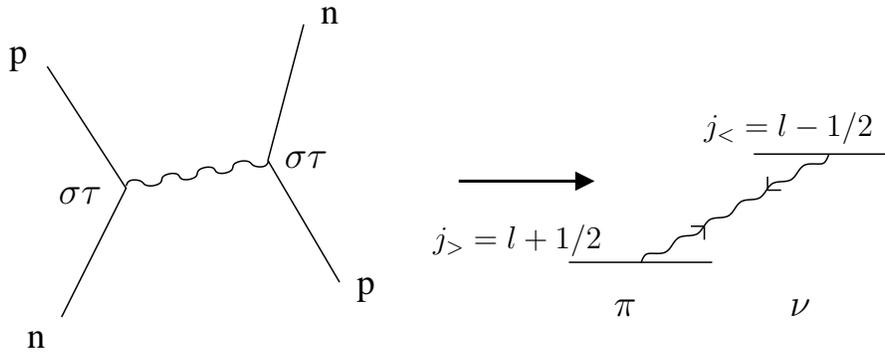
Figure 2.11: $\sigma\tau$ interaction between protons and neutrons with the same angular momentum l as described in [OTS01, OTS02]. An attractive force between the $j_> = l + 1/2$ and the $j_< = l - 1/2$ orbit causes the lowering of the $0d_{3/2}$ level in ^{30}Si compared to ^{24}O (see Fig. 2.10).

$$V_{\tau\sigma} = (\tau\tau) \cdot (\sigma\sigma) \cdot f_{\tau\sigma}(r) \tag{2.10}$$

with the scalar product of the isospin operator $(\tau\tau)$ and the spin operator $(\sigma\sigma)$ of the two nuclei and a function $f_{\tau\sigma}(r)$ depending on the distance r between two interacting nuclei [OTS01, OTS02]. The operator σ couples $j_>$ to $j_<$ (and $j_<$ to $j_>$) much stronger than $j_>$ to $j_>$ or $j_<$ to $j_<$ and thus the spin-flip process is favoured. This mechanism works similar for the τ operator. Combining these two properties results in $V_{\tau\sigma}$ matrix elements that are large for the spin-flip, isospin-flip process: proton in $j_>$ coupled to neutrons in $j_<$ and vice versa.

This change of the shell structure is caused by the strongly attractive $\sigma\tau$ interaction between protons and neutrons with the same angular momentum l as schematically shown in Fig. 2.11. The $j_> = l + 1/2$ proton orbits and $j_< = l - 1/2$ neutron orbits

with the same angular momentum l interact with each other. When increasing Z from 8 to 14 (from ^{24}O to ^{30}Si), 6 protons are added into the $0d_{5/2}$ shell. Due to a strong attraction between a proton in the $0d_{5/2}$ shell and a neutron in the $0d_{3/2}$ shell, the more protons are added into the $0d_{5/2}$ shell, the stronger a neutron in the $0d_{3/2}$ shell is bound and the ESPE of the $0d_{3/2}$ shell decreases with increasing proton number.

In stable nuclei with $N \sim Z$ with similar occupancy of the $j_>$ orbit in the valence shell, the proton (neutron) $j_<$ orbit is lowered by neutrons (protons) in the $j_>$ orbit, respectively. In exotic nuclei this lowering of the $0d_{3/2}$ shell can be absent, because the orbits are not occupied symmetrically. In this case the $0d_{3/2}$ orbit is located rather high, close to the upper shell.

In Fig. 2.9 the ESPE for $N = 20$ isotones are displayed [UTS99, OTS02]. The ESPE gap between the $0d_{3/2}$ shell and the $1s_{1/2}$ becomes even wider for neutron-rich nuclei with $Z < 14$ and the ESPE gap between the $0d_{3/2}$ shell and the $0f_{7/2}$ shell becomes narrower as the neutron number decreases. This causes the disappearance of the magic number $N = 20$ for exotic nuclei $Z = 9 - 14$ in favour of a new magic number $N = 16$ for ^{24}O.

2.4.4 Intruder states in the region of Magnesium isotopes

An intruder state describes a proton or neutron excitation over the large shell gap of a closed shell into the next higher-lying oscillator shell. This can be a $1p - 1h$ (1 particle – 1 hole) configuration or, as shown in Fig. 2.12, a $2p - 2h$ configuration. The $2p - 2h$ intruder configuration in this case has the same spin and parity (0^+) as the ground state.

The more valence nucleons are available (see Sect. 2.4.3), the larger the shell gap turns out to be. Thus the 'normal' $0p - 0h$ configuration corresponds to a spherical nuclear ground state as shown in Fig. 2.12 for ^{40}Ca, while the $2p - 2h$ intruder configuration, exemplary shown for ^{32}Mg in the right column of Fig. 2.12 corresponds to a deformed nuclear shape. Since the attractive $p - n$ interaction influences the size of the shell gap as a function of N and Z as described in Sect. 2.4.3, the intruder state excitation energies are lowered relative to the unperturbed (no $p - n$ interaction) values. If the energy gain due to dynamical correlations including deformation exceeds the energy loss in promoting nucleons across the shell gap, an intruder state can become the ground state. An example of such a nucleus is ^{32}Mg. This effect gives rise to the existence of the so-called 'Island of Inversion' around $N \sim 20$ (see Sect. 2).

Since the neutron shell gap is rather constant as a function of the neutron number, the correlation energy of the transition from a normal to an intruder ground state within an isotopic chain and its relative magnitude compared to the shell gap depends on the neutron number.

Fig. 2.13 schematically sketches the correlation energy of normal and intruder states for semi-magic (closed neutron shell) and open-shell nuclei [UTS04]. In Fig. 2.13(a) only the arrangement of the protons is relevant for the correlation energy, which is rather

Figure 2.12: Schematic drawing of a "normal" sd – shell configuration in the valley of stability (for example ^{40}Ca) and an $sd - pf$ - shell intruder configuration around the 'Island of Inversion' (for example ^{32}Mg). Due to the $\sigma\tau$ interaction described in Sect. 2.4.3, the shell structure of the intruder configuration differs significantly from the configuration in the valley of stability.

small in general. In the intruder configuration shown in Fig. 2.13(b) the correlation energy is very large due to the large number of particles and holes in active orbits. Also the interaction between protons and neutrons produces a much larger correlation energy than the interaction between nucleons of the same kind. This results in a much larger correlation energy of the intruder configuration compared to the normal configuration, thus favouring the intruder inversion even in the presence a large shell gap.

An open shell nucleus as shown in Figs. 2.13(c) and 2.13(d) already offers a neutron hole, thus increasing the neutron correlation energy. In this case strong proton-neutron two-body matrix elements contribute to the correlation energy. The intruder configurations in Fig. 2.13(d) gain correlation energy similar to the semi-magic intruder configuration (Fig. 2.13(b)). The difference in the correlation energies between the normal and the intruder configuration is larger in semi-magic nuclei than in open-shell nuclei, because of the saturation of the correlation energy in case of Fig. 2.13(d). This implies that for open-shell nuclei ($N < 20$) the intruder configuration becomes less favoured.

In this chapter it was demonstrated, that due to the $\sigma - \tau$ interaction the shell structure

Figure 2.13: Schematic illustration of the sources for the correlation energy between proton (π) and neutron (ν) orbits. Shown is a comparison between an intruder configuration and the "normal" configuration in case of semi-magic nuclei (i.e. exhibiting a closed neutron shell)(a) and (b) and open-shell nuclei (c) and (d). Typical configurations for these nuclei are shown. The proton-neutron interaction is illustrated by thick wave lines, while the proton-proton and the neutron-neutron interactions are illustrated by thin wave lines [UTS04].

changes and new shell gaps appear. This also may lead to deformed ground states in neutron-rich exotic nuclei at shell closures and to the 'Island of Inversion'.

2.5 The Relativistic Hartree-Bogoliubov model

As a relativistic theory a model is not formulated with a many-body Hamiltonian but using a Lagrange density $\mathcal{L}$. Then the model describes an interacting system of nucleons (p, n, possibly including excited nucleons like Δ or N^*) and mesons (σ, ω, ρ, δ, π ...). The Lagrangian has to be postulated. It is not derived from QCD, but symmetries are retained. Different assumptions correspond to different energy densities as a function of the density. Thus the problem is related to Energy Density Functional (EDF) theory [VRE05]. This models are often called Quantum Hadrodynamics (QHD).

The determination of the Hamiltonian or Lagrangian can be done in various ways: One is a phenomenological way. Here the energy density functional is parameterised and fitted to nuclear matter and/or finite nuclei [WAL95]. These models are usually treated in Hartree-approximation, called Relativistic Hartree or Relativistic Mean Field models.

In the standard representation of Quantum Hadrodynamics the nucleus is described as a system of Dirac nucleons coupled to the exchange mesons and the electromagnetic field through an effective Lagrangian. The isoscalar scalar σ-meson, isoscalar vector ω-mesons and the isovector vector ρ-meson build the minimal set of meson fields together with the electromagnetic field, which is necessary for a quantitative description of bulk and single-particle nuclear properties [RIN80, VRE05]. The model is defined by the Lagrangian density

$$\mathcal{L} = \mathcal{L}_N + \mathcal{L}_m + \mathcal{L}_{int} + \mathcal{L}_{der} + \mathcal{L}_{em}. \tag{2.11}$$

$\mathcal{L}_N$ denotes the Lagrangian of the free nucleon, $\mathcal{L}_m$ is the Lagrangian of the free meson fields and the minimal set of interaction terms is contained in $\mathcal{L}_{int}$, which is defined for the simplest assumption of exchange of σ- and ω-mesons with coupling constants g_s and g_v as

$$\mathcal{L}_{int} = -g_v \bar{\psi} \gamma^\mu \psi V_\mu + g_s \bar{\psi} \psi \phi, \tag{2.12}$$

where the vector current is $j^\mu = \bar{\psi} \gamma^\mu \psi$ and $\rho_s = \bar{\psi}\psi$ is the scalar density and ϕ and V^μ are the σ- and ω-fields, respectively.

When applied to finite nuclei, the model must include the coupling $\mathcal{L}^{em}$ of the protons to the electromagnetic field A^μ and derivative terms in $\mathcal{L}^{der}$. A medium dependence of the effective interaction can be included either by non-linear meson self-interaction terms in the Lagrangian or by assuming an explicit density dependency for the meson nucleon couplings [VRE05].

From the model Lagrangian density the classical variation principle leads to the equation of motion.

The single-nucleon Dirac equation is derived from the variation of the Lagrangian equation with respect to ψ:

$$[\alpha \left(-i\nabla + V(r)\right) + \beta \left(m + S(r)\right)] \psi_i(r) = \epsilon_i \psi_i(r). \tag{2.13}$$

The scalar potential $S(r)$ and the vector potentials $V(r)$ are

$$S = -\frac{g_\sigma^2}{m_\sigma^2} \rho_s, \tag{2.14}$$

and

$$V = \frac{g_\omega^2}{m_\omega^2} \rho_v \tag{2.15}$$

where m_σ and m_ω are the masses of the σ- and ω-mesons, respectively. The scalar density $\rho_s = \langle A|\bar{\psi}\psi|A\rangle$ and the vector density $\rho_s = \langle A|\psi^+\psi|A\rangle$ are taken as expectation values of the ground state $|A\rangle$, which are given in terms of the solution of the Dirac equation (2.13). Thus this method is a self-consistent determination of the single-particle wave functions and energies (Hartree method). The solutions of this self-consistent method is in general intrinsically deformed in open shell nuclei. The eigensolutions are characterised by the projection of the total angular momentum along the symmetry axis Ω_i, the parity π_i and the z component of the isospin t_i.

For the Beyond Mean Field method described in the next section one needs solutions of these equation with a prescribed deformation q. This is achieved by constrained RMF calculations in which the constraint is included by means of a Lagrange multiplier. These solutions are then given as $\psi_i(r, q)$.

For a quantitative description of structure phenomena in open-shell spherical and deformed nuclei it is essential to include pairing correlations in the self-consistent mean-field single-nucleon potential.

The Relativistic Hartree-Bogoliubov (RHB) theory provides a unified description of ph- and pp-correlations in nuclei. Formulating the self-consistent RHB equations in coordinate space, it allows also for a treatment of continuum effects in the presence of pairing. The RHB-wave function $|\Phi\rangle$ is defined as the vacuum of the quasi-particles:

$$\alpha_k^+ = \sum_n U_{nk} c_n^+ + V_{nk} c_n \tag{2.16}$$

with $\alpha_k|\Phi\rangle = 0$.

In the case of superfluid nuclei the density functional

$$E = E(\rho, \kappa) \tag{2.17}$$

depends on the normal density

$$\rho_{nn'} = \langle\Phi|c_{n'}^+ c_n|\Phi\rangle = \sum_k V_{nk}^* V_{n'k} \tag{2.18}$$

and the pairing tensor:

$$\kappa_{nn'} = \langle\Phi|c_{n'} c_n|\Phi\rangle = \sum_k V_{nk}^* U_{n'k}. \tag{2.19}$$

The variation with respect to ρ and κ gives two coupled equations for the RHB wave functions $U_k(r)$ and $V_k(r)$ with two potentials, the nominal mean field

$$h_D = \frac{\delta E'}{\delta \rho'} \tag{2.20}$$

and the pairing field

$$\Delta = \frac{\delta E}{\delta \kappa'}. \tag{2.21}$$

The Fermi surface $\rho^2 = \rho$ is no longer sharp, but there is still a constraint:

$$\hat{\rho}^2 - \hat{\rho} = \hat{\kappa}\hat{\kappa}^* \tag{2.22}$$

which means, that the quasi-particles are independent with the occupation numbers 0 and 1.

In the relativistic case this gives the relativistic Hartree-Bogoliubov equations [SER01, VRE05, RIN80], also known as the Dirac-Hartree-Bogoliubov equations, defined as:

$$\begin{pmatrix} h_D - \lambda & \Delta \\ -\Delta^* & -h_D + \lambda \end{pmatrix} \begin{pmatrix} U_k(r) \\ V_k(r) \end{pmatrix} = \begin{pmatrix} U_k(r) \\ V_k(r) \end{pmatrix} E_k \tag{2.23}$$

where h_D is the Dirac Hamiltonian, λ is a Lagrange parameter insuring the conservation of the particle number on the average, Δ is the pairing field, E_k is the quasi-particle energy and $V_k(r)$ and $U_k(r)$ are the quasi-particle wave functions.

These equations can be applied for a fully self-consistent description of open-shell nuclei, where the possible deformed mean field and the pairing field are determined simultaneously. Also the ground state properties of weakly bound nuclei far from stability can be described.

2.6 Beyond Mean Field Approach

A quantitative description of shell evolution, and in particular the treatment of shape coexistence phenomena, necessitates the inclusion of many-body correlations beyond the mean-field approximation. The starting point is usually a constrained HFB or RHB calculation of the potential energy surface with the mass quadrupole moment as constrained quantity.

2.6.1 The Generator Coordinate Method

The most effective approach for configuration mixing calculations is the generator co-ordinate method (GCM), with multipole moments used as coordinates that generate the intrinsic wave functions. The GCM is based on the assumption that approximate eigenstates of the nuclear Hamiltonian

$$|\Psi_\alpha\rangle = \sum_j f_\alpha(q_j)|\psi(q_j)\rangle \tag{2.24}$$

can be built from a set of mean-field states $|\phi(q)\rangle$ depending on the collective coordinate q:

$$q = \langle\Psi|Q_{20}|\Psi\rangle. \tag{2.25}$$

A detailed description of the GCM can be found in [RIN80]. The basis states $|\phi(q)\rangle$ are Slater determinants of single-nucleon states generated by solving the constrained HFB (non-relativistic) or RHB (relativistic) equations. Thus the mass quadrupole moment is used as the generating coordinate q. Since the axially deformed mean field breaks rotational symmetry, the basis states $|\phi(q)\rangle$ are not eigenstates of the total angular momentum. Since pairing is included, they are also not eigenstates of the neutron and proton number.

In the following this method is explained for the general case. In case of 0^+ states $K = 0$ and thus the calculation becomes more trivial. States with good angular momentum

$$|\Psi_\alpha^{JM}\rangle = \sum_{j,K} f_\alpha^{JK}(q_j)\hat{P}_{MK}^J|\phi(q_j)\rangle \tag{2.26}$$

are constructed using the angular-momentum-projected operator

$$\hat{P}_{MK}^J = \frac{2J+1}{8\pi^2}\int d\Omega D_{MK}^{J*}(\Omega)\hat{R}(\Omega) \tag{2.27}$$

with the rotation matrices [VAR88]

$$D_{MK}^J(\Omega) = e^{-\imath M\alpha}d_{MK}^J(\beta)e^{-\imath K\gamma}, \tag{2.28}$$

the rotation operator

$$\hat{R}(\Omega) = e^{-\imath\alpha\hat{J}_z}e^{-\imath\beta\hat{J}_y}e^{-\imath\gamma\hat{J}_z} \tag{2.29}$$

and the Euler angles $\Omega = [\alpha, \beta, \gamma]$. The weight functions $f_\alpha^{JK}(q_j)$ are determined from the variation

$$\delta E^J = \delta\frac{\langle\Psi_\alpha^{JM}|\hat{H}|\Psi_\alpha^{JM}\rangle}{\langle\Psi_\alpha^{JM}|\Psi_\alpha^{JM}\rangle} = 0. \tag{2.30}$$

Requiring that the expectation value of the energy is stationary with respect to an arbitrary variation δf_α^{JK} leads to the Hill-Wheeler equation

$$\sum_{j,K} f_\alpha^{JK}(q_j) \left[\langle \Phi(q_i)|\hat{H}\hat{P}_{MK}^J|\Phi(q_j)\rangle - E_\alpha^J \langle \Phi(q_i)|\hat{P}_{MK}^J|\Phi(q_j)\rangle \right] = 0 \qquad (2.31)$$

The basis states $|\Phi(q_j)\rangle$ are not eigenstates of the proton and neutron number operator $\hat{Z}$ and $\hat{N}$. The adjustment of the Fermi energies in a Hartree-Fock Bogoliubov calculation ensures only that the average value of the nucleon number operator corresponds to the actual number of nucleons. Consequently, the wave functions $|\Psi_\alpha^{JM}\rangle$ are generally not eigenstates of the nucleon number operators. Thus for more precise results also the proton and neutron numbers have to be projected using appropriate projectors $\hat{P}^N$ and $\hat{P}^z$ [RIN80]. The projection of angular momentum and particle numbers can be done after the variation (Eq. 2.31) or before, which obviously is the more accurate procedure.

In the following sections two particular calculations will be discussed. One is a calculation by T.R. Rodríguez and J.L. Egido [ROD08] using non-relativistic HFB states. The other by T. Nikšić and P. Ring [NIK08] uses relativistic constrained RHB states. The results of this calculations will be shown in Sect. 8.2 and compared to experimental data.

2.6.2 Non-relativistic BMF calculation

The BMF calculations by T.R. Rodríguez and J.L. Egido [ROD08] proceed in three steps:

In a first step the collective subspace of HFB wave functions is generated using quadrupole constrained particle number projection before the variation by minimising the energy

$$E^{N,Z}(q) = \frac{\langle \Phi^{N,Z}(q)|\hat{H}|\Phi^{N,Z}(q)\rangle}{\langle \Phi^{N,Z}(q)|\Phi^{N,Z}(q)\rangle}, \qquad (2.32)$$

with the corresponding constraint on the quadrupole moment with

$$|\Phi^{N,Z}(q)\rangle = \hat{P}^N \hat{P}^Z |\phi(q)\rangle, \qquad (2.33)$$

where $\hat{P}^N$ and $\hat{P}^Z$ are the projectors onto the neutron and proton numbers, respectively. $|\phi(q)\rangle$ are HFB-type wave functions and q is the quadrupole deformation.

Since the wave functions determined in the first step are not eigenstates of the angular momentum, they are projected onto the angular momentum in the second step using

$$|\Phi^{N,Z,J}(q)\rangle = \hat{P}^J \hat{P}^N \hat{P}^Z |\phi(q)\rangle, \qquad (2.34)$$

where $\hat{P}^J$ is the projector onto good angular momentum. With this wave function the energy

$$E^{N,Z,J}(q) = \frac{\langle \Phi^{N,Z,J}(q)|\hat{H}|\Phi^{N,Z,J}(q)\rangle}{\langle \Phi^{N,Z,J}(q)|\Phi^{N,Z,J}(q)\rangle}, \qquad (2.35)$$

can be calculated to produce energy surfaces as a function of q for different values of the angular momentum.

Each of the wave functions $|\Phi^{N,Z,J}(q)\rangle$ thus obtained is determined for one deformation. In the third step mixing of the wave functions of different deformations is allowed. This is realised by a new ansatz for the final wave functions in the generator coordinate system (GCM) framework taking linear combinations of the particle number and angular momentum projected wave functions

$$|\Psi^{N,Z,J,\sigma}\rangle = \int f^{N,Z,J,\sigma}(q)|\Phi^{N,Z,J}(q)\rangle dq \qquad (2.36)$$

obtained in the second step. Then, the variational principle applied to the weights $f^{N,Z,J,\sigma}(q)$ gives the generalised eigenvalue problem and thus the eigenstates $|\Psi^{N,Z,J,\sigma}\rangle$ and the eigenvalues $E^{N,Z,J,\sigma}$ are obtained by solving the Hill-Wheeler equation (2.31). The eigenenergies $E^{N,Z,J,\sigma}$ are the final values for the energy of the states 0_1^+, 0_2^+, 2_1^+, etc. The eigenstates $|\Psi^{N,Z,J,\sigma}\rangle$ allow to calculate other quantities like spectroscopic moments, transition probabilities and so on. In this calculation, the finite range density dependent Gogny force with the D1S parameterisation [BER84], which is well known for its successful predictions, is used.

This angular-momentum-projected GCM with axial quadrupole moments as the generating coordinate and intrinsic configurations calculated in the HFB model with the finite-range Gogny interaction has been applied in studies of shape-coexistence phenomena. Good agreement with experimental data has been obtained for the 2^+ excitation energies and B(E2) transition probabilities of the $N = 20$ neutron-rich isotones [RG02b]. The systematic study of the ground and low-lying excited states of the even-even $^{20-40}$Mg [RG02a] is particularly interesting, because this chain of isotopes includes three spherical magic numbers: $N = 8$, 20, 28. It has been shown, that the $N = 8$ shell closure is preserved, whereas deformed ground states are calculated for $N = 20$ and $N = 28$. In a similar analysis of the chain of even-even isotopes $^{20-34}$Ne [RG03], it has been shown that the ground state of the $N = 20$ nucleus ^{30}Ne is deformed, but less than the ground state of its isotone ^{32}Mg. The model has recently been applied in an analysis of shape coexistence and quadrupole collectivity in the neutron-deficient Pb isotopes [RG04], especially for rotational bands built on coexisting low-lying oblate and prolate states (see Sect. 3.1).

2.6.3 Relativistic Mean Field calculations

The Relativistic Mean Field calculations performed by T. Nikšić and P. Ring [NIK08] proceed in the following steps:

The starting point is a relativistic density-functional theory based on point-coupling nucleon-nucleon interactions. The parameter set PC-F1 is used, which was developed by Bürvenich et at. [BÜR02]. In this approach the meson fields are eliminated and replaced by zero-range point couplings. These terms up to 8th order in the nucleon field and its derivative have to be included.

In the next step the particle number projected energy is minimised using an axially-symmetric quadrupole constraint using Eq. (2.25). This gives axially symmetric wave functions $|\Psi(q)\rangle$ depending on a set of q values. In this step the particle number projection is carried out via a Lipkin-Nogami approximation [NG74]. Also the angular momentum and particle number projected energy surface for $I = 0$ is obtained according to Eq. (2.35). Here an exact particle number projection is carried out.

In the last step the wave functions are superimposed in the GCM approach

$$|\Psi\rangle = \int dq f(q) P^{I=0} P^N |\Psi(q)\rangle. \tag{2.37}$$

The function $f(q)$ is obtained from the Hill-Wheeler equation.

3 0^+ States and E0 Transitions

Electric monopole or E0 transitions proceed solely between equal-parity states by internal conversion with zero units of angular momentum transfer ($\Delta I = 0$) to the ejected electron. γ ray emission of this multipole order is strictly forbidden. Electron – positron pair production is possible for transition energies $\Delta E > 2m_e c^2$.

In principle an E0 transition is possible between any two equal-parity states of the same spin. If the spin is not zero, the E0 internal conversion competes with the parallel and usually much faster M1 and E2 transitions in heavy nuclei. Here we concentrate on 0^+ states. The electric E0 transition transfers the nuclear excitation energy to an electron in the atomic shell. Since the overlap of an electron in an atomic orbit with the nucleus is largest for K electrons the transition mainly ejects K electrons, but also some L electrons. The measured electron energy is the difference between the transition energy and the binding energy of the corresponding atomic electron shell. The binding energies depend only on the nuclear charge Z and are listed in e.g. [FIR96].

The transition of an initial state Ψ_i to a final state Ψ_f can be expressed by the monopole matrix element $\mathcal{M}$(E0):

$$\mathcal{M}(\text{E0}) \equiv \langle 0^+_\text{g}|T(\text{E0})|0^+_\text{exc}\rangle \tag{3.1}$$

with the monopole operator T(E0). T(E0) can be expressed in terms of the effective charge e_k and the position of the nucleons relative to the centre of the mass [BOH69]:

$$T(\text{E0}) = \Sigma_k e_k r_k^2. \tag{3.2}$$

The diagonal matrix elements $\mathcal{M}_{fi}$ describe the distribution of the mean-squared charge radii, while the non-diagonal matrix elements describe electromagnetic transitions.

3.1 Shape coexistence

In many heavy nuclei along the nuclear chart the coexistence of states with the same angular momentum and parity, however with different deformations can be found. They are well-known to exist for 0^+ states in even-even nuclei for example in the Se region and in Mo, Ru (^{102}Ru), Cd (^{114,118}Cd) and Te (^{120}Te) nuclei. Also states with higher angular momentum can occur in coexistence within one nucleus.
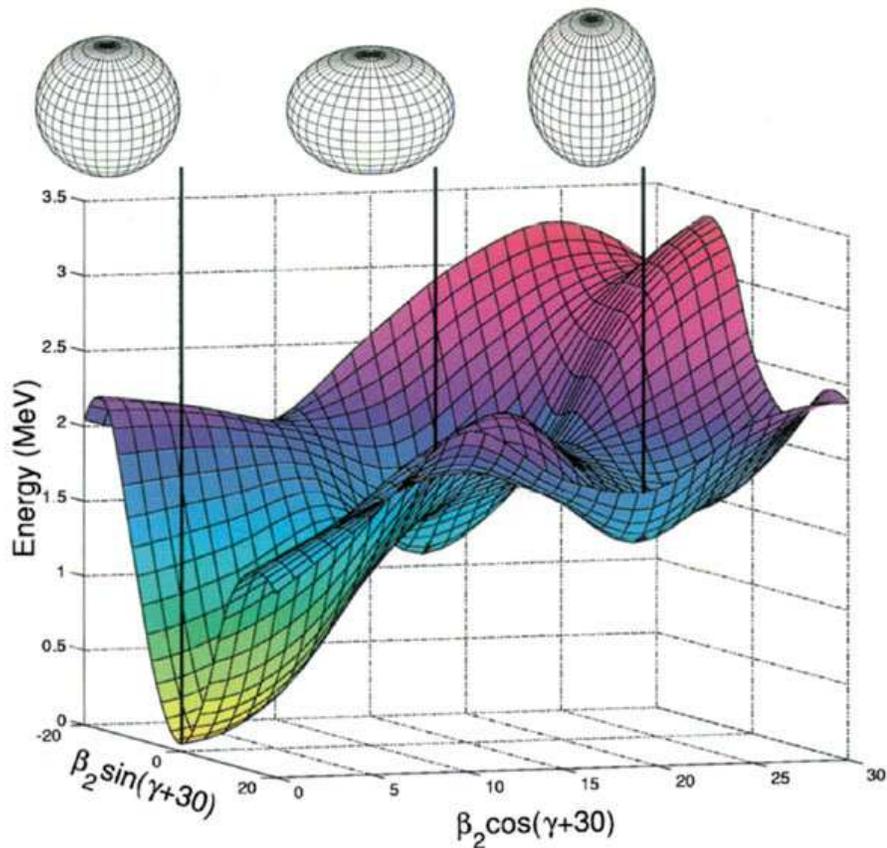
Figure 3.1: Calculated potential energy surface of ^{186}Pb. The lowest three states are
0$^+$ states with spherical, prolate and oblate shape. β_2 is the deformation
parameter, $\gamma = 0°$ corresponds to a prolate shape, while $\gamma = 60°$ describes
an oblate shape [AND00].

A convenient way to observe shape coexistence is to study low-lying 0$^+$ states. Often
they can be understood as ground states of different nuclear shapes. If two 0$^+$ states
are close in excitation energy, strong mixing of the different configurations is expected.

3.1.1 Shape coexistence in Pb isotopes

One of the most prominent examples of shape coexistence is given by the Pb iso-
topes at the closed shell $Z = 82$. In moderately neutron-deficient lead isotopes
(with $N > 106$) oblate-deformed structures coexist with spherical states, while for
$N \leq 106$ a coexistence between prolate deformed bands and spherical states occur
[BAX93, COC98, DRA98, HEE93].

The probably best known example for shape coexistence in this region is ^{186}Pb. The
lowest three states in the energy spectrum are spherical, oblate and prolate 0$^+$ states
[AND00]. The calculated nuclear potential energy surface is displayed in Fig. 3.1. Next

to the spherical minimum corresponding to the ground state, an oblate and a prolate minimum at excitation energies around 1 MeV are located.

Also ^{188}Pb provides a multiple shape coexistence of spherical-, oblate- and prolate-deformed states [COZ99]. ^{188}Pb has three low-lying 0^+ states. The 0_1^+ ground state has a spherical configuration, the 0_2^+ state at 591 keV has an oblate two-particle two-hole proton intruder configuration across the $Z = 82$ shell gap (see also Sect. 2.4.4) and the 0_3^+ state at 725 keV has a prolate configuration [COZ99]. The 0_3^+ state is probably the band head of a rotational band. The first 2^+ state has an excitation energy of 723.9 keV, placing it in between the 0_2^+ and the 0_3^+ states.

In these Pb isotopes the potential barrier between the 0^+ states of different deformations is not very high and thus the different potential minima are not well separated, giving rise to a rather strong coupling between them and resulting in a rather large mixing amplitude.

3.1.2 Shape coexistence in actinide isotopes

A much clearer spectroscopic situation exists for shape coexistence in the actinide mass region. Here we find the island of fission or shape isomers, which corresponds to isomeric states in the so-called second potential well of the double-humped fission barrier at large deformations of $\beta_2 \approx 0.6$ [THI02].

In these shape isomers we find a coexistence between the normal deformed ground state ($\beta_1 \approx 0.2$) and the superdeformed isomeric states, well-separated by a potential barrier of typically about 4 MeV height. So mixing between the different potential minima is strongly hindered and a decay from the second to the first minimum can only proceed via γ back decay or alternatively via a competing E0 transition.

So far experimental studies of this back decay have focused on the uranium isotopes ^{236}U and ^{238}U. In ^{236}U the γ back decay from the isomeric ground state at an excitation energy of 2814 keV to the ground state in the first well has been established as proceeding via a sequence of 5 E1-E1 two-photon cascades [REI93]. Complementary studies to search for the competing E0 decay branch have so far been inconclusive [SIN76].

The only E0 back decay from the second to the first potential well reported so far in literature comes from a measurement of Kantele et al. in ^{238}U [KAN83, KAN84]. In their experiment an E0 branch from the fission isomer at 2558 keV was reported, resulting in a value for the electric monopole strength $\rho^2(\text{E0}) = 1.7 \cdot 10^{-9}$. This is the weakest E0 transition known in nuclear physics, indicating very weak mixing of the 0^+ states provided by the large potential barrier of ~ 4 MeV between the first and the second potential minimum.

However, subsequent studies of this E0 decay provided contradicting results, so this decay branch cannot be validated as unambiguously established.

3.1.3 Shape coexistence in light nuclei

In light nuclei preferably doubly magic nuclei are spherical. All other nuclei are slightly deformed and thus shape coexistence is not known since the deformations of two states are similar. Only around the 'Island of Inversion' states with the same spin and parity and a relatively large difference in deformation are expected, thus giving rise to shape coexistence also in this mass region. This is also a reason for the active interest on spectroscopy in and around the 'Island of Inversion'.

3.2 The Monopole strength

The electric monopole operator $T(\mathrm{E0})$ gives rise to internal conversion processes and to the Dirac background resulting in internal pair (electron-positron) production. Higher-order processes like two-photon emission are also possible, but their probability is a factor of $\sim 10^{-4}$ smaller [WOO99].

The E0 transition is characterised by the electric monopole strength given by

$$\rho_{fi}^2 = \left| \frac{\langle f | \sum_k e_k r_k^2 | i \rangle}{eR^2} \right|^2 = \left| \frac{\mathcal{M}(\mathrm{E0})}{eR^2} \right|^2, \tag{3.3}$$

with the nuclear radius $R \simeq 1.2 \cdot A^{\frac{1}{3}}$ fm. $\rho^2(\mathrm{E0})$ contains the nuclear structure information. Typically it is of the order of 10^{-3} to 10^{-1} and thus given as $\rho^2 \cdot 10^{-3}$. It is linked in a simple way to the partial E0 lifetime $\tau(\mathrm{E0})$ of a 0$^+$ state:

$$\frac{1}{\tau(\mathrm{E0})} = \rho_{fi}^2 \cdot (\Omega_{\mathrm{K}} + \Omega_{\mathrm{L}} + \ldots + \Omega_{\mathrm{IP}}). \tag{3.4}$$

The Ω_i values are 'electronic' (non-nuclear) factors depending on the nuclear charge Z and the transition energy ΔE only. They can be calculated using the program OMEGA.BAS [KAN95] (internal conversion) and OMEGAIFP.BAS [KAN95] (internal pair creation). Also compilations of Ω_i for the internal conversion processes are given by [BEL70].

3.3 The two-level mixing model

In quantum mechanics a wave function can be expressed in terms of a complete set of basis states spanning a Hilbert space. A problem is considerably simplified if a basis exists in which the wave functions can be expressed in a simple way, e.g. if the wave function of each state consists of only one term. This means that the quantum numbers characterising the basis state are also characterising the eigenfunctions of the Hamiltonian.

$$\langle \Phi_1 | V | \Phi_2 \rangle \equiv V$$

$$\Psi_{\mathrm{I}} = \sqrt{1 - a^2}\, \Phi_1 + a \Phi_2$$
$$\Psi_{\mathrm{II}} = -a \Phi_1 + \sqrt{1 - a^2}\, \Phi_2$$
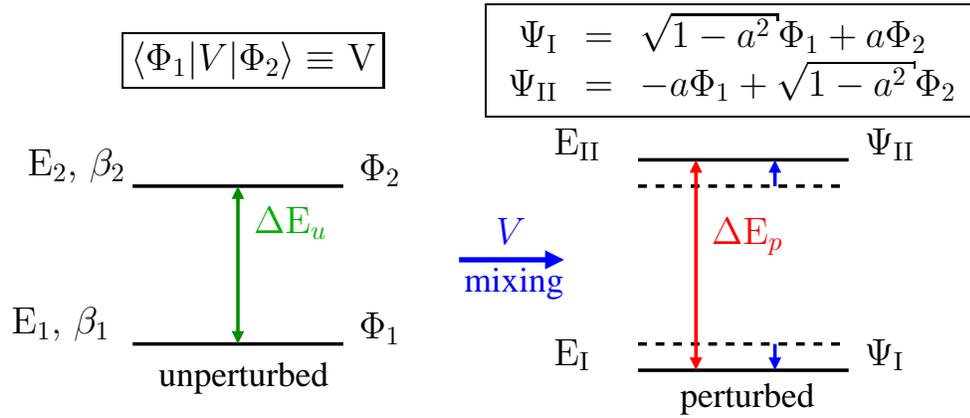
Figure 3.2: Schematic illustration of the simplifying two-level mixing model of two states interacting with each other. The unperturbed system is described by the energies $E_{1,2}$, deformations $\beta_{1,2}$ and wave functions $\Phi_{1,2}$. The unperturbed transition energy is given by ΔE_u. With the interaction between the two states, the perturbed transition energy becomes ΔE_p with the mixing matrix element V. The perturbed system is described by the energies $E_{\mathrm{I,II}}$ and wave functions $\Psi_{\mathrm{I,II}}$. In this model the unperturbed and perturbed wave functions are linked by the mixing amplitude a [CAS90, CT97, CT99, HEY07, HUN49].

Such pure configurations are rarely realised in practise. Typically the actual nuclear states are complex admixtures of many components. In this case, the Hamiltonian is decomposed into two parts: H_0, whose eigenfunctions are the basis states being used, and the perturbation H_1, which mixes the basis states. Then, the Hamiltonian

$$H = H_0 + H_1 = (T + V_0) + V_1 \tag{3.5}$$

is used in the Schrödinger equation

$$H\Psi = H_0\Psi + H_1\Psi = E\Psi. \tag{3.6}$$

In order to solve this equation, the Hamiltonian H is diagonalised in the basis states ϕ_i. The resulting wave functions are eigenfunctions of the Hamiltonian H given by

$$\psi_k = \sum_i a_i^k \phi_i \tag{3.7}$$

with the coefficients a_i^k for the ith state.

In the simplified case, where only two levels are relevant, the two-level mixing (see e.g. the discussion of this model in Ref. [CAS90, CT97, CT99, HEY07, HUN49]) between 0^+ states this problem becomes simple: The intrinsic (unperturbed) 0^+ configurations

with energies E_1 and E_2 and deformations β_1 and β_2 with a transition energy ΔE_u are described by the wave functions Φ_1 and Φ_2 (see Fig. 3.2).

The perturbed configurations are described by the energies E_I with E_II with a transition energy ΔE_p and wave functions Ψ_I and Ψ_II. The perturbed wave functions depend on the unperturbed ones via the mixing amplitude a:

$$
\begin{aligned}
\Psi_\text{I} &= \sqrt{1-a^2}\,\Phi_1 + a\Phi_2 \\
\Psi_\text{II} &= -a\Phi_1 + \sqrt{1-a^2}\,\Phi_2
\end{aligned}
\tag{3.8}
$$

3.3.1 The Mixing Matrix Element and Mixing Amplitude

The mixing matrix element

$$
\langle \Phi_1 | V | \Phi_2 \rangle \equiv V
\tag{3.9}
$$

describes the overlap of the wave functions of the intrinsic system. Since nuclear interactions are generally attractive, V is negative.

The wave functions are obtained by diagonalising the 2×2 matrix

$$
\begin{pmatrix} E_1 & V \\ V & E_2 \end{pmatrix}
\tag{3.10}
$$

and the perturbed energies are

$$
E_\text{I,II} = \frac{1}{2}(E_1 + E_2) \pm \frac{1}{2}\sqrt{(E_2 - E_1)^2 + 4V^2}.
\tag{3.11}
$$

In general the mixing depends on the initial transition energy ΔE_u and the mixing matrix element. A large value of ΔE_u reduces the effect of a given matrix element. Also a small matrix element may induce large mixing, if ΔE_u is small. The parameter

$$
R = \frac{\Delta E_u}{V}
\tag{3.12}
$$

describes the ratio between the unperturbed transition energy ΔE_u and the mixing matrix element V.

The transition energy ΔE_p in the perturbed system is enlarged by the mixing matrix element V compared to the unmixed system as shown in Fig. 3.2. It can be calculated using Eq. (3.11) and Eq. (3.12) to be

$$
\frac{\Delta E_p}{\Delta E_u} = \sqrt{1 + \frac{4}{R^2}}
\tag{3.13}
$$

as described in [CAS90].

The mixed wave functions $\Psi_{\mathrm{I,II}}$ are correlated with the intrinsic wave functions $\Phi_{1,2}$ via the mixing amplitude a (see Eq. (3.8)).

With the ratio R as defined in Eq. (3.12) the mixing amplitude a can be calculated using

$$a = \frac{1}{\sqrt{1 + \left(R/2 + \sqrt{1 + R^2/4}\right)^2}}. \tag{3.14}$$

The mixing amplitude a cannot be determined from $B(\mathrm{E2})$ values, which are typical observables determined in γ spectroscopy experiments. This means, that without knowing the mixing amplitude a, the deformation of the intrinsic states cannot be determined, since the admixture from the other state is not known. Another possibility to determine the mixing amplitude a is given in the following paragraph.

3.3.2 Dependence of ρ^2 on shape mixing

The mixing of a 0_i^+ ground state and an excited 0_f^+ state of different deformations can be described in the 2-level mixing model discussed in Sect. 3.3 according to [WOO99]. Fig. 3.3 shows the schematic potential energy surface as a function of the quadrupole deformation. A spherical 0_1^+ ground state and a deformed 0_2^+ excited state in the unperturbed system are coupled by the mixing amplitude a.

$$\begin{aligned}
|0_i^+\rangle &= a|0_1^+\rangle + b|0_2^+\rangle \\
|0_f^+\rangle &= -b|0_1^+\rangle + a|0_2^+\rangle
\end{aligned}$$

with

$$a^2 + b^2 = 1 \Longleftrightarrow b = \sqrt{1 - a^2}$$

As discussed before, the monopole strength $\rho^2(\mathrm{E0})$ describes the overlap between the wave functions of the 0_g^+ ground state and the 0_{exc}^+ excited state in the potential minima:

$$\rho_{fi}^2 = \left| \frac{\langle 0_i^+ | T(\mathrm{E0}) | 0_f^+ \rangle}{eR^2} \right|^2$$

Then the monopole matrix element $\rho_{fi}(\mathrm{E0})$ can be expressed as

$$\rho_{fi}(\mathrm{E0}) = \frac{1}{eR^2} \left[ab \left(\langle 0_1^+ | T(\mathrm{E0}) | 0_1^+ \rangle - \langle 0_2^+ | T(\mathrm{E0}) | 0_2^+ \rangle \right) + (a^2 - b^2) \langle 0_2^+ | T(\mathrm{E0}) | 0_1^+ \rangle \right]. \tag{3.15}$$
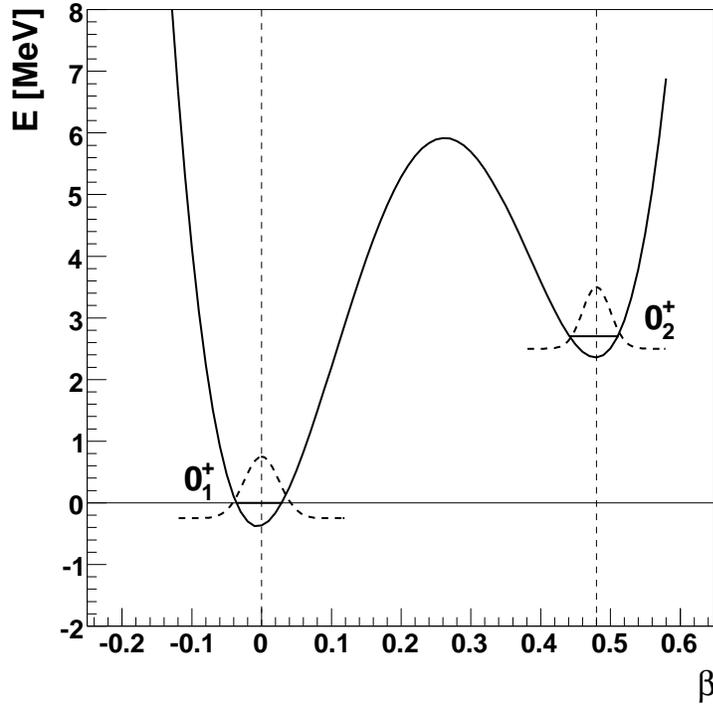
Figure 3.3: Schematic potential energy surface as a function of the quadrupole defor-
        mation. The two-level model with an almost spherical and a strongly de-
        formed shape is shown (see Sect. 3.3). Schematic collective wave functions
        are drawn with dashed lines.

Now two cases can be considered:

First the situation in which weak mixing occurs between configurations corresponding
to strongly different shapes. In this case $ab \simeq 0$ and $\langle 0_2^+|T(E0)|0_1^+\rangle \simeq 0$ and the wave
functions are localised in different potential minima at different deformations and thus
$\rho_{fi}^2 \simeq 0$. An example is observed in ^{238}U. The E0 decay from the fission isomeric
0^+ is the slowest E0 transition known with a monopole strength $\rho^2(\text{E0}) = 1.7 \cdot 10^{-9}$
[WOO99].

Also strong mixing can be considered. In this case also $\langle 0_2^+|T(E0)|0_1^+\rangle \simeq 0$, but

$$a \simeq -b \simeq \frac{1}{\sqrt{2}} \tag{3.16}$$

and thus the general result of Eq. (3.15) is approximated to be

$$\rho_{fi}(\text{E0}) = \frac{1}{eR^2} \cdot \frac{1}{2} \left[\langle 0_1^+|T(E0)|0_1^+\rangle - \langle 0_2^+|T(E0)|0_2^+\rangle \right] \tag{3.17}$$

The diagonal $T(E0)$ matrix elements can be related to the collective quadrupole defor-
mation space [WOO99], where the deformation parameter β is defined as

$$\beta_k^2 \equiv \langle 0_k^+ |\Sigma|\alpha_\mu|^2|0_k^+\rangle \tag{3.18}$$

with the time-dependent shape parameter α_μ, leading to the result

$$\rho_{fi}^2(\text{E0}) = \frac{1}{4}\left(\frac{3}{4\pi}\right)^2 Z^2 \left(\beta_1^2 - \beta_2^2\right)^2 . \tag{3.19}$$

In the particular situation of strong mixing between an almost spherical and a strongly deformed shape the result

$$\rho_{fi}^2(\text{E0}) = \frac{1}{4}\left(\frac{3}{4\pi}\right)^2 Z^2 \beta_{def}^4 \tag{3.20}$$

is obtained.

In general, considering an unperturbed system consisting of two states 0_{sph}^+ and 0_{def}^+ and a perturbed system consisting of two states 0_{g}^+ and 0_{exc}^+, which are mixed by the mixing amplitude a (see also Sect. 3.3),

$$\begin{aligned}
|0_{\text{g}}^+\rangle &= a|0_{\text{sph}}^+\rangle + \sqrt{1-a^2}|0_{\text{def}}^+\rangle \\
|0_{\text{exc}}^+\rangle &= -\sqrt{1-a^2}|0_{\text{sph}}^+\rangle + a|0_{\text{def}}^+\rangle
\end{aligned} \tag{3.21}$$

the monopole strength $\rho^2(\text{E0})$ can be expressed as (Eq. (51) from Ref. [WOO99] using Ref. [WOO96])

$$\rho^2(\text{E0}) = \left(\frac{3}{4\pi}Z\right)^2 \cdot a^2 \cdot (1-a^2) \cdot \left(\beta_{\text{sph}}^2 - \beta_{\text{def}}^2\right)^2 . \tag{3.22}$$

The quadrupole deformations $\beta_{\text{sph,def}}$ are the intrinsic deformations. In order to calculate the mixing amplitude a, the monopole strength $\rho^2(\text{E0})$ has to be determined experimentally. If the mixing is weak, the deformations β_{sph} and β_{def} of the ground state and the excited state can be calculated from the $B(\text{E2})$ quadrupole transition. Since this relation is model dependent, it is necessary to compare the results with microscopic calculations.

3.4 Shell Model estimates of the monopole strength

Expressing the initial and final state of a nucleus confining n nucleons in a single oscillator shell N as

$$|\psi_{i,f}\rangle = \sum_m a_m^{i,f}|\psi_m\rangle \tag{3.23}$$

the monopole strength $\rho^2(\mathrm{E}0)$ can be calculated as

$$\rho_{if}^2 = \frac{1}{e^2 R^4} \left| \sum_{m,l} a_m^i a_l^{f*} \langle \psi_l | \sum_{k=1}^{n} e_k r_k^2 | \psi_m \rangle \right|^2 = \frac{1}{e^2 R^4} \left| \sum_l a_l^i a_l^{f*} \langle \psi_l | \sum_{k=1}^{n} e_k r_k^2 | \psi_l \rangle \right|^2 \quad (3.24)$$

with the scalar r_k^2. Since the matrix elements r_k^2 are independent of l for a single harmonic oscillator shell and with orthogonal initial and final states,

$$\sum_l a_l^i a_l^{f*} = 0 \quad (3.25)$$

one obtains $\rho_{if}^2 = 0$ for nucleons confined to a single oscillator shell [WOO99]. This means that realistic nucleon wave functions are not eigenstates of the harmonic oscillator. The eigenstates of the Woods-Saxon potential can be expressed as linear combinations of harmonic oscillator eigenstates. They are dominated by oscillator eigenstates of a particular shell with admixtures of other shells. A simple estimate of $\rho^2(\mathrm{E}0)$ can be obtained by considering two states

$$\begin{aligned} |0_i^+\rangle &= \alpha |j_1^2, 0^+\rangle + \beta |j_2^2, 0^+\rangle \\ |0_f^+\rangle &= -\beta |j_1^2, 0^+\rangle + \alpha |j_2^2, 0^+\rangle \end{aligned} \quad (3.26)$$

with pairs of nucleons in oscillator configurations j_1 and j_2, ($|j_{1,2}^2, 0^+\rangle$), coupled to total spin zero. One obtains for the r^2 matrix

$$\langle 0_f | r^2 | 0_i \rangle = (\alpha^2 - \beta^2)\langle j_1^2, 0^+ | r^2 | j_2^2, 0^+\rangle + \alpha\beta(\langle j_2^2, 0^+ | r^2 | j_2^2, 0^+\rangle - \langle j_1^2, 0^+ | r^2 | j_1^2, 0^+\rangle). \quad (3.27)$$

For j_1 and j_2 belonging to different oscillator shells the second term is the difference in mean square radii of the two shells. For $j_{1,2}$ in neighbouring shells and maximum mixing ($\alpha = \beta = 1/\sqrt{2}$) this results in

$$\langle 0_f | r^2 | 0_i \rangle = \frac{\hbar}{m\omega} \quad (3.28)$$

and

$$\rho_{if}^2 = 0.5 \cdot A^{-2/3} \quad (3.29)$$

which is a simplified estimate and can only serve as a guide for the A-dependency of ρ^2.

3.5 Experimental determination of the electric monopole strength

In general the transition probability $\mathcal{T}$ of a transition is reciprocal to its lifetime τ. If an E0 transition is in competition to an E2 transition, the total lifetime τ of the 0^+ state can be calculated using

$$\frac{1}{\tau} = \mathcal{T}(\text{E0}) + \mathcal{T}(\text{E2}). \tag{3.30}$$

The transition probability $\mathcal{T}(\text{E0})$ is proportional to the monopole strength $\rho^2(\text{E0})$ and the non-nuclear electronic factors $\Omega(\text{E0})$ (see Sect. 3.2):

$$\mathcal{T}(\text{E0}) = \rho^2(\text{E0}) \cdot (\Omega_\text{K} + \Omega_\text{L} + \ldots + \Omega_\text{IP}) = \rho^2(\text{E0}) \cdot \Omega_\text{tot} \tag{3.31}$$

and

$$\mathcal{T}(\text{E0}) \propto I_\text{tot}^\text{E0} \tag{3.32}$$

with the transition intensity $I(\text{E0})$. The transition probability $\mathcal{T}(\text{E2})$ is also proportional to the transition intensity

$$\mathcal{T}(\text{E2}) \propto I_\gamma(1 + \alpha) \tag{3.33}$$

with the total conversion coefficient α.

Eq. (3.30) can be transformed to

$$\frac{1}{\tau} = \mathcal{T}(\text{E0}) \cdot \left(\frac{\mathcal{T}(\text{E2})}{\mathcal{T}(\text{E0})} + 1 \right), \tag{3.34}$$

which leads to:

$$\frac{1}{\tau} = \rho^2(\text{E0}) \cdot \Omega_\text{tot} \cdot \left(\frac{I_\gamma(1 + \alpha)}{I_\text{E0}^\text{K+L} \left(1 + \frac{\Omega_\text{IP}}{\Omega_\text{K}+\Omega_\text{L}} \right)} + 1 \right) \tag{3.35}$$

using Eq. (3.32), Eq. (3.33), the K and L signature of the E0 transition only and Ω_IP, denoting the Ω factor for internal pair creation.

In case of an 0_2^+ state decaying via an E0 transition with small intensity and very long partial lifetime competing with an E2 transition, the monopole strength can be determined by the ratio of the E0 and E2 K-conversion intensities q_k^2 and the E2 transition rate $W_\gamma(\text{E2})$ [KIB05]

$$\rho^2(\text{E0}) = q_K^2(\text{E0/E2}) \cdot \frac{\alpha_K(\text{E2})}{\Omega_\text{K}(\text{E0})} \cdot W_\gamma = \frac{I_K(\text{E0})}{I_K(\text{E2})} \cdot \frac{\alpha_K(\text{E2})}{\Omega_K(\text{E0})} \cdot \frac{1}{\tau_\gamma} \qquad (3.36)$$

$I_\text{K}(\text{E0})$ and $I_\text{K}(\text{E2})$ are the measured intensities of E0 and E2 K-conversion electrons. The conversion coefficient $\alpha_\text{K}(\text{E2})$ and the non-nuclear electronic factor $\Omega_\text{K}(\text{E0})$ can be calculated with the program package OMEGA.BAS [KAN95]. The (γ) lifetime of the excited 0^+ has to be taken from literature.

If the E0 transition is not in competition with any other transition, the monopole strength $\rho^2(\text{E0})$ can directly be obtained from the lifetime of the E0 transition using Eq. (3.4).

4 E0 spectroscopy using a Mini-Orange spectrometer

Mini-Orange spectrometer have proven to be versatile, compact and easy-to-use magnetic filter and detection systems for electron spectroscopy[KLI72, KLI75, KLI78].

The Mini-Orange spectrometer consists of a Si(Li)-detector in conjunction with a magnetic transport and filter system, the Mini-Orange. This spectrometer combines the excellent energy and time resolution of the Si(Li)-detector with the selectivity and high efficiency of the Mini-Orange.

4.1 The Si(Li) Detector

The Si(Li) detector used in our experiment is 5 mm thick with an active surface of 500 mm^2. This is thick enough to stop electrons up to a kinetic energy of 2.1 MeV.
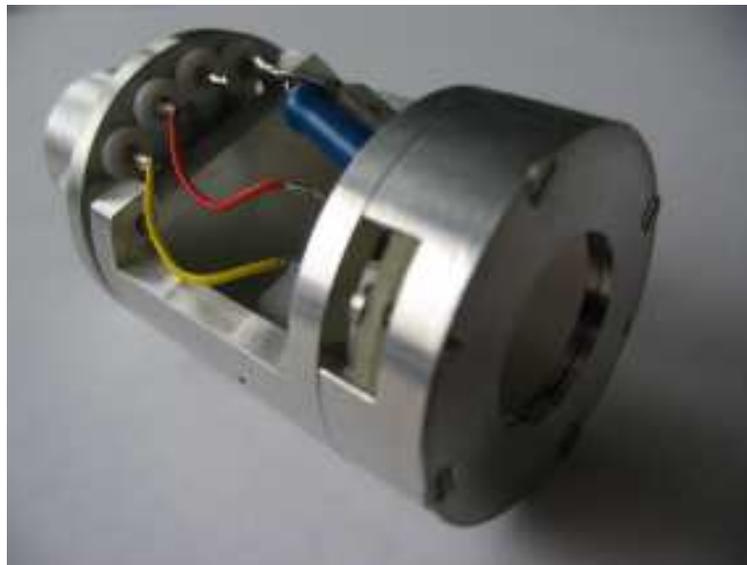
Figure 4.1: Photograph of the Si(Li) detector with a thickness of 5 mm and with an active surface of 500 mm^2 (type ESLB-500). It is thick enough to stop electrons with kinetic energies up to 2.1 MeV. The cabling of the FET is shown. The FET itself cannot be seen in this figure.

The detector was manufactured by EURISYS (type ESLB-500). Fig. 4.1 shows a photograph of the detector.

In order to achieve optimum energy resolution and to ensure a low noise level, the detector is operated at liquid nitrogen temperature. Also the preamplifier FET is located in the cold section of the detector system, while the remaining charge-sensitive preamplifier (model Eurisys PSC 761) is mounted outside the vacuum chamber at room temperature.
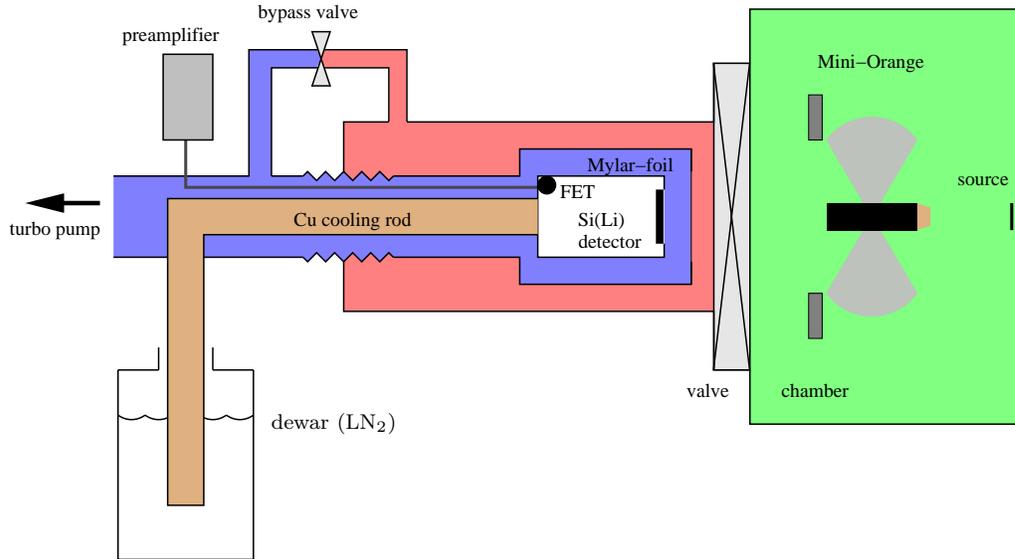
Figure 4.2: Layout of the Mini-Orange spectrometer. A 1.5 μm thick aluminised Mylar-foil separates the detector with its own vacuum system (blue) from the target chamber (green). A copper rod in contact with a LN$_2$ reservoir allows to cool the detector to about 110 K.

Since the cold detector surface would act as a cryotrap for any contamination of the residual gas, an operation of the detector at constantly optimum energy resolution can only be ensured if any condensation on the detector surface is avoided. Therefore the detector is kept in a separate vacuum system and cooling of the detector is not started before having reached a vacuum pressure in the detector chamber of $\leq 3 \cdot 10^{-6}$ mbar. Cooling is done via a 1.6 cm thick copper rod in contact with an LN$_2$ reservoir. A 1.5 μm thick aluminised Mylar foil is used as window to separate the two vacuum systems of the detector and target chamber. Moreover, a doubly-sealed threaded rod allows to retract the detector with its vacuum system behind a valve that can be closed to separate the target chamber. This allows to open the target chamber while keeping the Si(Li) detector cooled (see Fig. 4.2).

In order to study the response of the Si(Li) detector to monoenergetic electrons GEANT4 simulations were performed. Fig. 4.3 shows the geometrical setup used for the simulation. The monoenergetic electrons hit the detector in its centre with different impact angles. While the dominant part of the electrons is detected with their full
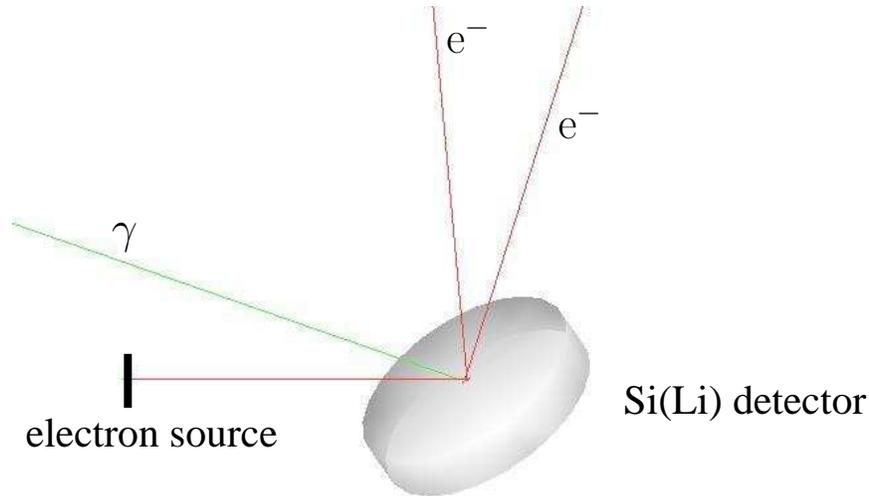
Figure 4.3: Geometry used for the GEANT4 simulation of the Si(Li) detector response. 10 monoenergetic electrons at 500 keV are hitting the centre of the Si(Li) detector (thickness: 5 mm, surface: 500 mm^2) at an incident angle of $\alpha = 45°$. Some of the electrons are backscattered, and do not deposit their total kinetic energy in the detector. The electron trajectories are marked with red lines and the γ trajectories with green ones.

energy, some electrons are backscattered and do not deposit their full energy in the detector. An example of the electron energy spectrum is displayed in Fig. 4.4, where 10^4 monoenergetic electrons ($E_{kin} = 500$ keV) hit the detector at an incidence angle of $\alpha = 45°$ have been simulated. It turns out that in 76% of all electron interactions the full kinetic energy is deposited in the detector, while the fraction of backscattered electrons amounts to 24% (see also [FAU75]).

Fig. 4.5 shows the measured electron spectrum using a ^{207}Bi source (see Sect. 4.3.3). Since the spectrum was measured using the Mini-Orange between the source and the Si(Li) detector, the incident angle α is necessarily larger than 10°. The tail of the peak towards the low-energy side can clearly be seen, caused by backscattered electrons, which do not deposit their total kinetic energy in the detector.

In Fig. 4.6 the fraction of backscattered electrons as a function of their kinetic energies between 0.5 MeV and 2 MeV and incident angles between $\alpha = 0°$ and $\alpha = 75°$ are shown. The data points with full triangles have been simulated using GEANT4 [GEA]. The results indicated by upright triangles are derived using an electron beam hitting the centre of the Si(Li) detector, while the inverted triangles indicate simulations derived from a point-like electron source radiating isotropically. Also an experimental value indicated by the full square is indicated. The open symbols indicate earlier simulations and calculations by Waldschmidt and Wittig [WAL68].

As the calculation shows, with increasing incident angle the fraction of backscattered
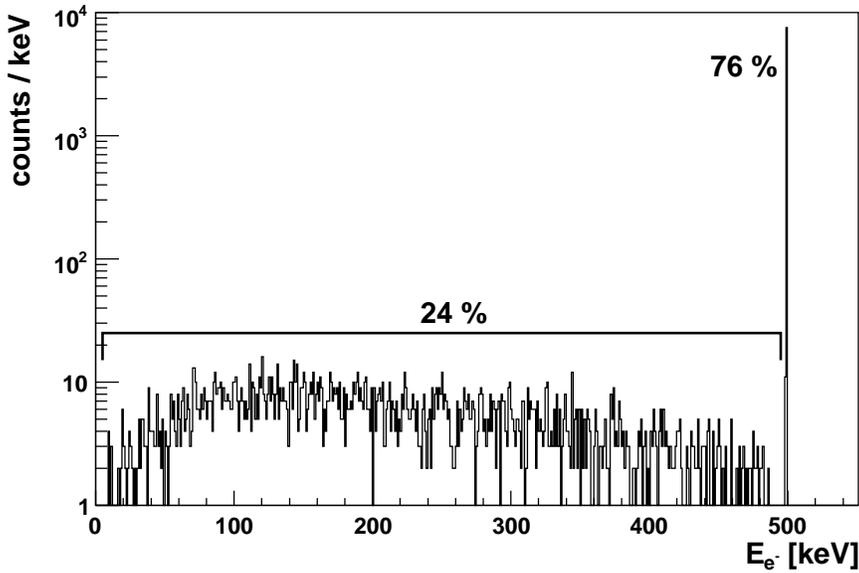
Figure 4.4: Simulated electron energy spectrum using 10000 monoenergetic electrons with $E_{kin} = 0.5$ MeV and for an incident angle $\alpha = 45°$. 76% of the electrons deposit their total kinetic energy in the detector, while the fraction of backscattered electrons amounts to 24%.

electrons steeply increases, while staying rather constant as a function of the kinetic energy for a fixed incident angle and a beam like electron source hitting the detector in its centre. For the more realistic scenario of an electron source radiating isotropically, a larger fraction of backscattered electrons is obtained due to the hitting of the detector edge. In this case the simulation most likely overestimates the experimental results. For $\alpha = 0°$ the earlier simulations and data points agree rather well. For larger values of the incident angle the older simulations underestimate the experimental values.

4.2 The Mini-Orange

The Mini-Orange spectrometer works similar to an optical lens (see Fig. 4.7). The electrons are focused onto the detector by the Mini-Orange as a function of the object distance g between the target and the Mini-Orange and the image distance b between the Mini-Orange and the detector. For fixed electron energies the Mini-Orange works according to the well-known optical relation for the focal length f

$$\frac{1}{f} = \frac{1}{g} + \frac{1}{b}.$$
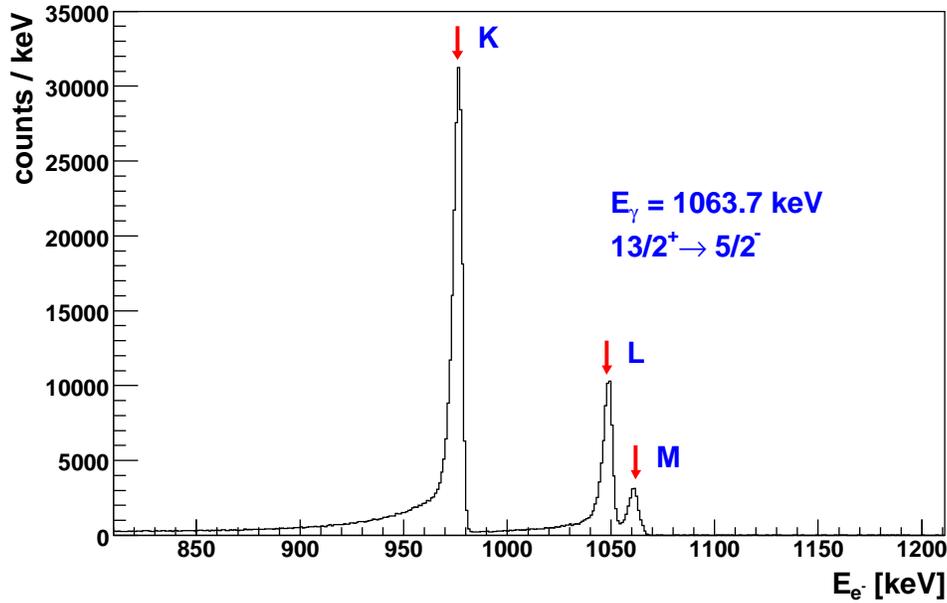
Figure 4.5: Electron spectrum using a ^{207}Bi source (see Sect. 4.3.3). Since the spectrum was measured using the Mini-Orange between source and Si(Li) detector, the incident angle is $\alpha > 10°$. Thus a large fraction of electrons is backscattered out of the detector, not depositing their total kinetic energy in the detector resulting in a tail towards the low-energy side.

Thus the Mini-Orange provides a high efficiency detecting conversion electrons, while simultaneously suppressing the abundant background of e.g. β-decay electrons.

The deflection radius r of the electrons in the magnetic sector field is given by:

$$r = \frac{E_{e^-}\beta}{eB\gamma c}.$$

E_{e^-} is the kinetic energy of the electrons and B is the magnetic field of the Mini-Orange.

The Mini-Orange used in our experiment consists of 8 wedge-shaped permanent magnets, which are arranged symmetrically around a cylindrical Pb absorber (see Fig. 4.8). The outer radius of the magnet wedges is 4 cm. The angle of the wedges is 6° in ϕ direction and 65° in θ direction symmetrically around 90°. The magnets are glued onto an aluminium holder, which is then screwed onto a metallic ring of 6.1 cm inner and 10.3 cm outer diameter. The lead absorber is 50 mm long and 8 mm in diameter at the front end towards the source and 10 mm in diameter at the back end towards the detector, with a central diameter of 18 mm. It is fixed in the centre of the wedges by a notch. The absorber protects the detector against direct sight to the target and thus against γ radiation originating from the target. In its final version (see Sect. 6.3.2)
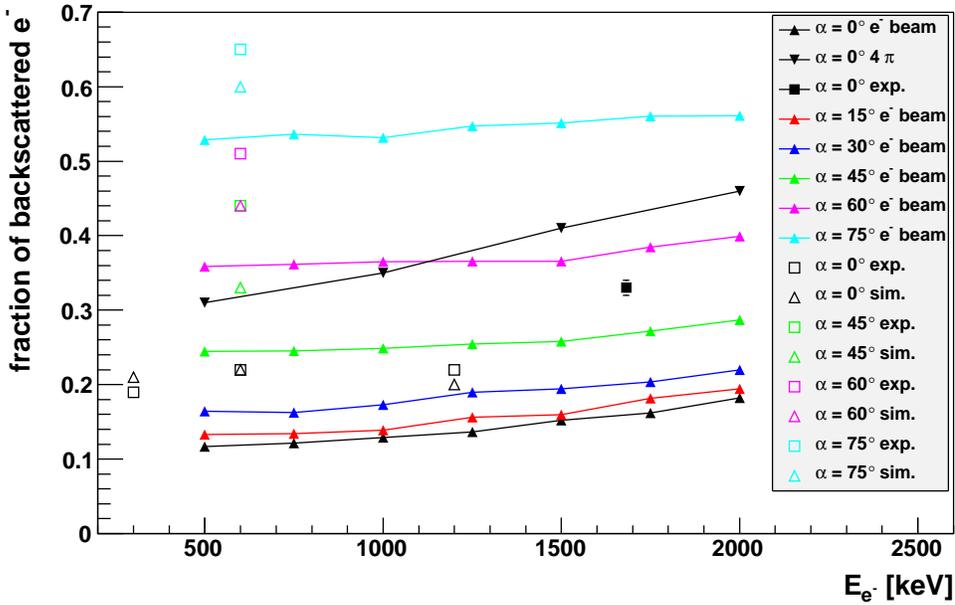
Figure 4.6: Fraction of electrons backscattered from the Si(Li) detector as a function of their kinetic energy displayed for various incident angles. Data points with full triangles have been simulated using GEANT4 [GEA]. The results indicated by upright triangles are derived using an e^- beam hitting the centre of the Si(Li) detector, while the inverted triangles indicate simulations derived from a point-like e^- source radiating isotropically. The black square is derived from measurements using a ^{207}Bi source (see Sect. 4.3.3). Open triangles and open squares denote older simulations and experimental data by Waldschmidt and Wittig [WAL68].

the Pb absorber was covered by a copper cap to absorb X-rays produced in the Pb absorber.

The B-field distribution of the Mini-Orange was measured in radial, axial and azimuthal direction using a Hall probe. The probe was positioned in the magnetic field of the Mini-Orange by an adjustable stand shown in Fig. 4.10. The results of these measurements are shown in Fig. 4.11. Panel a) shows the magnetic field strength measured in gap number 1 as a function of the azimuthal angle ϕ and for different radial distances r from the Mini-Orange centre. Panel c) shows the same result for all the gaps as panel a). In panel b) the field strength in the middle plane in each gap is shown in radial direction.

In the inner part of the Mini-Orange the magnetic field is rather constant for $r \leq 25$ mm with an average value of $B \sim 160$ mT. Towards the outer part of the Mini-Orange the magnetic field decreases linearly. In azimuthal direction (bottom panel of Fig. 4.11) the magnetic field distribution is almost identical within the various gaps. In the middle between two wedges the magnetic field falls off for radii larger then ~ 25 mm, while
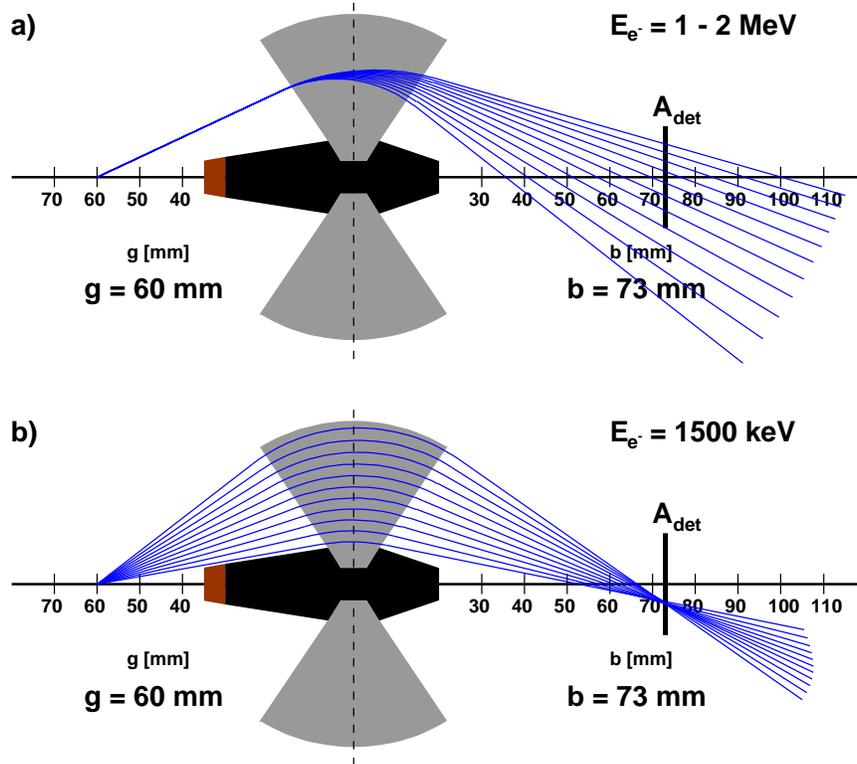
Figure 4.7: Panel a): Schematic drawing of electron trajectories passing the Mini-Orange spectrometer at energies between 1 MeV and 2 MeV for an object distance $g = 60$ mm between the Mini-Orange and the target and a fixed electron emission angle.

Panel b): Trajectories of electrons with a constant energy of $E_{kin} = 1500$ keV, but different emission angles focused onto the detector plane at $g = 73$ mm.

A homogeneous B field of 160 mT was used for the trajectory calculation.

towards the surface of the magnets fields up to 250 mT are measured.

4.3 Transmission Efficiency

The absolute transmission efficiency ϵ_{MOS} of the Mini-Orange spectrometer can be described as the product of the transmission efficiency of the Mini-Orange T and the detector efficiency ϵ_{SiLi}:

$$\epsilon_{\text{MOS}} = T \cdot \epsilon_{\text{SiLi}}. \tag{4.1}$$

Figure 4.8: Mini-Orange consisting of 8 wedge-shaped $Nd_2Fe_{14}B$ permanent magnets arranged around a cylindrical Pb absorber. The 5 mm thick copper cap on top of the absorber reduces X-rays produced by electrons scattered in the lead.

The detector efficiency ϵ_{SiLi} can also be expressed as $(1 - \kappa)$ with κ describing the fraction of backscattered electrons in the Si(Li) detector.

T is defined as the number of detected electrons using the Mini-Orange N_{MO} compared to the number of electrons N detected in the full solid angle of 4π in the same distance without the Mini-Orange:

$$T = \frac{N_{MO}}{N}. \tag{4.2}$$

N can be derived from the measured yield N_{det} using a detector with its surface A_{det} placed at a distance of $(g + b)$ from the target

$$N = N_{det} \cdot 4\pi(g + b)^2 \cdot \frac{1}{A_{det}} \tag{4.3}$$

where g is the object distance between the source and the centre of the Mini-Orange and b is the image distance between the centre of the Mini-Orange and the detector surface [KLI72].

4.3.1 Geometrical calculation of the transmission efficiency

The maximum of the transmission efficiency can be calculated using [KLI75]
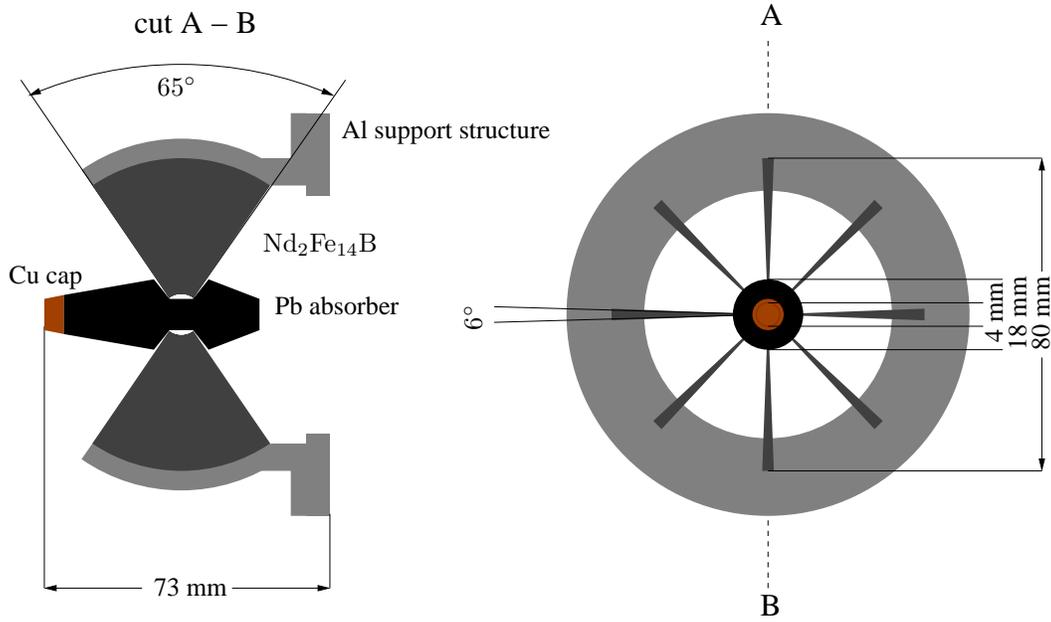
Figure 4.9: Layout of the Mini-Orange. The magnetic wedges are glued onto the support structure which is screwed onto a carrier ring. The Pb absorber is fixed in the centre of the Mini-Orange by the inner part of the magnet wedges fitting into a machined notch of the absorber.

$$\epsilon_{\mathrm{MOS}} = \frac{1}{2}(\cos\Theta_{min} - \cos\Theta_{max})(1-a)(1-\kappa) \qquad (4.4)$$

where a describes the geometrical blocking by the magnet wedges, κ is the fraction of the electrons which are backscattered in the Si(Li)-detector (see Fig. 4.6) and Θ_{min} and Θ_{max} are defined by the angular acceptance of the Mini-Orange.

In order to determine Θ_{min} and Θ_{max}, the trajectories of the electrons through the Mini-Orange were calculated. As a first approximation the magnetic field was assumed to be homogeneous and constant with $B = 160$ mT inside the gaps between the magnet wedges, while $B = 0$ T was assumed outside the magnet radii.

Θ_{min} is defined to be the smallest angle between the electron trajectory and the x axis which allows the electrons to pass the central absorber. The largest angle where the electron trajectory still completely proceeds inside the Mini-Orange is defined to be Θ_{max} (see Fig. 4.12). The detector surface was placed in the focus of the resulting optical projection, thus defining the image distance b.

The geometrical blocking of a magnetic wedge is given by its azimuthal angle of $6°$, resulting in a geometrical blocking of $a = 0.13$. Since the angle between an electron hitting the detector and the surface vector of the detector surface is smaller than $30°$, an upper limit for the fraction of backscattered electrons is $\kappa = 0.30$ (see Fig. 4.6) for energies between 1.5 MeV and 2 MeV.

Figure 4.10: Setup to measure the magnetic field of the Mini-Orange with a Hall probe. It enables to measure the magnetic field strength in radial, azimuthal and axial direction.

g [mm]	b [mm]	Θ_{min}	Θ_{max}	ϵ_{MOS}^{calc} [%]
50	105	18°	43°	6.7
60	90	12°	41°	6.8
70	75	9°	38°	6.1

Table 4.1: Results of the geometrically calculated transmission efficiency shown in Fig. 4.12 for $E_{e^-} = 1682$ keV using Eq. (4.4). The geometrical blocking of the magnetic wedges is $a = 0.13$ and an upper limit of the fraction of backscattered electrons is $\kappa = 0.30$.

Typically the transmission efficiency calculated from the geometry of the Mini-Orange is significantly higher than the measured one and thus only serves as an upper limit
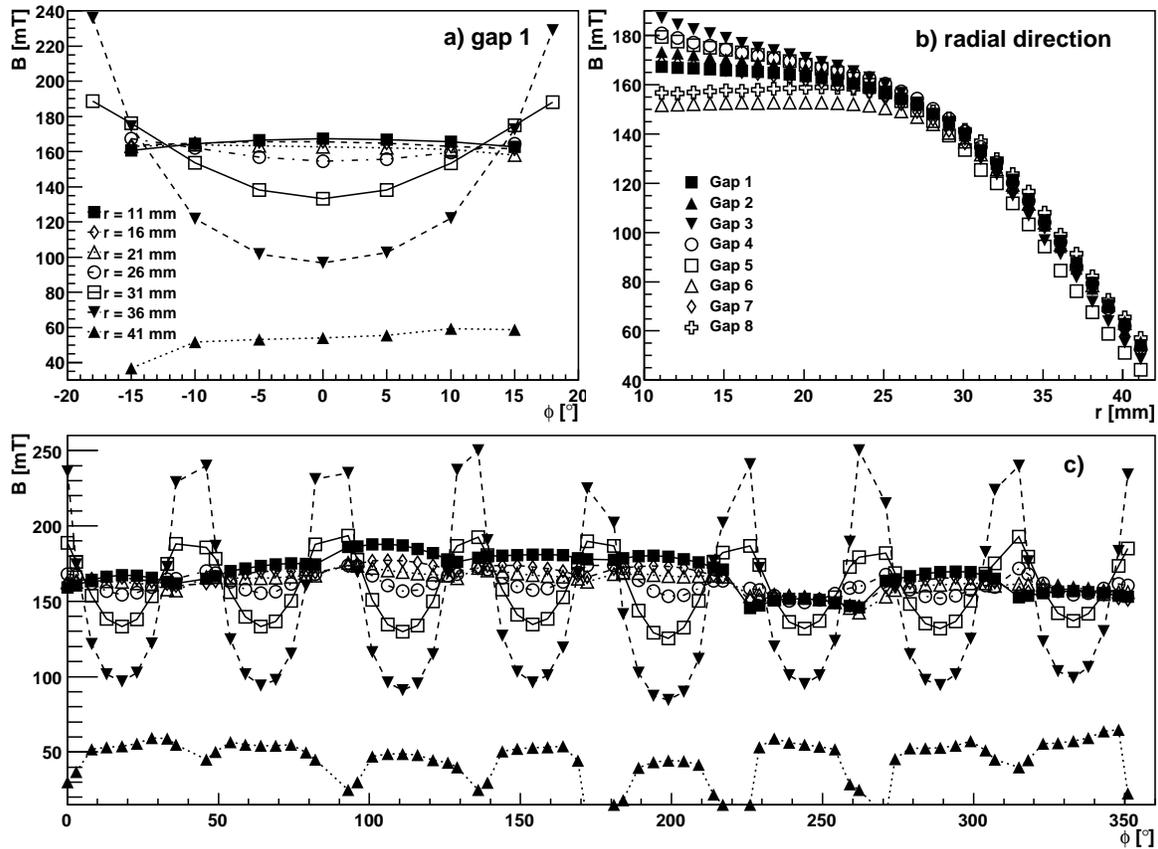
Figure 4.11: Panel a): Magnetic field of the Mini-Orange in gap number 1 as a function of the azimuthal angle ϕ in the gap and for different values of radial distances r from the Mini-Orange centre.
Panel b): Magnetic field strength in the middle plane in each of the 8 gaps as a function of the radial distance from the Mini-Orange centre.
Panel c): Magnetic field strength in all 8 gaps in azimuthal direction measured for the same radial distances as shown in panel a).

for the transmission efficiency.

4.3.2 GEANT4 simulation of the transmission efficiency

In addition to the coarse analytical estimates of the transmission efficiency, as described in Sect. 4.3.1, Monte Carlo simulations have been performed using the code GEANT4 [GEA]. Fig. 4.13 shows the geometrical model of the Mini-Orange as used in the GEANT4 simulation. The Si(Li) detector is marked in red and is hit by an electron passing the magnetic field of the Mini-Orange (red line).

In this simulation the magnetic field was chosen to be 160 mT in ϕ direction for distances $r \leq 28$ mm, while linearly decreasing for distances $r > 28$ mm with 8.6 mT/mm
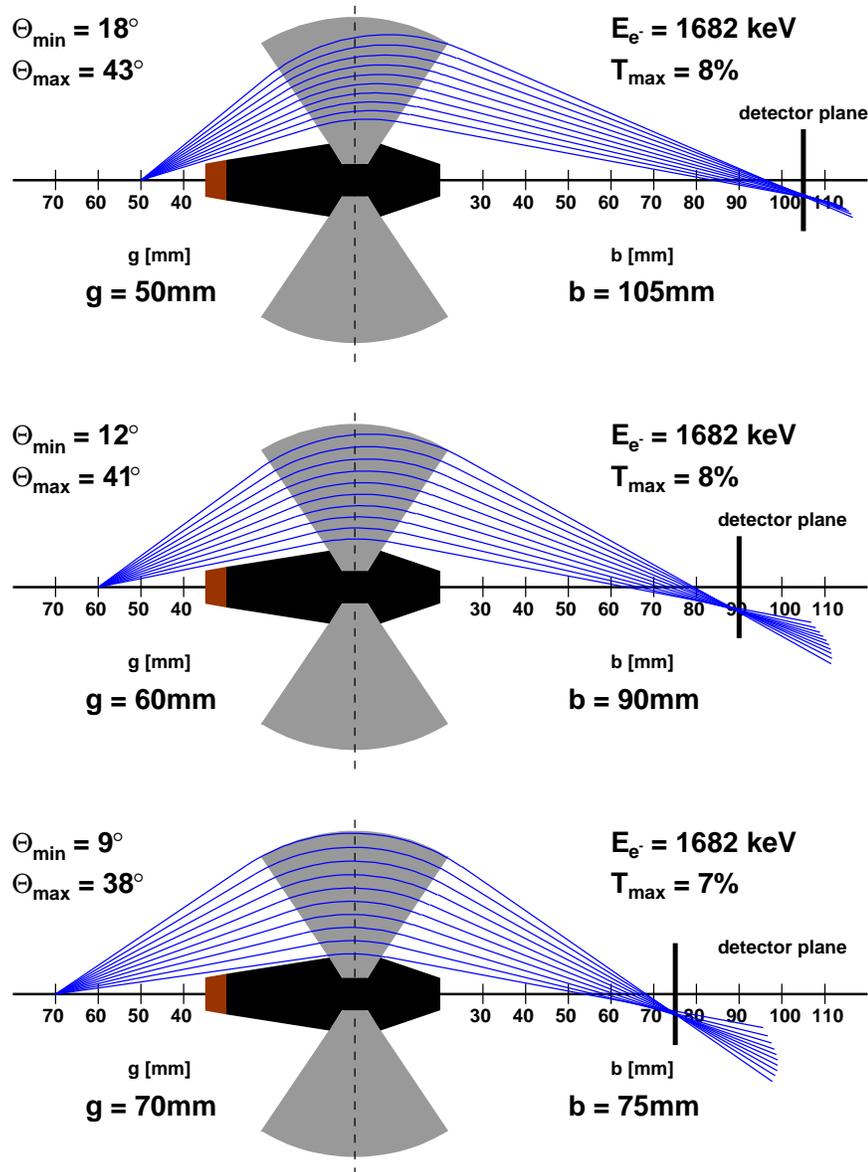
Figure 4.12: Calculated trajectories of electrons with kinetic energy $E_{e^-} = 1682$ keV from the ^{207}Bi decay for different values of the object distance g are shown. The detector surface is placed in the focus of the trajectories behind the Mini-Orange, which defines the image distance b for different values of the object distance g. In order to calculate the trajectories a homogeneous B-field of 160 mT over the whole radial size of the wedges was used. Θ_{min} and Θ_{max} are defined as the minimum and the maximum angle for which the trajectory still completely proceeds inside the magnetic field sector between the wedges.
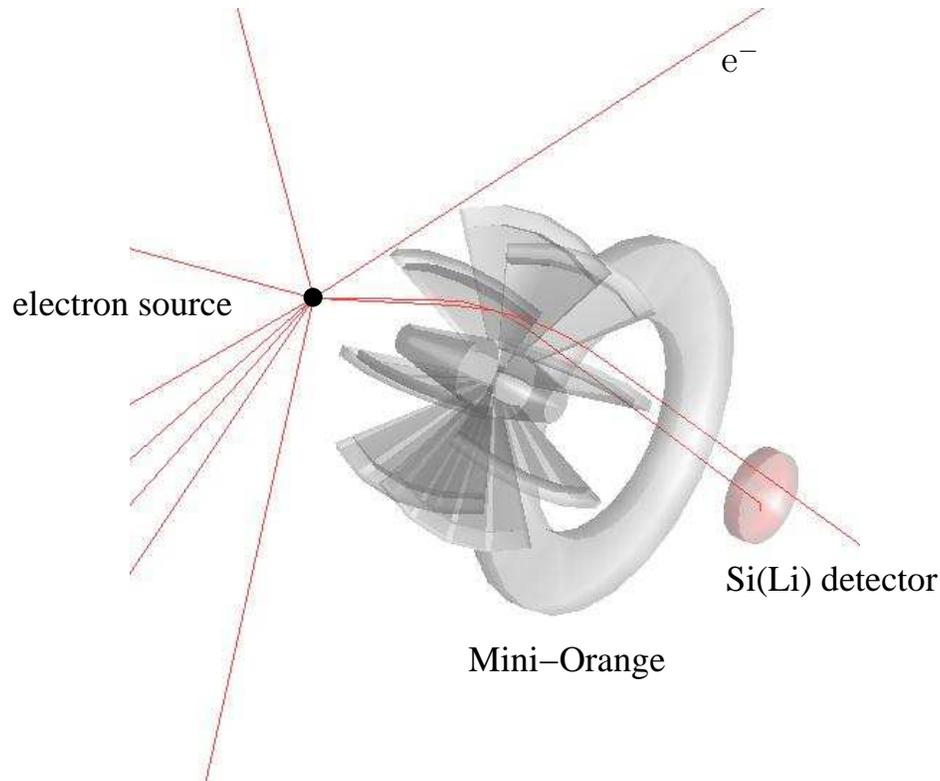
Figure 4.13: Geometrical model of the Mini-Orange used for the GEANT4 simulation.
The Si(Li) detector is shown in red. The red lines mark electron trajectories isotropically originating from the target spot. 10 simulated electron trajectories are shown.

as determined experimentally in Sect. 4.2. This r dependence is valid in ϕ direction between all the wedges. For azimuthal angles it is only valid inside the wedges ($57.5° \leq \theta \leq 122.5°$). Outside the magnetic wedges in azimuthal direction the magnetic field was chosen to vanish.

Fig. 4.14 shows the result of this simulation for an object distance of 60 mm and an image distance of 85 mm as used for the Mg experiment. The transmission curve peaks around 1800 keV with a transmission maximum of $\sim 5\%$. Despite of the ideal assumption on the magnetic field the calculated transmission maximum reproduces quite well the experimental value shown in Fig. 4.19. The maximum of the transmission efficiency is overestimated, since the inhomogeneities of the surrounding field are not taken into account.

4.3.3 Transmission efficiency measurements

While any kind of transmission efficiency calculations or simulations can only serve as a guideline for the design of the Mini-Orange, its actual performance can only be
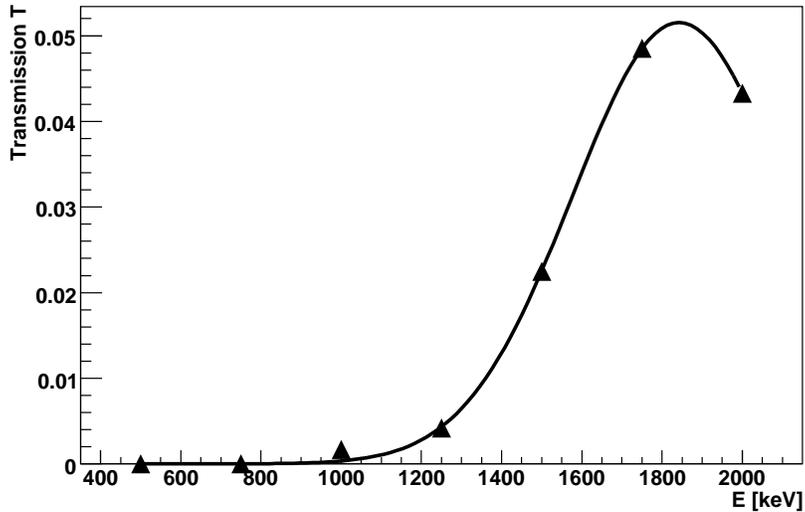
Figure 4.14: Simulated transmission curve of the Mini-Orange using GEANT4.

characterised experimentally. Since the transmission function depends on the kinetic energy of the electrons, sources providing discrete electron lines are used. In order to optimise the optical projection characteristics of the Mini-Orange spectrometer and to realise a transmission maximum around 1.8 MeV, measurements using ^{207}Bi and ^{152}Eu electron sources were performed. These sources provide several electron lines between 500 keV and 1.8 MeV listed in Tab. 4.2 and Tab. 4.3, respectively, together with their corresponding converted γ transitions.

Measurements using a ^{207}Bi source

^{207}Bi decays to excited states of ^{207}Pb via electron capture. The resulting level scheme of ^{207}Pb is shown in Fig. 4.15. This source provides three strong transitions at 569.7 keV, 1063.7 keV and 1770.2 keV. The transitions at 1063.7 keV and 1770.2 keV are in coincidence with the 569.7 keV transition.

The K-, L- and M- conversion electron lines are clearly identified in the electron spectrum measured using a Si(Li)-detector without the Mini-Orange as shown in Fig. 4.16. The energy of the conversion electrons is given by the γ-transition energy minus the binding energy of the K, L, and M electrons, which is 88.0 keV, 15.3 keV and 3.9 keV, respectively. Tab. 4.2 shows a list of the energies and intensities of the electron transitions together with their corresponding γ transitions [ENS07]. The value indicated with $\star$ is derived from the measured ratio K/L = 0.17(2) of the $7/2^- \rightarrow 5/2^-$ transition, which will be used later on to determine the efficiency ϵ_{MOS} of the Mini-Orange spectrometer.

In order to determine the transmission efficiency, the number of events decaying via the 1754 keV transition provided by the ^{207}Bi source were measured for various dis-
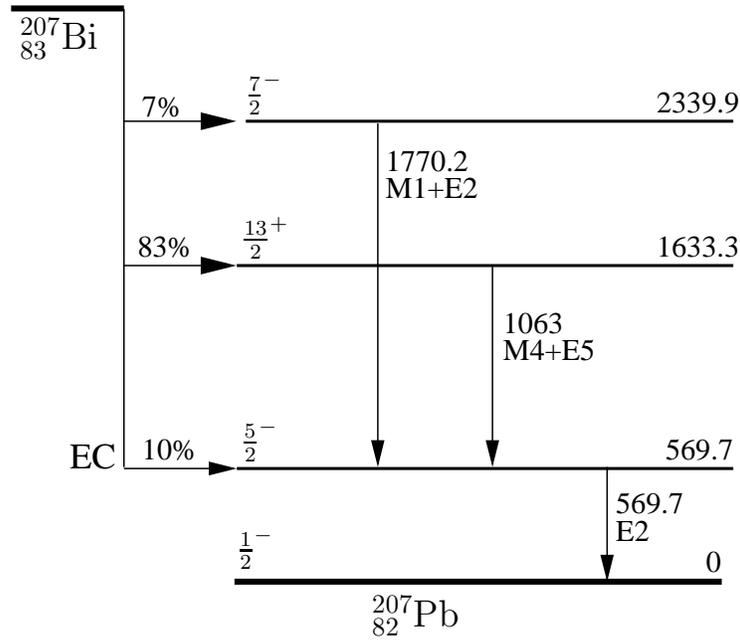
Figure 4.15: Level scheme of ^{207}Pb, populated by electron capture from ^{207}Bi.

^{207}Bi source						
E_γ [keV]	multi polarity	I_γ[%]	E_{el} [keV]	shell	$\alpha_{K,L,M}$	I_{e^-}[%]
569.7	E2	97.76(3)	481.7	K	0.0155(2)	1.515(20)
			554.4	L	0.00448(6)	0.438(6)
			565.8	M	0.0015(2)	0.147(20)
1063.7	M4+E5	74.6(5)	975.7	K	0.0942(17)	7.03(13)
			1048.1	L	0.0247(6)	1.843(45)
			1059.8	M	0.0073(9)	0.545(67)
1770.2	M1+E2	6.87(3)	1682.2	K	0.00351(15)	0.024(1)
			1754.4	L	0.00049(8)	0.0034(5)
					0.00060(8)	0.0041(5)*
			1766.3	M	0.00013(3)	0.0009(21)

Table 4.2: γ ray and conversion electron energies of the ^{207}Bi source. The binding energies of the K-, L- and M-electrons are 88.0 keV, 15.3 keV and 3.9 keV, respectively. Also listed are the conversion coefficients α and the intensities of the conversion electron decays I_{e^-}. The values are taken from [ENS07]. The value indicated with * is derived from the measured ratio K/L = 0.17(2) of the $7/2^- \rightarrow 5/2^-$ transition.

tances r between detector and source. Since the radiation of the source is isotropically distributed in 4π and was measured with a defined detector surface, the count rate is expected to be proportional to $1/r^2$.
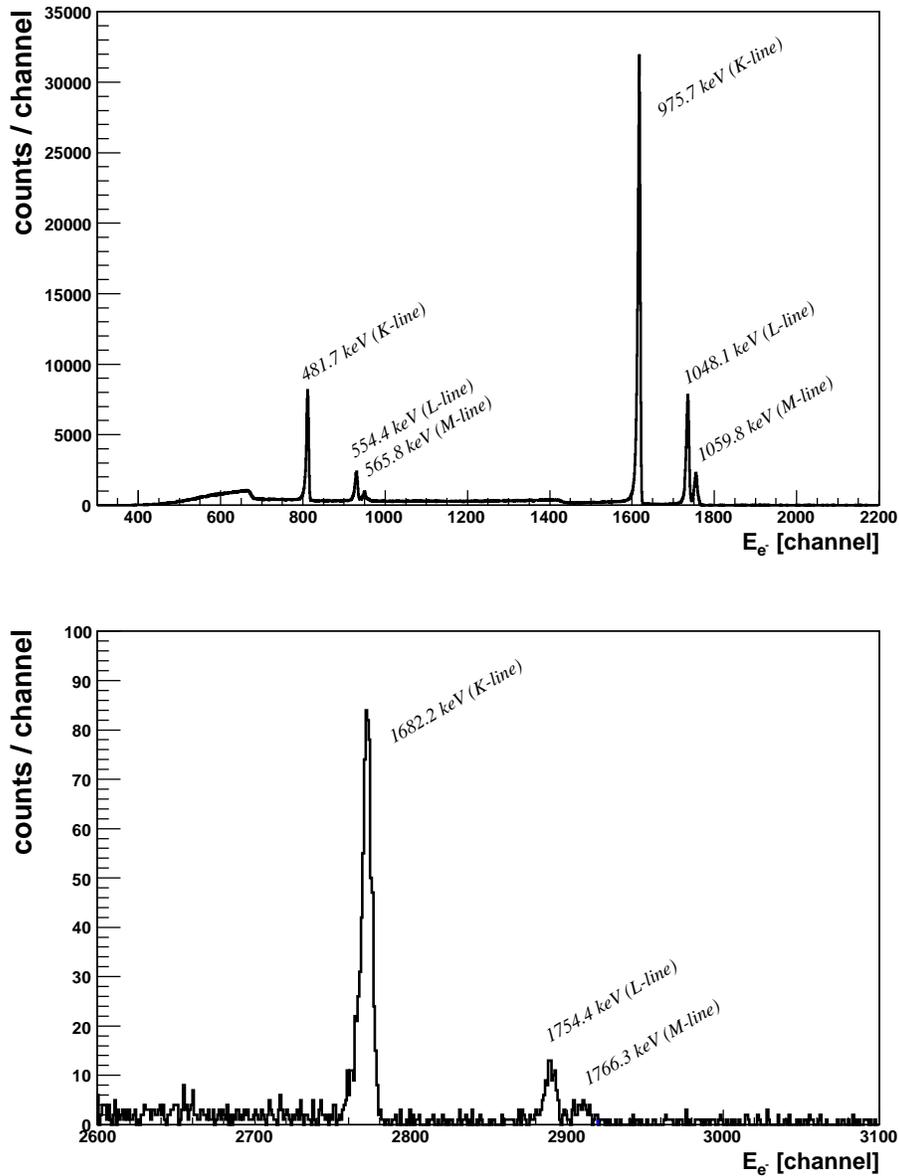
Figure 4.16: Conversion electron spectra of the ^{207}Bi source.

Measurements using a ^{152}Eu source

In addition measurements using an ^{152}Eu electron source were performed. The ^{152}Eu source provides several converted electron lines between ~ 100 keV and ~ 1400 keV. Fig. 4.17 a) shows the ^{152}Eu electron energy spectrum measured with the Si(Li) detector. Due to the huge background from β decay electrons, only the K-lines were used to determine the transmission function of the spectrometer. Fig. 4.17 b) shows the energy spectrum measured with the Mini-Orange between the source and the Si(Li) detector.
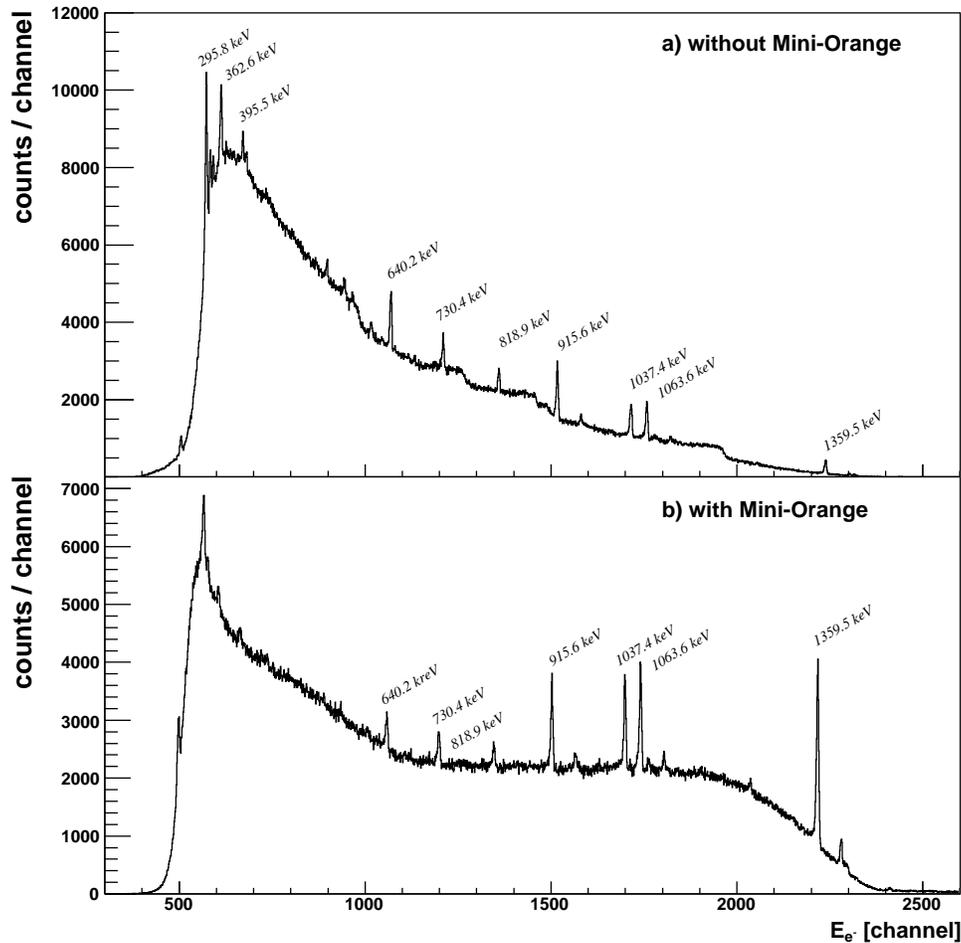
Figure 4.17: Panel a): Conversion electron energy spectrum of the ^{152}Eu source measured without the Mini-Orange. The discrete conversion lines sit on top of a strong background from β decay.
Panel b): Conversion electron energy spectrum of the ^{152}Eu source measured with the Mini-Orange. Compared to panel a) the convolution of the β decay energy spectrum with the transmission function can be seen.

Compared to the energy spectrum measured without the Mini-Orange (Fig. 4.17 a)), the convolution of the β decay energy spectrum with the transmission function can be seen.

Since the position of the Mini-Orange and Si(Li) detector, respectively, were optimised to achieve a transmission maximum around 1.8 MeV, only conversion electron lines with energies larger than 600 keV were used for the analysis. Tab. 4.3 shows a list of the energies and intensities of the strongest γ transitions together with the corresponding intensity I_K of the K conversion electron transition.

^{152}Eu source					
E_γ [keV]	multi polarity	I_γ [%]	E_{el} [keV]	α_{K}	I_{K} [%]
121.8	E2	28.67(15)	73.3	0.669(11)	19.18(33)
244.7	E2	7.61(4)	196.2	0.0815(20)	0.620(16)
444.0	E1(+M2)+E2	3.16(3)	395.5	0.0065(5)	0.00213(20)
688.7	E0+E2+M1	0.86(1)	640.2	0.0359(13)	0.0309(12)
778.9	E1(+M2)	12.98(15)	730.4	0.00154(6)	0.01999(81)
867.4	M1+E2	4.26(3)	818.9	0.0031(3)	0.0132(13)
964.1	M1+E2	14.65(7)	915.6	0.00238(9)	0.0349(14)
1085.9	E2	10.24(5)	1037.4	0.00207(8)	0.02119(83)
1089.7	E2+M1	1.75(1)	1041.2	0.00230(5)	0.00402(87)
1112.1	M1+E2	13.69(7)	1063.6	0.00186(12)	0.0255(17)
1408.0	E1	21.07(10)	1359.5	0.00050(3)	0.01053(63)

Table 4.3: γ ray and conversion electron energies and intensities of the ^{152}Eu source [ENS07] together with the K conversion coefficient α_{K}. The binding energy of the K electron is 48.5 keV [FIR96].

Results of the transmission efficiency measurements

In order to determine the transmission function of the Mini-Orange, various measurements for different object distances g and image distances b were performed using ^{207}Bi and ^{152}Eu sources. Fig. 4.18 shows the resulting transmission efficiencies as a function of the image distance b for the object distances $g = 50$ mm (blue), $g = 60$ mm (red) and $g = 70$ mm (green). The vertical lines indicate the detector position with an achieved transmission maximum around 1.8 MeV, as required to identify the predicted E0 transition in ^{30}Mg.

For a defined object and image distance the transmission function depending on the kinetic energy of the electrons can be given. Fig. 4.19 shows the result for the measured object distances. For an object distance of 50 mm or 60 mm the transmission maximum is around 1800 keV with an absolute efficiency of 3.5%. Typically the transmission function reaches its maximum for a certain energy if the object distance and the image distance is about the same size. Then the electron trajectories are almost symmetrical with respect to the focal plane of the Mini-Orange.

Varying the object and image distance of the spectrometer, the energy of the transmission maximum can be shifted. Fig. 4.20 shows the transmission curves obtained from different choices of object and image distances, resulting in transmission maxima around 1000 keV, 1400 keV and 1800 keV, respectively, with a corresponding transmission efficiency of 6.8%, 4.8% and 3.5%.

For the E0 transition experiment in ^{30}Mg at 1789 keV an object distance $g = 60$ mm and an image distance $b = 82$ mm was chosen.

Absolute transmission efficiency measurements

In general the absolute efficiency of the whole Mini-Orange spectrometer

$$\epsilon_{\mathrm{MOS}}(E_{e^-}, b, g) = T(E_{e^-}, b, g, A) \cdot \epsilon_{\mathrm{SiLi}}(E_{e^-}, \alpha(r, b, E_{e^-})) \tag{4.5}$$

is the product of the transmission efficiency T depending on the electron energy E_{e^-}, the distances b and g and the detector surface A and the detector efficiency ϵ_{SiLi} depending E and the incidence angle α. For a fixed spectrometer system the transmission T is known (see Fig. 4.19). Since the exact incident angle between the electron and the detector plane is not known, the detector efficiency ϵ_{SiLi} cannot be calculated.

In order to determine the efficiency of the Mini-Orange spectrometer ϵ_{MOS} the ^{207}Bi source was calibrated using a calibrated ^{152}Eu source with 2 % accuracy. In this measurement the deadtime of the data acquisition system was also taken into account. The activity of the ^{207}Bi source was determined to be 25.6(6) kBq and for the ^{152}Eu source the activity was determined to be 138(3) kBq.

The absolute efficiency of the spectrometer can be determined from the calibrated ^{207}Bi and ^{152}Eu source using

$$\epsilon_{\mathrm{MOS}} = \frac{I_{\mathrm{MO}}}{I_{\mathrm{abs}} \cdot \alpha_{\mathrm{K,L,M}}} = \frac{I_{\mathrm{MO}}}{I_{\mathrm{K,L,M}}} \tag{4.6}$$

with the intensity of the conversion electron transition $I_{\mathrm{K,L,M}}$ shown in Tab. 4.2 and 4.3, respectively.

Fig. 4.21 shows the absolute transmission efficiency ϵ_{MOS} of the Mini-Orange spectrometer resulting in a transmission efficiency maximum of 2.6(1)% at 1550 keV, 4.1(2)% at 1350 keV and 5.9(3)% at 1000 keV. For the E0 transition in ^{30}Mg at 1788 keV a transmission efficiency $\epsilon_{\mathrm{MOS}} = 1.8(2)$% is obtained using a linear extrapolation of the K and L conversion electron line of the $7/2^- \rightarrow 5/2^-$ transition in ^{207}Pb at 1682.2 keV and 1754.5 keV, respectively.
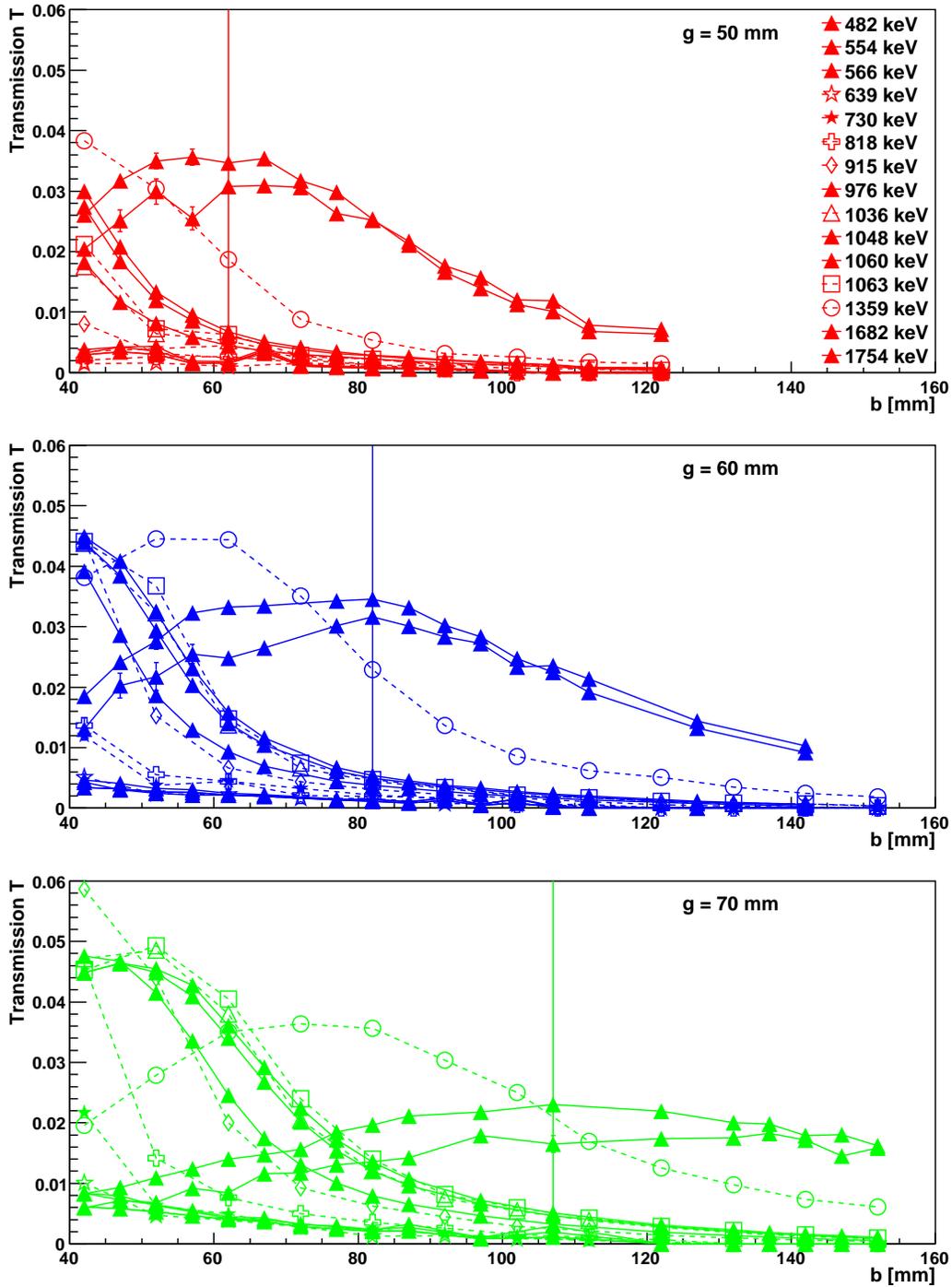
Figure 4.18: Transmission measurements of the Mini-Orange for different object distances g and image distances b using a calibrated ^{207}Bi and ^{152}Eu source. The object distances $g = 50$ mm (blue), $g = 60$ mm (red) and $g = 70$ mm (green) were used to measure the transmission efficiency as a function of the image distance. The vertical lines indicate the detector position with maximum electron transmission efficiency at an electron energy of 1.8 MeV.
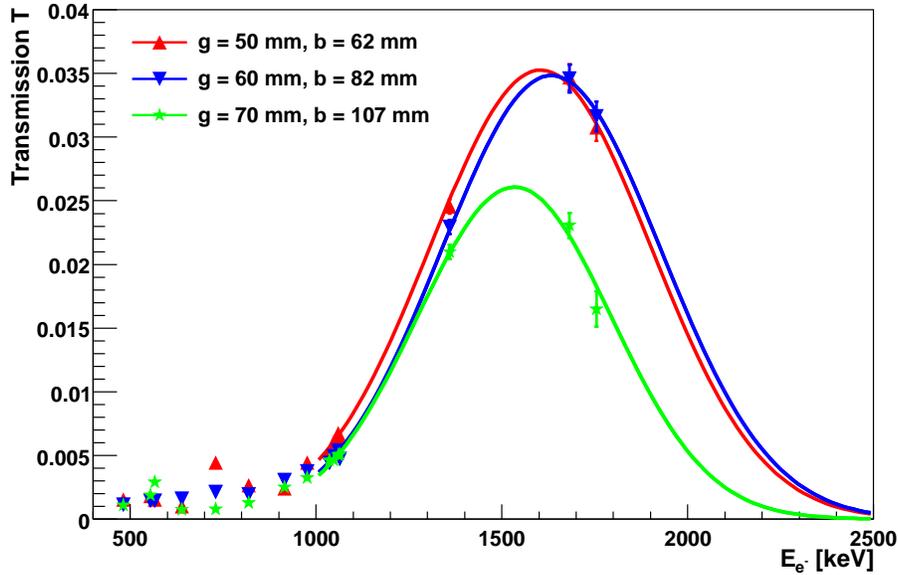
Figure 4.19: Measured transmission curves T of the Mini-Orange.
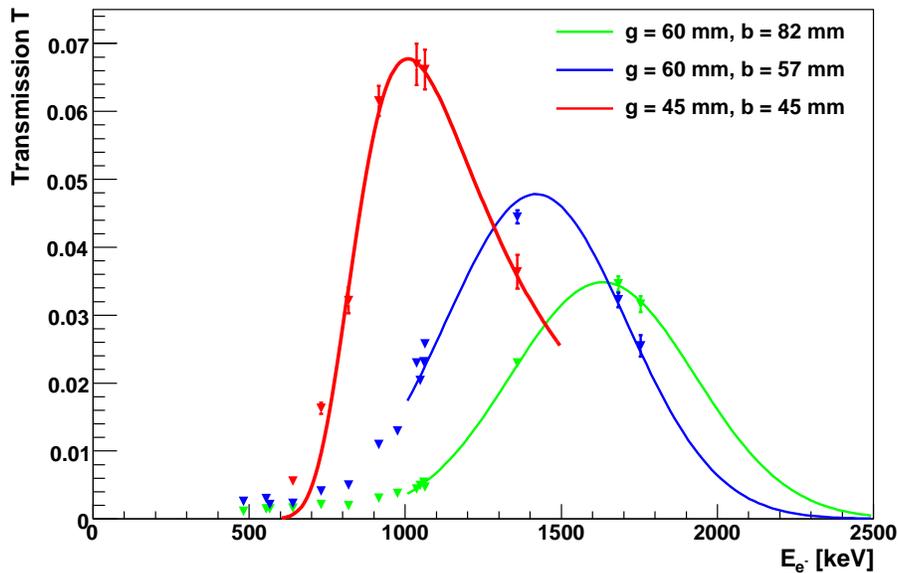
Figure 4.20: Transmission curves of the Mini-Orange T. By changing the object distance g and the image distance b the energetic position of the transmission maximum of the Mini-Orange can be varied. Three examples for transmission curves obtained for different geometrical choices of the object and the image distance are displayed. They result in transmission maxima around 1000 keV, 1400 keV and 1800 keV with a transmission efficiency of 4.6%, 3.5% and 2.3%, respectively.
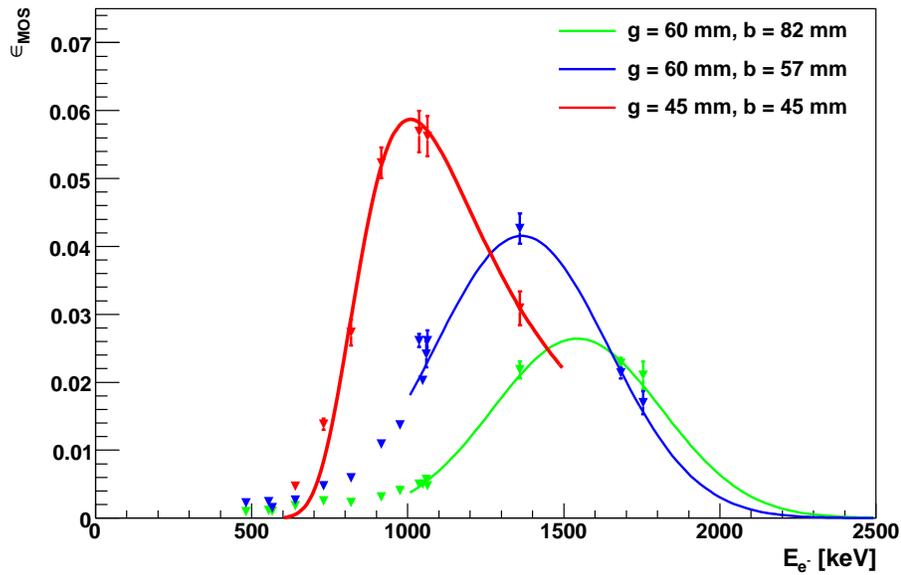
Figure 4.21: Measured absolute transmission curves taking into account the transmission T of the Mini-Orange as well as the backscattering probability $(1-\kappa)$ on the surface of the Si(Li) detector.

5 The E0-Transition in ^{30}Mg at 1789 keV

As a result of γ spectroscopy measurements of the β decay of ^{30}Na and the β-delayed neutron emission of ^{31}Na using the 'fast timing' technique [MAC05], performed at the ISOLDE facility [ISO] at CERN [CER], the 1789 keV level in ^{30}Mg was identified as a strong candidate for the deformed 0_2^+ intruder state. To identify the deformed 0_2^+ intruder state via its E0 decay to the spherical 0_1^+ ground state conversion electron studies in ^{30}Mg were conducted.

5.1 γ spectroscopic properties of ^{30}Mg

The analysis of the γ spectroscopy data from fast timing experiments in ^{30}Mg [MAC05] gave clear evidence for a 1789 keV γ transition. These $\gamma\gamma$ coincidence measurements
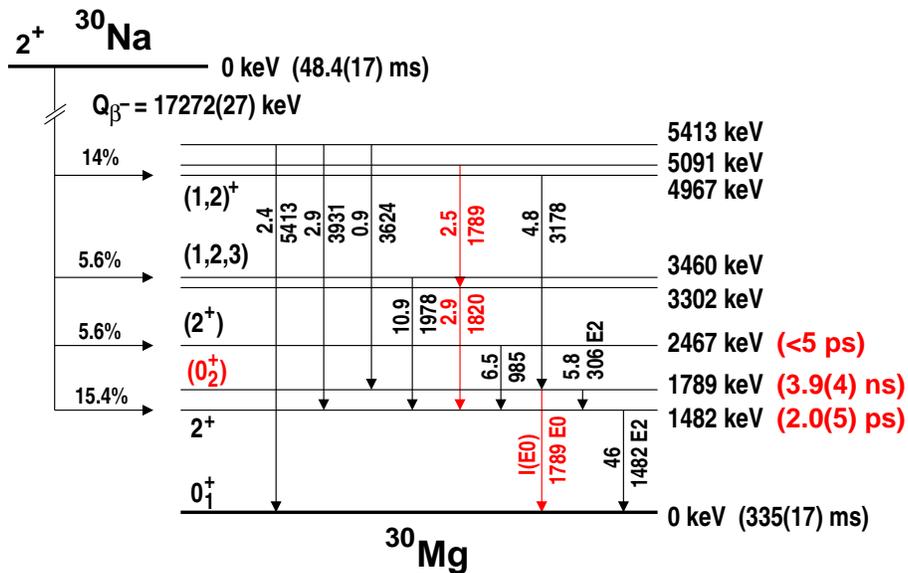
Figure 5.1: Populated levels in ^{30}Mg via the β decay of ^{30}Na. Different assignments by H. Mach et al. [MAC05] compared to the previously published decay scheme of ^{30}Na→^{30}Mg in the "Table of Isotopes" [FIR96] are marked in red.

resulted in a re-assignment of transitions in the ^{30}Mg level scheme compared to data published earlier [KLO93]. It turned out that the 1789 keV transition is not in coincidence with the 3178 keV transition feeding the 1789 keV level, however it was found to be in coincidence with the 1482 keV $2^+ \rightarrow 0_1^+$ transition and the 1820 keV transition feeding into the 2^+ level instead (see Fig. 5.1). This finding forced the placement of the 1789 keV transition on top of the level at 3302 keV and not as initially expected depopulating the 1789 keV level to the ground state, thus leading to a new level at 5091 keV. Consequently the 1789 keV level has no direct γ decay branch to the ground state, but only decays with a 306 keV E2 transition via the 1482 keV 2_1^+ state. The present knowledge of the low-lying levels in ^{30}Mg is displayed in Fig. 5.1. Different assignments compared to the published decay scheme of ^{30}Na$\rightarrow$ ^{30}Mg in the "Table of Isotopes" [FIR96] are marked in red.

Also a rather long lifetime of 3.9(4) ns was measured for the 1789 keV level. In addition an initial imbalance of γ intensity for the 1789 keV state in the ^{31}Na $\rightarrow$ ^{30}Mg neutron-delayed β decay appeared from the feeding via the 3178 keV transition and the de-exciting via the 306 keV transition [MAC05, KLO93] of the order of a few percent of intensity. In a further data analysis this strong imbalance could not be confirmed, however it triggered our initial search for a strong E0 transition in ^{30}Mg.

A possible explanation of the long lifetime of the 1789 keV level together with the absence of a ground state γ transition led to the assignment of the 1789 keV level as a candidate for the (deformed) 0_2^+ state in ^{30}Mg, serving as motivation for our experimental campaign to identify this state via its E0 decay to the ground state.

5.2 Estimate of the mixing amplitude a

A mixing matrix element of -200 keV in ^{32}Mg was calculated by Utsuno et al. [UTS99] by comparing the energy shift of a pure $2p - 2h$ configuration to a calculation, where a $0p - 0h$ configuration was included as well. Also this calculated mixing matrix element should only be considered as a rough guideline for the interaction between the two potential minima in ^{30}Mg. Assuming the mixing of the 0^+ states in ^{30}Mg to be of about the same size, this mixing matrix element can be used to roughly estimate the mixing amplitude a in ^{30}Mg as shown in Sect. 3.3.1. The transition energy of the intrinsic system follows as 1.59 MeV. With a ratio $R = 7.95$ Eq. (3.12) a mixing amplitude of $a_{\text{calc}} = 0.12$ can be deduced, which will be seen to be in remarkably good agreement with the value derived from our experimental study.

5.3 Estimates of the E0 strength in ^{30}Mg

For designing the experimental setup with an appropriate sensitivity for the E0 decay branch, an estimate for the expected E0 transition strength is needed.
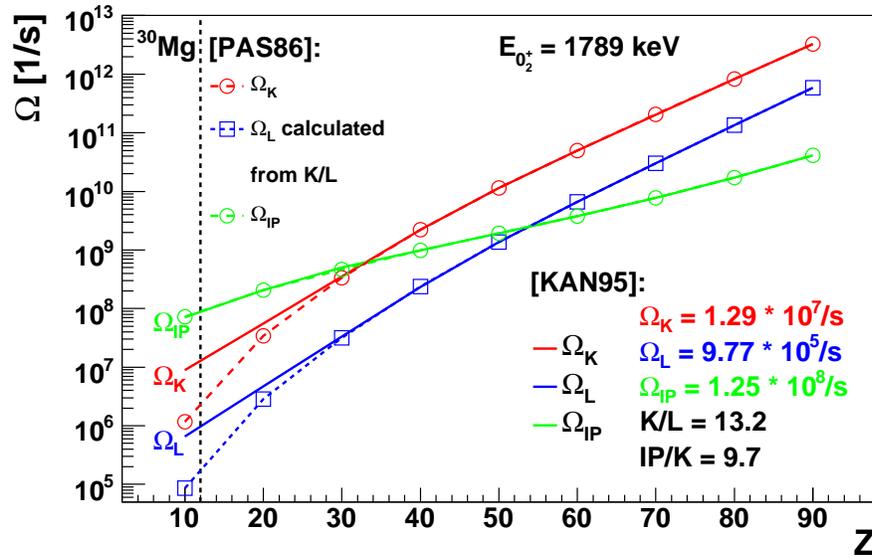
Figure 5.2: Ω_i values calculated with the program OMEGA.BAS [KAN95] and OMEGAIFP.BAS [KAN95] for stable nuclei as a function of the nuclear charge Z. For the transition energy ΔE the excitation energy of the potential 0_2^+-state of ^{30}Mg (1789 keV) was used for all nuclei. The Ω_i values, K/L- and IP/K-ratios are indicated for ^{30}Mg.
Also the Ω_i calculated using [PAS86] are indicated.

Quantity	$Z = 12$, $A = 30$ $E = 1788$ keV	fraction [%]
Ω_{IP}	$9.367 \cdot 10^7/\text{s}$	97.1
Ω_K	$2.752 \cdot 10^6/\text{s}$	2.9
$\sum_i \Omega_i$	$9.642 \cdot 10^7/\text{s}$	

Table 5.1: Electronic Ω_i-factors for ^{30}Mg using [PAS86].

In Fig. 5.2 the Ω_i-values are shown calculated using the programs OMEGA.BAS and OMEGAIFP.BAS by [KAN95] and using [PAS86]. Since the Ω_i values calculated by [KAN95] are only a rough extrapolation from nuclei around $Z = 30$ the values calculated using [PAS86] are considered to describe the Mg more reasonable. Fig. 5.2 shows the Ω_i-values over a wide range of nuclear charge values Z calculated for the potential excitation energy of the 0_2^+ state of ^{30}Mg at 1789 keV. Tab. 5.1 gives the calculated Ω_i values for ^{30}Mg. In light nuclei ($Z \lesssim 30$) internal pair creation is the dominant process, while with increasing Z the Ω_i values for electron conversion are increasing.

The K/L-ratio by [KAN95] for the internal conversion is 13.2 for ^{30}Mg, while the ratio between internal pair creation and K electron conversion amounts to $\Omega_{IP}/\Omega_K = 9.7$. Therefore in ^{30}Mg the internal pair creation is about a factor of 10 stronger than the conversion electron decay. Using [PAS86] the Ω_{IP}/Ω_K-rato is 34. In order to exploit

the larger yield from the internal pair creation process, a high-efficiency e^+e^- pair spectrometer would have been a favourable design for the setup. However, due to the distinct experimental signature offered by the 1789 keV conversion electron decay of the 0_2^+ state, a rather simple and compact setup was chosen on the basis of a Mini-Orange spectrometer, focusing on the weaker electron conversion decay branch for ^{30}Mg.

In order to calculate the expected partial lifetime of the E0 decay, the sum of all Ω-values has to be taken into account, resulting in $\Sigma_i\Omega_i = 9.642 \cdot 10^7$/s for ^{30}Mg.

In the absence of any quantitative microscopic predictions for the nuclear deformations of the 0_1^+ and 0_2^+ states in ^{30}Mg at the starting time of our experimental project, a coarse phenomenological estimate for the effective deformation of the 0_1^+ ground state of ^{30}Mg was derived within the rigid rotor model from the measured $B(E2, 0_1^+ \rightarrow 2_1^+)$ value [NIE05] to be $\beta_1 = 0.39$ according to Eq. (8.2). For the deformation β_2 of the excited 0_2^+ state of ^{30}Mg the measured large deformation of the ground state of ^{32}Mg $(\beta_1 \sim 0.51)$ derived as described before from the $B(E2)$ value was assumed.

Since the measured β values of the two physical 0^+ states already contain admixtures from the other basic 0^+ states, the large effective deformation $\beta_1 = 0.39$ extracted from $B(E2, 0_1^+ \rightarrow 2_1^+) = 241(31)$ e^{2}fm^4 [NIE05] for the ground state in ^{30}Mg may originate from admixtures of the deformed 0_2^+ state. Measuring the E0 strength $\rho^2(E0)$ allows to extract the mixing amplitude a.

In our simplified model, assuming a mixing between the two potential minima with $a_{\text{calc}} = 0.12$, we obtain an estimate for the electric monopole strength of

$$\rho^2(^{30}\text{Mg}, \text{E0}) = 2.0 \cdot 10^{-3}. \tag{5.1}$$

From this estimate of $\rho^2(E0)$ the partial lifetime of the 0_2^+ state in ^{30}Mg can be calculated to be

$$\tau_{\text{tot}}(\text{E0}) = 7.3 \ \mu\text{s}. \tag{5.2}$$

Since in our experiment only conversion electrons were measured, the corresponding partial E0 lifetime is estimated to be $\tau_K(\text{E0}) = 176 \ \mu\text{s}$.

This lifetime is much longer than the measured total lifetime for the 1789 keV level of 3.9 ns, which is dominated by the fast E2 transition $0_2^+ \rightarrow 2_1^+$ at 306 keV. This results in a rather small branching ratio for the E0 transition and makes the experiment more challenging. In the β decay of ^{30}Na the 306 keV transition has been observed in 5.8% of all decays. Therefore we expect in the scenario of our estimate a rather small intensity of $I(\text{E0}) \sim 6.3 \cdot 10^{-4}$.

6 Preparatory Experiments at ISOLDE

The ISOLDE facility (Isotope Separator On Line) [ISO] produces radioactive nuclides in spallation, fission or fragmentation reactions. It is part of the European Organisation for Nuclear Research (CERN [CER]), the world's largest particle physics centre. It is located astride the Franco-Swiss border near Geneva.

Radioactive nuclides like ^{30,31,32}Na and ^{96}Y as used in the presented experiments are produced by bombarding a uranium carbide/graphite target (UC$_x$) with a pulsed 1.4 GeV proton beam with an intensity up to $3.2 \cdot 10^{13}$ protons per pulse, provided by the PS Booster with a repetition time of 1.2 s. For radioprotection reasons the integrated proton beam current is limited to $< 2~\mu$A. Since the PS Booster delivers protons also to the CERN Proton Synchrotron (PS) and thus to all CERN high-energy
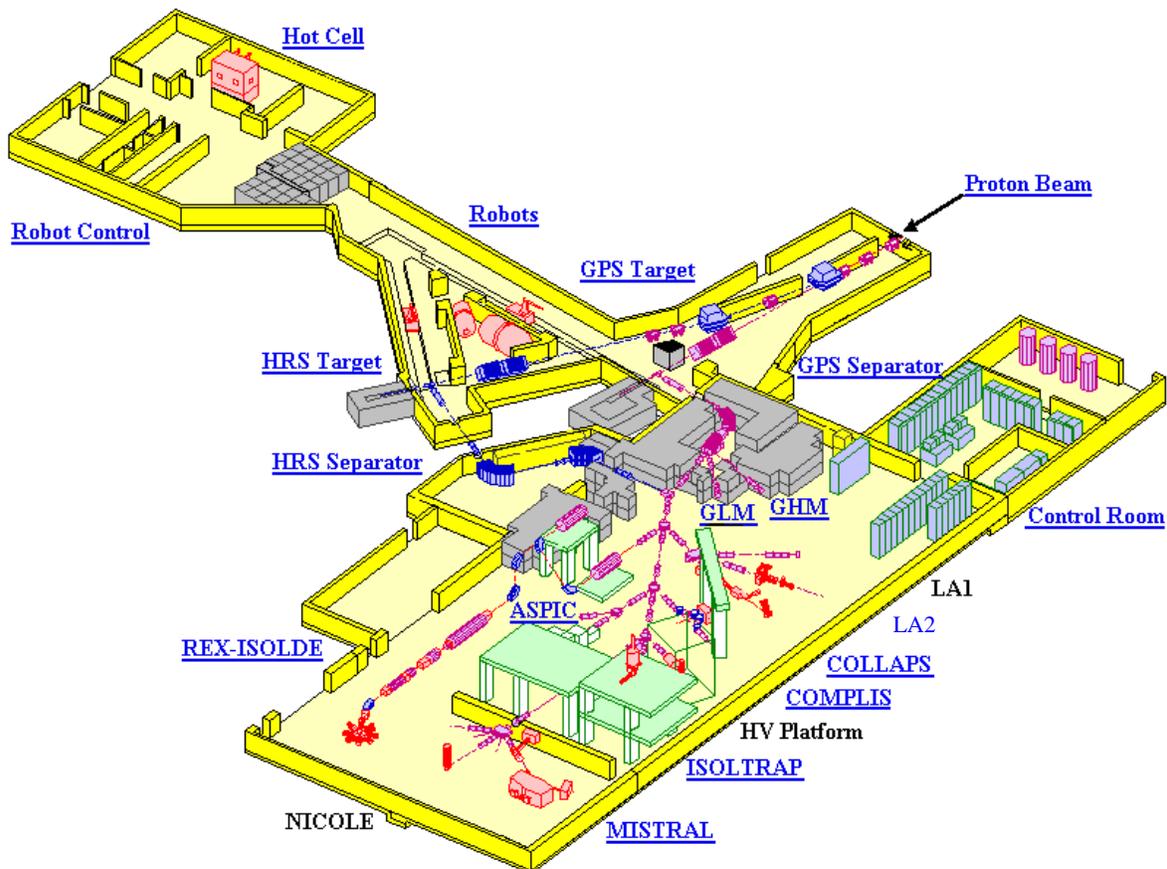
Figure 6.1: The ISOLDE facility [ISO] at CERN [CER].

experiments, not all the pulses may be used. In our experiments only up to half of the pulses in the super cycle containing 12 pulses is brought to bombard the ISOLDE target with an integrated beam current below the limitation.

In order to extract the nuclei from the target, they are ionised using a surface ion source consisting of a tungsten tube, which has a higher work function than the atom that should be ionised. Both, target and ion source, were operated at 2050 °C.

A beam consisting of a certain mass over charge ratio was separated in the High Resolution Separator (HRS) consisting of two magnets (one 90° and one 60° dipole magnet) at a kinetic energy of 40 keV. A mass resolution of $m/\Delta m > 5000$ can be reached.

In order to allow the ions from the target to reach the separator and the experiment, a beam gate consisting of an electrostatic steerer has to be opened. This opening can be synchronised with the beam pulse. Due to the different half lives of elements with the same mass, the duration of the beam gate opening and its delay with respect to the proton pulse can be used to influence the fraction of certain elements in the beam.

This 40 keV beam is then guided through the beamline to the experiment by various electrostatic deflectors, steering modules and lenses.

6.1 First feasibility study of E0 measurements in ^{30}Mg

In August 2005 a first test experiment was performed to study the feasibility of conversion electron spectroscopy at ISOLDE. Therefore the known E0 transition in ^{96}Zr was studied using an $A = 96$ beam to determine the sensitivity of the setup. Also the E0 transition in ^{30}Mg at a transition energy of 1789 keV was searched by studying the β decay of ^{30}Na and also the β-delayed neutron emission of ^{31}Na.

6.1.1 Experimental setup and electronics

Fig. 6.2 shows a photograph of the experimental setup, while Fig. 6.3 displays a schematic view. The mass-separated particle beam was stopped in the centre of the target chamber on a catcher foil (0.1 mm thick Al foil), which is turned by 45° towards the Mini-Orange spectrometer to guide the electrons directly towards the Si(Li) detector with minimum energy loss in the foil. The catcher foil was mounted on a load lock system in order to enable target manipulations without breaking the vacuum of the target chamber. The load lock system was mounted on top of the cubic target chamber. Also a calibration source can be inserted to the target chamber using the same mechanism. A "pocket-type" aluminium cylinder with a wall thickness of 3 mm, reaching into the target chamber, was mounted opposite to the Mini-Orange spectrometer (see Fig. 6.3). Inside the cylindrical pocket at atmospheric pressure a germanium detector was positioned in order to identify the beam composition. A 7 cm thick lead collimator with an outside diameter of 10 cm was mounted in the beamline at the entrance of
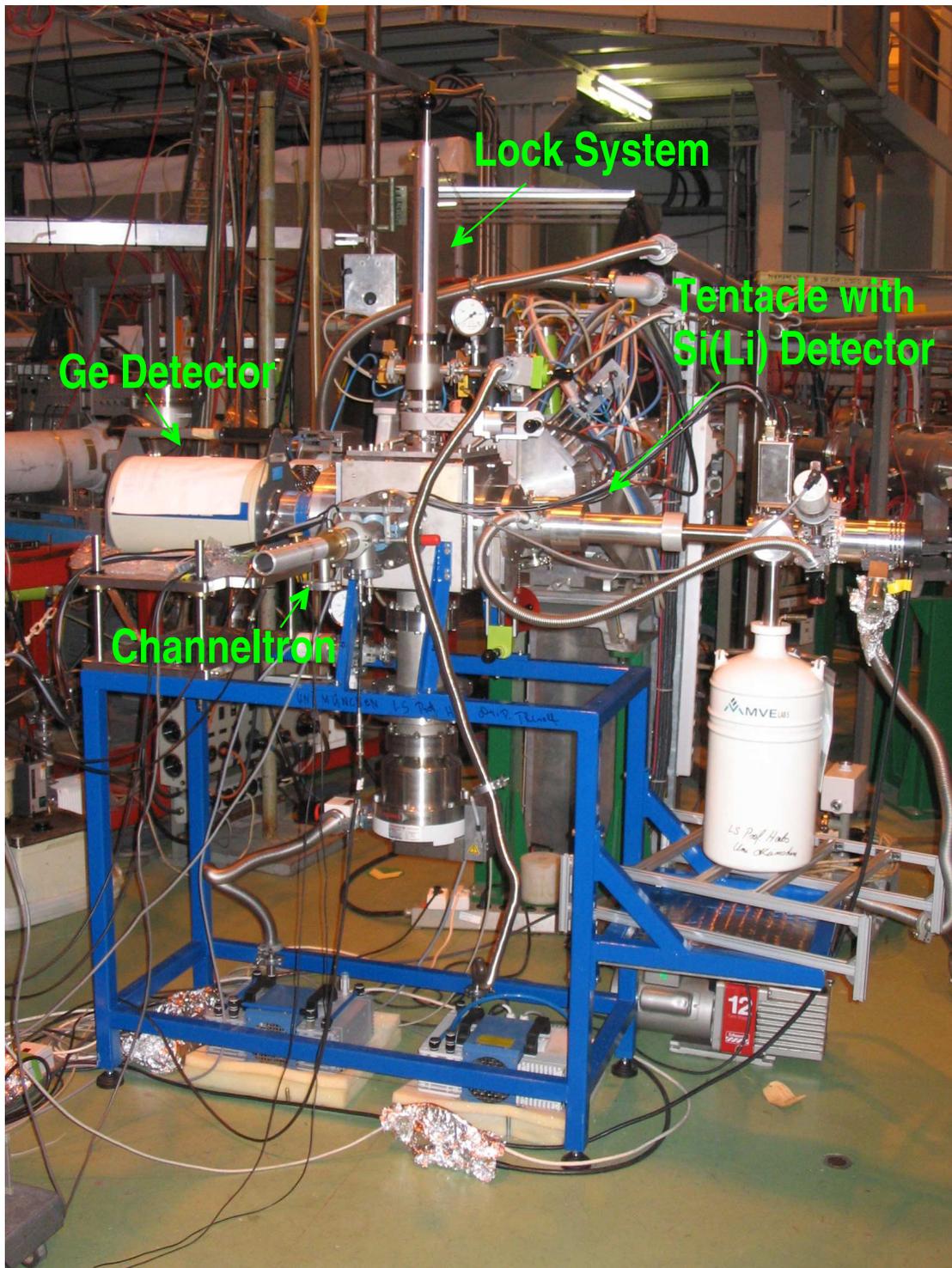
Figure 6.2: Picture of the experimental setup used for the first feasibility study at ISOLDE in August 2005.
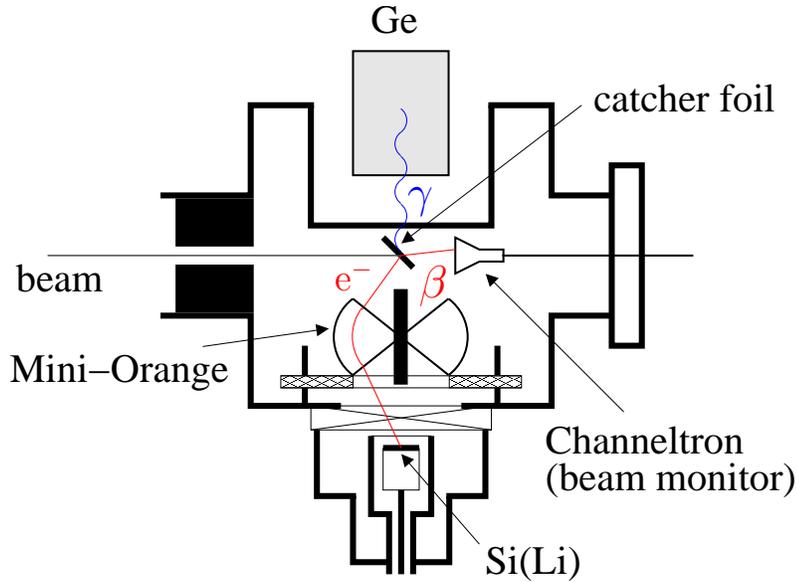
Figure 6.3: Sketch of the conversion electron spectroscopy setup used in the exploratory experiment during the August 2005 run at ISOLDE (bottom view). Electrons were detected with a Mini-Orange spectrometer, a germanium detector was used to identify the beam composition and a channeltron served as beam monitor.

the target chamber leaving a central hole of 5 mm diameter, thus allowing to focus the beam onto the catcher foil and to avoid any contamination of the target chamber. It also protects the germanium detector from γ rays emitted along the beamline. Due to the low beam intensity ($\sim 10^4$ particles per second) and due to the resulting low counting rate a channeltron could be mounted from the back side of the catcher foil detecting electrons following the β decay and thus serving as beam monitor.

The signal processing electronics used for the Si(Li) and the germanium detector are similar to the electronics shown in Fig. 7.3. For the data acquisition an MBS-based acquisition system [MBS] from ISOLDE was used.

6.1.2 Reference measurement in ^{96}Zr

In order to prove the feasibility of conversion electron experiments at ISOLDE and to test the reliability of our experimental technique, the well-known E0 transition in ^{96}Zr was studied. Therefore excited levels in ^{96}Zr were populated following the β decay ($Q_\beta = 7100(22)$ keV) of neutron-rich $A = 96$ elements. ^{96}Zr has a 0_2^+ state at 1582 keV with an absolute intensity of the ground state E0 transition of 1.41(12)% [MAC90]. The half-life of the 0_2^+ state is 38.0(7) ns [ENS07] and thus the monopole strength can be calculated to be $\rho^2(E0) = 7.4(3) \cdot 10^{-3}$. The transition energy is close to the maximum of the transmission curve of the Mini-Orange spectrometer ($\sim$1700 keV).
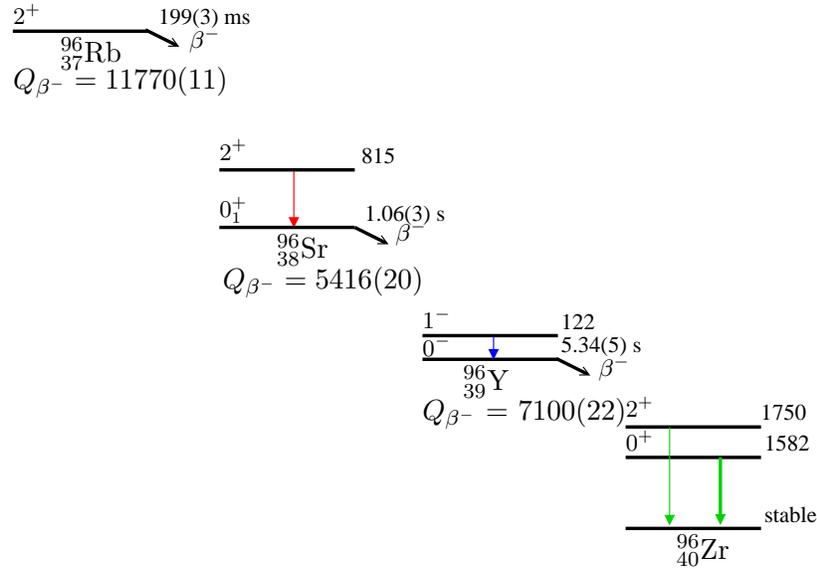
Figure 6.4: Decay chain of neutron-rich mass 96 isobars. Only the ground state transitions in the daughter nuclei are shown.

Therefore it provides a good test case for the setup. Due to the short lifetime of the mass 96 elements ($t_{1/2} \leq 5.34$ s) the target chamber is not contaminated with long-lived activity. The decay chain of mass 96 elements in the beam is shown in Fig. 6.4.

Quantity	$Z = 40, A = 96$ $E = 1582$ keV	fraction [%]
Ω_{IP}	$3.22 \cdot 10^8$/s	13.6
Ω_{K}	$1.84 \cdot 10^9$/s	78.0
Ω_{L1}	$1.95 \cdot 10^8$/s	8.3
Ω_{L2}	$1.52 \cdot 10^6$/s	0.06
$\sum_i \Omega_i$	$2.36 \cdot 10^9$/s	~ 100

Table 6.1: Electronic Ω_i-factors for the E0 transition in ^{96}Zr at 1582 keV. The values were calculated using the programs OMEGA.BAS [KAN95] and OMEGAIFP.BAS [KAN95]

In Fig. 6.5 the Ω_i values are shown calculated using the programs OMEGA.BAS and OMEGAIFP.BAS by [KAN95] and using [PAS86]. The $\Omega_{\text{K,L,IP}}$ values in ^{96}Zr are listed in Tab. 6.1. Compared to the Mg case (see Tab. 5.1), the $\Omega_{\text{K,L}}$ values in ^{96}Zr are three orders of magnitude larger. The K/L-ratio is 9.4 and the ratio between internal pair creation and K electron conversion amounts to $\Omega_{\text{IP}}/\Omega_{\text{K}} = 0.18$, which is about a factor of 50 smaller than Ω_{IP} in ^{30}Mg. The sum of all Ω_i values is $2.36 \cdot 10^9$/s, which is about a factor of 17 higher than in the ^{30}Mg case.
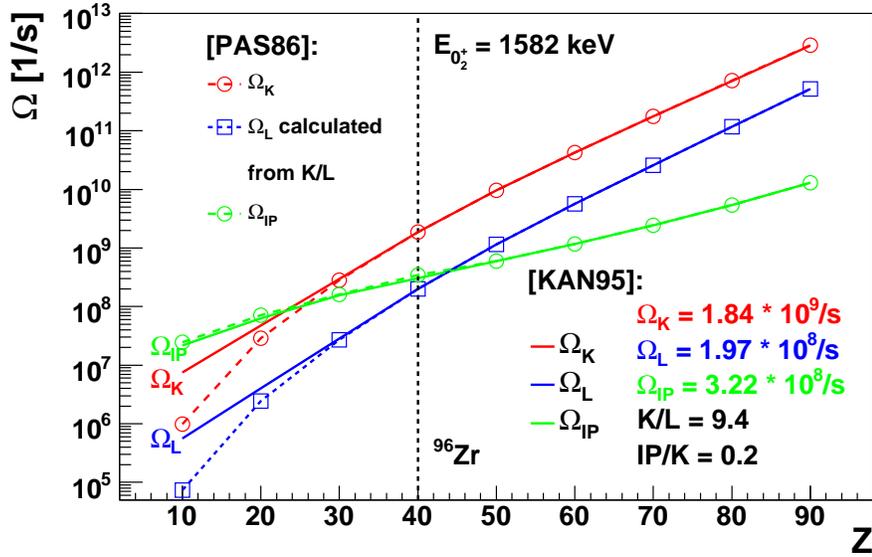
Figure 6.5: Ω_i values calculated with the program OMEGA.BAS [KAN95] and OMEGAIFP.BAS [KAN95] for stable nuclei as a function of the nuclear charge Z. For the transition energy ΔE the excitation energy of the 0_2^+ state of ^{96}Zr was used for all nuclei. The Ω_i values, K/L- and IP/K-ratios are given for ^{96}Zr.

Also the Ω_i calculated using [PAS86] are indicated.

Fig. 6.6 shows the result of a 2.2 h measurement. The shape of the continuous background energy distribution is given by the transmission function of the Mini-Orange spectrometer. Derived from the $2^+ \rightarrow 0_1^+$ γ-transition at 1750 keV ~ 210 ^{96}Y decays per second were obtained. The germanium detector efficiency for this transition energy is 0.28 %. The counting rate in the Si(Li) detector was ~ 90/s, while the germanium detector registered ~ 570 counts per second.

The K and L transition lines can clearly be identified and separated. In the K transition line 3205(98) counts could be detected, while in the L transition line 402(64) counts were registered. The resulting K/L ratio of 8.0(1.5) is consistent with the theoretical K/L ratio of 9.3 [CHU56]. The visibility of the L-line demonstrates that a conversion decay intensity as low as ~ 0.1 % with about 400 counts can be detected on top of the continuous background from the β decay.

6.1.3 First E0 experiment with an $A = 30$ beam

Fig. 6.7 displays the electron energy spectrum accumulated with the Mini-Orange spectrometer during the $A = 30$ run. The runtime was 11 h. Already at first glance the spectrum does not exhibit the strong E0 transition at 1788 keV, which was initially expected when attributing an imbalance of γ intensities feeding and depopulating the
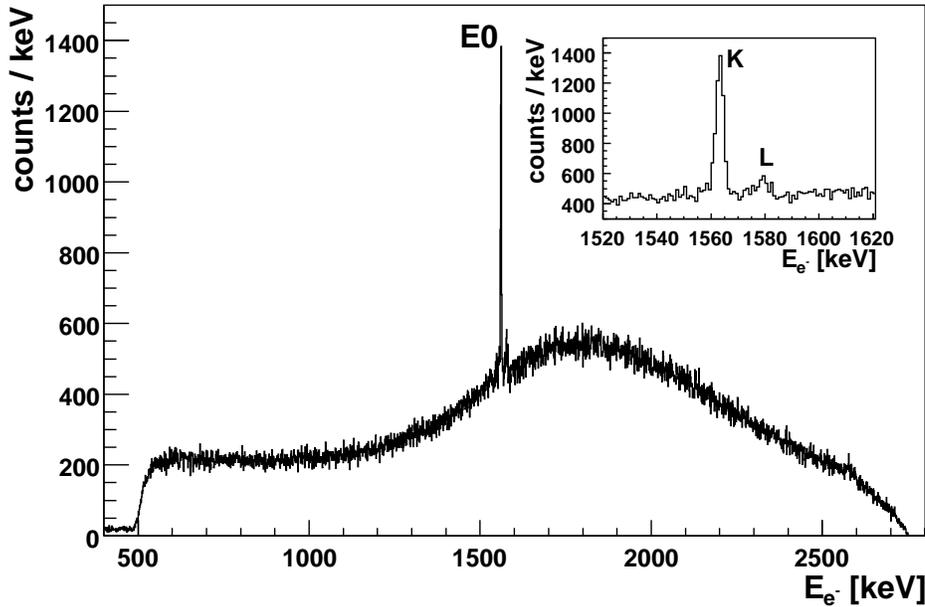
Figure 6.6: Electron spectrum from the decay of $A = 96$ isobars with the prominent E0 transition in ^{96}Zr at 1563 keV measured with the Mini-Orange spectrometer in 2.2 h. ~ 210 ^{96}Y decays per second were obtained, as derived from the γ spectrum measured with the germanium detector.

1789 keV state in ^{30}Mg to a potential strong E0 branch (see Sect. 5.1).

The experimental sensitivity for the E0 transition in ^{30}Mg could be derived from the reference measurement in ^{96}Zr (see Sect. 6.1.2) to be $I_{\mathrm{E0}} \leq 0.1\%$, which corresponds to $\rho^2(\mathrm{E0}) \leq 0.26$. This first test run was clearly limited by strong continuous background from β decay electrons in the Si(Li) detector. Therefore a modified setup was realised in order to allow for a coincidence measurement.

6.1.4 Yield test with the (^{31}Na, βn) reaction

Also the β delayed neutron emission of the (^{31}Na, βn) reaction was used to populate excited states in ^{30}Mg. Since the Q value of this decay ($Q_\beta = 13490(21)$ keV) is smaller compared to the Q value of the β decay of ^{30}Na ($Q_\beta = 17272(27)$ keV) and since in this case a neutron is emitted, which removes a sizable part of the excitation energy, it can be expected that this decay channel predominantly populates lower-lying excited levels in ^{30}Mg. Also the different spin of the ground state in ^{31}Na ($I = 3/2^+$) causes a different population intensity of the low-lying states in ^{30}Mg.

In this experiment also no E0 transition in ^{30}Mg was found and thus the initially expected strong E0 transition could not be confirmed. Since the $A = 31$ beam intensity
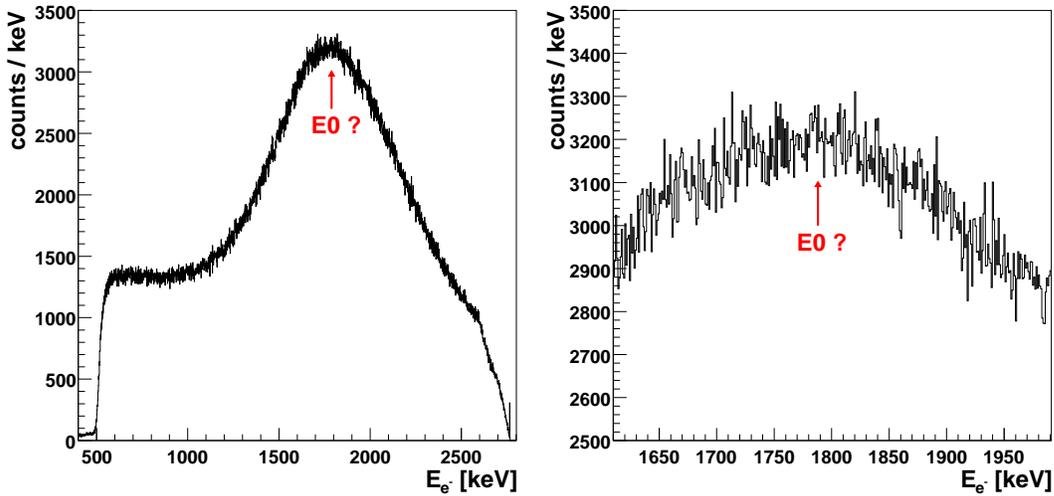
Figure 6.7: Electron spectrum from the decay of $A = 30$ isobars measured with the Mini-Orange spectrometer. Indicated is the expected position of the potential E0 decay in ^{30}Mg at 1788 keV. The beam intensity was ~ 650 ^{30}Na decays per second and the runtime was 11 hours.

is reduced by typically an order of magnitude compared to the $A = 30$ mass yield and since the (βn) decay probability of ^{31}Mg is only 37.0(5) %, this decay channel has not been further pursued during our studies of ^{30}Mg.

6.1.5 Conclusion

Despite the fact that no E0 transition in ^{30}Mg could be identified neither from the β decay of ^{30}Na nor from the neutron delayed β emission from ^{31}Na, the feasibility of conversion electron experiments under ISOLDE conditions could be demonstrated during this first beamtime.

6.2 Modified coincidence experiment

As a result of the first feasibility study it turned out that the sensitivity of the measurement had to be increased. Therefore a test experiment was performed at ISOLDE in June 2006 to study the performance of a $\beta - E0$ coincidence setup.

The modified experimental setup is shown in Fig. 6.8 and schematically depicted in Fig. 6.9. A 2 inch photomultiplier (EMI, Type 9814kB) with a 2 mm thick plastic scintillator (BC-408) was mounted opposite to the Mini-Orange spectrometer outside the evacuated chamber volume (however reaching into the chamber via a cylindrical "pocket") in a distance of 13 mm to the source, resulting in a geometrical solid angle coverage of $\Omega/4\pi = 25$ %. As entrance window a 75 μm thick Kapton foil with the
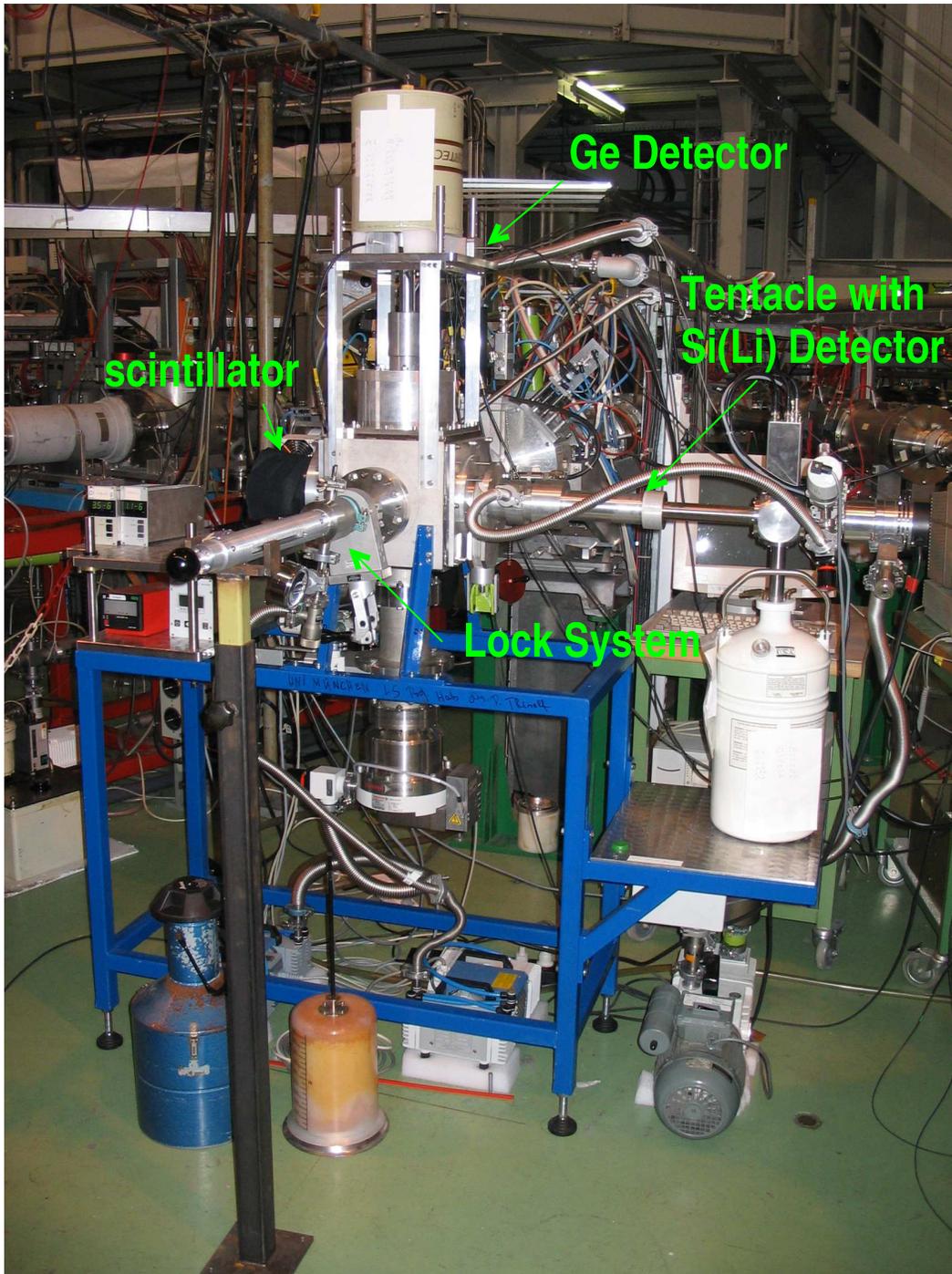
Figure 6.8: Picture of the modified experimental setup at ISOLDE in June 2006, which was extended by a β scintillation detector mounted on the left side of the target chamber opposite to the Si(Li) detector for a β – E0 coincidence measurement.
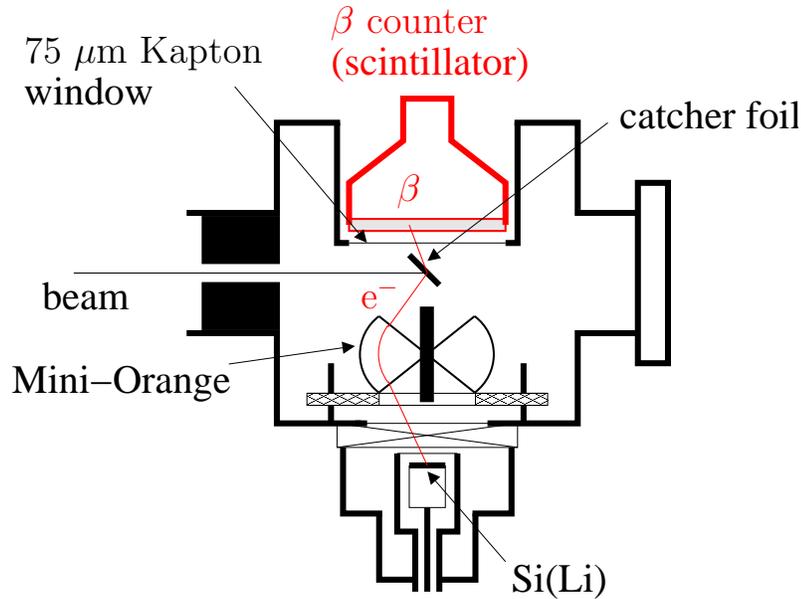
Figure 6.9: Sketch of the modified setup used in the 2006 test experiment (bottom
          view), introducing a β detector operated in coincidence with the Si(Li)
          detector of the Mini-Orange spectrometer. The γ detector to determine
          the beam composition and intensity was mounted on top of the chamber
          (not shown here).

same diameter as the photomultiplier was used. From inside the target chamber it was
supported by a grid consisting of 4×4 0.5 mm thick steel wires glued in a distance
of 9 mm onto a 1.2 mm thick steel ring to avoid bulging into the vacuum chamber
(see Fig. 6.10). The transmission of the window was geometrically determined to be
91 %. The efficiency for electron detection in the scintillator is about 100 %, while
its γ efficiency is expected to be close to zero in order not to create misleading trigger
signals. A low interaction probability for γ radiation could be realised due to the
relatively small thickness of the detector.

The germanium detector was mounted on top of the target chamber reaching into the
chamber volume via the aluminium cylinder already used in the previous experiment.
This time a detector with a relative efficiency of $\sim$ 20 % was available and mounted
in a larger distance from the target, thus resulting in a total γ efficiency of $\epsilon_\gamma = 0.0018$
at 1408 keV. Since this detector only served as a monitor for the beam intensity and
composition, sufficient statistics could be achieved during typical runtimes.

The coincidence condition was provided by a trigger on the β decay derived from
signals in the plastic scintillator, in order to suppress β decay background in the Si(Li)
detector.
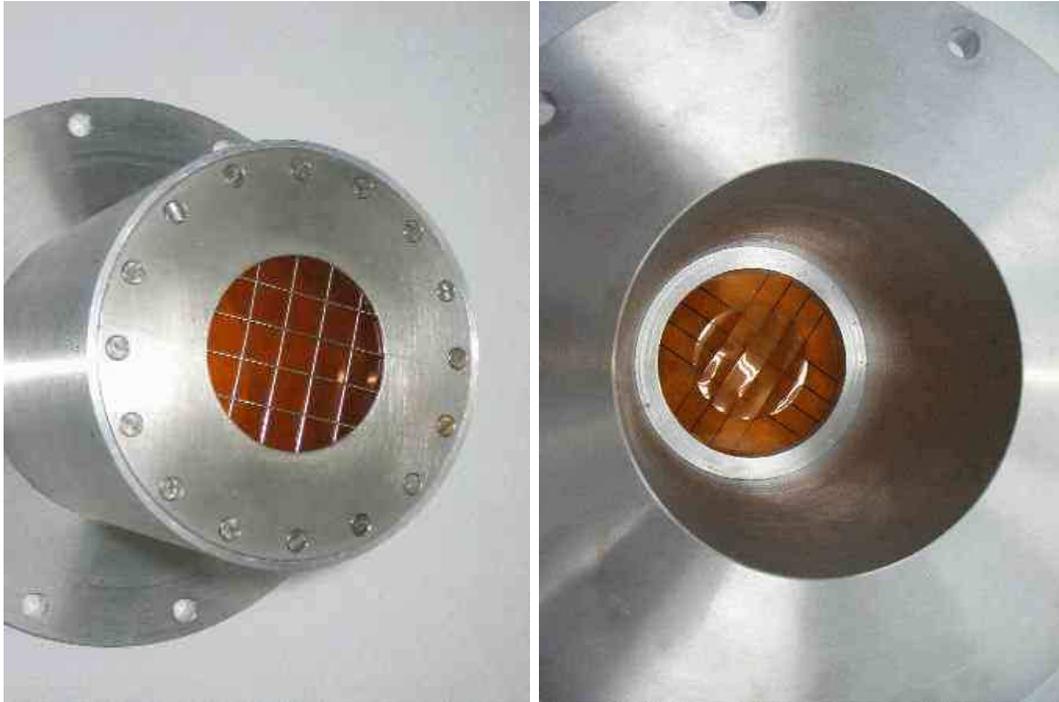
Figure 6.10: View on the entrance window support grid from inside the target chamber (left) and from the outside (right). It consists of 4×4 0.5 mm thick steel wires glued onto a 1.2 mm thick steel ring in a distance to each other of 9 mm. The grid prevents the Kapton foil from bulging into the vacuum chamber. The geometrical transmission of the window grid amounts to 91 %.

6.2.1 Signal processing electronics

The signal processing electronics used for these measurements was similar to the electronics shown later in Fig. 7.3 for the final experiment. The time difference between the plastic scintillator and the Si(Li) detector signals was measured using a Time-to-Analog converter (TAC). The slower Si(Li) detector signal served as start signal. The faster signal from the photomultiplier was delayed by 600 ns and used to stop the TAC. Due to the larger angular acceptance, the photomultiplier provides a much higher signal rate than the Si(Li) detector. In order not to produce exceedingly deadtime, in general the more abundant signal has to be used as stop signal. The same ISOLDE MBS data acquisition system as used in the previous experiment was also employed for the coincidence experiment.
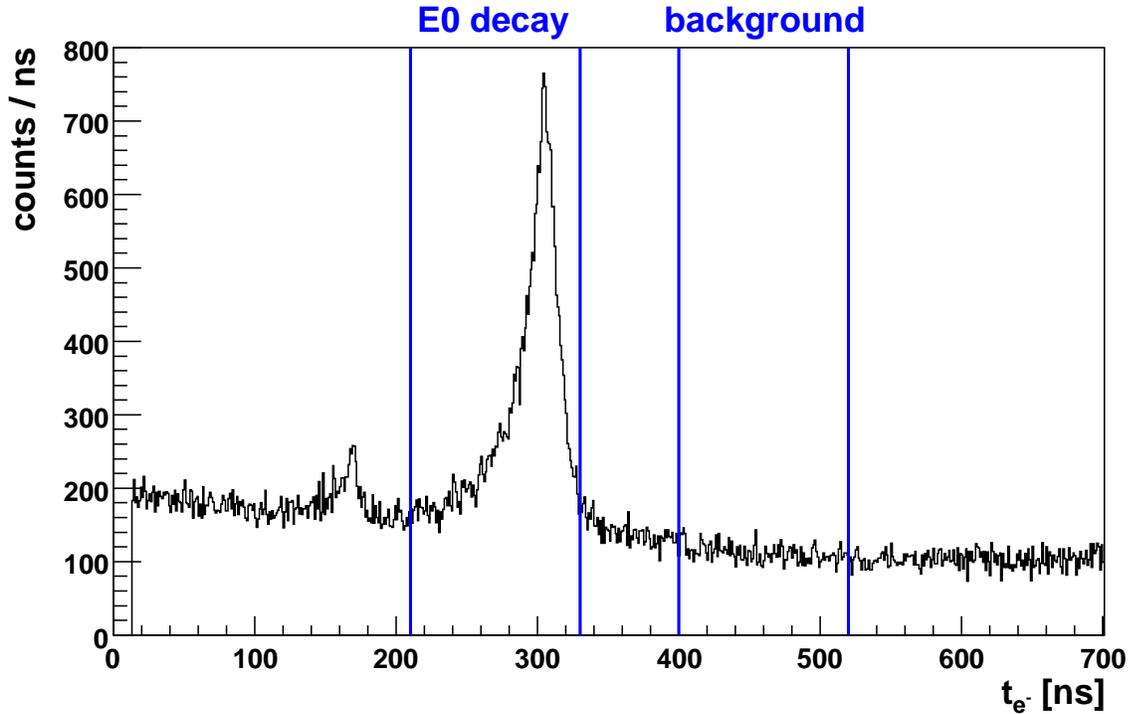
Figure 6.11: Timing spectrum of the E0 decay in ^{96}Zr measured using a TAC. The TAC
was started with a signal from the Si(Li) detector and stopped with a signal
from the β counter. The faster β signal was delayed by 600 ns. Due to the
long lifetime of the E0 decay (38 ns), the coincidence window was chosen
to be 120 ns (3 half lives). A background window of the same width as the
coincidence window was chosen to generate the corresponding spectrum
for background subtraction. The small peak at 160 ns is an electronic
artefact.

6.2.2 Experimental Results

E0-transition in ^{96}Zr

Fig. 6.11 shows the timing spectrum of the reference E0 decay in ^{96}Zr measured using a
TAC. Due to the long lifetime of the E0 decay (38.0(7) ns), the width of the coincidence
window was chosen to be 120 ns (3 half lives), while a second window of identical width
was used for background subtraction.

Fig. 6.12 shows the resulting background-subtracted electron spectrum. Compar-
ing this coincident electron spectrum (gated on the coincident TAC time peak and
background-subtracted) with the singles measurement from the previous experiment
as shown in Fig. 6.6, an improvement of the peak-to-background ratio of the K line by
a factor of $\sim$ 12 can be concluded. The experimental sensitivity for this setup can be
determined by concluding that due to the significantly improved peak-to-background
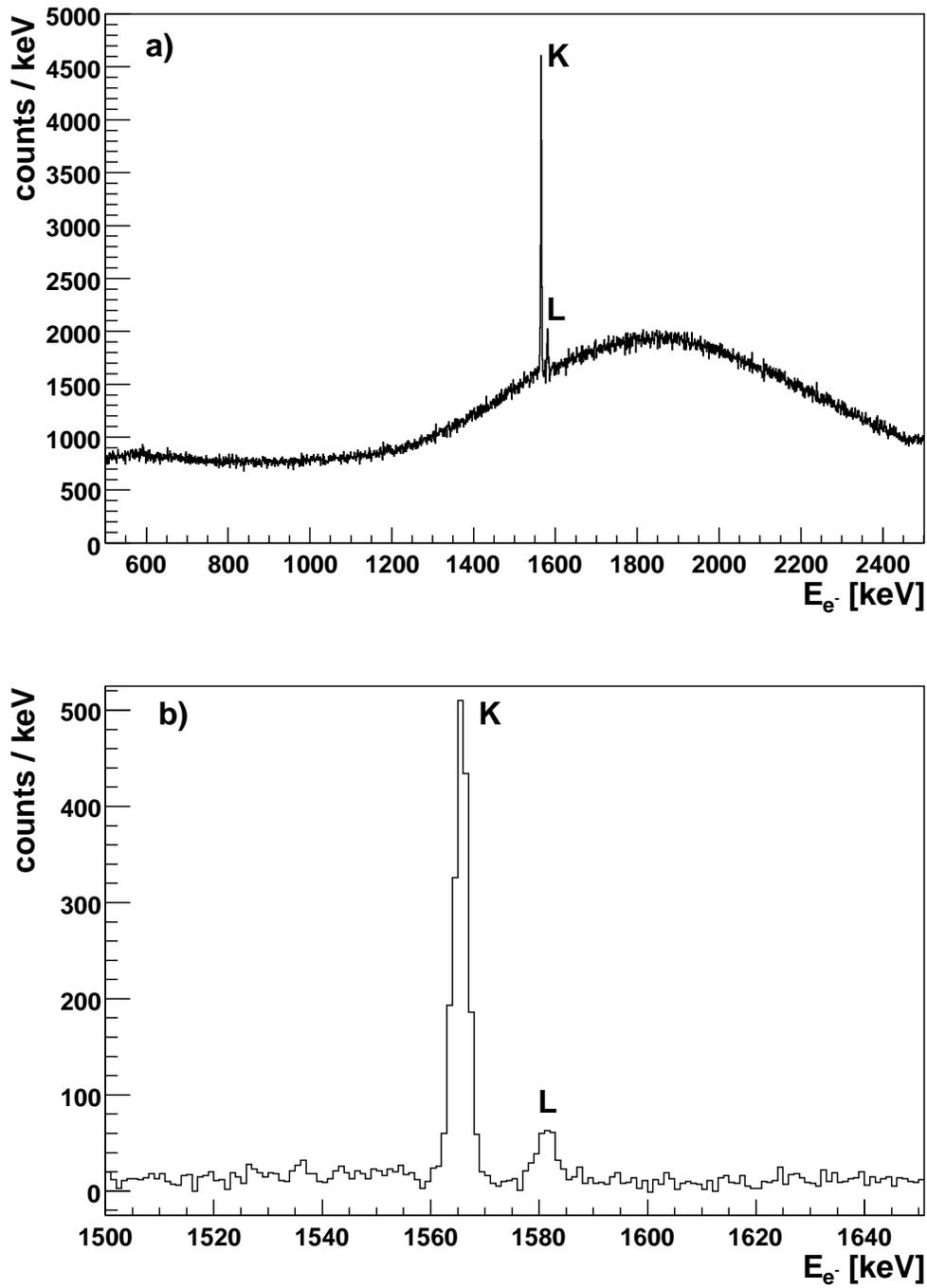
Figure 6.12: a) Electron singles spectrum from the decay of $A = 96$ isobars with the prominent E0 decay of ^{96}Zr, measured with the Mini-Orange spectrometer. b) Background-subtracted electron spectrum in coincidence with β decay electrons.

ratio an E0 transition with as low as ~ 20 % of the L-line intensity in ^{96}Zr (~ 0.14 %) could be unambiguously identified. This leads to the sensitivity limit of the coincidence setup as used in this test experiment of $I \leq 0.02$ % (corresponding to an E0 strength of $\rho^2(\text{E0}) \leq 0.05$).

Measurement in ^{30}Mg
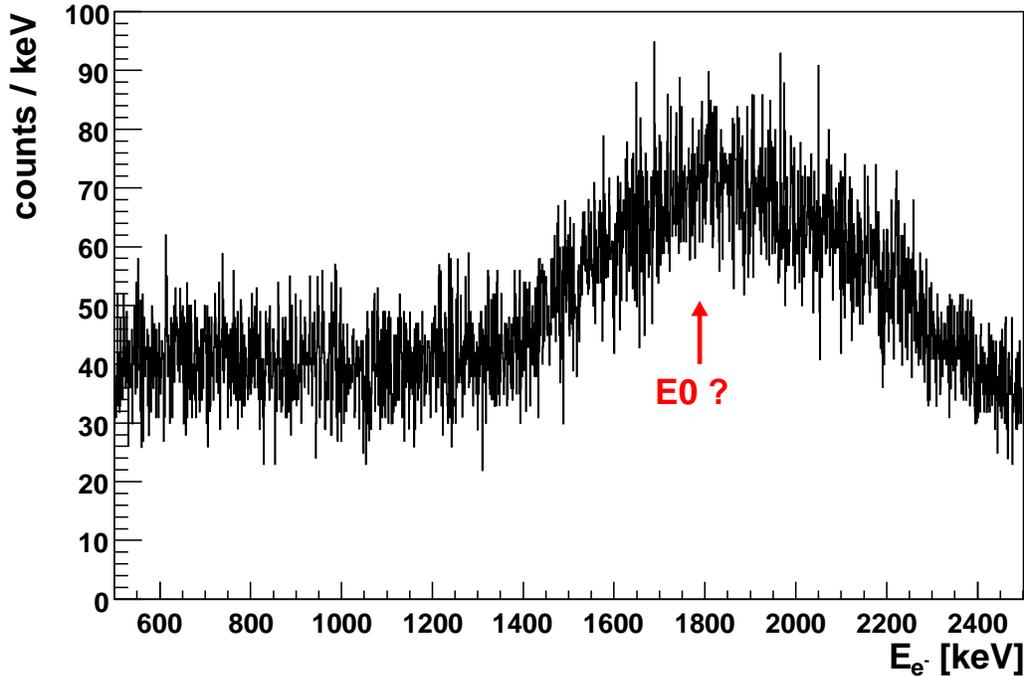
Figure 6.13: Electron spectrum from the decay of $A = 30$ isobars measured with the MO spectrometer in coincidence with β decay. The spectrum is normalised for 1000 ^{30}Na decays per second for a one hour measurement.

In Fig. 6.13 the background-subtracted E0 spectrum in coincidence with β-decay electrons is shown for the $A = 30$ run. Obviously there is still a background component surviving the coincidence condition. In the test run of 21 h of beamtime no indication of the E0 transition in ^{30}Mg could be found.

We conclude the corresponding intensity limit of the K+L conversion electron E0-transition in the ^{30}Na decay to ^{30}Mg as $I(^{30}\text{Mg}, \text{K} + \text{L E0}) \leq 0.02$ %, or for the monopole matrix element: $\rho^2(\text{E0}) \leq 0.05$.

6.2.3 Conclusion

Despite of the improvement of the experimental setup using a β – E0 coincidence measurement to suppress the huge background from the β decay, the existence of the E0 transition in ^{30}Mg at 1789 keV could not be proven during the coincidence experiment. Only the previously obtained upper limit of its transition strength from the first feasibility study could be lowered.

There was still a large remaining background component surviving the coincidence condition, whose origin had to be understood in order to reduce it and thus to increase the sensitivity of the measurement. This procedure will be described in the following sections.

6.3 Setup design for optimised E0 sensitivity

Different laboratory test cases were studied after the ISOLDE coincidence experiment in order to understand the background surviving the coincidence condition, which may be caused by γ rays or (Compton-) scattered electrons due to the large Q value of the ^{30}Na decay ($Q = 17.3$ MeV). The goal was not only to understand the background, but also to reduce it to the technically feasible limit and thus to increase the sensitivity to its maximum.

6.3.1 Measurement of the E0 transition in ^{90}Zr using an ^{90}Y source

In order to test the sensitivity and to get a better understanding of the remaining coincident background of the experimental setup, the E0 transition in ^{90}Zr from the 0_2^+ state at 1761 keV to the 0_1^+ ground state was measured using an ^{90}Y source. The advantage of using this β emitter is not only the suitable E0 energy for our setup optimised for the expected E0 transition in ^{30}Mg, but also the fact that during the decay of ^{90}Y practically no γ rays are emitted (see Fig. 6.15). Also the half-life $t_{1/2} = 64.1$ h of ^{90}Y facilitates the handling of this source.

Preparation of the ^{90}Y source

A source with an activity of ~ 120 kBq was produced at the Radiochemistry Institute of the Technical University in Munich. Therefore a reservoir of ^{90}Sr was flushed with hydrochloric acid dissolving ^{90}Y only. A drop of 10 μl of the solution with ~ 120 kBq activity was dripped onto a 20 μg/cm^2 carbon foil. In order to position the drop in the centre of the foil the pipette was guided by a conus. After that the table with the source was turned sideways and the drop was dried using an infrared lamp. This procedure takes only a few minutes. Fig. 6.14 (left) shows the setup used for the source production. Subsequently the source was covered by a Plexiglas transport container.
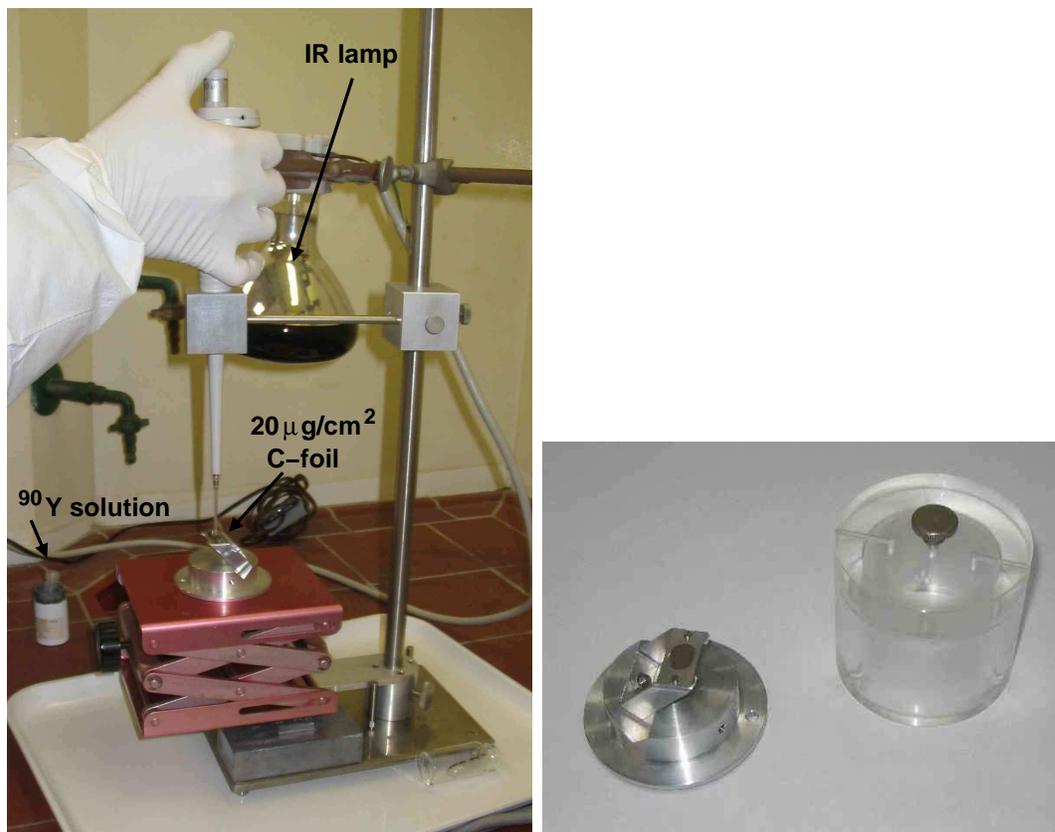
Figure 6.14: Left: Setup to produce an ^{90}Y source at the Radiochemistry Institute of the Technical University in Munich. The pipette containing ^{90}Y dissolved in hydrochloric acid is guided by a conus to position a drop of 10 μl of the solution in the centre of a 20 μg/cm^2 carbon foil. After depositing the solution on the carbon foil, the table is turned sideways underneath an infrared lamp used to dry the solution.
Right: The carbon foil is mounted on a holder, which is fixed to a support stand. After the source production the source holder was covered by a Plexiglas transport container to shield against the β radiation.

The source and the container is shown in Fig. 6.14 (right). For the source transport the Plexiglas box was placed inside a Pb transport box.

Modified experimental setup for $\beta - $ E0 coincidence measurement

^{90}Y decays with 99.99 % to the ground state of ^{90}Zr via β decay. Fig. 6.15 shows the level scheme of ^{90}Zr. The decay branch of γ emission is only $1.4 \cdot 10^{-6}$ % and thus negligible and the intensity of the $0_2^+ \rightarrow 0_1^+$ E0 transition is 0.0115 % [ENS07]. Using Eq. (3.4) the monopole strength can be calculated to be ρ^2(E0) $= 3.30(17) \cdot 10^{-3}$.

Since the E0 transition energy exceeds more than 75 % of the Q value, the remaining
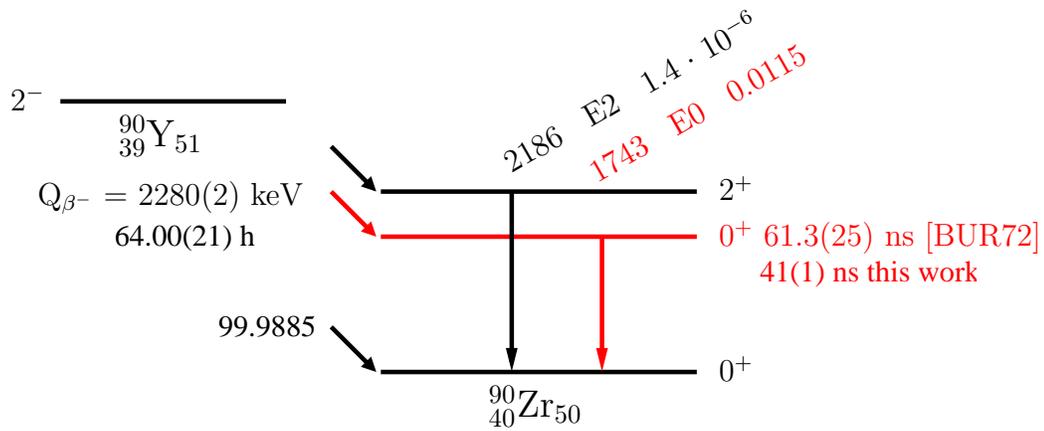
Figure 6.15: Levels in ^{90}Zr populated by the β decay of ^{90}Y [ENS07].
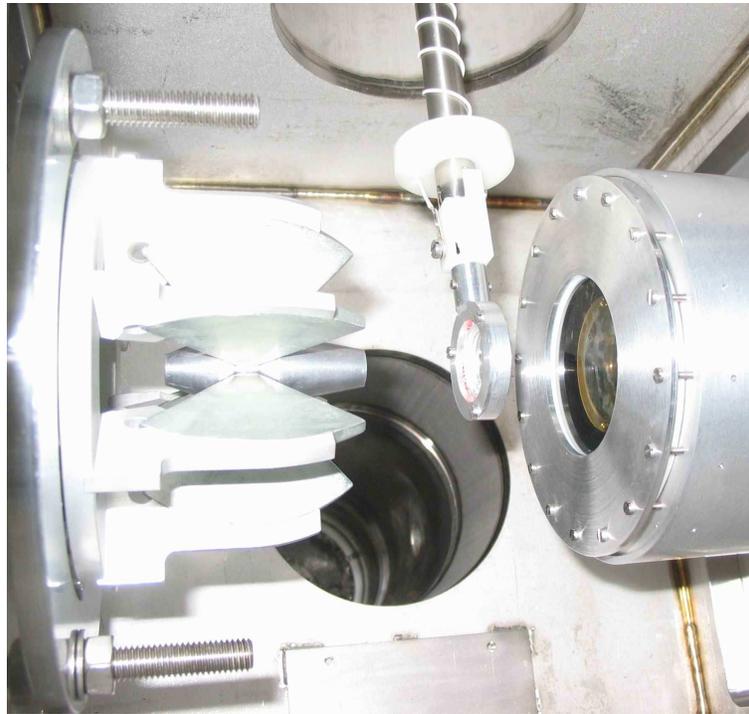
Figure 6.16: View inside the target chamber. Due to the low energy of the β-decay electrons from the decay of ^{90}Y ($E_\beta \leq 519$ keV) feeding the 0_2^+ state, a 5 mm thick plastic scintillator (NE-110) was used as vacuum entrance window, while the photomultiplier was directly glued onto it from outside the vacuum chamber.

energy for the β-decay electrons is $E_{e^-} \leq 519$ keV and thus the maximum of the energy distribution is around 250 keV. The corresponding kinetic energy is not sufficient to pass a 75 μm thick Kapton foil (as used so far for the vacuum entrance window) and the black tape covering the scintillator surface. Thus no measurable signal could be

generated in the scintillation detector. In order to overcome this limitation, a 5 mm thick scintillator plate (material: NE-110, diameter 89 mm) was used as window to the vacuum chamber, while the photomultiplier was directly glued onto it from outside the vacuum using optical grease. A view inside the target chamber is shown in Fig. 6.16, where the Mini-Orange is mounted on the left of the central electron source, while the plastic scintillator faces the source from the opposite direction.

E0 measurement using the ^{90}Y source

Quantity	$Z = 40, A = 90$ $E = 1761$ keV	fraction [%]
Ω_{IP}	$8.48 \cdot 10^8/\mathrm{s}$	26.2
Ω_{K}	$2.16 \cdot 10^9/\mathrm{s}$	66.6
Ω_{L1}	$2.29 \cdot 10^8/\mathrm{s}$	7.1
Ω_{L2}	$1.87 \cdot 10^6/\mathrm{s}$	0.06
$\sum_i \Omega_i$	$3.24 \cdot 10^9/\mathrm{s}$	100

Table 6.2: Electronic Ω_i-factors for the E0 transition in ^{90}Zr at 1761 keV. The values were calculated using the programs OMEGA.BAS [KAN95] and OMEGAIFP.BAS [KAN95]

The source was produced with an initial activity of $A_0 = 120$ kBq. The total number of decays during a specific time period Δt can be calculated with

$$N_{tot} = \int\limits_{t_0}^{t_0+\Delta t} A_0 \cdot e^{-\lambda t} dt = \frac{A_0}{\lambda} e^{-\lambda t_0} \left(1 - e^{-\lambda \Delta t}\right) \tag{6.1}$$

The decay constant λ can be derived from the half-life of 64.1 h as $\lambda = 0.011/\mathrm{h}$. The measurement was started at $t_0 = 26$ h after the target production and lasted for another $\Delta t = 66$ h. During the measurement $1.54 \cdot 10^{10}$ ^{90}Y atoms decayed. With an excitation probability of the excited 0_2^+ state in ^{90}Zr of 0.000115 [ENS07], a transmission efficiency of the Mini-Orange spectrometer of $\epsilon_{\mathrm{MOS}} = 0.018(2)$ (see Fig. 4.19) and a K (L) conversion probability of 66.6 % (7.1 %) (see Tab. 6.2), $2.12(24) \cdot 10^4$ $(2.26(25) \cdot 10^3)$ E0 transitions would be expected in the K (L) conversion line of the electron singles spectrum, respectively.

Fig. 6.17 shows the electron singles spectrum measured with the Mini-Orange spectrometer. Since the electron spectrum reflects the transmission function of the Mini-Orange spectrometer peaking at ~ 1700 keV folded with the β-decay energy spectrum of ^{90}Y (maximum around $Q_\beta/2 = 1140$ keV), the maximum is shifted to lower energies and thus appears around 1500 keV. The K and L line at transition energies of 1743 keV and 1758 keV are clearly visible. The binding energy of the K (L) electron is 18.0 keV
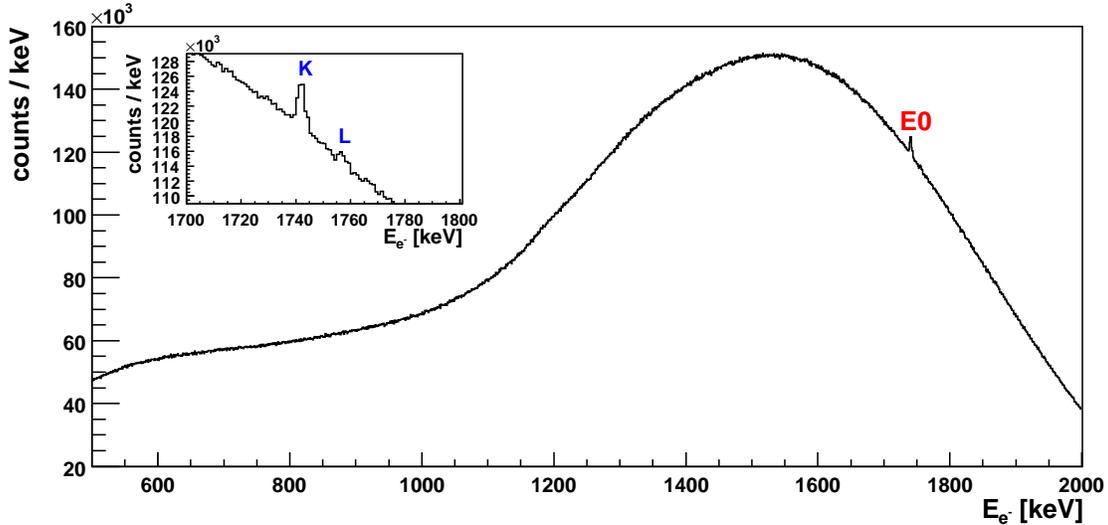
Figure 6.17: Total electron spectrum of the ^{90}Y decay folded with the transmission curve and measured with the Si(Li) detector within 66 hours. The initial source activity was ~ 120 kBq. The K and L conversion electron lines at 1743 keV and 1758 keV are clearly visible. Since the electron spectrum reflects the transmission function of the Mini-Orange spectrometer peaking at ~ 1700 keV folded with the β-decay energy spectrum of ^{90}Y (maximum around $Q_{\beta^-}/2 = 1140$ keV), the maximum is shifted to lower energies and thus appears around 1500 keV.

(2.5 keV), respectively. $1.93(9) \cdot 10^4$ $(2.66(71) \cdot 10^3)$ counts were measured in the K (L) line. The counting rate of the Si(Li) detector was ~ 120/s on average and the deadtime was $\sim 30\%$. Taking the deadtime into account, $2.76(13) \cdot 10^4$ $(3.8(10) \cdot 10^3)$ E0 transitions were measured in total for the K (L) line, respectively.

The measured event statistics lies within the expected amount as calculated from the source activity. This means, that during the evaporation process almost no activity vaporised.

Fig. 6.18 shows the time difference between electrons detected in the plastic scintillator and electrons detected in the Si(Li) detector as a function of the electron energy (see also Sect. 7.4.2). The β – E0 coincidence is visible, showing the uncompensated "walk effect" of the constant fraction discriminator for low-energy electrons. Also the K line of the E0 transition at 1743 keV can be seen. Due to the long lifetime of the 0_2^+ state (reported as 61.3(25) ns [BUR72]) the E0 decay is spread over a wide time range (marked by the white rectangle).

In Fig. 6.19 the projection of the two-dimensional E – T distribution of Fig. 6.18 onto the time axis is shown for electron energies ≥ 1 MeV in the Si(Li) detector. Events fulfilling the coincidence condition are selected by setting a window with a width of 110 ns around the coincidence peak. The background is determined by setting a window
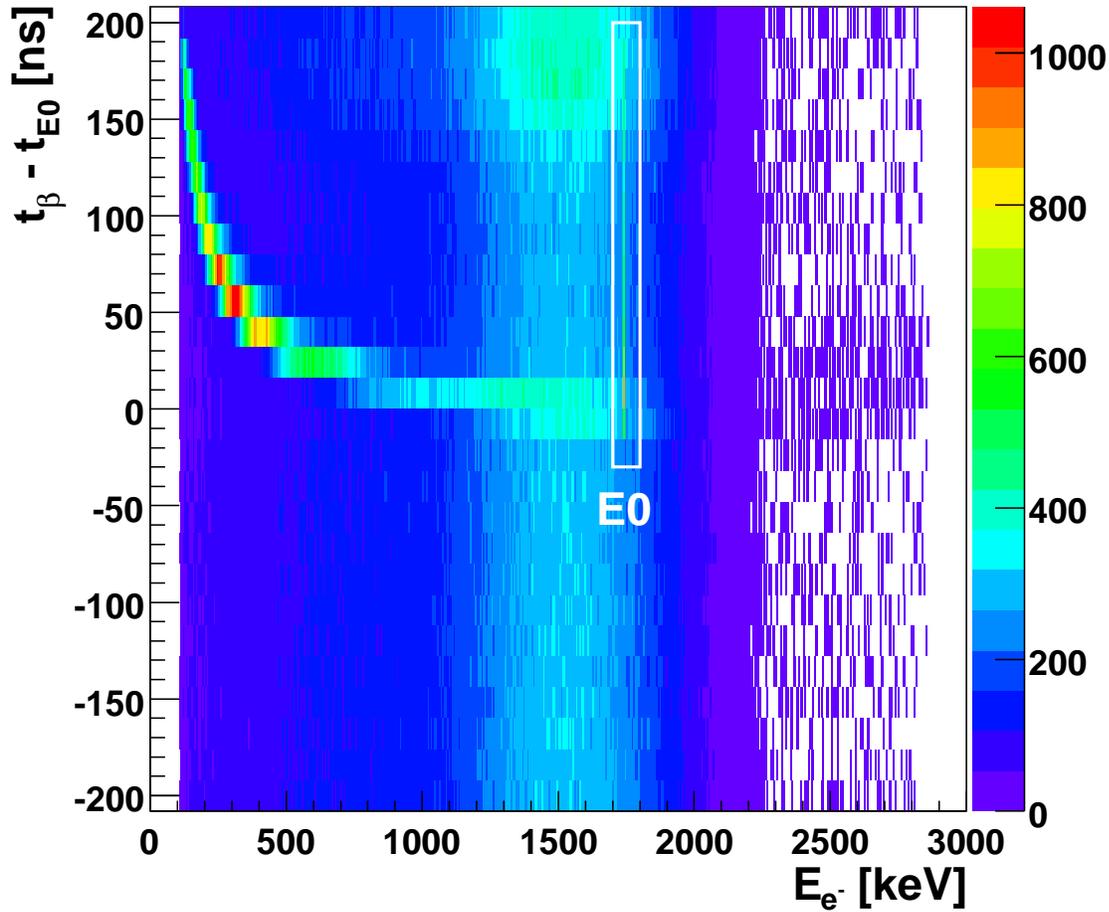
Figure 6.18: Time difference of electrons detected in the plastic scintillator and electrons detected in the Si(Li) detector as a function of the electron energy for the decay of an ^{90}Y source. The $\beta - $E0 coincidence is visible, showing the uncompensated "walk effect" of the constant fraction discriminator at low energies. Due to the long lifetime of the 0_2^+ state (61.3(25) ns according to [BUR72]) the E0 transition in ^{90}Zr (1743 keV) is spread over a wide time range (indicated by the white rectangle).

with the same width next to the coincidence peak.

Background-subtracted electron energies for events surviving the coincidence condition are shown in Fig. 6.20. The K and L conversion electron lines are visible on top of an almost negligible background. 3509(63) (418(28)) counts were measured in the K (L) line, respectively. Since the solid angle coverage of the plastic counter can be calculated from the ratio of counts in the K or L line in the coincident spectrum and the singles spectrum, $\Omega/4\pi$ results to be 18 %. The distance between source and window (corresponding directly to the scintillator surface) is about 23 cm, resulting in a calculated solid angle coverage of $\Omega/4\pi = 16$ %, which fits well with the measurement.
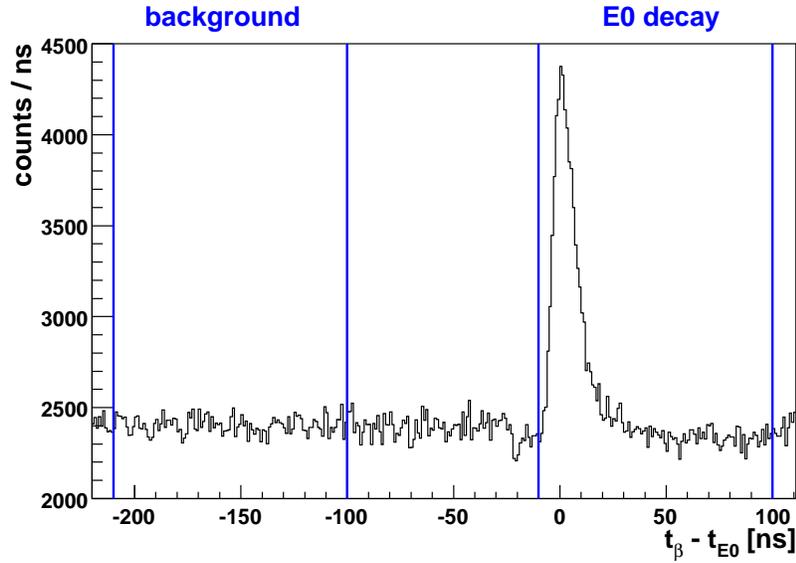
Figure 6.19: Time difference between signals in the plastic scintillator and the Si(Li) detector from the decay of ^{90}Y. Only events with an electron energy ≥ 1 MeV in the Si(Li) detector are included (see Sect. 7.4.2). In order to select the coincident events, a window was set around the coincidence peak. In order to determine the background, a window with the same width was set next to the coincidence peak. Due to the long lifetime of the 0_2^+ state (61.3(25) ns according to [BUR72]), the width of the coincidence window was chosen to be 110 ns.

Revision of the lifetime of the 0_2^+ state in ^{90}Zr

Since Fig. 6.18 displays the time difference between the E0 electron and the corresponding β decay electron, the lifetime of the 0_2^+ state in ^{90}Zr can be determined. The background-subtracted time information of the K line at 1743 keV is plotted in the right panel of Fig. 6.21. Since the transmission function of the Mini-Orange is linear in a small energy range around the K line, the background is determined setting two windows with half of the coincidence window width below and above the K line, as indicated in the left panel of Fig. 6.21.

In order to determine the half-life of the 0_2^+ state in ^{90}Zr, the decay curve shown in Fig. 6.21 was fitted using the exponential function

$$N(t) = N_0 \cdot e^{-\lambda t}. \tag{6.2}$$

The decay constant λ was determined as $\lambda = 0.0169(5)$/ns, which results in a half-life of the 0_2^+ state of $t_{1/2} = 41(1)$ ns, in contrast to the published value of 61.3(25) ns [BUR72]. The published value was derived via the ^{90}Zr(p,p'e) reaction using a 8.16 MeV proton beam. In this reaction the isomeric 8^+ (5^-) states at 3589.4 keV (2319.0 keV)
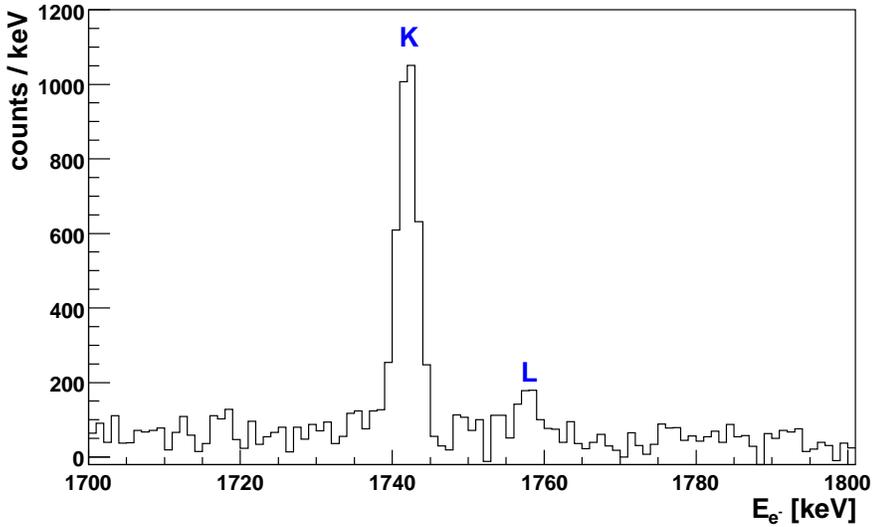
Figure 6.20: Background-subtracted electron spectrum from the decay of ^{90}Y measured with the Mini-Orange spectrometer in coincidence with β decay electrons. The initial source intensity was ~ 120 kBq. The decay was measured for 66 h. The K and L lines are clearly visible on top of an almost negligible background.

with a lifetime of 131(4) ns (809.2(20) ms [BRA72]) could be populated. Both states have transitions feeding the 0_2^+ state (see Fig. 6.22).

Most likely this isomeric states or the feeding of the 1760.7 keV 0_2^+ state was not known at the time of the published experiment on ^{90}Zr in 1972, which then led to the wrong extracted lifetime of the 0_2^+ state. In our experiment the isomeric 8^+ or 5^- state could not be populated, since the Q value of the ^{90}Y decay is smaller than the excitation energy of the 8^+ or 5^- state. So this measurement leads to the correct half-life of the 0_2^+ state of $t_{1/2} = 41(1)$ ns, resulting also in a corrected value for the E0 strength of $\rho^2(\text{E0}) = 5.2(1) \cdot 10^{-3}$.

Conclusion

This test case of ^{90}Zr was chosen to determine the sensitivity of our setup to weak E0 transitions in the energy range, where the decay in ^{30}Mg is expected. The resulting sensitivity limit of an E0 intensity of 0.0115 % and $\rho^2(\text{E0}) = 5.2(1) \cdot 10^{-3}$ in a situation without γ-induced background can be regarded as a lower limit for the attainable sensitivity in ^{30}Mg with our present setup, provided that γ-induced background can be minimised for the ^{30}Na decay at ISOLDE.
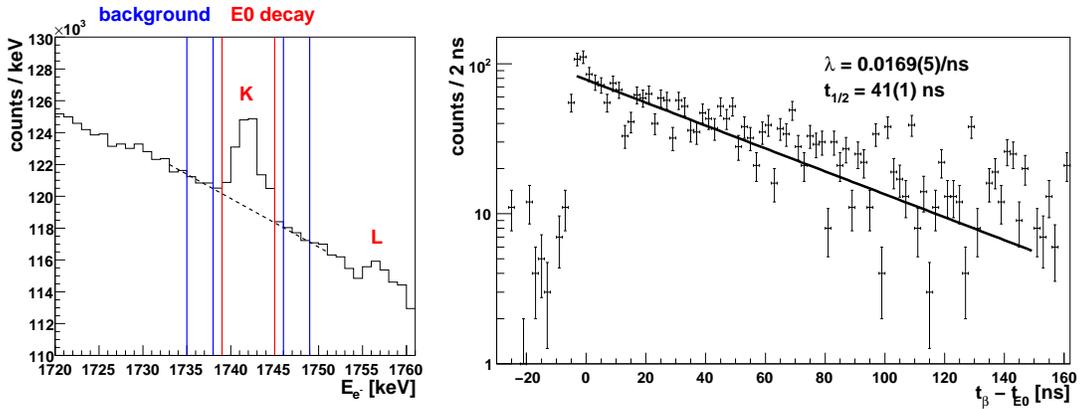
Figure 6.21: Left: Part of the singles electron energy spectrum from the decay of ^{90}Y. The transmission function of the Mini-Orange is linear in a small range around the K line. In order to determine the background, two windows with half of the coincidence window width are set below and above the K line.

Right: Resulting background-subtracted time spectrum of the E0 decay in ^{90}Zr. In order to derive the lifetime of the 0_2^+ state, the spectrum was fitted using an exponential function. The resulting decay constant $\lambda = 0.0169(5)$/ns allows to determine a half-life of the 0_2^+ state of $t_{1/2} = 41(1)$ ns.
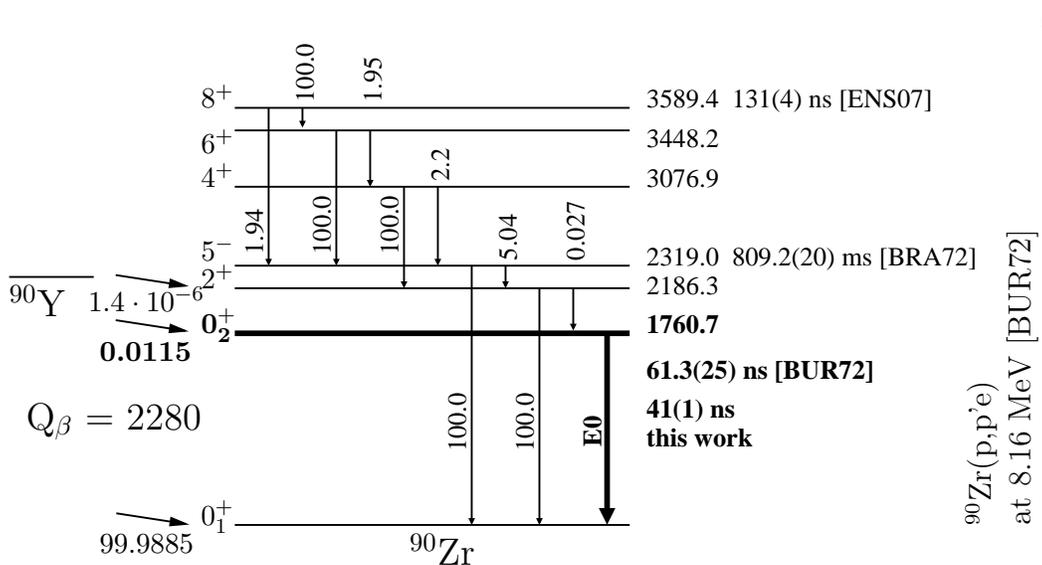
Figure 6.22: Part of the level scheme of ^{90}Zr [ENS07] together with the corrected half-life of the 0_2^+ state, determined in this work.

6.3.2 Test measurements using an ^{152}Eu source

In Sect. 6.3.1 is could be demonstrated that weak E0 transitions following a β decay with almost no γ transitions can be measured with a Mini-Orange spectrometer to suppress the background from β decay electrons using a β – E0 coincidence measurement. In this section the influence of coincident γ induced background as a function of the β detector thickness will be studied.

Therefore a ^{152}Eu source was used, which provides various γ transitions following the β decay and electron capture in contrast to the ^{90}Y β decay, which proceeds almost without γ emission.
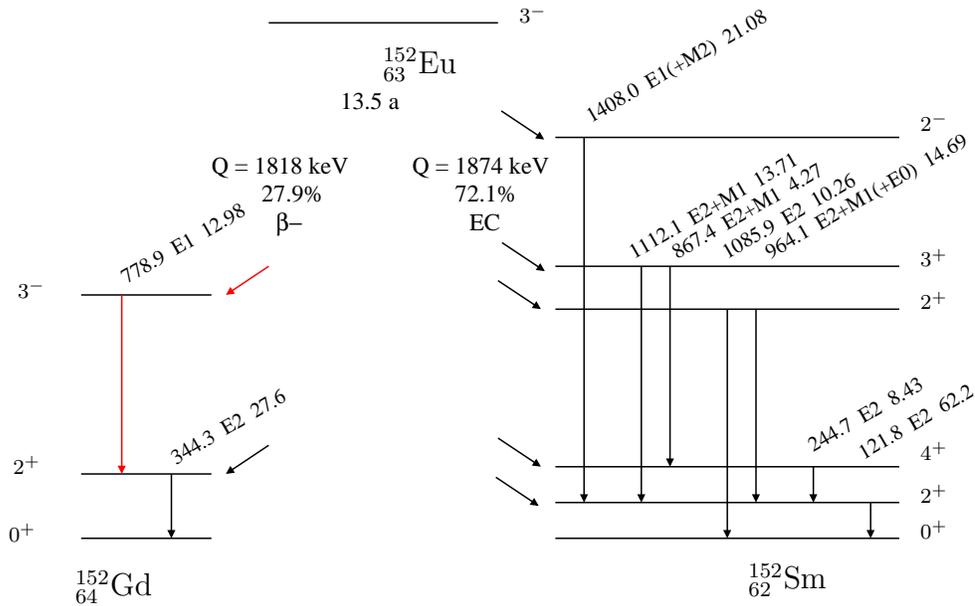
Figure 6.23: The level schemes show the strongest transitions in ^{152}Gd and ^{152}Sm from the decay of ^{152}Eu [ENS07]. The 778.9 keV E1 transition in coincidence with β decay electrons is marked in red. Our interest was focused on this transition, since it is close to the transmission maximum of the Mini-Orange spectrometer.

^{152}Eu decays by 27.9 % to ^{152}Gd via β decay and by 72.1 % to ^{152}Sm via electron capture (see Fig. 6.23). The strongest transitions in ^{152}Gd are the 778.9 keV E1 transition (12.98 %) and the 344.3 keV E2 transition (27.6 %). These transitions provide conversion electrons in coincidence with β decay electrons and γ transitions. The electron capture decay to ^{152}Sm provides conversion electrons in coincidence with γ rays only. Thus it is expected that the measured intensity of the converted electrons from the 778.9 keV E1 transition stays rather constant as a function of the scintillator thickness. In contrast to that the amount of conversion electrons detected in coincidence with γ transitions following the electron capture to ^{152}Sm should change while varying the thickness of the β detector.

The K electron binding energy in ^{152}Sm is 46.8 keV and the L electron binding energy is 7.7 keV. In ^{152}Gd the K and L electron binding energies are 50.2 keV and 8.4 keV, respectively. An overview of the decay properties and intensities of ^{152}Eu is shown in Tab. 4.3.

For this measurement the Mini-Orange spectrometer was optimised for 1 MeV electrons with a maximum transmission efficiency of ~ 4.6 % by a modification of the Mini-Orange and Si(Li) positions [WIM07]. So we focus on the 778.9 keV E1 transition, which is close to the transmission maximum.

Fig. 6.24 shows the electron spectra of the ^{152}Eu decay measured in coincidence with the plastic detector (BC-404) for various scintillator thicknesses. The converted E1 transition at 730.4 keV ($\alpha_K = 0.0015$) is clearly visible after 6 hours of measurement. The source activity was ~ 150 kBq. The peak is sitting on top of a continuous background folded with the transmission curve. Also the intense electron lines from the EC decay at 818.9 keV, 915.6 keV, 1037.4 keV, 1063.6 keV, and 1359.5 keV of ^{152}Eu decaying to ^{152}Sm are visible. These lines are measured in coincidence with the 121.8 keV γ transition or X-rays originating from the lead absorber of the Mini-Orange, which can be detected in the plastic detector with high efficiency.

In a first series of experiments scintillators (BC-404) with a thickness of 2, 4 and 6 mm were used, respectively. It can be seen that the total integrated coincident background decreases linearly with decreasing scintillator thickness (see Fig. 6.26). The number of counts measured in the transition lines in ^{152}Sm is decreasing with decreasing scintillator thickness, while the number of counts in the 730.4 keV E1 transition line stays rather constant (see Fig. 6.27).

In a second experiment the coincident background using thinner scintillators (BC-404) with a thickness of 2, 1, 0.5 and 0.2 mm was studied. In order to suppress X-rays from the lead absorber hitting the plastic detector, the absorber of the Mini-Orange was covered with a 5 mm thick copper cap towards the plastic scintillator. The electron spectra are shown in Fig. 6.25. It can be concluded that a thinner plastic scintillator is less sensitive to γ radiation resulting in a reduced coincident background.

Fig. 6.26 shows the integrated number of coincident electrons measured in the Si(Li) detector as a function of the scintillator thickness, normalised to 1 h of measurement time. It exhibits a linear dependency on the scintillator thickness. For a 2 mm thick plastic scintillator the copper cap suppresses the number of coincident electrons (blue) by 20 % compared to the number of coincident electrons without using the copper cap (black). Comparing the use of a 2 mm thick plastic scintillator in the first ISOLDE experiment to a scintillator of 0.2 mm thickness in conjunction with the copper cap, the amount of surviving coincident background electrons decreases by a factor of three.

The dependence of the count rate registered in the 778.9 keV E1 transition peak and the 964.1 keV E2+M1(+E0) transition peak on the detector thickness is shown in Fig. 6.27. The number of counts in the 778.9 keV transition stays constant within the error bars as expected. This corresponds to a constant β detection efficiency after reducing the scintillator thickness. The 964.1 keV transition (thus close to the
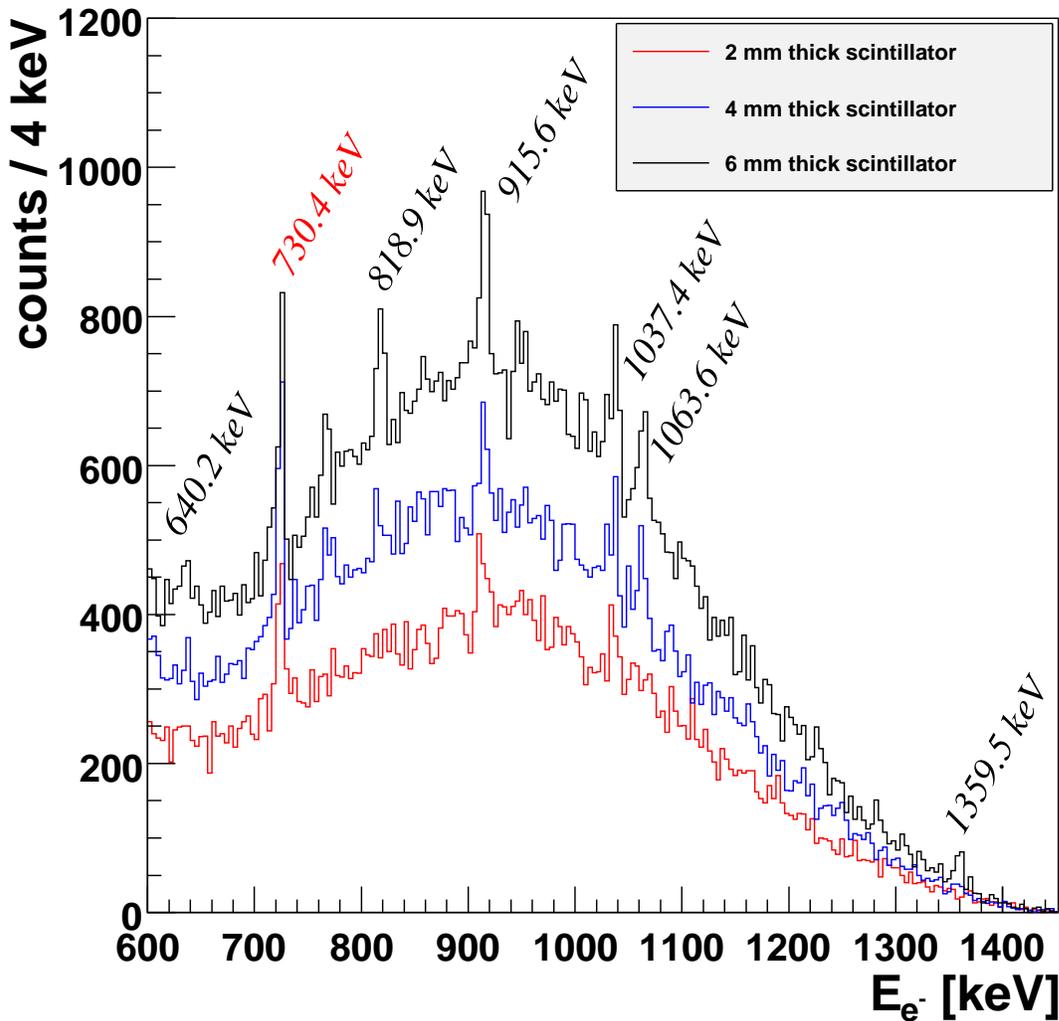
Figure 6.24: Electron spectrum from the ^{152}Eu decay, measured with the Mini-Orange
spectrometer (transmission maximum around 1 MeV) in coincidence with
signals registered in a plastic scintillator (BC-404) of different thicknesses.
The source intensity was $\sim$ 150 kBq. The decay was measured for 6 h. The
730.4 keV line (marked in red) is clearly visible in coincidence with the β
decay to ^{152}Gd. Also the transitions at 818.9 keV, 915.6 keV, 1037.4 keV,
1063.6 keV, and 1359.5 keV (marked in black) from the EC decay to ^{152}Sm
are visible. Those transitions occur in coincidence with γ transitions.

transmission maximum of the Mini-Orange) following the electron capture to ^{152}Sm is
one of the strongest transitions. It also has a large conversion coefficient. The detected
intensity in the peak increases with increasing scintillator thickness due to the higher
γ sensitivity of the scintillator as expected.

Fig. 6.28 shows the signal-to-background ratio of the 730.4 keV transition in ^{152}Gd.
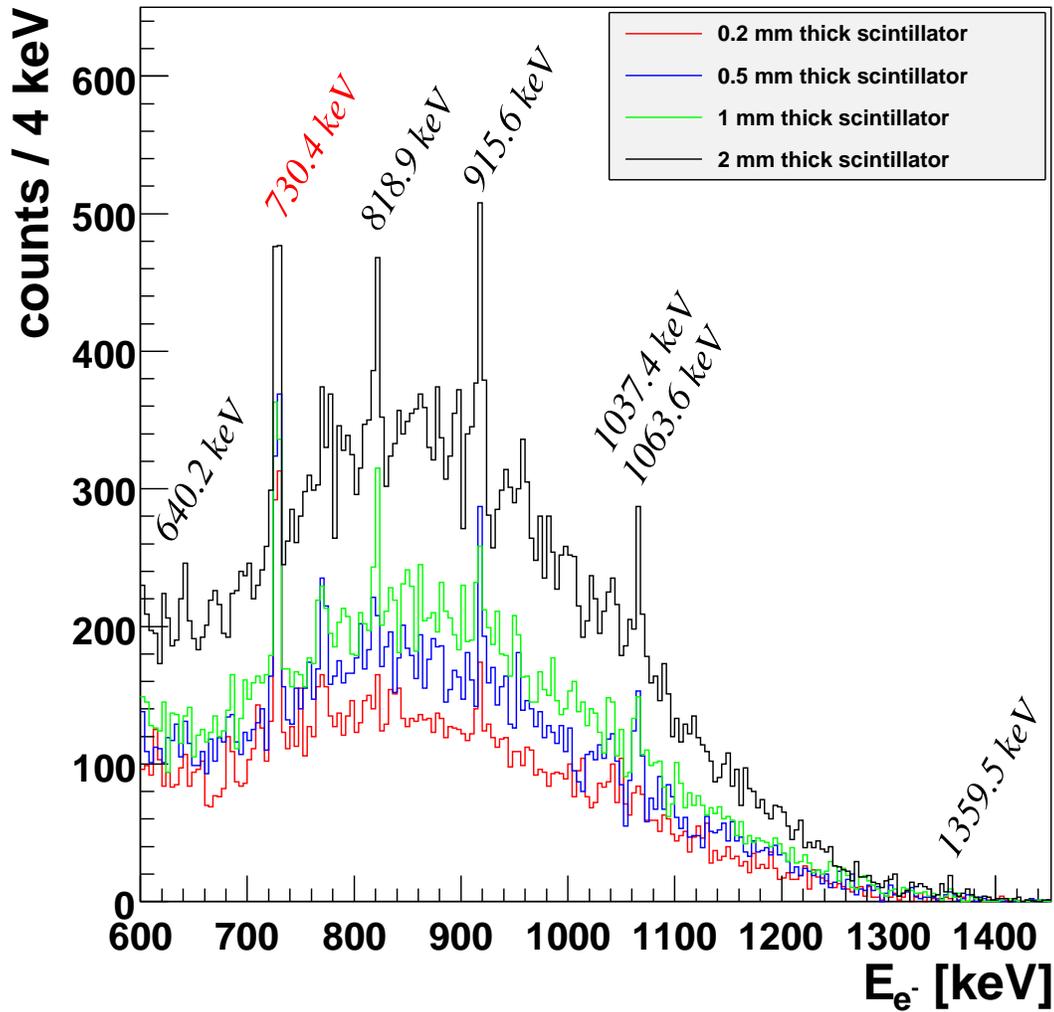
Figure 6.25: Electron spectrum from the ^{152}Eu decay analogue to Fig. 6.24. For these measurements also a 5 mm thick copper cap was mounted on the Pb absorber of the Mini-Orange towards the scintillator in order to absorb X-rays produced in the lead. With decreasing scintillator thickness also the L line at 770.9 keV can be identified with increasing peak-to-background ratio, thus proving an increased sensitivity for weak E0 transitions.

During the first measurement it stayed almost constant for various detector thicknesses, while during the second measurement including the copper cap the signal-to-background ratio increased with decreasing scintillator thickness as expected.
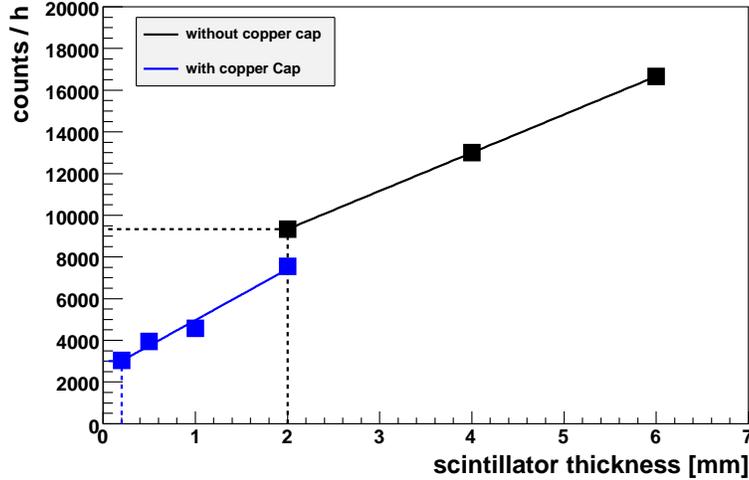
Figure 6.26: Correlation between the integrated number of coincident electrons measured in the Si(Li) detector and the thickness of the plastic scintillator (BC-404), derived from measurements using the integrated intensity (γ and electrons) of the ^{152}Eu source. In a second measurement (blue symbols) a copper cap on top of the central lead absorber of the Mini-Orange was mounted in order to suppress X-ray production.

6.3.3 Setup optimisation via GEANT simulations

The main difference between the laboratory test measurements and the ^{30}Na β decay at ISOLDE is the large Q value of 17.3 MeV in the ^{30}Na β decay, resulting in a high intensity of multi-MeV γ rays. Therefore Compton scattering and pair creation will play a major role in creating background for the E0 measurement also in the coincidence setup. Thus an extensive survey was started using GEANT4 simulations of the experimental setup in order to quantify the contribution of different setup components to the reduction of background and to identify the potential of background reduction by changes of the materials and components of the setup. Fig. 6.29 displays a model of the experimental geometry used for the simulations together with a visualisation of the particle and γ-ray trajectories from 10 ^{30}Na decays.

Different geometries and materials of the target chamber were simulated each for $5 \cdot 10^5$ ^{30}Na decays in order to study their effect on scattered γ radiation and (Compton-) scattered electrons hitting the plastic detector.

In our experiments as discussed so far a target chamber consisting of aluminium ($\sim$ 40 %) and stainless steel ($\sim$ 60 %) components was used and a Germanium γ detector was mounted using a pocket flange reaching inside the target chamber close to the target.

It turns out that a consequent reduction of high-Z components and measures to prevent the re-entry of scattered background electrons into the interior of the target chamber
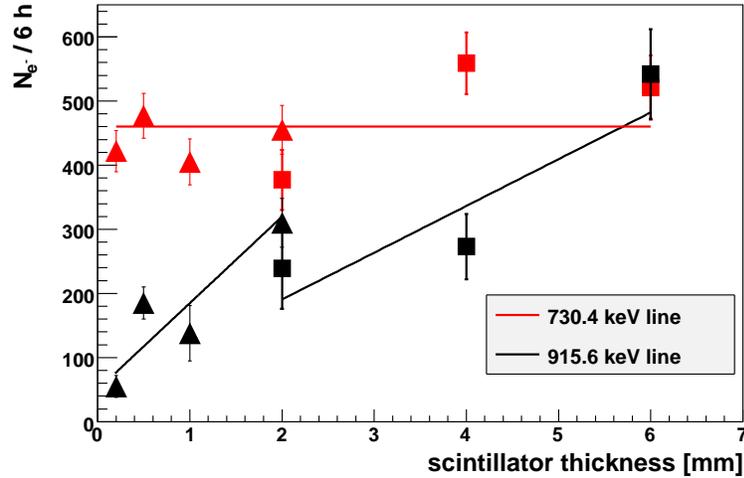
Figure 6.27: Electron count rate measured in the 778.9 keV E1 transition and the 964.1 keV E2+M1(+E0) transition for various scintillator thicknesses. The data points for the 778.9 keV transition following the β decay of ^{152}Eu to ^{152}Gd stay rather constant, while the count rate measured from the 964.1 keV transition following the electron capture to ^{152}Sm decreases with smaller scintillator thickness due to the reduced interaction probability for γ rays in thinner scintillators. The square symbols display the measurements without the 5 mm thick copper cap, while the triangular symbols correspond to measurements including the copper cap.

can significantly reduce background contributions. Especially rebuilding the target chamber completely from aluminium and retracting the Ge-detector to a position outside the chamber will reduce the total production of Compton scattered electrons. Consequently the detected background in the plastic β detector from electrons and γ-rays will decrease by a factor of 3. If in addition the interior surfaces of the target chamber will be covered with 15 mm thick Teflon plates in order to stop Compton scattered electrons from re-entering into the chamber volume, an overall background suppression by a factor of 8 can be reached.

6.3.4 Conclusion

So the final conclusion of these series of experiments was to prepare a β scintillation detector with a thickness of 0.2 mm, resulting (together with the copper cap of the lead absorber) in a background reduction of about a factor of 3 compared to the setup used in the ISOLDE coincidence experiment. Also the construction of a new target chamber made of low-Z material (aluminium) covered with 15 mm thick Teflon plates in order to stop Compton scattered electrons from re-entering into the chamber volume, derived from GEANT4 simulations, a background suppression by a factor of 8 can be reached.
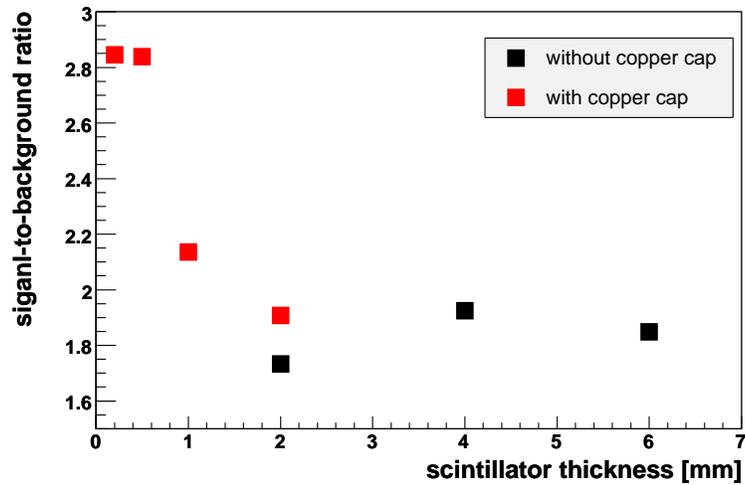
Figure 6.28: Signal-to-background ratio of the 730.4 keV transition in ^{152}Gd. With decreasing scintillator thickness the background decreases, resulting in an increasing signal-to-background ratio.
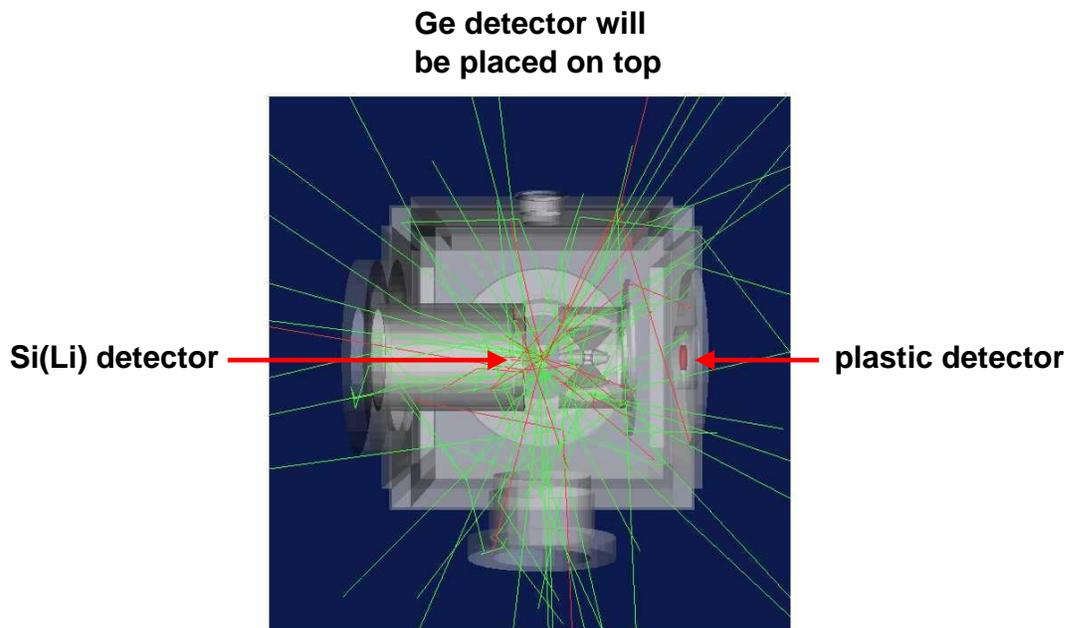
Figure 6.29: Experimental geometry used in GEANT4 simulations. 10 ^{30}Na decays are visualised. γ rays are marked with green and electron with red lines.

The maximum overall background suppression factor is expected to ≈ 24.

7 Identification of the $0_2^+ \rightarrow 0_1^+$ E0 Transition in ^{30}Mg

7.1 Target chamber for the main experiment

After the first coincidence experiment at ISOLDE in June 2006 it turned out that the remaining background surviving the coincidence condition still was too high and thus the sensitivity of the measurement was not sufficient to detect the E0 transition in ^{30}Mg. As a result of the preparatory experiments described in Sect. 6, a completely new setup was built to reduce the coincident background to the feasible minimum.

Fig. 7.1 shows the newly designed target chamber completely made from aluminium and coated with Teflon at the interior. This low-Z material was chosen to reduce Compton-scattered electrons due to the high Q value of the ^{30}Mg decay ($Q = 17.3$ MeV). The frame of the cubic chamber consists of an aluminium part milled out of a massive cube. The bottom plate is 20 mm thick, while the edges of the cubic frame are 20 mm × 20 mm thick. The cover plates of the chamber are 10 mm thick. The interior is coated with 15 mm thick Teflon plates, also the "pocket" flange for the β scintillation detector, which is covered with a 5 mm thick Teflon tube.

Naturally the Teflon-coating of the vacuum chamber is counteracting the requirement of optimum vacuum conditions in the presence of the cooled Si(Li) detector. Therefore with the Teflon coating two days of pumping were required to reach a pressure of $< 3 \cdot 10^{-6}$ mbar inside the vacuum chamber, which is mandatory to operate the Si(Li) detector.

7.2 Signal processing electronics

Fig. 7.3 shows the schematic layout of the signal processing electronics. The signals of the Germanium detector and the Si(Li) detector are first amplified by preamplifiers, which are placed close to each detector. Then the energy signal is further amplified and shaped by a spectroscopy amplifier and digitised by an Analog to Digital Converter (ADC module CAEN V785).

For the timing branch a second signal provided by the preamplifier is amplified and shaped by a Timing Filter Amplifier (TFA), converted into an logic signal using a Constant Fraction Discriminator (CFD) and fed to the trigger box (TB 8000). In order

Figure 7.1: Pictures of the newly designed target chamber made from aluminium.

Top left: The frame consists of a single part of aluminium milled out of a massive cube. The bottom plate is 20 mm thick, while the edges of the cubic frame are 20 mm × 20 mm thick.

Top right: Frame with covers showing the "pocket" flange for the β scintillation detector. The wall thickness of the cover plates is 10 mm.

Bottom: View inside the target chamber seen from top. The interior of the chamber is coated with 15 mm thick Teflon plates, while the pocket flange for the β scintillator is covered with a 5 mm thick Teflon tube.

to measure the time differences between the signals from the Germanium detector, plastic scintillator and Si(Li) detector, the CFD signals are used to start the Time to Digital Converter (TDC module CAEN V775). The TDC is running in "common stop" mode, therefore the gate signal which stops it is delayed by 350 ns.

The logic "OR" signal of the different trigger types is guided to the VME trigger module (TRIVA 4 from GSI), which triggers the acquisition Power-PC CPU (PPC) and provides the gate for the ADC and the scaler module. While the VME trigger module is processing data, it returns a busy signal to the TB 8000 trigger box to
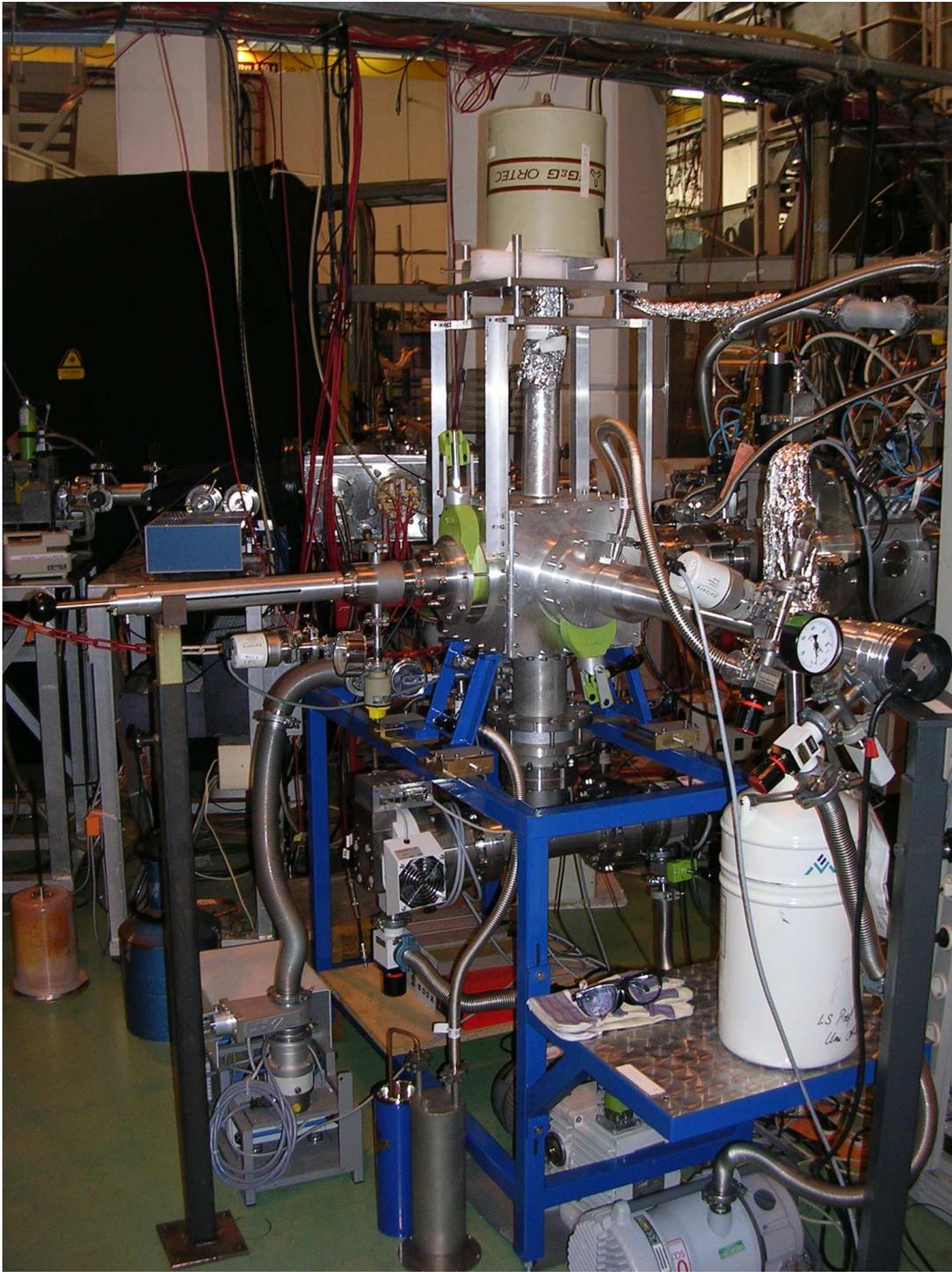
Figure 7.2: Picture of the main experiment at ISOLDE in August 2007. A completely new setup was designed as a result of the optimisation process following the previous measurements (see Sect. 6).
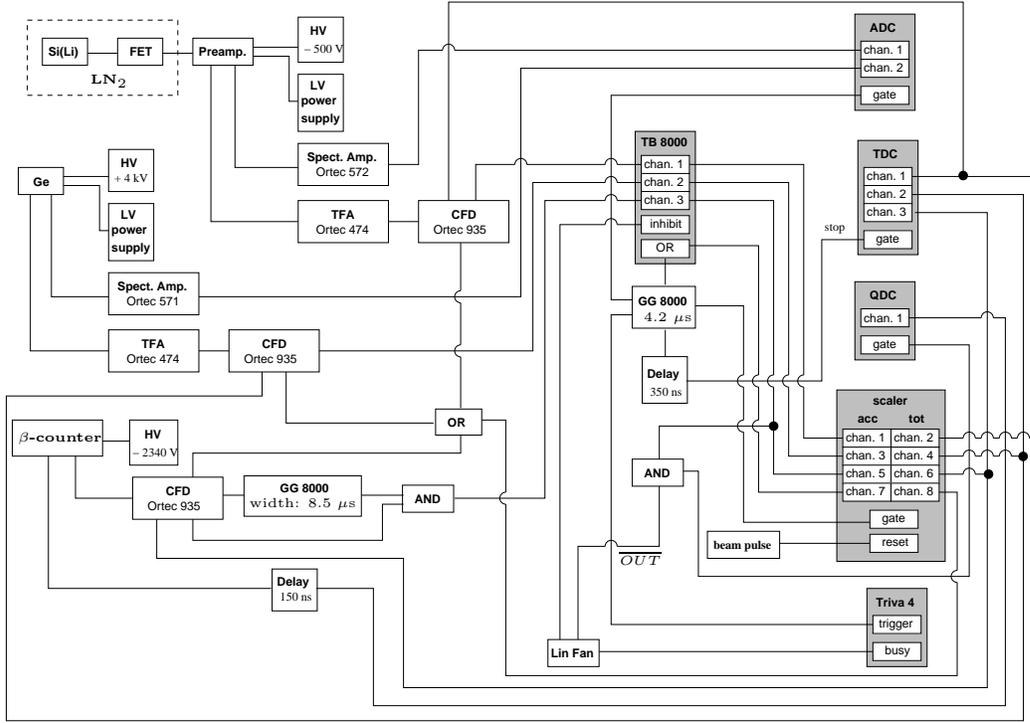
Figure 7.3: Schematic layout of the signal processing electronics.

inhibit further trigger generation.

The β detector signal is mainly used as trigger, however its energy signal is also digitised by a QDC charge integrator (CAEN V965). In order to avoid pileup events, the gate signal for the QDC is derived from a logical coincidence of the β detector signal and the logically inverted "busy" signal provided by the VME trigger unit.

The deadtime of the data acquisition system was measured using a scaler module (SIS 3820). Each CFD signal is connected to a scaler channel to measure the free counting rate $I_{\rm tot}$ of each detector. The overall counting rate from all detectors is measured using the logic "OR" of all CFD channels in another scaler channel. The accepted counting rate $I_{\rm acc}$ (including the deadtime) for each detector individually and for all detectors together is provided by the VME trigger unit and was measured with the scaler. The percentage of deadtime event losses for each detector and for the whole system can be calculated by

$$I_{\rm loss} = 1 - \frac{I_{\rm acc}}{I_{\rm tot}}. \tag{7.1}$$

The scaler module was operated in a mode, where the module provided an internal 50 MHz clock which was reset with the beam pulse signal. With each trigger signal the clock entry was read out, which contains the time information between the particle production in the ISOLDE target and the event time measured in the target chamber

and is therefore correlated with the lifetime of the particles in the beam. This provides a useful condition for the data analysis, which will be used later on in this chapter.

The MAR$_a$B$\emptyset$U data acquisition system [LUT03] was used for data readout from the VME modules as well as for the data presentation and online analysis. It consists of a front-end system for setup, data readout, run control, event building and data transport based on the GSI MBS code package [MBS]. Also a back-end system enabling data analysis, histogramming and data storage is included, based on the ROOT framework from CERN [ROO07]. In addition to the online data acquisition, the MAR$_a$B$\emptyset$U system can also be used for the offline data analysis. In this case the data files are read in, analysed and spectra can be stored in histograms.

7.3 Experimental Procedure

The $A = 96$ elements for the E0 reference measurement are produced in the target with high intensity. Therefore only every 4th proton pulse with $(2.8 - 3.0) \cdot 10^{13}$ protons per pulse was used on average. The beam gate (see the description of ISOLDE in Sect. 6) was opened 1.8 s after each proton pulse and remained open until the next proton pulse to increase the fraction of ^{96}Y due to its long half-life (5.34 ms) (see Fig. 6.4).

detector	downscale factor	singles rate [1/s]	accepted rate [1/s]	deadtime [%]
Si(Li)	2^0	~ 3300	~ 1350	59.0
β	2^5	~ 74000	~ 900	61.1
γ	2^0	~ 1900	~ 760	59.7
'OR' of all	$-$	~ 79000	~ 3000	60.1

Table 7.1: The singles counting rates, the counting rates, which are accepted by the data acquisition system and the resulting deadtime of each detector is shown for the $A = 96$ beam. In order not to create exceedingly deadtime, the singles counting rate of the β detector was downscaled by a factor of 2^5.

Tab. 7.1 shows the singles counting rates, the data rates accepted by the trigger system, and the resulting deadtime for each detector type. In order not to create exceedingly deadtime, the single events measured using the β detector were scaled down by a factor of 2^5. This value was chosen to achieve a similar counting rate of all detectors. The deadtime of this detector was calculated according to Eq. (7.1) using

$$I_{\text{loss}} = 1 - \frac{I_{\text{acc}}}{\frac{I_{\text{tot}}}{\delta}} \qquad (7.2)$$

with the downscale factor δ. This downscale factor affects only the β singles spectrum and not the coincidence measurement, since every trigger created by the Si(Li) detector initiates a readout of all detector signals.

detector	downscale factor	singles rate [1/s]	accepted rate [1/s]	deadtime [%]
Si(Li)	2^0	~ 350	~ 250	28.0
β	2^5	~ 7900	~ 160	35.2
γ	2^0	~ 1100	~ 800	25.9
'OR' of all	$-$	~ 9300	~ 1200	29.3

Table 7.2: The singles counting rates, the counting rates, which are accepted by the data acquisition system and the resulting deadtime of each detector is shown for the $A = 30$ beam. In order not to create exceedingly deadtime, the singles counting rate of the β detector was downscaled by a factor of 2^5.

In order to extract the maximum number of ^{30}Na ions, the beam gate was opened already 1 ms after the proton pulse and remained open for 300 ms due to the short half-life of ^{30}Na (48.4(17) ms) (see Fig. 7.10). Also the maximum number of available proton pulses was used (every second pulse on average) with the maximum of protons per pulse ($\sim 3 \cdot 10^{13}$). Tab. 7.2 lists the detector count rates and deadtimes for the main measurement with the $A = 30$ beam.

7.4 Data Analysis

7.4.1 Energy Calibration

Si(Li) Detector

The energy signal from the Si(Li) detector was calibrated using a ^{207}Bi electron source mounted on target position. For all three transitions at 569.7 keV, 1063.7 keV and 1770.2 keV the K, L and M conversion electrons can be resolved, as shown in Fig. 7.4. Due to the largely differing intensities of the three transitions, the vertical scale of the histogram in Fig. 7.4 has been scaled individually for each of the transition groups.

During the 7 days of the beamtime the energy calibration of the Si(Li) detector was checked several times during the measurement in order to monitor the stability of the energy calibration. The calibration characteristics was found to be strictly linear. In Fig. 7.5 (left) the values of the gain and offset calibration constants of each calibration run are shown. Obviously the calibration parameters remained constant during the experiment within the statistical errors of the linear fit parameters. The resulting linear calibration curve is shown in the right-hand part of Fig. 7.5. A gain of 0.6964(6) keV/channel and an offset of $-68.0(8)$ keV are determined as average values for all calibration runs. The energy resolution of the Si(Li) detector amounts to 4.3 keV for the K electron line of the 1063.7 keV transition. Since the electron source is covered with a thin Mylar foil, the detector resolution using an open source is significantly better, as it will be shown in Sect. 7.5.1.
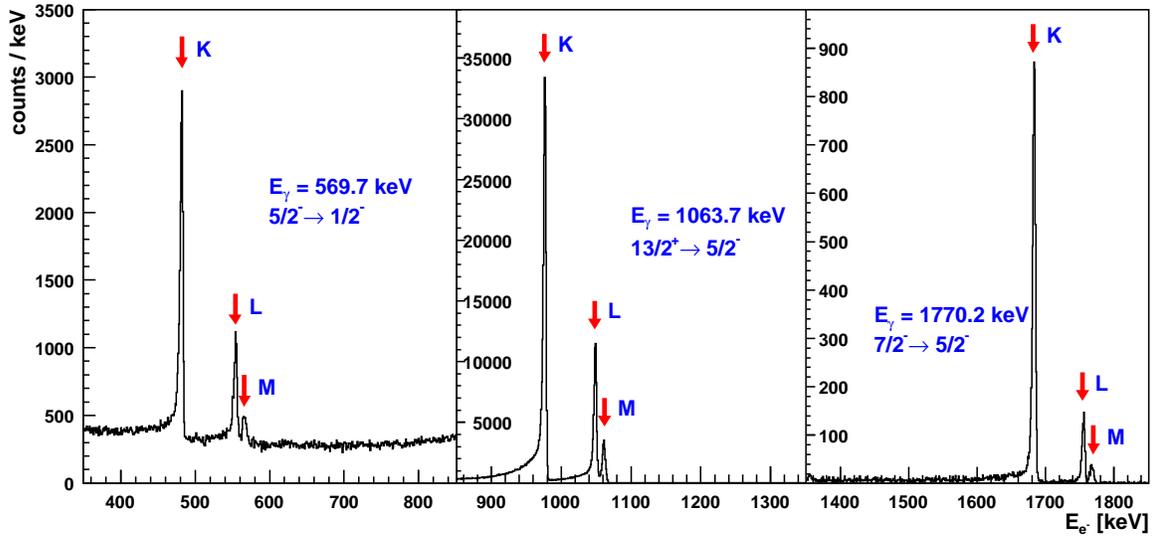
Figure 7.4: Electron energy spectrum of the ^{207}Bi calibration source. The three transitions at 569.7 keV, 1063.7 keV and 1770.2 keV can be resolved with their K, L and M conversion components. The transmission maximum of the Mini-Orange spectrometer was set to 1.7 MeV. Since the intensities of the three transitions differ significantly from each other, the y axis has been scaled individually for each of the three transition groups.

Germanium Detector

Fig. 7.6 shows the γ-ray energy spectrum measured with the Germanium detector using a ^{207}Bi and a ^{152}Eu source, respectively. In Fig. 7.7 (left) the linear calibration curve is shown and the resulting calibration parameters are indicated.

Energy [keV]	Intensity [%]	ϵ_{ph} [‰]
121.8	28.37	3.23
244.7	7.53	2.22
344.3	26.57	1.80
778.9	12.97	1.06
867.4	4.214	0.99
964.1	14.63	0.92
1085.9	11.86	0.86
1112.1	13.54	0.84
1408.0	20.85	0.72

Table 7.3: γ transitions and their relative decay intensities of the ^{152}Eu calibration source used for the efficiency calibration of the germanium detector. In the last column the corresponding absolute photopeak efficiency is listed.
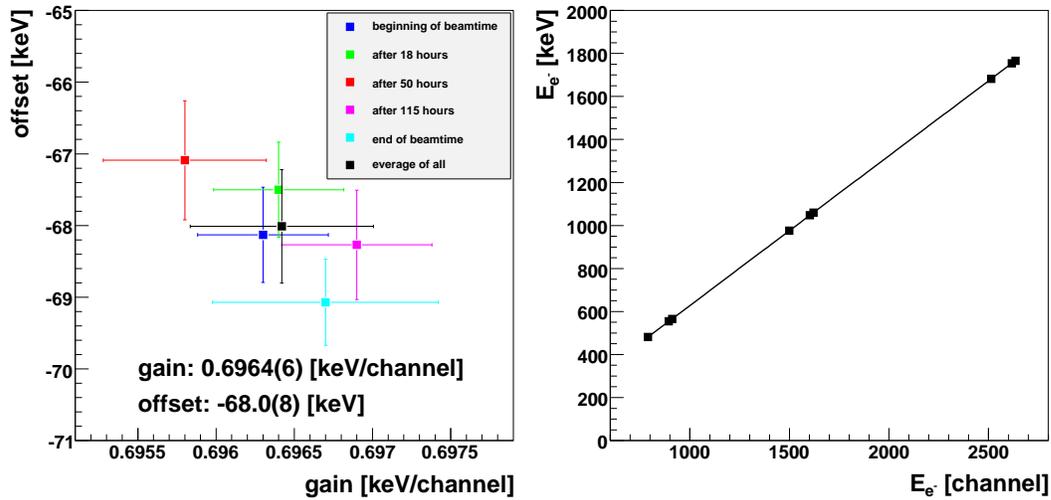
Figure 7.5: Left: During the online measurement at ISOLDE several energy calibration runs for the Si(Li) detector were performed. The gain and offset factors for each of the corresponding linear energy calibration functions are displayed. The average values of the calibration constants are indicated in black. Within the error bars the energy calibration remained constant during the measurement.

Right: Example of a linear calibration curve of the Si(Li) detector.
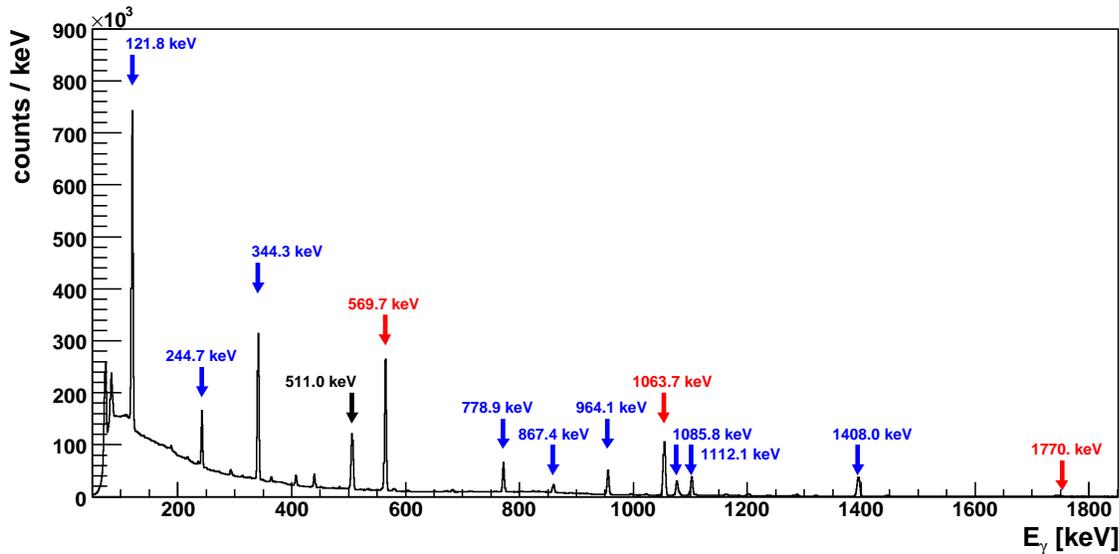
Figure 7.6: γ-ray energy spectrum measured using a ^{207}Bi (red) and a ^{152}Eu (blue) source simultaneously.

In addition the corresponding absolute photopeak efficiency of the germanium detector was determined. Therefore a ^{152}Eu γ source with an activity of 23.9 kBq was mounted
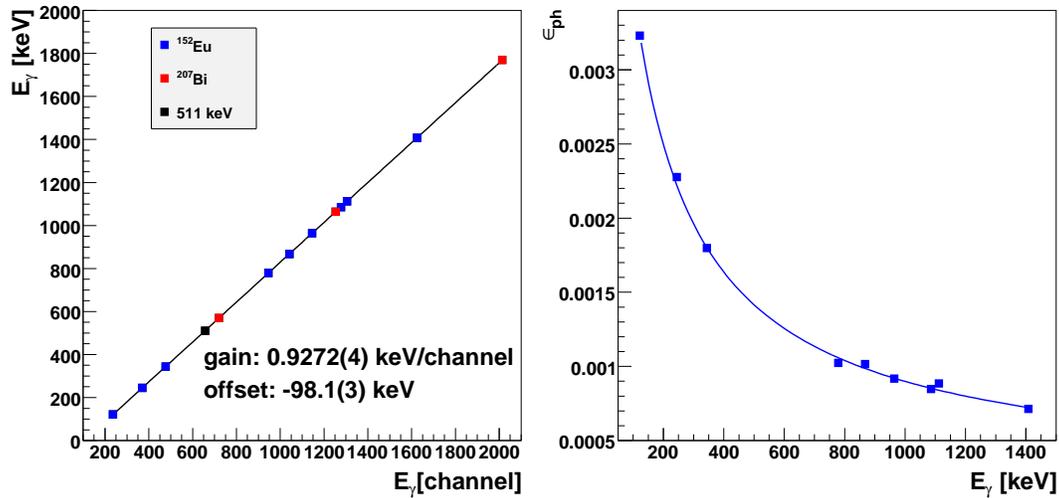
Figure 7.7: Left: Calibration characteristics of the germanium γ-ray detector. The linear calibration constants are indicated.
Right: Absolute photopeak efficiency of the germanium detector as a function of the γ-ray energy.

on target position. The energies and relative intensities of the transitions are shown in Tab. 7.3. The deadtime of the detector was determined to be 13.0 %. The runtime was about 5.75 h, which was enough to achieve more than 10^4 counts in the weakest 867.4 keV line and thus to limit the errors to about 1 %. The result of the efficiency calibration is shown in the right-hand part of Fig. 7.7, where the data points together with an exponential fit curve are displayed. The efficiency values for the ^{152}Eu decay energies are listed in the last column of Tab. 7.3.

7.4.2 Time Measurement

β − E0 coincidences

Time differences between different detector signals are measured with the TDC. In our experiments the TDC was started with a detector signal and stopped with the delayed common gate signal, which is the "OR" of all signals. Thus time differences between two detectors are obtained by subtracting the corresponding time values from each other. In Fig. 7.8 (left panel) the time difference between a signal in the photomultiplier tube of the plastic scintillator (β detector) and an electron detected in the Si(Li) detector is shown as a function of the electron energy. For low-energy electrons the time signal is slower compared to the time signal obtained from high values of the electron energy. This is caused by the constant fraction discriminator ("walk" effect). Fig. 7.8 (right panel) shows the projection of Fig. 7.8 (left panel) onto the time axis. While the black curve shows the time difference between β decay electrons and electrons in the Si(Li) detector, the red curve contains only those events with electron energies above
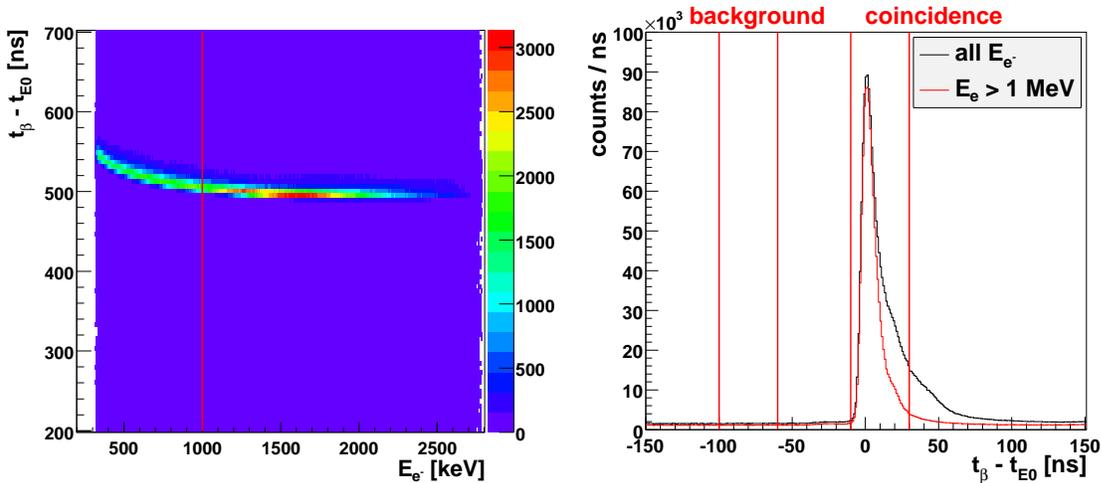
Figure 7.8: Left: The time difference of a signal in the photomultiplier of the plastic scintillator and an electron detected in the Si(Li) detector is plotted versus the electron energy. Caused by the constant fraction discriminator, the time signal is slower for low-energy electrons ("walk" effect).
Right: Projection onto the time axis for all events (black curve) and for events with $E_{e^-} > 1$ MeV (red curve).

1 MeV. The vertical lines mark the coincidence window between conversion and β decay electrons as used in the analysis.

$\beta - \gamma$ coincidences

Fig. 7.9 shows the time difference between signals in the scintillator and the γ detector. Due to the uncorrected "walk" effect of the constant fraction discriminator (see Sect. 7.4.2) the peak is rather wide. In order to determine the composition of the beams, the background-subtracted $\beta - \gamma$ coincidence spectrum was analysed. It was derived by setting a window on the coincidence peak in the time spectrum of Fig. 7.9 and subtracting the background by setting a window with the same width beneath the coincidence peak as shown in the figure.

Time measurement relative to the proton beam pulse

As described earlier in Sect. 7.2, the time difference between the isotope production by the proton pulse hitting the production target and the subsequent detection of the decay event was determined using a scaler module operating with an internal 50 MHz clock. This particle lifetime information can be exploited in our case to separate the short-lived ^{30}Na decays ($t_{1/2} = 48.4(17)$ ms) from longer-lived potential isobaric contaminants
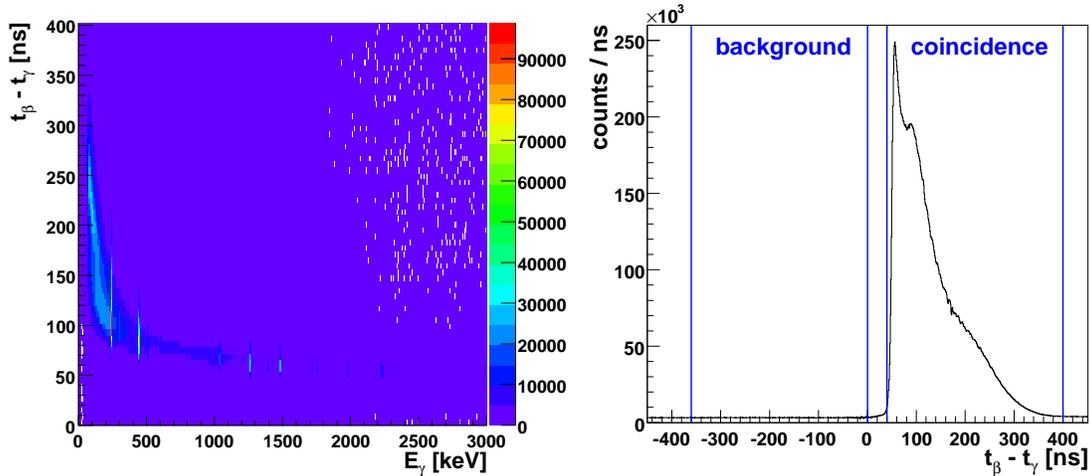
Figure 7.9: Left: Time difference between a signal in the photomultiplier of the plastic scintillator and a γ ray detected in the Germanium detector as a function of the γ-ray energy. Due to the uncorrected "walk" effect of the constant fraction discriminator (see Sect. 7.4.2), the time signal is slower for low-energy γ rays.

Right: The background-subtracted γ spectrum in coincidence with β decay electrons was derived by setting a gate condition on the coincidence peak, while for the random background a neighbouring window with the same width was used.
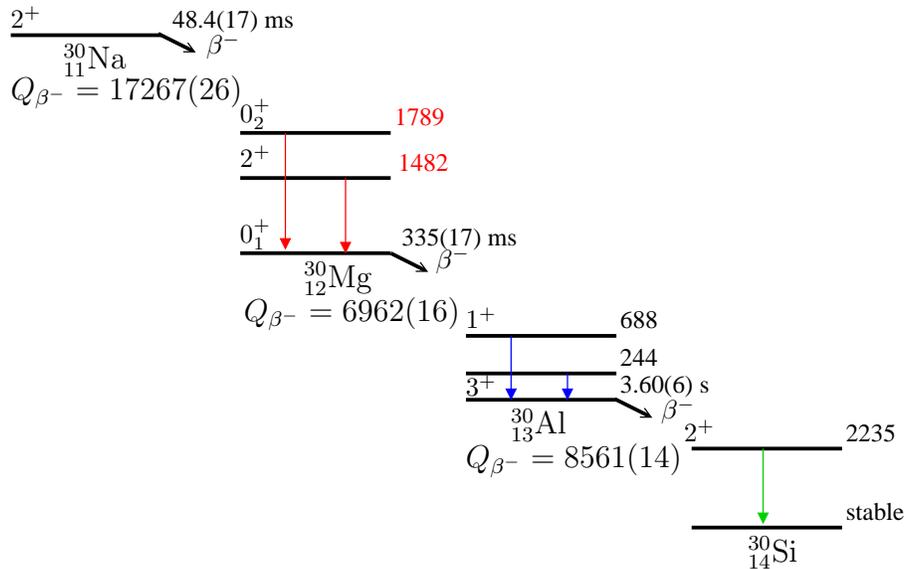
Figure 7.10: Decay chain of neutron-rich mass 30 elements. Only the ground state transitions in the daughter nuclei are shown.

or decay products such as ^{30}Mg ($t_{1/2} = 335(17)$ ms) or ^{30}Al ($t_{1/2} = 3.60(6)$ s) in the data analysis. The β decay sequence of $A = 30$ isobars is displayed in Fig. 7.10.

In case of the $A = 96$ reference measurement this method cannot be used, since the lifetime of ^{96}Y (5.34(5) s) is the longest in this decay chain.
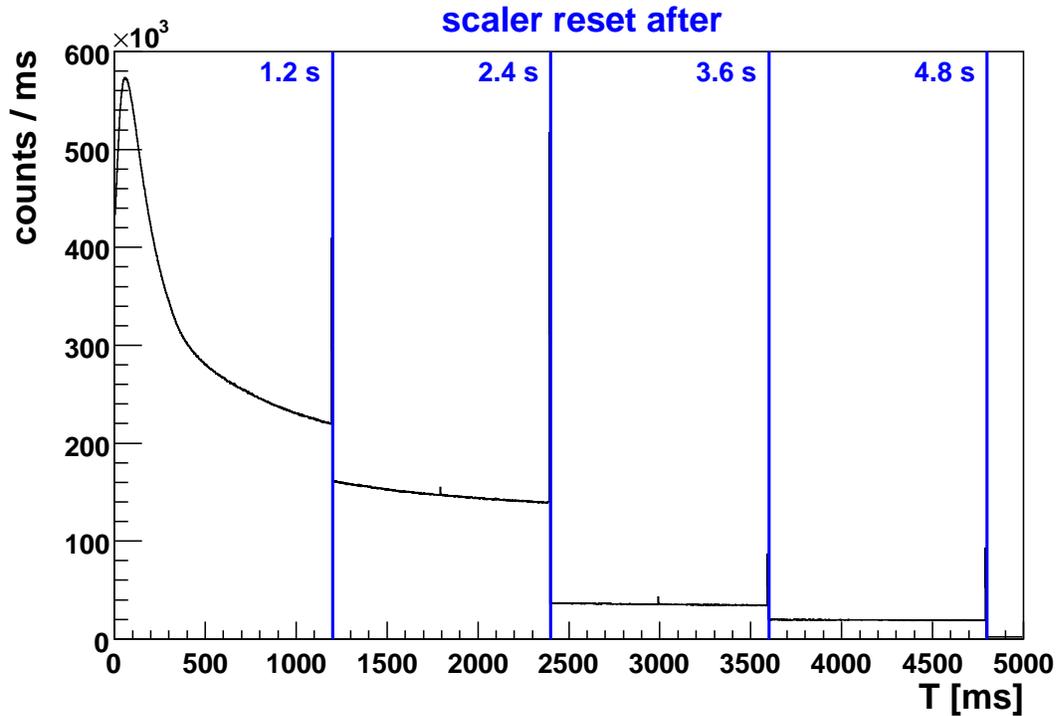
Figure 7.11: Scaler spectrum of an $A = 30$ beam from the ISOLDE target. The internal clock is running with 50 MHz and the scaler is reset with the beam pulse. The time difference between two proton beam pulses is an integer multiple of 1.2 s.

Fig. 7.11 shows the total scaler spectrum of the $A = 30$ ISOLDE beam. Since the time difference between two proton beam pulses is an integer multiple of 1.2 s, the spectrum consists of several parts with a duration of 1.2 s. If the time difference between two proton pulses is 2.4 s, the scaler is reset after that time and thus the scaler spectrum is filled until 2.4 s. This happens for 3.6 s, 4.8 s and so on, respectively. Since the focus of this experiment is on the ^{30}Na decay with the shortest half life of 48 ms, only the first part of the scaler spectrum is of interest.

In Fig. 7.12 the background-subtracted scaler spectra gated on the $2_1^+ \rightarrow 0_1^+$ γ transition in the daughter nucleus (^{30}Mg, ^{30}Al and ^{30}Si) is shown. The background was determined by setting a window with the same width as used for the γ transition gate condition beneath the transition peak. Due to the relatively long lifetime of ^{30}Al (3.60(6) s) the corresponding events are distributed over the whole time range between two pulses. At the beginning of the measurement the concentration of ^{30}Al is still rising, because it is
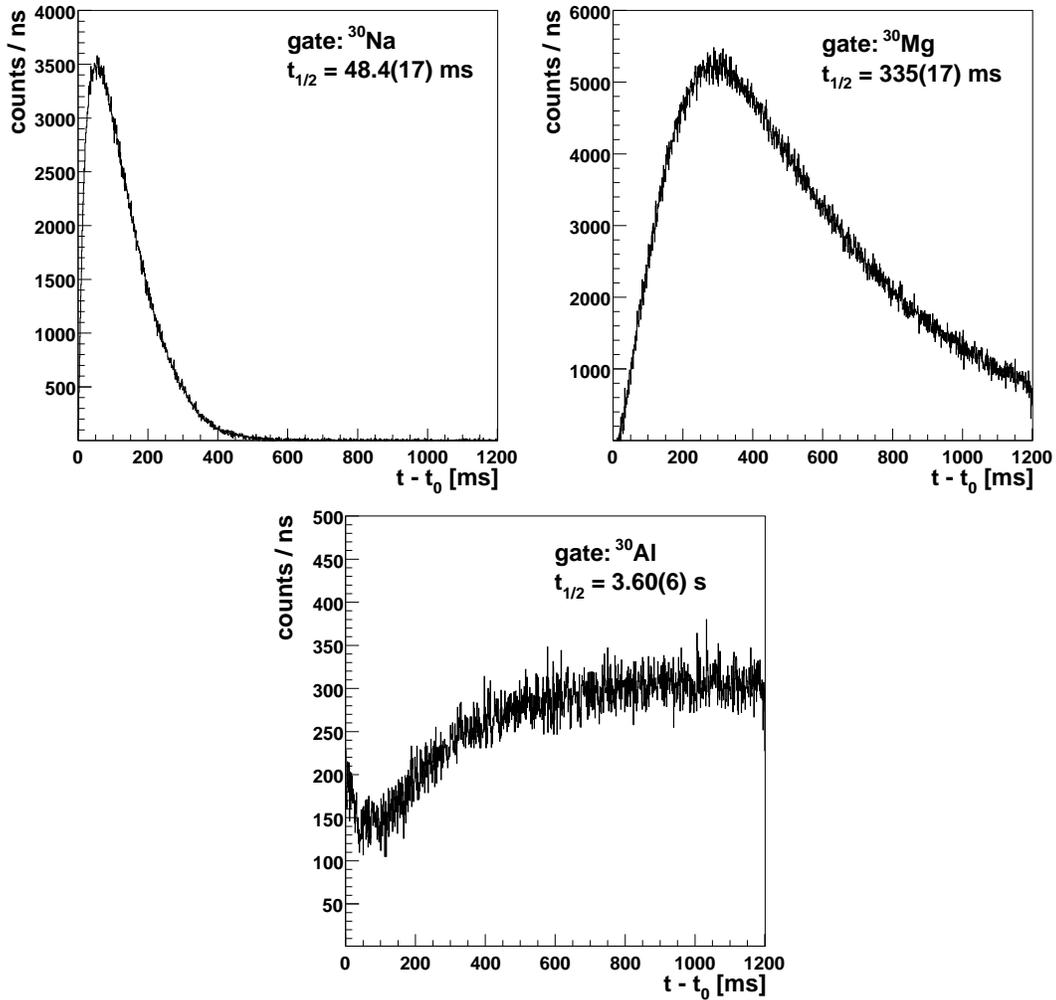
Figure 7.12: Time difference between the initial proton pulse hitting the production target and the detection of the event for the ^{30}Na, ^{30}Mg and ^{30}Al decay. A gate condition was applied on the corresponding ground state γ transition and background was subtracted by setting a gate condition with the same width beneath the transition peak in the corresponding daughter nucleus.

fed by the ^{30}Na and ^{30}Mg decay. The lifetime of ^{30}Mg is shorter than the proton pulse interval of 1.2 s, thus the number of decays reaches a maximum and decreases very fast. Since the lifetime of ^{30}Na is the shortest, a gate condition on the first 200 ms can be set in order to select the ^{30}Na decay, while simultaneously suppressing the background from longer-lived isobars.

Determination of the deadtime

The deadtime is a function of the counting rate. As it was shown in Fig. 7.11, the counting rate largely varies during the experiment due to the pulsed beam structure and the different lifetimes of the beam contaminants and decay products. In order to determine the time dependence of the deadtime relative to the beam pulse producing the $A = 30$ isobars, the singles counting rate and the accepted rate of the γ detector was determined in intervals of 25 ms for the shortest time between two proton pulses of 1.2 s.
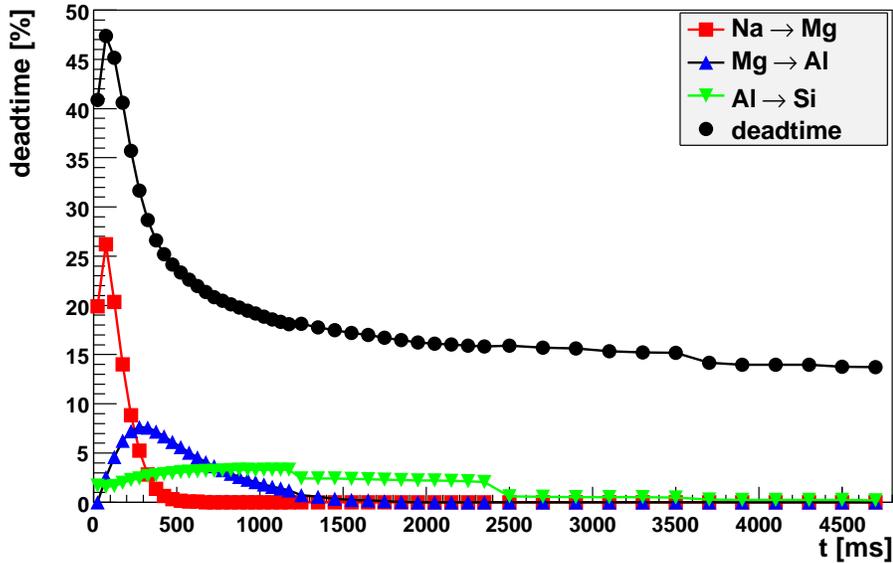
Figure 7.13: The deadtime (black points) as a function of the time elapsed relative to the particle production is displayed. Also the decay curves for ^{30}Na, ^{30}Mg and ^{30}Al measured using the scaler module and gated on the respective γ ground-state transition in either of the three beam components is shown. The integral of each decay curve was normalised to one.

Fig. 7.13 shows the percentage for the deadtime for the γ detector in intervals of 25 ms relative to the particle production time. Also the measured decay curves are shown. The integral of each decay curve was normalised to one. During the first hundred milliseconds after the particle production, the deadtime ranges between 40% and 50%. Then it decreases to $\sim 20\%$ and stays rather constant for the last 600 ms.

In order to determine the deadtime of the measurement for the γ transitions in ^{30}Mg, ^{30}Al and ^{30}Si, respectively, the decay curves have to be folded with the deadtime curve.

Fig. 7.14 shows the deadtime folded with the decay curve. In order to calculate the lifetime-corrected deadtime curve for the ^{30}Na, ^{30}Mg and ^{30}Al decays, the integral of each curve was calculated. The results are 41.7 %, 27.4 % and 24.4 %, respectively.
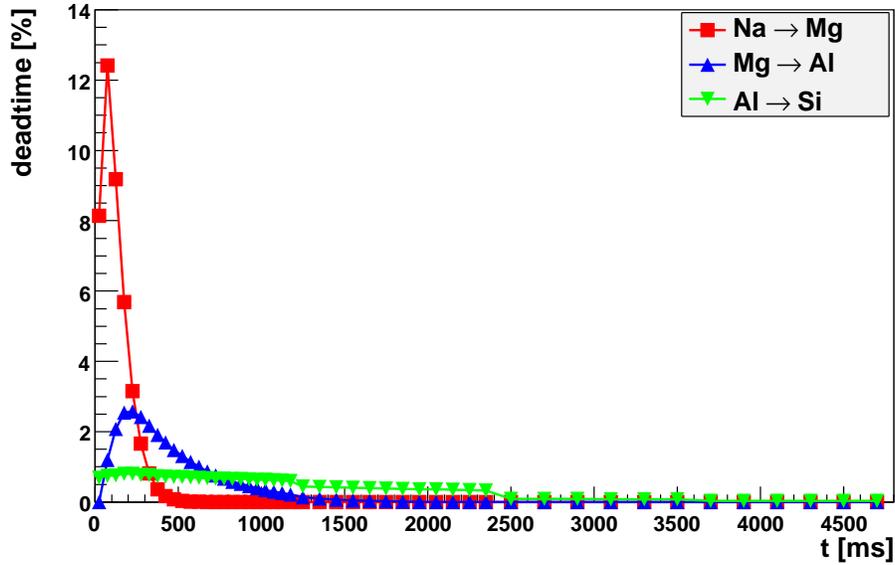
Figure 7.14: Deadtime folded with the decay curves of the three dominant $A = 30$ decay chain constituents. The deadtime for the ^{30}Na, ^{30}Mg and ^{30}Al decay is calculated by the integral of each curve, resulting in 41.7 %, 27.4 % and 24.4 %, respectively.

7.5 Experimental Results

7.5.1 Reference measurement in ^{96}Zr

The new experimental setup was also characterised at ISOLDE using the E0 transition in ^{96}Zr as reference measurement (see also Sect. 6.1.2 and 6.2.2). The excited states in ^{96}Zr were populated by the β decay of ^{96}Y (see Fig. 6.4). Since ^{96}Zr is stable and represents the end point of the $A = 96$ decay chain

$$^{96}\text{Rb} \xrightarrow{\beta^-} {}^{96}\text{Sr} \xrightarrow{\beta^-} {}^{96}\text{Y} \xrightarrow{\beta^-} {}^{96}\text{Zr}$$
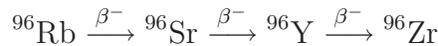
the whole intensity of the $A = 96$ beam finally decays to ^{96}Zr (the longest half-life within the decay series being $t_{1/2}(^{96}\text{Y}) = 5.34(5)$ s).

Tab. 7.4 shows the composition of the $A = 96$ beam as derived from the $\beta - \gamma$ coincidence spectrum. The absolute number of produced particles was determined from the (efficiency-corrected) peak contents in the γ-ray energy spectrum, the absolute intensity of the γ transitions [ENS07] and the solid angle coverage of the β scintillator. Due to the opening conditions of the beam gate and the long lifetime of the nuclei, the time dependency of the deadtime of the acquisition system is not considered. Only an average value is used for the data analysis. Mostly ^{96}Sr is produced by the fragmentation process in the ISOLDE target and extracted. The total number of ^{96}Y decaying to ^{96}Zr is $8.42 \cdot 10^4$/s.
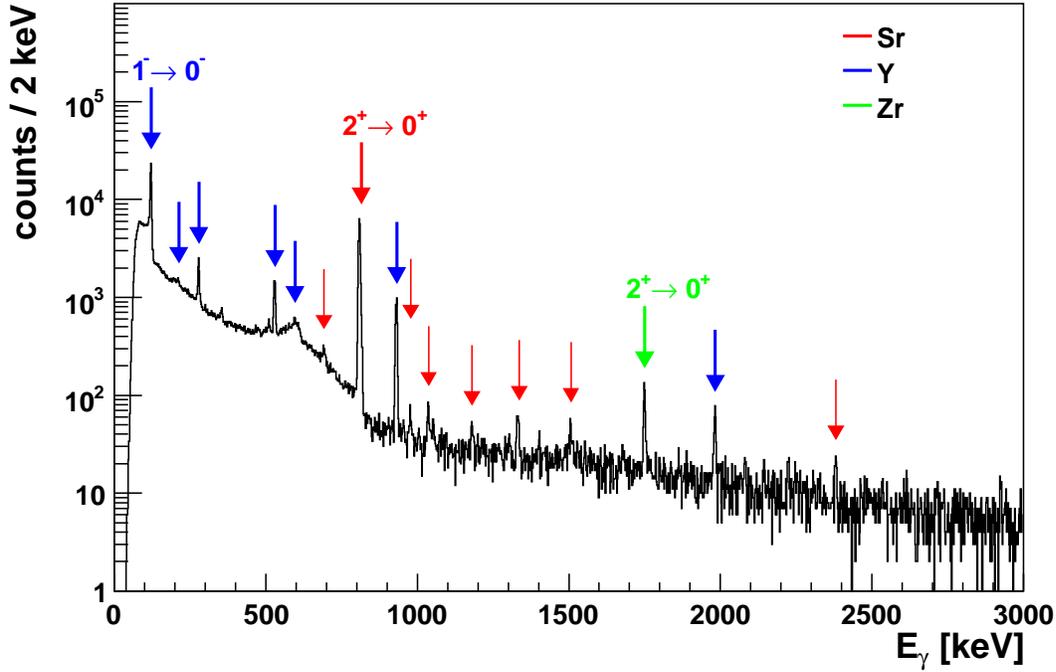
Figure 7.15: γ energy spectrum of the $A = 96$ ISOLDE beam in coincidence with events in the plastic scintillator. Transitions in Sr are marked in red, transitions in Y in blue and transitions in Zr in green.

element	half-life	decay rate [1/s]	fraction
^{96}Rb	199(3) ms	$1.12 \cdot 10^4$	13 %
^{96}Sr	1.06(3) s	$6.74 \cdot 10^4$	80 %
^{96}Y	5.34(5) s	$5.61 \cdot 10^3$	7 %
all		$8.42 \cdot 10^4$	100 %

Table 7.4: Composition of the $A = 96$ beam. Due to the short lifetime of the isobars, 100 % of the radioactive beam was used to populate the strong E0 transition in ^{96}Zr.

Fig. 7.16 shows the singles electron spectrum measured using an $A = 96$ beam. The K and L line of the prominent E0 transition in ^{96}Zr at 1563.3 keV and 1578.8 keV are nicely resolved after a 1 h measurement. $(3.43 \pm 0.25) \cdot 10^4$ counts were measured in the K line and $(4.17 \pm 0.17) \cdot 10^3$ counts in the L line. In 1 h of beamtime $3.03 \cdot 10^8$ ^{96}Y atoms were produced, decaying to ^{96}Zr as derived from the γ spectrum. Taking into account the absolute intensity of the E0 transition, the transmission efficiency of the Mini-Orange spectrometer (2.2 % at 1550 keV), the fraction of K (L) conversion (see Tab. 6.1) and the deadtime of the data acquisition for the Si(Li) detector (59.0 %),
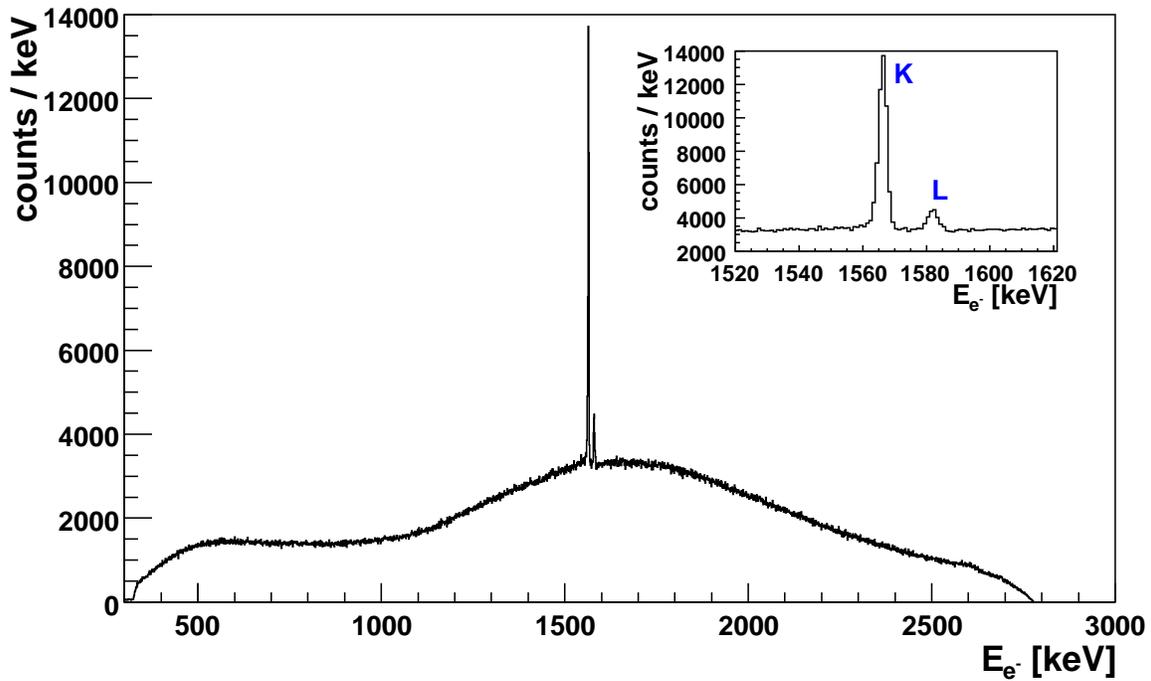
Figure 7.16: Total electron energy spectrum of the $A = 96$ decay products folded with the transmission curve and measured with the Si(Li) detector within 1 h. The K and L conversion electron lines of the strong E0 transition in ^{96}Zr at 1563.3 keV and 1578.8 keV are nicely resolved.

a final peak content of $3.01 \cdot 10^4$ $(3.20 \cdot 10^3)$ counts would be expected in the K (L) transition line, respectively. This agrees reasonably well with the measured values.

Fig. 7.17 shows the background-subtracted β – E0 coincidence spectrum. $7.15(9) \cdot 10^3$ $(9.5(4) \cdot 10^2)$ counts are remaining in the K (L) line, respectively, sitting on top of the negligible background resulting in a peak-to-background ratio of 44 for the K-line.

The solid angle coverage of the scintillation detector for this setup was experimentally determined from the ratio of counts in the K conversion line in the β – E0 coincidence spectrum and the conversion electron singles spectrum as $d\Omega/4\pi = 0.21$. This agrees very well with the calculated value of 24 %, derived from the distance between detector and source of 13 mm.

In analogy to the E0 decay of ^{90}Zr, that has been analysed in Sect. 6.3.1, Fig. 7.18 displays the background-subtracted decay spectrum of the 0_2^+ state in ^{96}Zr gated on the K line of the E0 decay. The histogram was fitted using an exponential curve. The decay parameter λ was determined to be 0.0187(5)/ns, which corresponds to a half-life of the 0_2^+ state in ^{96}Zr of 37.0(13) ns, in perfect agreement with the published value of 38.0 ns [ENS07].
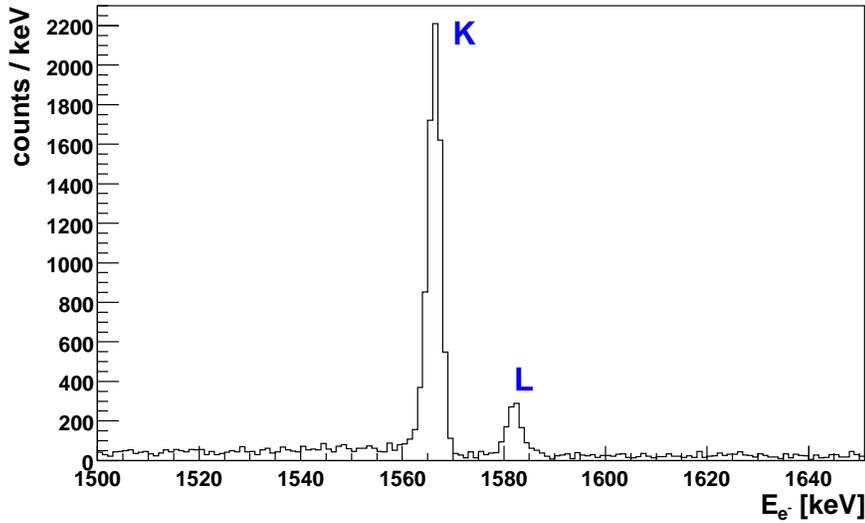
Figure 7.17: Background-subtracted electron spectrum from the $A = 96$ decay products measured with the Mini-Orange spectrometer in coincidence with β decay electrons. The K and L transition lines are clearly visible on top of an almost negligible background after 1 h of measurement.

This test experiment showed that the experimental setup and the data acquisition system were working in a well-understood way.

7.5.2 Results from the $A = 30$ main measurement

After all preparatory offline and online test experiments the new experimental setup was ready to search for the E0 transition in ^{30}Mg at 1788 keV.

Composition of the $A = 30$ beam

In order to determine the beam composition, the number A_0 of produced ^{30}Na, ^{30}Mg and ^{30}Al nuclei was determined using

$$A_0 = \frac{N_\gamma}{\epsilon_\gamma I_\gamma (1 - t_{dead})} \tag{7.3}$$

with the number of measured counts N_γ, the detector efficiency ϵ_γ, the decay transition probability I_γ and the deadtime t_{dead}.

Fig. 7.19 shows the γ spectrum which was used to determine the beam composition.

Tab. 7.5 shows the composition of the $A = 30$ beam. The absolute number of produced particles was determined from the (efficiency-corrected) peak contents in the γ-ray
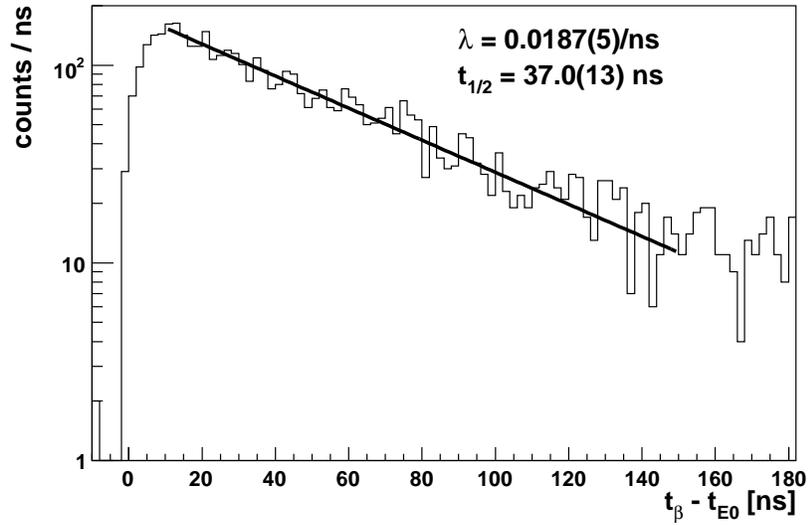
Figure 7.18: Background-subtracted decay spectrum of the 0_2^+ state in ^{96}Zr gated on the E0 decay. An exponential decay function was fitted to the time spectrum in order to determine the lifetime of the 0_2^+ state. The resulting decay constant $\lambda = 0.0187(5)$/ns allows to determine a half-life of the 0_2^+ state of $t_{1/2} = 37.0(13)$ ns, in agreement with the literature value of 38.0 ns [ENS07].

element	half-life	decay rate [1/s]	fraction
^{30}Na	48.4(17) ms	$\sim 6.4 \cdot 10^3$	$\sim 100~\%$
^{30}Mg	335(17) ms	~ 0	$\sim 0~\%$
^{30}Al	3.60(6) s	~ 0	$\sim 0~\%$
all		$\sim 6.4 \cdot 10^3$	$100~\%$

Table 7.5: Composition of the $A = 30$ beam.

energy spectrum and the absolute intensity of the γ transitions [ENS07]. Also the deadtime of the γ detector derived from the deadtime folded with the decay curves (see Sect. 7.4.2) was taken into account. Due to the opening conditions of the beam gate, the beam consists of almost 100 % ^{30}Na. ^{30}Mg cannot be surface ionized in the source [KÖS08] and thus no ^{30}Mg is contained in the beam delivered from the ISOLDE HRS separator. Also the fraction of ^{30}Al is negligible. γ transition lines in ^{30}Mg, ^{30}Al and ^{30}Si are visible in the γ spectrum (Fig. 7.19) since the ^{30}Na beam is stopped in the target chamber and subsequent decays in the $A = 30$ decay chain (see Fig. 7.10) lead to emission of γ rays from $A = 30$ isobars.
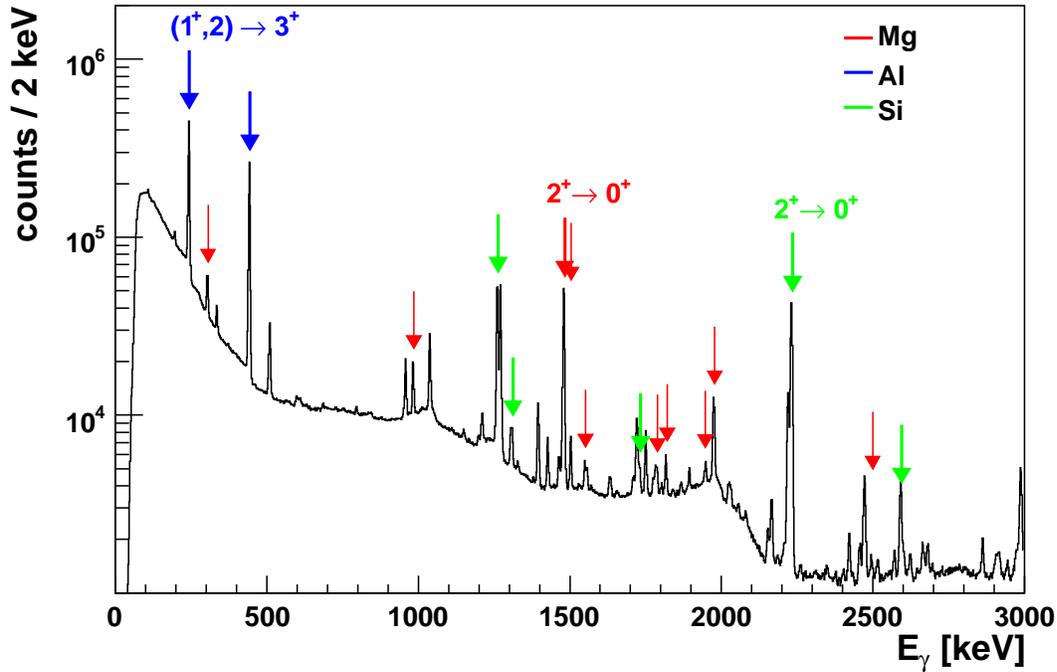
Figure 7.19: γ energy spectrum of the $A = 30$ ISOLDE beam. Transitions in Mg are marked in red, transitions in Al in blue and transitions in Si in green. This spectrum was used to determine the beam composition.

E0 transition measurement

In Fig. 7.20 the electron singles spectrum folded with the transmission curve of the Mini-Orange measured using the $A = 30$ beam is shown, where no obvious E0 transition can be identified on top of the β decay-dominated background.

Fig. 7.21 shows the conversion electron spectrum in coincidence with β decay electrons. Also a gate condition according on the short lifetime of ^{30}Na was used as described previously. The E0 transition at 1788 keV is clearly visible exactly at the expected energy.

Tab. 7.6 shows an overview of the experimental values derived from the $\beta - $ E0 and the $\beta - \gamma$ coincidence spectrum also including the gate condition on short lifetimes. According to Eq. (3.35) ρ^2(E0) can be determined using the efficiency corrected transition intensities

$$I_\gamma^{\text{E2}} = 2.768(20) \cdot 10^7 \qquad (7.4)$$

and
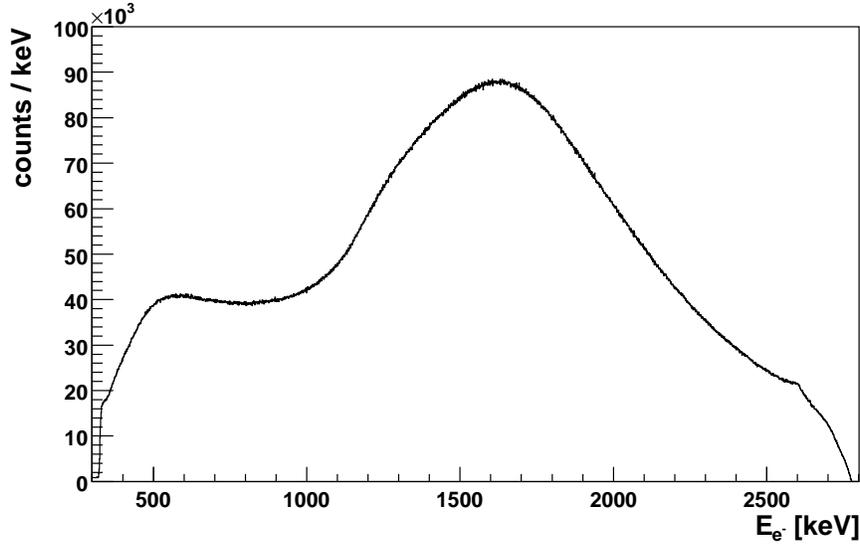
Figure 7.20: Electron singles spectrum of the $A = 30$ isobars measured at ISOLDE. The β decay spectra of ^{30}Na, ^{30}Mg and ^{30}Al are folded with the transmission curve.
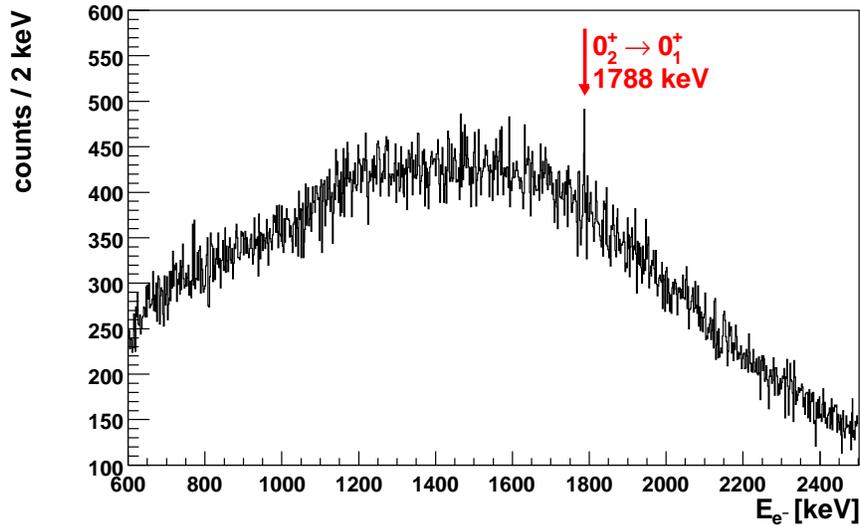
Figure 7.21: Resulting electron – electron coincidence spectrum including the gate condition on the short lifetime of ^{30}Mg. The E0 transition at 1788 keV is clearly visible at the expected energy position.

$$I_{\mathrm{K+L}}^{\mathrm{E0}} = 1.12(30) \cdot 10^4 \qquad (7.5)$$
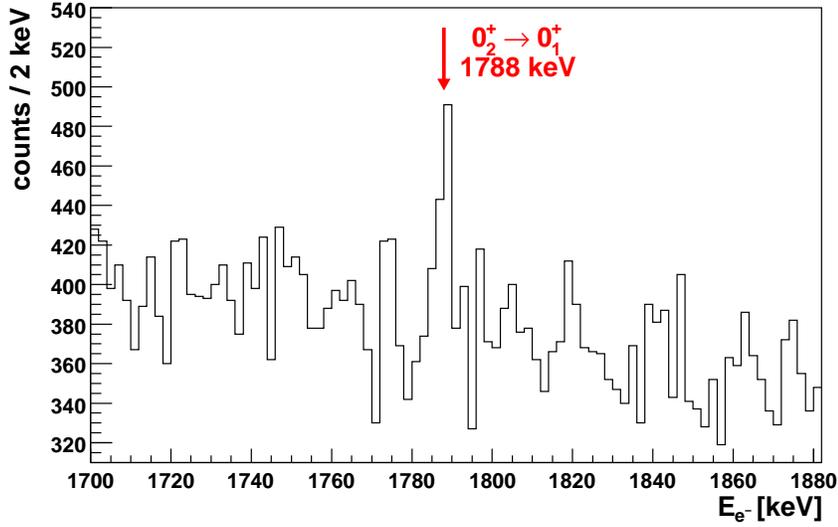
Figure 7.22: Resulting coincidence spectrum according to Fig. 7.21 showing the E0 transition in more detail.

	E0 transition at 1789 keV	γ transition at	
		305.9 keV	1482.1 keV
counts	201(50)	$5.37(4) \cdot 10^4$	$1.5 \cdot 10^5$
det. efficiency	0.018(2)	0.00194	0.00070
deadtime	0.44	0.44	0.44

Table 7.6: Overview of the experimental values derived from the $\beta - E0$ and the $\beta - \gamma$ coincidence spectrum also including the gate condition on short lifetimes.

derived from the values shown in Tab. 7.6, the Ω_i values ($\Omega_{\mathrm{K}} = 2.752 \cdot 10^6$, $\Omega_{\mathrm{IP}} = 9.367 \cdot 10^7$, see Tab. 5.1), the conversion coefficient $\alpha = 9.10(13) \cdot 10^{-4}$ of the competing E2 transition and the total lifetime $\tau = 5.6(6)$ ns ($t_{1/2} = 3.9(4)$ ns) of the 0_2^+ state. A value of

$$\rho^2(\mathrm{E0}) = 26.2(7.5) \cdot 10^{-3} \tag{7.6}$$

is obtained. This small value indicates weak mixing of the two 0^+ configurations residing in differently deformed potential minima. The absolute intensity of the E0 transition following the β decay of ^{30}Na results to

$$I(\mathrm{E0}) = 2.0(4) \cdot 10^{-5} \tag{7.7}$$

derived from the transition intensity of the $2_2^+ \to 0_2^+$ γ transition of 0.051(4) [ENS07]

populated by the β-decay of ^{30}Na during the experiment.

Using Eq. (3.31) the partial lifetime of the E0 transition can be calculated to be

$$\tau(\text{E0}) = 396(113) \text{ ns}. \tag{7.8}$$

Since the 0_2^+ state in ^{30}Mg has been identified the $B(\text{E2})$ value of the competing $0_2^+ \rightarrow 2_1^+$ E2 γ transition can be identified:

$$B(\text{E2}, 0_2^+ \rightarrow 2_1^+) = 53(6) \text{ e}^2\text{fm}^4. \tag{7.9}$$
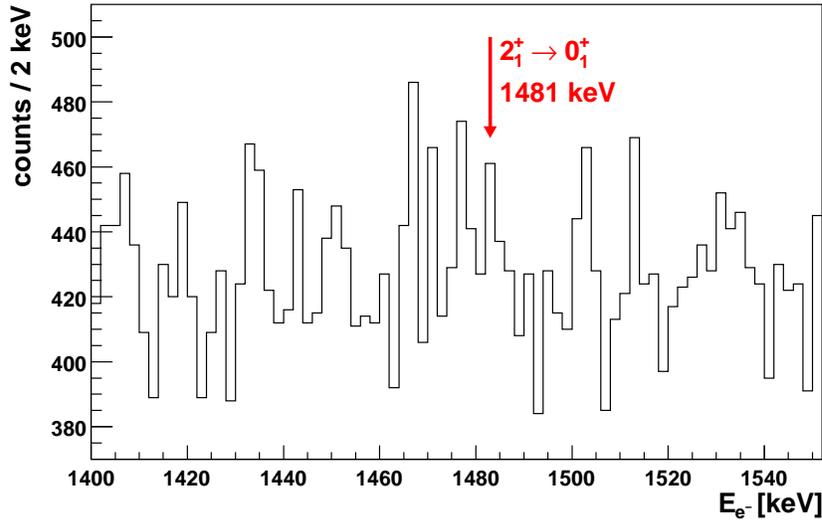
Figure 7.23: Resulting coincidence spectrum according to Fig. 7.21 indicating the position of the expected converted E2$_{\text{K+L}}$ transition of the E2 $2_1^+ \rightarrow 0_1^+$ ground state transition at 1482 keV.

Since the E2 $2_1^+ \rightarrow 0_1^+$ ground state transition at 1482.1 keV has been detected with good statistics ($1.5 \cdot 10^5$ counts) in the γ-ray spectrum, one can also search for the corresponding converted electron transition in the $\beta - \text{E0}$ coincidence spectrum. With a conversion coefficient $\alpha_{\text{K+L}} = 8.4 \cdot 10^{-6}$ ca. 40(2) counts can be expected in the electron spectrum. Fig. 7.23 shows the relevant energy region of the coincident electron spectrum. While no clear indication of the converted electron peak is visible in the presence of a rather large background, a tentative Gaussian fit, constraining the width of the assumed transition to the detector resolution of ~ 3.5 keV, results in a possible E2$_{\text{K+L}}$ contribution of 97(58) counts at the expected position (1481 keV), which is within the expected intensity range, while being clearly statistically insignificant.

8 Interpretation of the experimental results

Our picture of nuclear shapes at the borderline of the 'Island of Inversion' expects the 0_1^+ ground state in ^{30}Mg as an almost spherical configuration, while the excited 0_2^+ state is described as a highly deformed intruder state with a deformation similar to the one of the 0_1^+ intruder ground state in ^{32}Mg. So far in both isotopes only reduced transition probabilities $B(\text{E2}, 0_1^+ \rightarrow 2_1^+)$ have been measured. In ^{30}Mg the rather large measured value of $B(\text{E2}) = 241(31)$ e^{2}fm^4 [NIE05] might be interpreted in a simplistic view within the rigid rotor model as a large deformation of the 0_1^+ ground state in ^{30}Mg ($\beta_2 \approx 0.39$), which could be explained by a large mixing with the 0_2^+ state, caused by a rather small potential barrier between the two potential minima. However, this interpretation is in contrast to our experimental findings of a small value for the electric monopole strength of $\rho^2(\text{E0}, ^{30}\text{Mg}) = 26.2(7.5) \cdot 10^{-3}$. This points to weak mixing between the 0^+ states, which seems to be in contradiction to the measured large $B(\text{E2})$ value.

8.1 Phenomenological Approach

In Sect. 3.3 the two-level mixing model was explained in detail. In this model the mixing amplitude a describes the overlap of the wave functions of the 0_1^+ state and the 0_2^+ state in the laboratory system. Since the monopole strength $\rho^2(\text{E0}, ^{30}\text{Mg})$ is very weak, effective deformations are considered, neglecting the transformation from the system of (mixed) configurations accessible in the laboratory to the intrinsic (unmixed) states.

8.1.1 Extraction of the Mixing Amplitude a

In order to extract the mixing amplitude a from the measured $\rho^2(\text{E0})$ monopole strength in ^{30}Mg according to Eq. (3.22), the intrinsic deformations of the two 0^+ states are needed. This deformation parameters can be determined in a phenomenological approach calculating the β values via the $B(\text{E2})$ values of the $0_1^+ \rightarrow 2_1^+$ in the rigid rotor model using Eq. (8.1) and Eq. (8.2) (see next Sect.).

In Fig. 8.1 the correlation between the electric monopole strength $\rho^2(\text{E0})$ and the squared mixing amplitude a^2 is displayed for various deformation parameters β. The
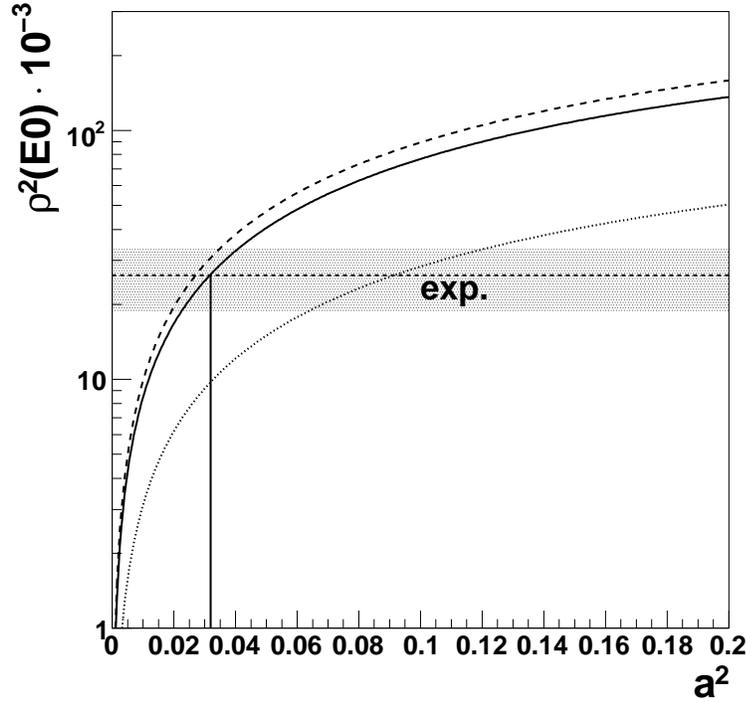
Figure 8.1: Dependency of $\rho^2(E0)$ on the squared mixing amplitude for ^{30}Mg according Eq. (3.22). The experimental value with the determined uncertainty is indicated by the shaded area. The solid line represents the correlation using the calculated deformation values $\beta_1 = 0.16$ and $\beta_2 = 0.59$ from [ROD08], the dashed line illustrates the limiting case of a spherical ground state ($\beta_1 = 0, \beta_2 = 0.59$) and the dotted line the limiting case of a deformed ground state ($\beta_1 = 0.39, \beta_2 = 0.59$) calculated from the experimental $B(E2)$ value using the rigid rotor model.

solid line displays the situation with $\beta_1 = 0.16$ and $\beta_2 = 0.59$, as calculated by T.R. Rodriguez and J.L. Egido [ROD08] (see Sect. 8.2.2). The dashed curve illustrates the limiting case of a spherical 0_1^+ ground state ($\beta_1 = 0$) in ^{30}Mg, while the dotted curve shows the limiting case of a deformed 0_1^+ ground state ($\beta_1 = 0.39$) as derived from the experimental $B(E2)$ value using the rigid rotor model. In all cases $\beta_2 = 0.59$ was used for the deformation of the 0_2^+ state. Also the experimental value is indicated by the dashed line with its error bar indicated by the shaded area.

From the experimental value of $\rho^2(E0)$ using the deformation parameters $\beta_1 = 0.16$ and $\beta_2 = 0.59$ a value of $a^2 = 0.0319(76)$ can be extracted. This value results in a mixing amplitude of $a = 0.179(83)$ for the mixing amplitude between the two 0^+ states.

8.1.2 Calculation of deformations using the Grodzins Systematics

The Grodzins systematics [RAM01] describes a correlation between the B(E2) value and the transition energy of the $2_1^+ \rightarrow 0_1^+$ ground state transition for collective rotations of axially symmetric nuclei. Over the whole mass range of the chart of nuclides this simple phenomenological correlation is able to reproduce the experimental values within a factor of two. In its most recent (global) parameterisation by Raman et al. [RAM01] the Grodzins systematics is given by

$$B(\text{E2}) \cdot E(2_1^+) = (2.57 \pm 0.45) \cdot Z^2 \cdot A^{-2/3}. \tag{8.1}$$

In the rigid rotor model the deformation of a 0^+ ground state can be calculated from the B(E2) value using

$$\beta = \left(\frac{4\pi}{3ZR^2} \right) \left(\frac{B(\text{E2})}{e^2} \right)^{1/2} \tag{8.2}$$

with $R = 1.2$ fm $\cdot A^{1/3}$.

	B(E2)$[e^2 fm^4]$		β using Eq. (8.2)	
transition	exp.	Grodzins	exp.	Grodzins
^{30}Mg $0_1^+ \rightarrow 2_1^+$	241(31) [NIE05]	259(26)	0.39(3)	0.40(4)
^{32}Mg $0_1^+ \rightarrow 2_1^+$	454(78) [SCH05]	414(41)	0.51(4)	0.49(4)

Table 8.1: Measured and predicted B(E2, $0_1^+ \rightarrow 2_1^+$) values using the Grodzins systematics Eq. (8.1) for ^{30,32}Mg. Also the deformations β derived within the rigid rotor model from the B(E2) values using Eq. (8.2) are shown.

Tab. 8.1 shows the measured B(E2) values and the expected ones for ^{30,32}Mg as derived from the Grodzins systematics. For both nuclei the predicted B(E2) values agree remarkable well within error bars with the measured values. Also the calculated deformations using Eq. (8.2) are shown for the experimental B(E2) values together with the predicted values.

In Fig. 8.2 the systematics of $2^+ \rightarrow 0^+$ transition energies in the Mg isotopic chain is shown. This is done for the transitions between strongly deformed states ($2_1^+ \rightarrow 0_1^+$ inside the 'Island of Inversion') and for isotopes located outside ($2_2^+ \rightarrow 0_2^+$). Also the spherical (or much less deformed) $2^+ \rightarrow 0^+$ transitions (^{24,26,28}Mg: [ENS07]; ^{30}Mg: [MAC05]; ^{32}Mg: [MOT95], $E(2_2^+ \rightarrow 0_2^+)$ extrapolated from ^{30}Mg with 2_2^+ assignment of the 2551 keV level; ^{34}Mg: [IWA01]; ^{36}Mg: [GAD07]) are indicated. Since the position of the 0_2^+ state in ^{32}Mg is not yet known, it is extrapolated using the systematics to be around $E(0_2^+) = 1100(100)$ keV. The $2_2^+ \rightarrow 0_2^+$ transition energy of 678 keV included in Fig. 8.2 for the deformed intruder states in ^{30}Mg is based on the assignment of the 2467 keV level as being the (deformed) 2_2^+ state. This assumption will be discussed in the following paragraph.
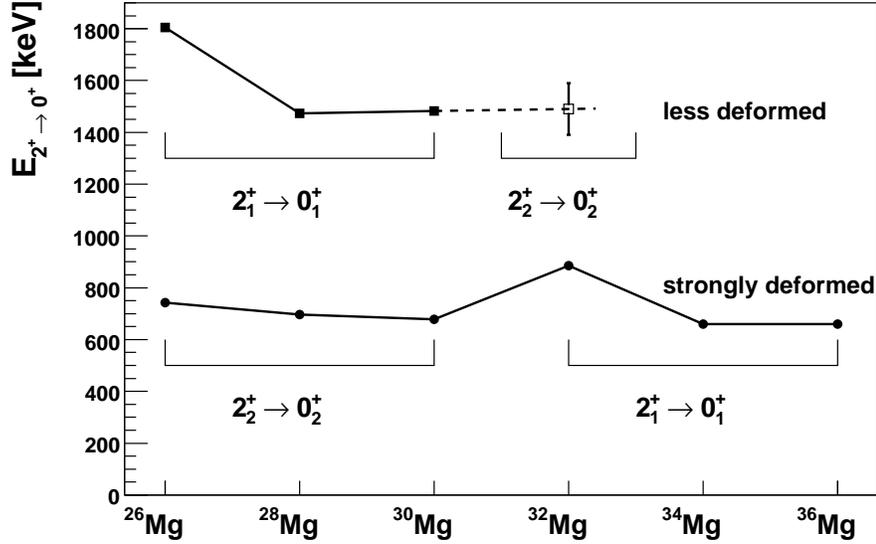
Figure 8.2: Systematics of strongly deformed and spherical (or much less deformed) $2^+ \to 0^+$ transition energies in Mg isotopes. This is done for the transitions between strongly deformed states ($2^+_1 \to 0^+_1$) inside the 'Island of Inversion' and for isotopes located outside ($2^+_2 \to 0^+_2$). Also the spherical (or much less deformed) $2^+ \to 0^+$ transitions (^{24,26,28}Mg: [ENS07]; ^{30}Mg: [MAC05]; ^{32}Mg: [MOT95], $E(2^+_2 \to 0^+_2)$ extrapolated from ^{30}Mg with 2^+_2 assignment of the 2551 keV level; ^{34}Mg: [IWA01]; ^{36}Mg: [GAD07]) are indicated. Since the position of the 0^+_2 state in ^{32}Mg is not yet known, it is extrapolated using the systematics to be around $E(0^+_2) = 1100(100)$ keV.

From the resulting $2^+_2 \to 0^+_2$ transition energy of 678 keV a $B(\text{E2}, 0^+_2 \to 2^+_2)$ value of 565(100) [e^{2}fm^4] is obtained using the Grodzins systematics formulated in Eq. (8.1). With this $B(\text{E2})$ value a deformation $\beta_2 = 0.59(10)$ can be extracted using Eq. (8.2).

This estimated deformation of the 0^+_2 state fits quite well with the value obtained from a microscopic calculation by T.R. Rodriguez and J.L. Egido [ROD08] in the Beyond Mean Field approach as described later on in this section.

8.1.3 Extraction of 0^+ and 2^+ mixing matrix elements

In Sect. 3.3 the two-level mixing model was introduced explaining the mixing of two levels with the same spin and parity by the mixing amplitude a and the mixing matrix element V_J. An application of this model is described by P. Van Duppen et al. in Ref. [DUP90] calculating the mixing matrix elements of intruder and normal 0^+ and 2^+ states in the $^{196-200}$Pb isotopes. This analysis in the framework of the phenomenological two-level mixing model is based on Eq. (3.11), leading to an expression for the (larger) mixing amplitude

$$1 - a^2 = \frac{1}{1 + \left(\frac{V}{E_1} - E_I\right)^2}. \tag{8.3}$$

This expression corresponds to Eq. (3.14) derived earlier for the (smaller) mixing amplitude.

		ΔE_p [keV]	ΔE_u [keV]	R	a_J	V_J [keV]
theo.	$0_2^+ \to 0_1^+$	1789	~ 1590	7.9	0.12	200 [UTS99]
exp.	$0_2^+ \to 0_1^+$	1789	~ 1700	5.5(24)	0.179(83)	309(135)
exp.	$2_2^+ \to 2_1^+$	985	~ 935	5.5(24)	0.179(83)	170(74)

Table 8.2: Resulting mixing amplitudes and mixing matrix element V_J for the mixing of the $0_{1,2}^+$ and $2_{1,2}^+$ states. Also a theoretically calculated mixing matrix element V_0 by Utsuno et al. [UTS99], already introduced in Sect. 5.2, is shown.

The mixing amplitude of the $0_{1,2}^+$ states was experimentally deduced to be $a_0 = 0.179(83)$. This result allows to derive the mixing matrix elements in ^{30}Mg using Eq. (3.12 - 3.14). Tab. 8.2 shows the resulting mixing matrix element V_0 for the mixing of the $0_{1,2}^+$ states. Also a theoretically calculated mixing matrix element by Utsuno et al. [UTS99], already introduced in Sect. 5.2, is shown, which agrees reasonably well with our experimentally determined value.

Eq. (8.1) corresponds to the global parameterisation of the Grodzins systematics derived from a fit spanning the whole mass range. However, using a local fit in the relevant mass range $A \approx 30$ allows to reduce the error of the Grodzins prediction from ~ 17 % of the global fit to about 10 % in case of the local systematics (as can be seen from Fig. IV of Ref. [RAM01]).

When aiming at an extraction of the mixing between the $0_{1,2}^+$ and $2_{1,2}^+$ states from our data in ^{30}Mg using a similar procedure, two different scenarios can be pursued:

In the first case we assign the 2467 keV state in ^{30}Mg as being the deformed 2_2^+ intruder state on top of the 0_2^+ state at 1789 keV, leading to the deformed $2_2^+ \to 0_2^+$ transition energy of 678 keV already included in Fig. 8.2. This interpretation is supported by the smooth systematic behaviour of the deformed $2_2^+ \to 0_2^+$ transitions in the Mg isotopic chain as shown in Fig. 8.2. However, strong doubts may arise from the at present non-observation of this transition. Nevertheless, when following the above assumption on the 2_2^+ energy and assuming the mixing amplitude a of the $2_{1,2}^+$ states to be the same as for the $0_{1,2}^+$ states, the mixing matrix element can be determined to be $V_2 = 170(74)$ keV.

On the other hand, as mentioned above, no 678 keV transition has been observed so far, raising strong doubts about the deformed 2_2^+ interpretation of the 2467 keV level. It could as well be an excited 2^+ state in the normal deformed potential minimum (e.g.

of two-phonon excitation character), while the population of the 2_2^+ intruder state is inhibited by the β decay properties. In this scenario we are still able to quantify the mixing amplitude between the $2_{1,2}^+$ states in the two potential minima by exploiting the predictions obtained from the Grodzins systematics as described in paragraph 8.1.2. As can be seen from Tab. 8.1, the measured $B(E2, 0^+ \rightarrow 2^+)$ values are reproduced within an uncertainty of ~ 10 % by the Grodzins systematics. This remarkable quality of the systematical prediction can only be explained by a rather weak coupling between the two potential minima, since otherwise larger mixing would lead to stronger deviations between calculated and measured $B(E2)$ values. In turn the deviation between the two of about 10 % can be used to quantify the upper limit of the mixing amplitude between the (spherical) 2_1^+ and (deformed) 2_2^+ states.

According to Eq. 3.22 the squared mixing amplitude a^2 correlates with the squared deformation parameter β^2, which according to Eq. (8.2) linearly depends on $B(E2)$. Therefore a deviation between calculated and measured $B(E2)$ values of 10 % as discussed above corresponds to a mixing value of the 2^+ mixing amplitude of $a_2 = 0.3$. Taking into account the 10 % accuracy of the Grodzins predictions in the $A \approx 30$ mass range finally allows to conclude a 2^+ mixing amplitude of $a_2 = 0.15(15)$.

This small mixing amplitude turns out to be of the same order of magnitude as derived for the $0_{1,2}^+$ mixing ($a_0 = 0.179(83)$), thus justifying the assumption made in the first scenario. As derived for the 0^+ states, also a weak mixing between the 2^+ states and thus pure states in the two potential wells are found.

8.2 Microscopic Calculations

As already mentioned in Sect. 2.2, microscopic theoretical calculations are necessary to interpret the experimental values. In such calculations the excitation energies of the states are obtained. The wave function itself is also calculated, which allows to get a more detailed picture on the nuclear structure. It also gives input to interpret the experimental values, which will be demonstrated later on in this section.

In Tab. 8.3 experimental values and theoretical values in ^{30}Mg and ^{32}Mg are shown. The experimental values for the excitation energies are taken from [ENS07], the $B(E2; 0_1^+ \rightarrow 2_1^+)$ values for ^{30}Mg and ^{32}Mg are published in [NIE05] and [SCH05], respectively, and the $B(E2; 0_2^+ \rightarrow 2_1^+)$ value and the $\rho^2(E0)$ value was measured in this experiment (see Sect. 7.5.2). The Relativistic Mean Field calculations (RMF) were performed by T. Nikšić and P. Ring [NIK08], while the Beyond Mean Field ("Gogny") results originate from calculations by T.R. Rodriguez and J.L. Egido [ROD08]. The results of these calculations will be discussed and compared to the experimental data in the following sections.

E [keV]	^{30}Mg			^{32}Mg	
B(E2) [e^{2}fm^4]	exp.	RMF [NIK08]	Gogny [ROD08]	exp.	Gogny [ROD08]
$E(0_2^+ - 0_1^+)$	1789 [ENS07]	4089	2110	$-$	2600
$E(2_1^+ - 0_1^+)$	1482 [ENS07]	2440	2030	855 [ENS07]	1350
$B(\text{E2}; 0_2^+ \to 2_1^+)$	53(7)	$-$	181.5	$-$	56.5
$B(\text{E2}; 0_1^+ \to 2_1^+)$	241(31) [NIE05]	306	334.6	454(78) [SCH05]	455.7
ρ^2(E0)	$26.2(7.5) \cdot 10^{-3}$	$15 \cdot 10^{-3}$	$46 \cdot 10^{-3}$	$-$	$41 \cdot 10^{-3}$

Table 8.3: Experimental and theoretical values for spectroscopic properties in ^{30}Mg and ^{32}Mg are shown. The experimental values for the excitation energies are taken from [ENS07], the $B(\text{E2}; 0_1^+ \to 2_1^+)$ values for ^{30}Mg and ^{32}Mg are published in [NIE05] and [SCH05], respectively, and the $B(\text{E2}; 0_2^+ \to 2_1^+)$ value and the ρ^2(E0) value was measured in this experiment (see Sect. 7.5.2). The Relativistic Mean Field calculations (RMF) were performed by T. Nikšić and P. Ring [NIK08], while the Beyond Mean Field results originate from calculations by T.R. Rodriguez and J.L. Egido [ROD08].

8.2.1 Relativistic Mean Field Approach

The results presented in this paragraph have been calculated by T. Nikšić and P. Ring within the Relativistic Mean Field approach.
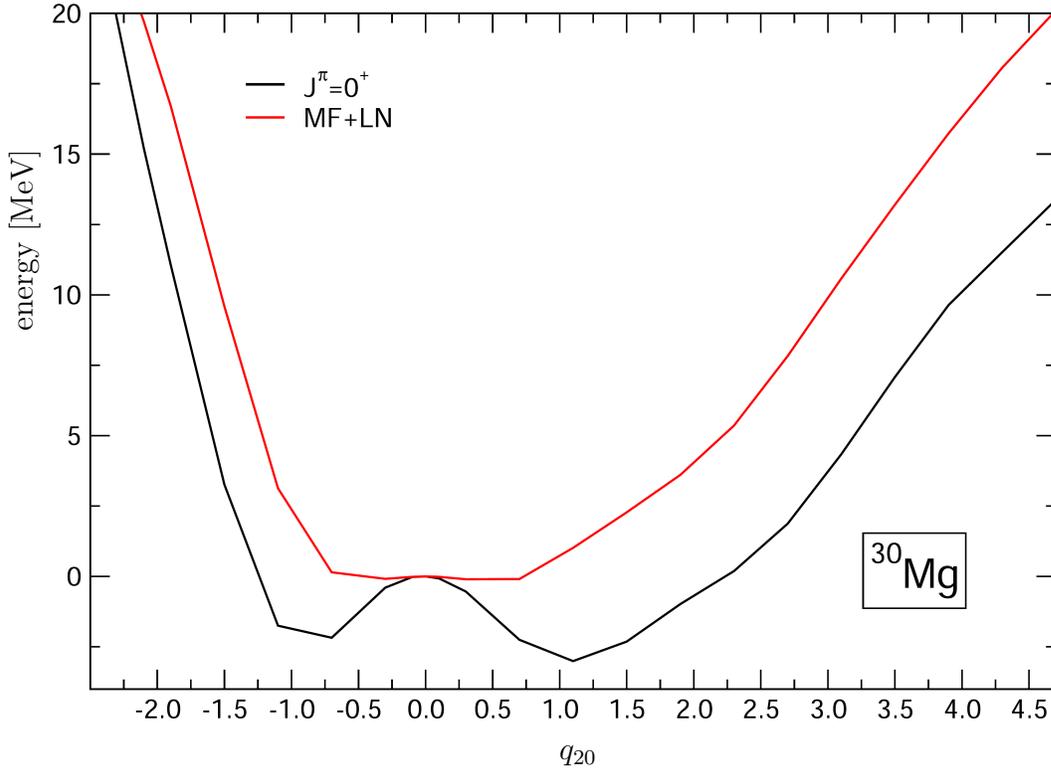
Figure 8.3: The energy surface obtained from a particle number projection in Lipkin-Nogami approximation is shown (red curve) as a function of the quadrupole deformation q_{20}. Also the angular momentum and particle number projected energy surface is displayed for $J = 0^+$ (black curve).

In Fig. 8.3 the energy surface obtained from a particle number projection in the Lipkin-Nogami approximation [NG74] is shown (red curve). Also the angular momentum and particle number projected energy surface is displayed for $J = 0^+$ (black curve).

Tab. 8.3 shows the excitation energies and the $B(\text{E2}; 0_2^+ \rightarrow 2_1^+)$ value calculated in the Relativistic Mean Field (RMF) model. The excitation energies of the 2_1^+ state and the 0_2^+ state turn out to overestimate the experimental values by about a factor of two, while the calculated $B(\text{E2}; 0_2^+ \rightarrow 2_1^+)$ value agrees rather well with the experimental value. The calculated monopole strength $\rho^2(\text{E0})$ differs only by a factor of 2 from the experimental value.

8.2.2 Gogny Approach

The results presented here have been calculated by T.R. Rodriguez and J.L. Egido [ROD08]. They are similar to the calculations presented in [RG02a], using the same interaction. Only the theoretical approach including particle number projection in the variation after projection (VAP) on the Hartree-Fock Bogoliubov (HFB) and the generator coordinate method (GCM) level is more involved.

The results of these calculations for ^{30}Mg are listed in Tab. 8.3 and compared to experimental values. The calculated excitation energy of the 2^+_1 state and the 0^+_2 state agree reasonably well with the experimental values. Also the calculated $B(E2)$ values are in reasonable agreement with experimental data. However, the value of $\rho^2(E0) = 46 \cdot 10^{-3}$ is clearly overestimating the experimental result, it can still be qualified as relatively small (compared for example to $\rho^2(E0) = 305(40) \cdot 10^{-3}$ in ^{24}Mg [WOO99]), indicating that this theoretical approach also predicts small mixing and that we can rely on it to interpret the experimental findings (see also the discussion of the triaxial calculations below).

In Fig. 8.4 the panels (a) and (b) show the results of the BMFA calculation for the 0^+ states and the 2^+ states in ^{30}Mg, respectively, while the panels (c) and (d) display the respective states in ^{32}Mg. The results obtained after each of the three steps of the calculation (see section 2.6.2) are described as follows:

1. In all four panels the dotted black lines represent the HFB (VAP) energy according to Eq. (2.32) as a function of the deformation parameter β. The deformation parameter β correlates with the quadrupole deformation q_{20} (as it was used in the RMF calculations shown in Fig. 8.3) via Eq. (2.2) from [RIN80]

$$q_{20} = \sqrt{\frac{16\pi}{5}} \frac{3}{4\pi} Z e R_0^2 \beta \qquad (8.4)$$

   with the radius R_0^2 of a sphere with the same volume. The energy of the calculated 0^+_1 state in Fig. 8.4 is set to zero and all other energies are referred to this level.

2. Since the wave functions determined in the first step (see Sect. 2.6.2) are not eigenstates of the angular momentum operator, the wave functions are projected onto the angular momentum. The continuous black line in Fig. 8.4 (a) and Fig. 8.4 (c) correspond to the $J = 0$ angular momentum projected energy surfaces according to Eq. (2.35) and the dashed line in Fig. 8.4 (b) and Fig. 8.4 (d) to the $J = 2$ projection, respectively. This demonstrates the effect of the angular momentum projection.

3. In Fig. 8.4 (a) and Fig. 8.4 (c) the blue dashed-dotted line corresponds to the wave function of the 0^+_1 state, while the blue dashed line represents the 0^+_2 state in ^{30}Mg (a) and ^{32}Mg (b), respectively. In Fig. 8.4 (b) and Fig. 8.4 (d) the red dashed-dotted line corresponds to the wave function of the 2^+_1 state. These
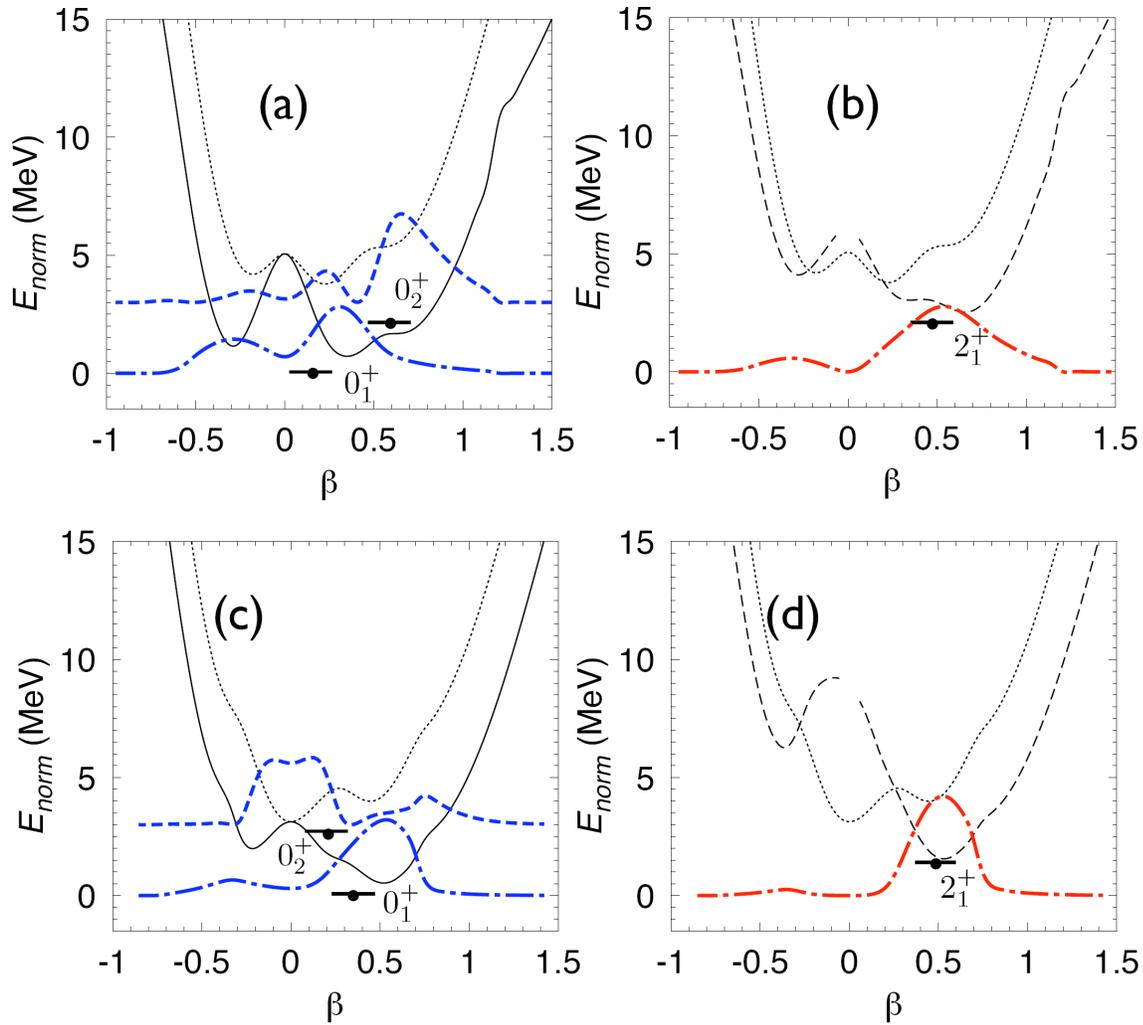
Figure 8.4: Energy curves for ^{30}Mg (panels (a) and (b)) and ^{32}Mg (panels (c) and (d)).
The black dotted lines correspond to Hartree-Fock-Bogoliubov (HFB) cal-
culations in the "variation after projection" (VAP) approach. The continu-
ous black line in the panels (a) and (c) represents the $J = 0$ energy surface,
the blue dashed-dotted line represents the probability density of finding the
0_1^+ state with a given deformation β and the blue dashed line represents
the probability density of the 0_2^+ state. In the panels (b) and (d) the black
dashed line represents the $J = 2$ energy surface and the red dashed-dotted
line the probability density of the 2_1^+ state. These calculations were done
by T.R. Rodriguez and J.L. Egido [ROD08].

coloured lines represent the probability density of finding the state with a given
deformation β.

In these plots the main components of the configuration mixing in terms of the

deformation can be seen. The bullets in Fig. 8.4 (a) and Fig. 8.4 (c) correspond to the energy and intrinsic deformations of the 0_1^+ and 0_2^+ state and thus to the eigenstates $E^{N,Z,J,\sigma}$ of Eq. (2.36) for $J = 0$ and $\sigma = 1$ and 2, respectively. The bullets in Fig. 8.4 (b) and Fig. 8.4 (d) represent the excitation energy and intrinsic quadrupole moment of the first 2_1^+ state.

Looking at the probability density of the 0_1^+ state and the 2_1^+ state, it can be seen, that the main contribution to the $B(\text{E2})$ value is provided by the prolate peak ($\beta > 0$) with a small contribution of the oblate one ($\beta < 0$). This explains the extraction of a large deformation $\beta = 0.39$ from the $B(\text{E2})$ value in the rigid rotor model, which identifies this deformation as the intrinsic prolate one.

In order to calculate the real intrinsic deformation of the 0_1^+ ground state, the product of the squared modulus of the wave function and the deformation parameter is integrated over the deformation. In this case a significantly smaller deformation parameter $\beta = 0.16$ is obtained. This result obviously originates from the negative contribution of the oblate bump of the probability density of the 0_1^+ state in ^{30}Mg to the sum.

In ^{32}Mg the wave functions of the 2_1^+ state and the 0_1^+ state look very similar. Both are well deformed prolate configurations, confirming that both are members of a rotational band. For the monopole strength $\rho^2(\text{E0},^{30}\text{Mg}) = 46 \cdot 10^{-3}$ was calculated, clearly overestimating our experimental result. Looking at the literature (see for example [BEN06]) reveals that also large deviations compared to the experimental value are obtained for this type of calculations in other mass regions. As mentioned in the references [BOU03] and [PET00], the results of a $\rho^2(\text{E0})$ calculation are very sensitive to small variations of the matrix elements of the interaction. In particular they strongly depend on small admixtures of different shapes, which means that $\rho^2(\text{E0})$ is much more sensitive to the composition of the wave functions than to other observables like $B(\text{E2})$ transition probabilities. This is obviously due to the strong dependence on the deformation β shown in Eq. (3.22).

The measurement of the E0 decay is very important in limiting situations like the one we are interested in, in which two configurations compete for the ground and first excited state. In the 'Island of Inversion' the deformed configuration based on two neutrons being excited from the $\nu d_{3/2}$ to the intruder orbital $\nu f_{7/2}$ behaves in parallel with the normal spherical one as illustrated by the well-known case of ^{32}Mg, where the intruder state even becomes the ground state. In such a situation of competing configurations and in the absence of mixing one expects either a deformed 0_1^+ and a nearly spherical 0_2^+ state or the other way around. Since the E0 operator is a 'single particle' one, one expects in both cases small values of the monopole matrix element $\rho^2(\text{E0})$. If configuration mixing is present, somewhat larger values of $\rho^2(\text{E0})$ can be expected. In ^{30}Mg the small experimental value of $\rho^2(\text{E0}) = 26.2(7.5) \cdot 10^{-3}$ indicates the absence of mixing. However, the main question which remains to be answered is the nature of the two 0^+ states and if appropriate the amount of mixing of the $\nu d_{3/2}$ and $\nu f_{7/2}$ configuration. Concerning the 0_1^+ state there are strong experimental

[PRI99, NIE05] and theoretical [CAU01, RG02a, OTS04] indications that in ^{30}Mg the inversion has not yet taken place.
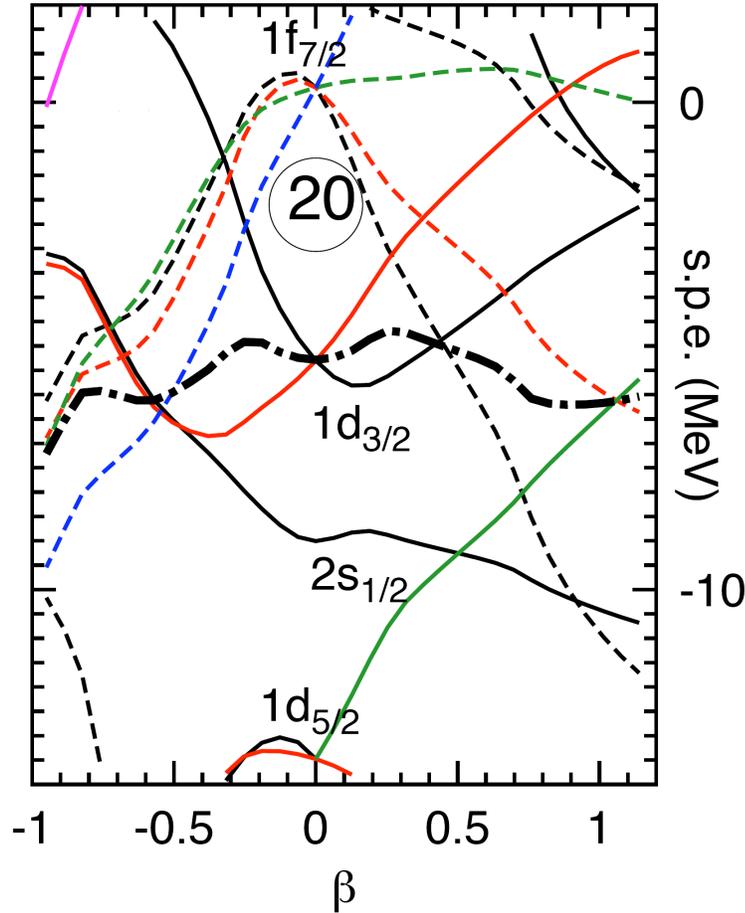
Figure 8.5: Neutron single-particle energies for ^{30}Mg. The thick dashed-dotted line represents the Fermi energy E_F, which indicates the maximum energy allowing to fill up the single-particle levels (calculated by T.R. Rodriguez and J.L. Egido [ROD08]).

In Fig. 8.5 the neutron single-particle energies are shown for ^{30}Mg. The thick dashed-dotted line represents the Fermi energy E_F, which indicates the maximum energy allowing to fill up the single-particle levels. The two minima at moderate deformation in Fig. 8.4 a) correspond to the two minima of the single-particle energies of the $\nu d_{3/2}$ orbitals just below the Fermi energy, while a shoulder appears at deformations at which two neutrons already occupy the $\nu f_{7/2}$ orbital. This is not the case in ^{32}Mg as shown in [RG02a]. The angular momentum projection provides an additional energy lowering with respect to the particle number projected energy, see the continuous line in Fig. 8.4 a), and finally configuration mixing leads to the 0_1^+ and 0_2^+ states positioned in the E $- \beta$ plane according to their energy and average deformation. The composition of the

wave functions of these two states, i.e., the weights of the corresponding β values being admixed, indicates the character of the state. We can see that the 0_1^+ state (dotted-dashed line) is a mixture of prolate and oblate $\nu d_{3/2}$ configurations which average to a small intrinsic deformation of $\beta = 0.16$. The 0_2^+ state, on the other hand, is a well deformed state with $\beta = 0.59$ consisting to a large part of a $\nu f_{7/2}$ configuration with very small admixtures of the $\nu d_{3/2}$ configurations. This interpretation is quite consistent with the experimental finding of a very small matrix element connecting both levels.

The presented BMFA calculations [ROD08] have been performed in an axially symmetric configuration space, which means that the γ degree of freedom has not been included. All calculations were executed with $\gamma = 0$, including only prolate and oblate shapes. This restriction is due to the complexity of a triaxial angular momentum projection compared to the axially symmetric one-dimensional calculation. The γ degree of freedom after angular momentum projection cannot be calculated yet. It can only be calculated at the level of Hartree-Fock-Bogoliubov calculations including particle number projection. However the then missing final step of angular momentum projection may completely change the resulting shape of the $\beta - \gamma$ plane.

The results of these axially symmetric calculations, plotted in the usual way by showing a contour plot in the $\beta - \gamma$ plane, are shown in Fig. 8.6 for ^{30}Mg (left) and ^{32}Mg (right). Following the $\gamma = 0$ and the $\gamma = 60$ axis it can be seen that the values correspond to the dotted lines of the energy curves of Fig. 8.4 for ^{30}Mg and ^{32}Mg, respectively. For ^{30}Mg the deformations, where the 0_1^+ and the 0_2^+ states develop, are situated around $\beta_1 = 0.25$ and $\beta_2 = 0.55$, respectively. These points are marked by crosses in Fig. 8.6. Two important observations have to be mentioned concerning the calculated $\rho^2(E0)$ value: first one has to realise in Fig. 8.6 that the equipotential lines at large deformations are very stiff in the direction perpendicular to the $\gamma = 0°$ axis, while second ^{30}Mg turns out to be γ soft at small deformations.

It is obvious that allowing for the γ degree of freedom in the GCM calculations the wave functions of the 0_1^+ state will extend further out towards $\gamma \approx 30°$ and the one of the 0_2^+ state – following the equipotential contour – will also shift to triaxial shapes. In Fig. 8.6 (left) two stars are placed in the centre of the probability distribution of both wave functions. A rough estimate of the change on the calculated $\rho^2(E0)$ value caused by the change of the γ degree of freedom leads to trend towards a smaller value of $\rho^2(E0)$.

In the case of ^{32}Mg the γ degree of freedom plays a much less important role, because this nucleus favours axially symmetric shapes. Therefore the calculated $\rho^2(E0)$ value in ^{32}Mg is expected to better predict the result of a future experiment in this isotope (see Sect. 9).
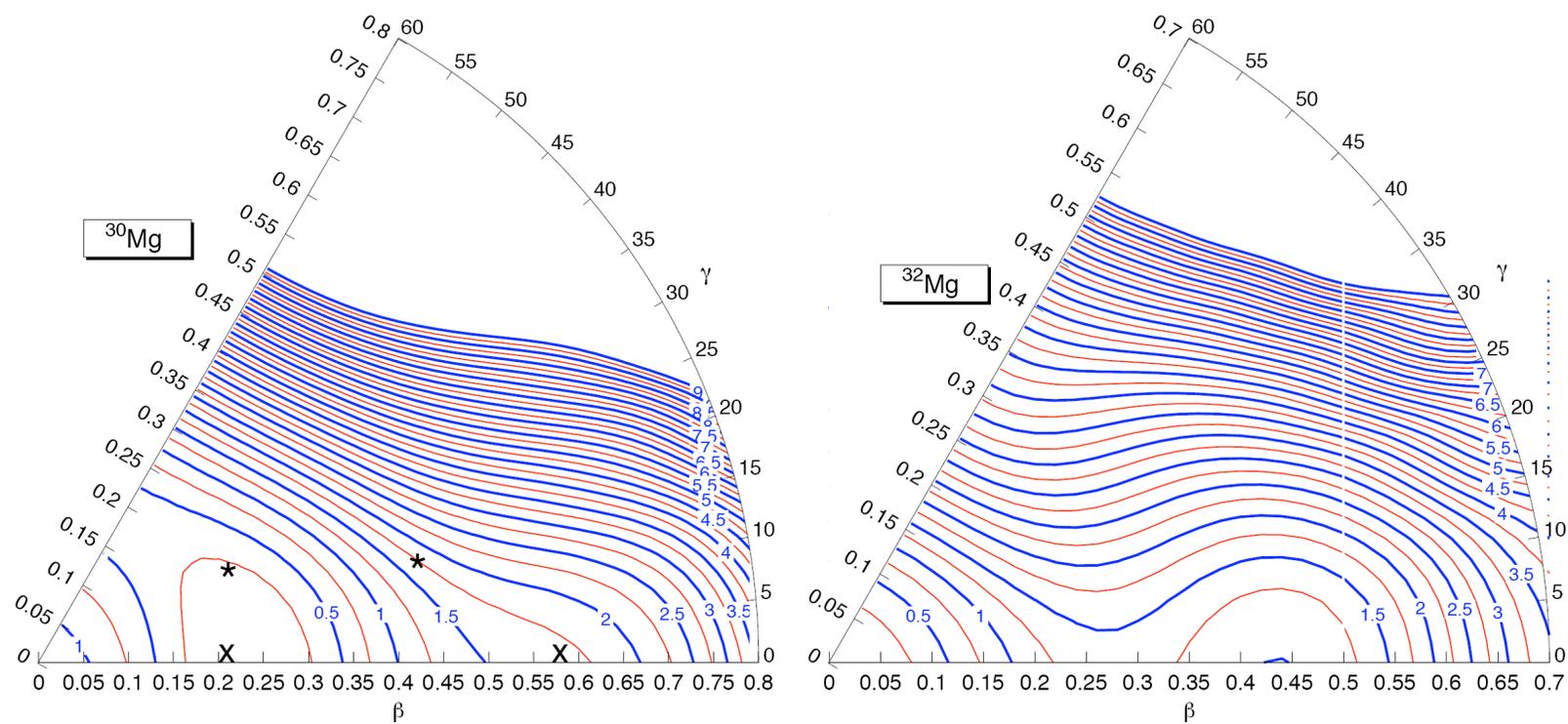
Figure 8.6: Contour plot for ^{30}Mg (left) and ^{32}Mg (right) in the (β, γ) plane [ROD08]. Each contour line amounts to an energy difference to its neighbour of 250 keV.

8.3 Conclusion

In a sequence of several conversion electron experiments at ISOLDE with continuously increased suppression of the large background from β decay electrons ($Q_\beta(^{30}Na) = 17.3$ MeV) the 1789 keV level in ^{30}Mg could be identified as the (deformed intruder) 0_2^+ state. The suppression of the background was realised by building a target chamber made of low-Z material (aluminium) coated inside with an electron absorber (Teflon). The setup was optimised using GEANT4 simulations and offline measurements using ^{152}Eu and ^{90}Y electron sources. The conversion electrons were measured in coincidence with β decay electrons using a Mini-Orange spectrometer. Using this highly sensitive setup the weak E0 transition depopulating the 0_2^+ state in ^{30}Mg could be identified for the first time. The electric monopole strength extracted from the measurement of the $0_2^+ \rightarrow 0_1^+$ E0 transition is $\rho^2(E0) = 26.2(7.5) \cdot 10^{-3}$, corresponding to an intensity of the E0 transition of $I(E0) = 2.0(4) \cdot 10^{-5}$ and a partial E0 lifetime of $\tau(E0) = 396(113)$ ns. This result allows for the first time to deduce the mixing amplitude between shape-coexisting 0^+ states near the 'Island of Inversion' in a two-level mixing model as $a = 0.179(83)$ and represents the first unambiguous experimental identification of an E0 back decay from e deformed second potential minimum into the normally deformed first well.

Microscopic configuration mixing calculations performed by T.R. Rodríguez and J.L. Egido in the Beyond Mean Field approach allow to characterise the configurations of the 0^+ states. The 0_1^+ ground state is a mixture of prolate and oblate $\nu d_{3/2}$ configurations which average to a small intrinsic deformation of $\beta = 0.16$. The 0_2^+ state, on the other hand, is a well deformed state with $\beta = 0.59$, consisting to a large part of a $\nu f_{7/2}$ configuration with very small admixtures of the $\nu d_{3/2}$ configurations. This interpretation is quite consistent with the experimental finding of a very small matrix element connecting both levels.

In the BMFA calculation done by L. Egido the 0_1^+ ground state of ^{30}Mg turns out to be almost spherical ($\beta = 0.16$) and the 0_2^+ state turns out to be strongly deformed. In contrast to ^{30}Mg the ground state in ^{32}Mg is strongly deformed ($\beta = 0.51$). Also the wave functions of the 0_1^+ state and the 2_1^+ state look very similar. Both are well deformed prolate states confirming that both are members of a rotational band. The wave function of the 0_2^+ state corresponds to a spherical nucleus clearly showing an inversion of states.

9 Outlook

9.1 Improvement of the experimental setup

Since the suppression of background surviving the coincidence condition turned out to be the key issue of the experiment, an improvement could be achieved by placing the Si(Li) detector further away from the centre of the target chamber in order to reduce the sensitivity to Compton scattered electrons.

This could be realised by replacing the present Mini-Orange inside the target chamber by a quadrupole channel consisting of magnetic lenses made of permanent magnets guiding the electrons towards the detector surface at a remote position with respect to the interior of the target chamber. Such miniature lenses have been developed and successfully tested in the framework of laser acceleration projects. The measured field gradient of such a lens amounts to 503 T/m [EIC07]. Fig. 9.1 shows a picture of such a miniature quadrupole magnet consisting of 12 permanent magnets arranged as a cylinder with a diameter of the central hole of 6 mm. In Fig. 9.2 a schematic view of the 12 segment Halbach design [EIC07] of one quadrupole magnet is shown. While 4
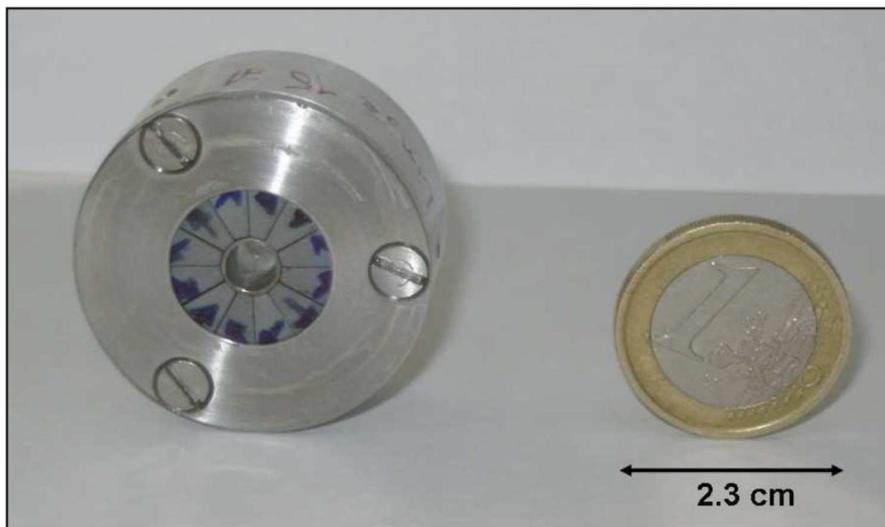
Figure 9.1: Photograph of a miniature quadrupole magnet consisting of 12 permanent magnets arranged in a cylinder with a diameter of the central hole of 6 mm. The measured field gradient amounts to 503 T/m [EIC07].
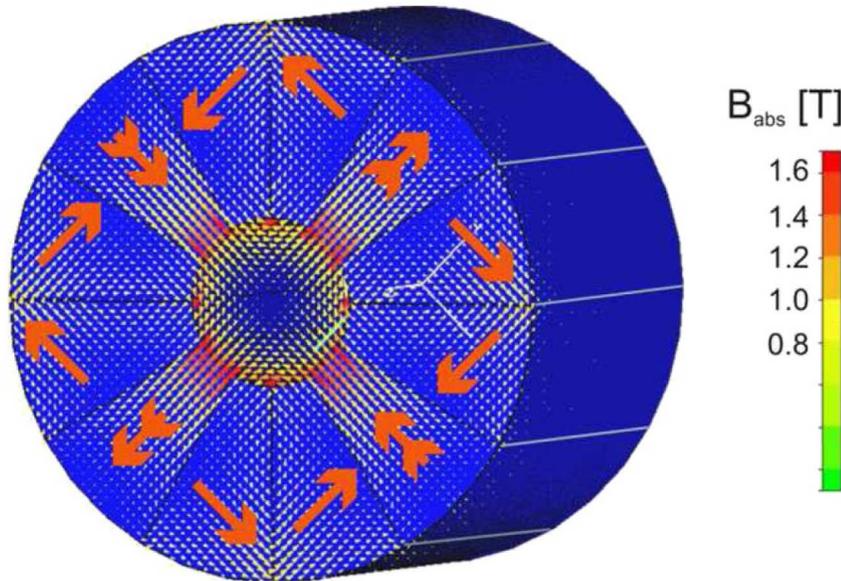
Figure 9.2: Schematic view of the 12 segment Halbach design of a magnetic quadrupole magnet. While 4 radially magnetised segments define the quadrupole field, 8 segments are used for the outer field closures. The thick arrows are indicating the direction of magnetisation. The coloured small arrows illustrate the simulated strength and direction of the resulting quadrupole field inside a bore of 6 mm diameter. The maximum field strength amounts to $B(r = 3\,\text{mm}) \sim 1.5$ T [EIC07]. CST EM Studio [CST] was used for this simulation.

radially magnetised segments define the quadrupole field, 8 segments are used for the outer field closures. The thick arrows are indicating the direction of magnetisation. The coloured arrows illustrate the simulated strength and direction of the resulting quadrupole field inside a bore of 6 mm diameter. The maximum field strength amounts to $B(r = 3\,\text{mm}) \sim 1.5$ T [EIC07]. The corresponding simulations have been performed using the program CST EM Studio [CST].

A quadrupole channel can be realised consisting of several such magnetic lenses placed along the transport axis and modified by a larger bore diameter in order to allow for a transport of electrons from the target to the detector. In order to optimise the transport efficiency of the quadrupole channel, the electrons need to be focused into the solid angle accepted by the channel. This could be achieved by a conventional Mini-Orange, ending at the central plane almost orthogonal to the axial dimension ('half Mini-Orange'). This Mini-Orange would be designed to form an (almost) parallel electron beam entering the quadrupole transport channel acceptance. Thus the Si(Li) detector could be placed in a distance of e.g. more than half a meter from the target.

Fig. 9.3 shows a simulation for 1700 keV electron trajectories e.g. in the $x - z$ plane
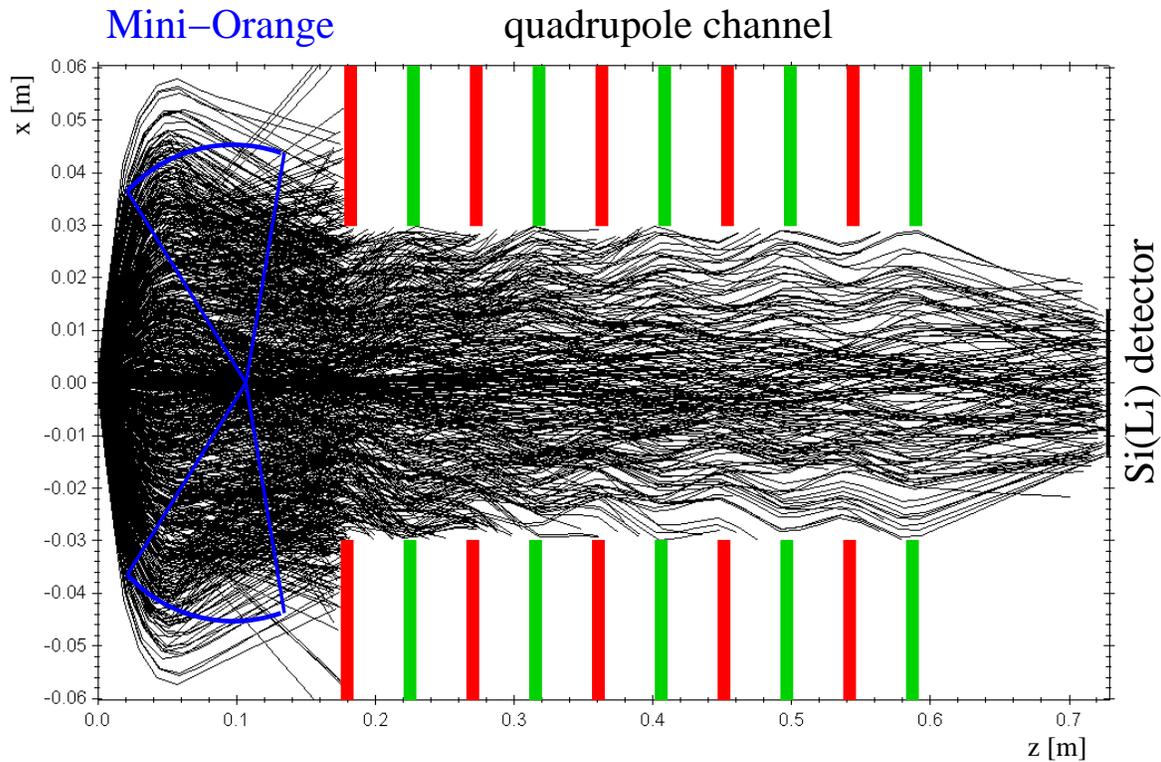
Figure 9.3: Trajectories for 1700 keV electrons transported in the x – z plane [BEC08], calculated using the simulation code CST EM Studio. A modified Mini-Orange (indicated in blue) consisting of 8 wedges was used. The Mini-Orange produces a parallel beam, which is transported by the quadrupole channel towards the detector surface. In this simulation 10 quadrupole lenses with a thickness of 10 mm were placed at a distance of 35 mm between each other. Each lens is turned by 90° around the z-axis with respect to the previous one in order to exploit the focusing and defocusing properties of a quadrupole lens for beam transport.

[BEC08] calculated with the simulation code CST EM Studio [CST]. A Mini-Orange (indicated in blue) consisting of 8 wedges similar to the one used in this experiments was used. The Mini-Orange produces a parallel beam, which is transported by the quadrupole channel towards the detector surface. In this simulation 10 quadrupole lenses with a field gradient of 6 T/m and a thickness of 10 mm were placed in a distance of 35 mm between each other. Each lens is turned by 90° around the z-axis with respect to the previous one in order to exploit the focusing and defocusing properties of a quadrupole lens for beam transport.

As it was shown in Sect. 6.3, even a very thin plastic scintillator of 200 μm thickness is sensitive to γ rays causing background surviving the coincidence condition. In order to reduce this background (in addition to the component of scattered Compton electrons that will be suppressed by a remote position of the Si(Li) detector behind the

quadrupole channel) a second quadrupole transport channel could be realised including a bend that would allow to place the plastic scintillator out of the direct view towards the target to avoid γ ray detection.

With the improved sensitivity to weak E0 or converted transitions even in the presence of strong background the presented modification of the experimental setup could grant access to spectroscopic information that so far was buried under dominant background components from γ-rays or β or Compton electrons.

Already in the β-gated electron spectrum from Fig. 7.23 structures are visible which could be attributed to a converted or E0 transition, however backing statistical significance. These structures, together with other expected electron lines from converted transitions in ^{30}Mg (like the K and L electrons from the $2_1^+ \rightarrow 0_1^+$ transition) could be studied in detail when background would be removed using the described quadrupole transport channel. Conversion coefficients could be reliably determined, allowing to resolve ambiguities in the level scheme of ^{30}Mg by an unambiguous assignment of spin and parity values. This optimised and highly sensitive electron spectroscopy technique could then also be applied in other regions of the chart of nuclides, where shape coexistence between 0^+ states of different deformation is expected, complementing the spectroscopic information attainable from γ spectroscopy studies.

9.2 E0 transition measurement in ^{32}Mg

After the successful identification of the 0_2^+ state in ^{30}Mg proving shape coexistence at the borderline of the 'Island of Inversion' it would be a natural next step to exploit the capabilities of our highly-sensitive experimental technique to study weak E0 transitions by applying it to ^{32}Mg, aiming to identify the 0_2^+ state in ^{32}Mg at the centre of the 'Island of Inversion'.

While in ^{30}Mg a clear candidate for the deformed 0_2^+ state existed from fast timing studies, in ^{32}Mg no clear spectroscopic candidate for the 0_2^+ state is presently available. So far only a broad range of theoretical predictions for the 0_2^+ state in ^{32}Mg have been published [CAU01, HEY91, RG02a] placing this state in the energy region around 2 MeV. On the other hand Fig. 9.4 displays the most recent level scheme for ^{32}Mg obtained from β decay of ^{32}Na [MAC08]. The analysis of these data is still in progress, however this data sample contains at least about a factor of 30 more statistics compared to the most recent published level scheme for ^{32}Mg from the work of Mattoon et al. [MAT07].

In addition to the 2_1^+ state at 885 keV the 2321 keV level is the obvious candidate for the 4^+ state of the ground state band. A strong β feeding to the 4817 keV and 3036 keV levels with $log ft < 5$ [KLO93] indicates that these are negative parity states. They do not deexcite to the ground state, suggesting their spins to be 3^- and 2^- (or vice versa). The deexcitation pattern of the 3552 keV and 5245 keV states imply that these are medium spin states (above 2^+ and not 2^-), certainly excluding 0^+ or 2^+.
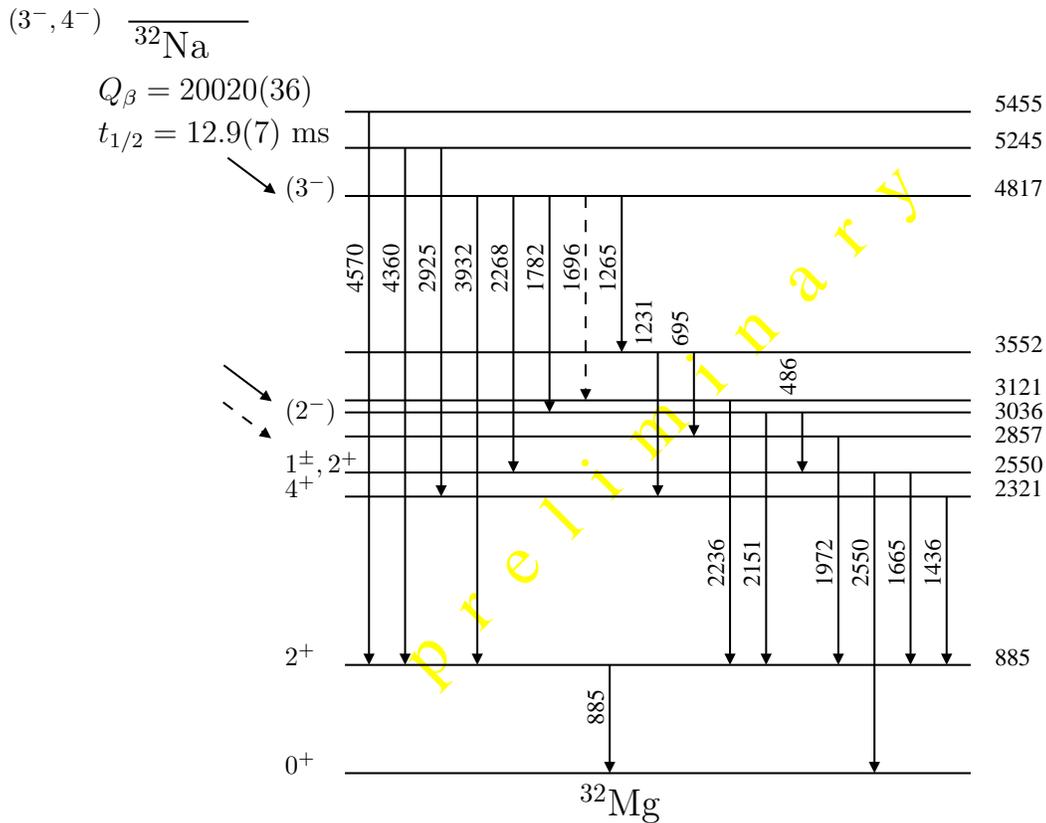
Figure 9.4: Decay scheme in ^{32}Mg as observed from β decay of ^{32}Na. Data are taken from an ongoing analysis [MAC08].

The 2857 keV state is fed by this medium spin state, again excluding this level from being a 0^+ candidate. Also the 3121 keV state cannot be a 0^+ candidate since it is fed by a 2^- or 3^- state. However, either of these two states could be the 2^+ intruder. The 2550 keV level feeds the ground state rather strongly, while only a rather weak branch to the 885 keV 2_1^+ state was observed. Thus its spin is either 1^-, 1^+ or 2^+. This state is only fed by two γ rays from the negative-parity 2^- and 3^- states, which could either result from a strong feeding of these states or due to selection rules preferring the deexcitation to the same parity states. This would imply this level to be a 1^- state. However, it could as well be a 2^+ state. In this case it could be the 2^+ state from the γ band. However, this scenario is disfavoured by the strong feeding to the ground state. On the other hand, if the 2550 keV state would be the (spherical) 2_2^+ intruder state, the ground state decay would be in agreement with this assignment.

The identification of the spherical 0_2^+ state in ^{32}Mg would mark a milestone in the study of shape coexistence in the 'Island of Inversion'. However, the success of an experimental search of this state strongly depends on the energetic position of the 0_2^+ state.

In the unfavourable case of a high-lying 0_2^+ state (i.e. above ~ 1.2 MeV) competition

of the E2 transition to the 2_1^+ state together with the limited beam intensity for ^{32}Na as presently available at ISOLDE would prevent the observation of the E0 transition. Nevertheless even in this case a lower limit could be established for the energy of the 0_2^+ state.
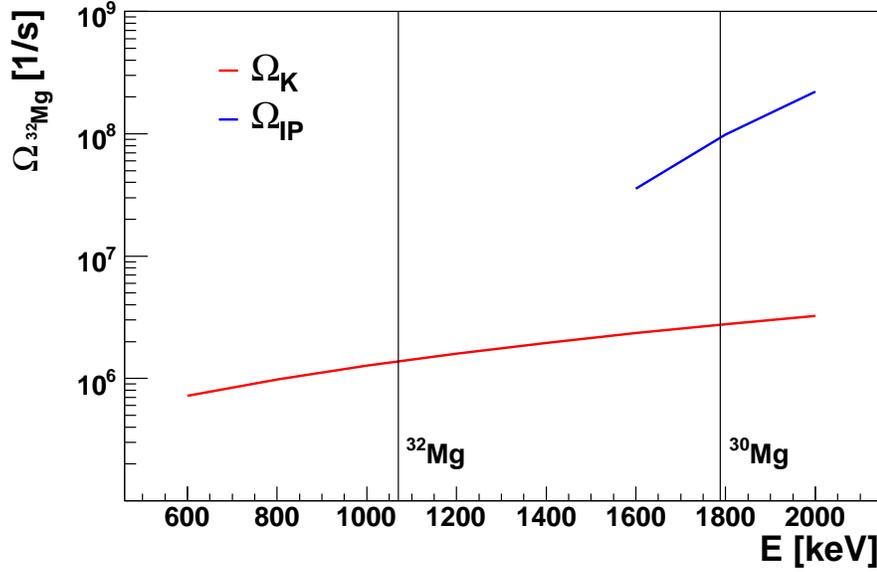
Figure 9.5: Ω_i values calculated using [PAS86] for ^{32}Mg. The Ω_i values are shown as a functions of the excitation energy of the potential 0_2^+ state.

Fig. 9.5 shows the Ω_K and Ω_{IP} values for ^{32}Mg as a function of the E0 transition energy. For transition energies larger than 1.2 MeV pair creation occurs and becomes the dominant process.

In Fig. 8.2 the systematics of $2^+ \rightarrow 0^+$ transitions in the Mg isotopic chain is shown. This is done for the transitions between strongly deformed states ($2_1^+ \rightarrow 0_1^+$) inside the 'Island of Inversion' and for isotopes located outside ($2_2^+ \rightarrow 0_2^+$). Also the spherical (or much less deformed) $2^+ \rightarrow 0^+$ transitions (^{24,26,28}Mg: [ENS07]; ^{30}Mg: [MAC05]; ^{32}Mg: [MOT95], $E(2_2^+ \rightarrow 0_2^+)$ extrapolated from ^{30}Mg with 2_2^+ assignment of the 2550 keV level; ^{34}Mg: [IWA01]; ^{36}Mg: [GAD07]) are indicated.

This picture already includes the underlying assumption used here to take the ground state transition energy from the (spherical) 2_1^+ state (1482 keV) as an indicator for the analogue (spherical) $2_2^+ \rightarrow 0_2^+$ transition in ^{32}Mg. The excitation energy of the 0_2^+ state in ^{32}Mg is extrapolated using the systematics to be around 1100(100) keV.

However, if the assignment of the 2550 keV level being the 2_2^+ state were true, then the searched spherical 0_2^+ state would be located significantly below this state. Taking the $2_1^+ \rightarrow 0_1^+$ transition energy of the neighbouring ^{30}Mg, than the search for the spherical 0_2^+ state should focus on a rather low-lying candidate around 1070 keV. In such a scenario the competing E2 transition energy to the 2_1^+ state would amount to 185 keV, thus being significantly smaller compared to the 306 keV in ^{30}Mg for the

analogue E2 transition. According to the E^5 scaling, the E2 competition to the E0 decay would be reduced by more than an order of magnitude relative to the situation in ^{30}Mg. Moreover, in ^{32}Mg the 0_2^+ state is expected to be longer-lived compared to ^{30}Mg (due to the reduced E2 competition which increases the E0 lifetime), thus reducing the contributions from prompt background if applying a delayed β-E0 coincidence gating condition. Also the shorter half-life of ^{32}Na (13.2(4) ms) compared to ^{30}Na (48.4(17) ms) would allow for a more strict gating condition, which besides improving the signal-to-background ratio would also be advantageous to discriminate against potential contributions from multiply-charged ions. In addition competition by internal pair creation will completely vanish in the case of ^{32}Mg, as can be seen from Fig. 9.5, where the electronic Ω factors for K- and L conversion as well as for internal pair creation are plotted for Mg as a function of the 0_2^+ energy [KAN95]. While for ^{30}Mg with $E(0_2^+) = 1789$ keV pair creation was dominating by an order of magnitude over conversion, in the scenario of a low-lying 0_2^+ state this contribution vanishes.
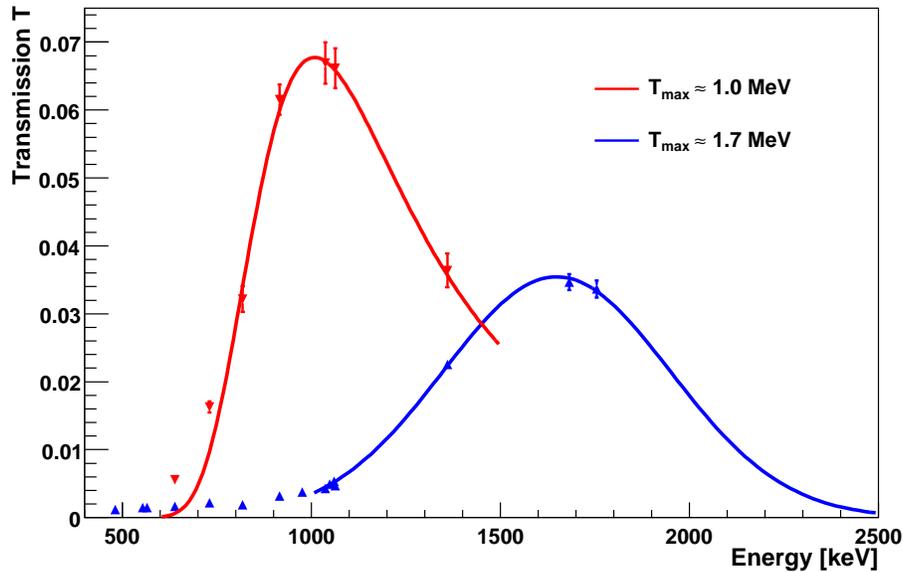
Figure 9.6: Transmission curve of the Mini-Orange transport and filter system, optimised for the measured E0 transition energy of 1788 keV from the 1789 keV 0_2^+ state in ^{30}Mg (blue curve). The red curve displays the transmission curve optimised for the search of a low-lying E0 transition energy around 1 MeV in ^{32}Mg.

In the case of ^{30}Mg the transmission curve of the Mini-Orange was optimised for the expected E0 transition energy of 1788 keV (binding energy of K-electron = 1.3 keV in ^{30,32}Mg), resulting in a detection efficiency of 3.5% at this energy, as can be seen in Fig. 9.6. Searching for a low-lying E0 transition in ^{32}Mg around 1 MeV the transmission curve can be optimised in order to achieve an improved efficiency of 7.0% as can be seen from the red curve in Fig. 9.6.

Based on a beam intensity from ISOLDE of 100 particles/s for ^{32}Na (as provided by

ISOLDE in previous studies with ^{32}Na β decay), this reduction of beam intensity by a factor of 40 relative to ^{30}Na will be partly compensated by the efficiency gain (factor 2) and the reduced E2 competition (factor 12.5). Moreover, for a low-lying 0_2^+ state no competition by internal pair production will be present, which dominated over internal conversion by a factor of 10 in ^{30}Mg. Thus scaling from our ^{30}Mg experiment we expect about 1.4 counts in the E0 peak per hour (for a ~ 1 MeV E0 transition). So in about one week sufficient statistics would be obtained to identify the E0 transition and to give a value for the monopole strength ρ^2(E0).

This conversion electron experiment would represent a complementary experimental approach to an upcoming two-neutron transfer experiment that will be performed in fall 2008 at ISOLDE to search for the 0_2^+ in ^{32}Mg [KRÖ08].

A Publications (draft)

The following publications (drafts) resulting from the experiments of this thesis have been submitted. The first paper concerning the E0 transition in ^{30}Mg has been submitted for publication to Physical Review Letters. The second paper about the corrected lifetime of the 0_2^+ state in ^{90}Zr has be submitted for publication to Physical Review C.

Shape coexistence near the neutron number N= 20:
First identification of the E0 decay from the deformed first excited $J^\pi = 0^+$ state in ^{30}Mg

W. Schwerdtfeger[1], P.G. Thirolf[1], K. Wimmer[1], D. Habs[1], H. Mach[2], T.R. Rodriguez[4],
V. Bildstein[3], J.L. Egido[4], L.M. Fraile[5], R. Gernhäuser[3], R. Hertenberger[1], K. Heyde[6],
P. Hoff[7], H. Hübel[8], U. Köster[9], T. Kröll[3], R. Krücken[3], R. Lutter[1], T. Morgan[1] and P. Ring[3]

[1] *Ludwig-Maximilians-Universität München, D-85748 Garching, Germany*
[2] *Department of Nuclear and Particle Physics, Uppsala University, SE-75121 Uppsala, Sweden*
[3] *Physik Department E12, Technische Universität München, D-85748 Garching, Germany*
[4] *Universidad Autonoma de Madrid, E-28049 Madrid, Spain*
[5] *Universidad Complutense, E-28040 Madrid, Spain*
[6] *Department of Subatomic and Radiation Physics, Universiteit Gent, B-9000, Gent, Belgium*
[7] *Department of Chemistry, University of Oslo, N-0315 Oslo, Norway*
[8] *Helmholtz-Institut für Strahlen- und Kernphysik, Universität Bonn, D-53115 Bonn, Germany*
[9] *Institut Laue-Langevin, F-38000 Grenoble, France*
(Dated: February 18, 2009)

The 1789 keV state in ^{30}Mg was identified as the first excited 0^+ state by measuring its E0 transition to the ground state. The measured small value of $\rho^2(E0, 0_2^+ \rightarrow 0_1^+) = (26.2 \pm 7.5) \cdot 10^{-3}$ implies within a two-level model a small mixing of competing configurations with largely different intrinsic quadrupole deformation near N=20. Axially symmetric configuration mixing calculations identify the ground state of ^{30}Mg to be based on neutron configurations below the $N = 20$ shell closure, while the excited 0^+ state mainly consists of a two neutrons excited into the $\nu\ 1f_{7/2}$ orbital.

PACS numbers: 23.40.-s,23.20.Nx,23.20.Js,27.30.+t

One of the most studied phenomena in the region of neutron-rich atomic nuclei around the $N = 20$ shell closure is the occurrence of strongly deformed ground states in Ne, Na and Mg isotopes. This so-called 'island of inversion' [1] finds its origin in the promotion of a pair of neutrons across the $N = 20$ shell gap, thus leading to the intrusion of deformed low-lying (2p2h) configurations compared to nuclei closer to β stability. Despite considerable efforts the precise localization of the transition from normal to intruder-dominated configurations is not yet finally settled and even the origin of the large collectivity of the $0_{gs}^+ \rightarrow 2_1^+$ transition in ^{32}Mg is still under debate [2]. A coexistence of spherical and deformed 0^+ states is predicted to exist within a small region around N=20 in the neutron-rich Mg nuclei [3, 4], the 'island of inversion'. So far studies on spectroscopic properties have focused on B(E2) values between the 0^+ ground state and the first excited 2^+ state [5–10], however, no excited 0^+ state has yet been observed in these nuclei. While ^{32}Mg, which is conventionally considered a closed-shell nucleus, exhibits a strongly deformed ground state as indicated by the large value of B(E2;$0_{gs}^+ \rightarrow 2_1^+$)=454(78)e^{2}fm^4 [5], the ground state of ^{30}Mg is expected to be much less deformed, whereas a (deformed) excited 0_2^+ state is predicted at an energy between 1.7 and 2 MeV [11–14].

It is the purpose of this Letter to report the first identification of the coexisting 0_2^+ state in ^{30}Mg using conversion electron spectroscopy and to discuss the configuration mixing between normal and intruder configurations at the border of the 'island of inversion'.
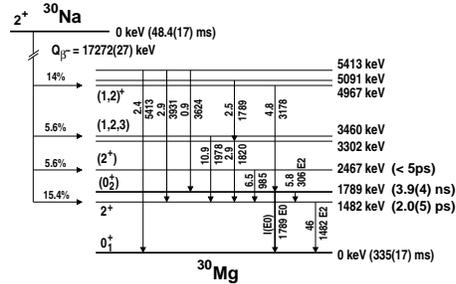
FIG. 1: Low-energy part of the level scheme of ^{30}Mg [15].

Resulting from fast timing γ-spectroscopy studies [15], the 1789 keV level in ^{30}Mg emerged as a strong candidate for the deformed first excited 0_2^+ state due to its long half-life of 3.9(4) ns and the absence of a ground state γ transition. Fig. 1 displays our present knowledge on the low-energy part of the level scheme of ^{30}Mg [15], triggering our search for the deformed 0_2^+ state in ^{30}Mg via conversion electron spectroscopy following β decay of ^{30}Na at the ISOLDE facility at CERN [17]. In contrast to earlier publications [15], according to new high-statistics experimental data no imbalance between feeding and de-excitation of the 1789 keV level exists any more [16]. The radioactive ^{30}Na atoms [$t_{\frac{1}{2}} = 48.4(17)$ ms] were produced by sending 1.4 GeV protons provided by the CERN PS Booster with an intensity up to $3.2 \cdot 10^{13}$ p/pulse onto a
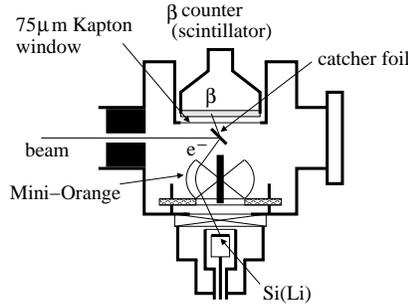
FIG. 2: Sketch of the experimental setup (top view). The Germanium detector that was mounted vertically on top of the target chamber is not shown.

FIG. 3: a) Background-subtracted electron spectrum measured in coincidence with signals in the plastic detector, gated on time differences ≤ 200 ms between the proton pulse and the β decay signal. Also shown is the transmission efficiency of the MO spectrometer as derived by a fit through the data points (black circles) obtained from individual converted transitions in calibrated sources (see text). b) Expanded view to the electron spectrum around the E0 transition in ^{30}Mg.

UC_x/graphite target (heated to $\sim 2050^oC$). On average every second pulse (average repetition period of 2.4 s) was used. The reaction products diffusing out of the target were surface-ionized and the extracted 1^+ ions were mass separated by the ISOLDE High Resolution Separator at a kinetic energy of 40 keV. This $A = 30$ beam was sent to the experimental setup (see Fig. 2). The beam was stopped in the center of the target chamber in a 0.1 mm thick Al foil to examine the β decay of ^{30}Na to excited states of ^{30}Mg. In order to detect the E0 decay electrons with high resolution (3.0 keV FWHM) a liquid nitrogen cooled Si(Li) detector (active surface: 500 mm^2, thickness: 5 mm) was used. The detector was operated in conjunction with a magnetic transport and focusing system consisting of 8 wedge-shaped ($Nd_2Fe_{14}B$) permanent magnets ('Mini-Orange', MO) [18]. They create a toroidal magnetic field (B$\sim$160 mT) arranged around a central Pb absorber (diameter: 16 mm, length: 50 mm) that blocks γ rays from the catcher foil. Towards the catcher foil the absorber was covered by a Cu cap to suppress X-ray production. The transmission efficiency of the spectrometer was 1.8(2) % at 1.788 MeV, optimized for the expected E0 transition in ^{30}Mg. A 0.2 mm thick plastic scintillator (BC-404, diameter 50 mm) read out by a 2" photomultiplier tube was mounted at a distance of 13 mm to the target, resulting in a solid angle coverage of $\Omega/4\pi = 21$ %. This detector served as trigger on β-decay electrons and was operated in coincidence with the Mini-Orange spectrometer. In order to identify the beam composition and for normalization purposes γ rays following the β decay were detected using a Ge detector mounted on top of the target chamber. In order to achieve optimum sensitivity for the expected weak E0 transition, the dominant coincident background from Compton electrons due to the large Q value of the ^{30}Na β decay (17272(27) keV) was reduced by covering the inside of the Al target chamber by 15 mm thick Teflon plates in order to absorb Compton-scattered electrons. The germanium detector served as monitor of the $A = 30$ beam

composition, which turned out to consist almost entirely of ^{30}Na at a total intensity of 4100 decays/second. Since the halflife of ^{30}Na decay is much shorter compared to ^{30}Mg or ^{30}Al originating from the β decay chain, during the analysis events occurring within a time window of 200 ms after proton impact on the ISOLDE target were selected to enhance the contribution from the short-lived ^{30}Na. The resulting electron spectrum detected with the Si(Li) detector in coincidence with β-decay electrons (coincidence window: 40 ns, threshold of β detector: 300 keV, time resolution of Si(Li) detector: 8 ns) is shown in Fig. 3. The upper panel a) displays the spectrum over a wide energy range, together with the transmission efficiency curve of the MO spectrometer (solid line), that has been derived by a fit through the data points (black circles) obtained from measurements of individual converted transitions using calibrated ^{152}Eu and ^{207}Bi sources. Below the transmission maximum coincident background yield remains from both the β decay energy spectrum (rapidly increasing with lower β-electron energy) and Compton electrons (Q_β =17.3 MeV). In Fig. 3b) the $0_2^+ \rightarrow 0_1^+$ E0 transition at 1788 keV is visible. 201(50) (background-corrected) counts were detected in the peak during 143 hrs of beamtime. With an energy

resolution of 3.0 keV for the Si(Li) detector spanning K and L conversion in ^{30}Mg (E_K =1.3 keV), the monopole strength ρ^2(E0) can be determined by the ratio of E0 (K+L) conversion intensity to the E2 γ intensity and the γ lifetime τ_γ of the 0_2^+ state as [19]

$$\rho^2(\text{E0}) = \frac{I_{\text{K+L}}(\text{E0})}{I_\gamma(\text{E2})} \cdot \frac{1}{\Omega_{\text{K+L}}(\text{E0})} \cdot \frac{1}{\tau_\gamma}. \qquad (1)$$

The γ yield of the E2 transition at 306 keV measured with the β - γ coincidence condition (width: 50 ns) using the Ge detector (threshold: 60 keV, time resolution: 20 ns) is N_γ(E2) = $5.37(4) \cdot 10^4$, resulting in an efficiency-corrected intensity $I_\gamma = N_\gamma/\epsilon_\gamma = 2.768(20) \cdot 10^7$ (ϵ_γ = 0.00194). The half-life of the 0_2^+ state was measured to be 3.9(4) ns [15] (i.e. $\tau_\gamma \approx \tau$ =5.6(6) ns) and the electronic Ω factor is $\Omega_K = 2.752 \cdot 10^6$/s [20]. This results in a square of the monopole transition strength $\rho^2(E0) = 26.2(75) \cdot 10^{-3}$. From the measured intensity ratio $I_{K,L}$(E0)/I_γ(E2) and the known intensity I_γ(E2) with respect to β decay of ^{30}Na the E0 intensity was determined as $I(E0) = 2.0(4) \cdot 10^{-5}$. The partial E0 lifetime (including internal pair creation) was derived as $\tau(E0) =$ 396(113) ns. As will be shown, a small ρ^2(E0) indicates weak coupling between the two potential minima.

In the 'island of inversion' the deformed configuration based on two neutrons being excited from the $\nu\, 1d_{3/2}$ to the intruder orbital $\nu\, 1f_{7/2}$ keeps pace with the normal spherical one as illustrated by the case of ^{32}Mg, where the intruder state even becomes the ground state. In such a situation of competing configurations and in the absence of mixing one expects either a deformed 0_1^+ and a nearly spherical 0_2^+ state or vice versa. Since the E0 operator is a *single particle* one, one expects in both cases small values of the monopole matrix element and hence for the transition strength ρ^2(E0). Inducing configuration mixing, somewhat larger values of ρ^2(E0) can be expected. In ^{30}Mg the small experimental value of ρ^2(E0) = $(26.2\pm7.5) \cdot 10^{-3}$ points towards the presence of small mixing. However, the important question concerning the nature of the two 0^+ states and the amount of mixing of the $\nu\, 1d_{3/2}$ and $\nu\, 1f_{7/2}$ configurations remains to be answered. Concerning the 0_1^+ state there are strong experimental [7, 9] and theoretical [11, 12, 14] indications that in ^{30}Mg the inversion has not taken place.

In order to understand the experimental findings, calculations going beyond the mean-field by incorporating configuration mixing [22] have been performed using the finite range density dependent Gogny force with the D1S parameterization [23]. The results of these calculations for ^{30}Mg and ^{32}Mg are listed and compared to experimental values in Table I. The excitation energy of the 0_2^+ state as well as the values for B(E2;$0_1^+ \rightarrow 2_1^+$) and ρ^2(E0) agree reasonably well with the experimental values. In Fig. 4b), the particle number projected (PNP) potential energy curve displays both a mild prolate and an oblate minimum at small deformation and a shoulder at larger β values. Inspecting the neutron single-particle

	$E_x(2_1^+)$	$E_x(0_2^+)$	B(E2, $0_1^+ \rightarrow 2_1^+$)	ρ^2(E0)	B(E2, $0_2^+ \rightarrow 2_1^+$)
	(MeV)	(MeV)	$(e^2 fm^4)$	$\cdot 10^{-3}$	$(e^2 fm^4)$
^{30}Mg (T)	2.03	2.11	334.6	46	181.5
(E)	1.482	1.789	241(31) [9]	26.2± 7.5	53(6)
^{32}Mg (T)	1.35	2.60	455.7	41	56.48
(E)	0.885	-	454(78) [5]	-	-

TABLE I: Results from Beyond Mean Field calculations with Gogny force for ^{30}Mg and ^{32}Mg (indicated as 'T') compared to experimental values ('E').
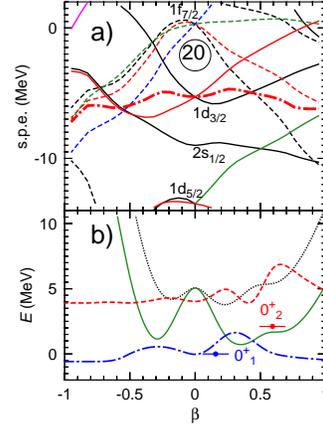
FIG. 4: Theoretical results for ^{30}Mg: a) Neutron single-particle energies as a function of deformation. The thick dash-dotted line represents the Fermi level. b) The dotted line corresponds to results of particle number projected (PNP) calculations, the green full line to the $J = 0$ energy surface and the blue (red) dashed-dotted (dashed) line represents the collective wave function of the 0_1^+ (0_2^+) state. (color)

energies in panel a), we see that the two minima at moderate deformation correspond to the two minima of the single-particle energies of the $\nu\, 1d_{3/2}$ orbitals just below the Fermi level (notice that this is not the case in ^{32}Mg, see [11]), while the shoulder appears at deformations at which two neutrons already occupy the $\nu\, 1f_{7/2}$ orbital. The angular momentum projection provides an additional energy lowering with respect to the PNP energy (the full line in panel (b)), and finally configuration mixing leads to the 0_1^+ and 0_2^+ states positioned in the E-β plane (Fig. 4b) according to their energy and average deformation. The composition of the collective wave functions of these two states, i.e. the weights of the corresponding β values being admixed, indicates the character of the state. We notice that the 0_1^+ state (blue dotted-dashed line) is a mixture of prolate and oblate $\nu\, 1d_{3/2}$ configurations which average to a small intrinsic deformation of $\beta = 0.16$. The 0_2^+ state (blue dashed line), on

4

the other hand, is a well deformed state with $\beta = 0.59$ consisting to a large part of a $\nu\, 1f_{7/2}$ configuration with very small admixtures of the $\nu\, 2d_{3/2}$ configuration. These results are consistent with the experimental finding of a small matrix element connecting both 0^+ levels. It is known [24, 25] that the calculation of $\rho^2(E0)$ is very sensitive to small variations of the interaction matrix elements and in particular to small admixtures of different shapes. Ideally, one needs to consider triaxial shapes in the calculations. Due to the complexity of a fully triaxial angular momentum projected calculation, at present, we had to restrict to axial symmetric states only. Neglecting triaxial effects might be a worse approximation in the calculation of $\rho^2(E0)$ than in the case of other observables like energies or B(E2) strengths, because in the latter cases the intrinsic state of the initial and final wave functions is the same, while in the case of $\rho^2(E0)$ these states have a rather different dependence on γ.

In order to quantify the mixing amplitude between the deformed and spherical configurations, we have also analyzed our experimental results making use of a phenomenological two-level mixing model [21]. Here $\rho^2(E0)$ strongly depends on the mixing amplitude a between the two intrinsic 0^+ states. Using the deformation values of the two 0^+ states as calculated above ($\beta_1(0_1^+) = 0.16$, $\beta_2(0_2^+) = 0.59$) together with the experimental value of $\rho^2(E0)$, a value of $a^2 = 0.0319(76)$ can be extracted (using Eq. (51) of Ref. [21]), resulting in a value of $a = 0.179(83)$ for the mixing amplitude between the two intrinsic 0^+ states. An identical value of $\beta_2(0_2^+) = 0.59$ can be inferred from the phenomenological Grodzins systematics [26], which empirically correlates the B(E2; $0_1^+ \rightarrow 2_1^+$) value and the excitation energy of the first excited 2^+ state (here based on the assignment of the 2467 keV level as being the rotational 2_2^+ state). For ^{30}Mg and ^{32}Mg the B(E2) values predicted by the Grodzins systematics ($256(45)$ e^2fm^4 and $410(73)$ e^2fm^4) agree remarkably well with the experimental values ($241(31)$ e^2fm^4 [9] and

$454(78)$ e^2fm^4 [5]). This also points to rather pure 0^+ and 2^+ states in the two potential minima.

To conclude, conversion electron measurements at ISOLDE have identified the 1789 keV level as the 0_2^+ state in ^{30}Mg. The conversion electrons were measured in coincidence with β decay electrons using a Mini-Orange spectrometer. The monopole strength extracted from measuring the $0_2^+ \rightarrow 0_1^+$ E0 transition is $\rho^2(E0,^{30}\text{Mg}) = (26.2 \pm 7.5) \cdot 10^{-3}$, which corresponds to a partial E0 lifetime of $\tau(E0) = 396(113)$ ns. The small value of the monopole strength indicates a weak mixing between shape-coexisting 0^+ states near the 'island of inversion'. Beyond-mean-field calculations identify the ground state as based on a mixture of prolate and oblate $\nu\, 1d_{3/2}$ orbitals and the excited 0_2^+ state on a rather pure $\nu\, 1f_{7/2}$ level, thereby confirming a sharp borderline of the 'island of inversion' and a very weak mixing between the competing configurations. It would be of great interest to extend this kind of study to a search for the (spherical) 0_2^+ state in ^{32}Mg. However, presently no spectroscopic candidate for this state is available. Due to the much reduced intensity of the ^{32}Na beam, only a low-lying 0_2^+ state could be detected by our technique, while theoretical predictions place this state at around 2 MeV [3, 11, 12]. Alternatively two-neutron transfer could lead to a population of the 0_2^+ state in ^{32}Mg, which is the subject of a current experimental project at ISOLDE [27].

Acknowledgments

[1] E.K. Warburton, J.A. Becker, B.A. Brown, Phys. Rev. **C 41** (1990) 1147.
[2] M. Yamagami, N. Van Giai, Phys. Rev. **C 69** (2004) 034301.
[3] K. Heyde and J.L. Wood, J. Phys. G**17** (1991) 135.
[4] J.L. Wood et al., Phys. Rep. **215** (1992) 101.
[5] T. Motobayashi et al., Phys. Lett. **B346** (1995) 9.
[6] H. Iwasaki et al., Phys. Lett. **B 522** (2001) 227.
[7] B. Pritychenko et al., Phys. Lett. **B 461** (1999) 322.
[8] V. Chisté et al., Phys. Lett. **B 514** (2001) 233.
[9] O. Niedermaier et al., Phys. Rev. Lett. **94** (2005) 172501.
[10] A. Gade et al., Phys. Rev. Lett. **99** (2007) 072502.
[11] R. Rodríguez-Guzmán, J.L. Egido, L.M. Robledo, Nucl. Phys. **A709** (2002) 201.
[12] E. Caurier et al., Nucl. Phys. **A693** (2001) 374.
[13] F. Nowacki et al., priv. communic. in: D. Guillemaud-Mueller et al., Eur. Phys. Journ. **A13** (2002) 63.
[14] T. Otsuka, Eur. Phys. Journ. **A20** (2004) 69.
[15] H. Mach et al., Eur. Phys. J. **A25** (2005) s01 105.
[16] H. Mach et al., to be published.
[17] E. Kugler et al., Nucl. Instr. Meth. **B70** (1992) 41.
[18] J.van Klinken et al., Nucl. Instr. Meth. **130** (1975) 427.
[19] T. Kibédi and R. H. Spear, Atomic Data and Nuclear Data Tables, **89** (2005) 77.
[20] A. Passoja and T. Salonen, Univ. of Jyväskylä JYFL Report RR-2/86 (1986).
[21] J.L. Wood et al., Nucl. Phys. **A651** (1999) 323.
[22] T.R. Rodriguez, J.L. Egido, Phys. Rev. Lett. 99 (2007) 062501.
[23] J.F. Berger, M. Girod, D. Gogny, Nucl. Phys. **A 428** (1984) 23c.
[24] E. Bouchez et al., Phys. Rev. Lett. **90** (2003) 082502.
[25] A. Petrovici et al., Nucl. Phys. **A665** (2000) 333.
[26] S. Raman, C.W. Nestor, P. Tikkanen, At. Data Nucl. Data Tab. 78 (2001) 1.
[27] T. Kröll et al., CERN-INTC-2008-P-239 (2008).

Revision of the lifetime of the first excited 0^+ state in ^{90}Zr

W. Schwerdtfeger[1], K. Wimmer[1], D. Habs[1], T. Kröll[2], H.J. Maier[1], J. Szerypo[1], P.G. Thirolf[1], B. Wierczinski[3]

[1] *Fakultät für Physik, Ludwig-Maximilians-Universität München, Am Coulombwall 1, 85748 Garching, Germany*
[2] *Physik Department E12, Technische Universität München, James-Franck-Straße, 85748 Garching, Germany*
[3] *Institut für Radiochemie , Technische Universität München,*
Walter-Meissner-Straße 3, 85748 Garching, Germany
(Dated: February 15, 2009)

The halflife of the first excited 0^+ state in ^{90}Zr was measured following the β decay from ^{90}Y. Using a Mini-Orange spectrometer in coincidence with a plastic scintillation detector a value of $t_{1/2} = 41(1)$ ns was determined. This value is $\sim 30\%$ smaller than the value so far reported in literature. This new value of the halflife leads to a significantly higher monopole strength of $\rho^2(\text{E0}) = 5.2(1) \cdot 10^{-3}$.

E0 transitions play a crucial role in determining nuclear structure properties of 0^+ states, giving e.g. access to study shape coexistence between nuclear configurations with different deformation [1]. The weak E0 transition in ^{90}Zr was studied in order to characterize the sensitivity limit of a $\beta - \text{E0}$ coincidence setup. It was designed to detect conversion electrons in a magnetic transport and filter system (Mini-Orange spectrometer) [2] and β decay electrons in a plastic scintillator aiming to identify the E0 transition in ^{30}Mg [3]. During preparatory offline measurements an ^{90}Y source with an activity of ~ 120 kBq (emitted in 2π) was produced at the Institut für Radiochemie of the Technische Universität München. In order to obtain ^{90}Y (decay chain: ^{90}Sr $\xrightarrow{\beta^-}$ ^{90}Y $\xrightarrow{\beta^-}$ ^{90}Zr) a reservoir of ^{90}Sr ($t_{1/2} = 28.64$ a) was flushed with hydrochloric acid dissolving ^{90}Y only. A drop of 10 μl of the solution was pipeted on a 20 $\mu g/\text{cm}^2$ thick carbon foil and subsequently dried using an infrared lamp.

Fig. 1 shows the β decay properties of ^{90}Y. It decays with a halflife of ~ 64.1 hours ($Q_\beta = 2.28$ MeV) almost entirely to the ground state of ^{90}Zr. A weak E0 transi-

FIG. 2: Sketch of the experimental setup.

tion with a transition energy of 1760.7 keV and a lifetime of 61.3(25) ns of the 0_2^+ state is so far reported in literature [4, 5], leading to an electric monopole strength of $\rho^2(\text{E0}) = 3.30(17) \cdot 10^{-3}$ [1] and an absolute intensity of 0.0115% [4] for this transition.

Fig. 2 shows a sketch of the experimental setup. The ^{90}Y source was positioned between a Mini-Orange spectrometer and a plastic scintillator under an angle of 45°. Since the E0 transition energy already exceeds more than 75% of the Q_β value, the remaining kinetic energy for the β decay electrons is $E_\beta \leq 519$ keV with a maximum of the energy distribution at ~ 250 keV. Due to this small kinetic energy of the β decay electrons, the plastic scintillation detector (5 mm thick diameter 89 mm, NE-110) was used simultaneously as window to the vacuum chamber, while a 2 inch photomultiplier tube was directly coupled to it from outside the vacuum chamber. The distance between source and scintillator was about 23 mm, resulting in a solid angle of $\Omega/4\pi = 18\%$.

In order to suppress the β-decay background detected in the Si(Li) detector and to increase the solid angle for conversion electron detection a Mini-Orange spectrometer [2] was used. It consists of 8 wedge-shaped permanent magnets arranged around a central Pb absorber, resulting in a toroidal magnetic field of $B = 160$ mT and a Si(Li) detector operated at liquid N_2 temperature with

FIG. 1: Part of the level scheme of ^{90}Zr [4] including the β decay properties of ^{90}Y. The corrected halflife of the 0_2^+ state, as determined in this work, is indicated and compared to a previous result from inelastic proton scattering [5].
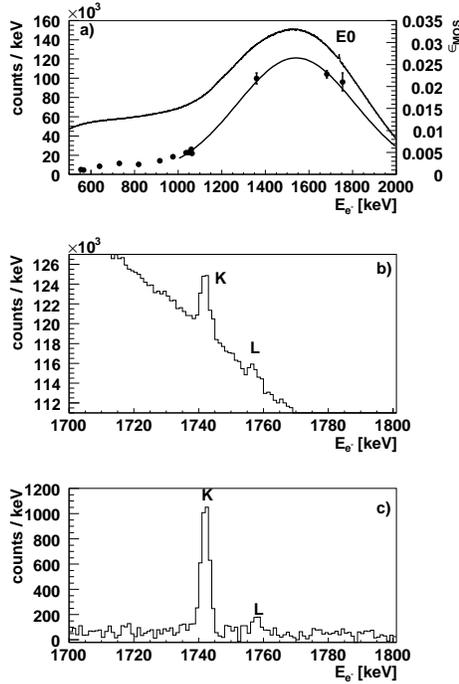
FIG. 3: a) Electron energy spectrum of the ^{90}Y decay folded with the transmission curve of the Mini-Orange and measured with the Si(Li) detector. The initial source activity was ~ 120 kBq. Also shown is the transmission efficiency curve of the Mini-Orange spectrometer consisting of 8 wedge-shaped permanent magnets, as determined with ^{152}Eu and ^{207}Bi electron sources. The transmission efficiency maximum is around ~ 1550 keV close to the electron energy of the E0 transition in ^{90}Zr (1743 keV), where the transmission efficiency is $\epsilon_{MOS} = 1.8(2)$ %. b) Expanded part of the electron energy singles spectrum showing the K and L conversion electron lines at 1743 keV and 1758 keV. c) Electron energy spectrum of the ^{90}Y decay measured in coincidence with β decay electrons and corrected for random coincidences.

~ 3.5 keV resolution at an electron energy of 1743 keV. The transmission curve of the Mini-Orange spectrometer was measured using a ^{152}Eu and a ^{207}Bi electron source and optimized for the E0 transition energy of 1760.7 keV, resulting in a detection efficiency of 1.8(2) % at this energy, as can be seen from Fig. 3. The Mini-Orange spectrometer was operated in coincidence with the scintillation detector.

Fig. 3a) shows the electron singles spectrum of the ^{90}Y decay. The K and L conversion lines are visible on top of the β decay background folded with the transmis-
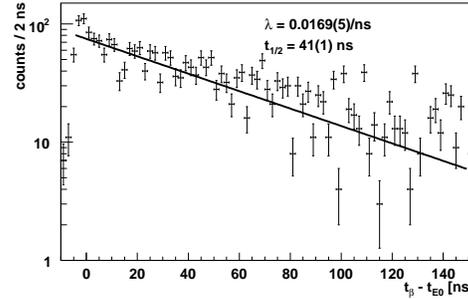
FIG. 4: Background-subtracted decay time spectrum of the 0_2^+ state in ^{90}Zr. In order to derive the halflife of the 0_2^+ state, the spectrum was fitted using an exponential function. The resulting decay constant $\lambda = 0.0169(5)$/ns allows to determine the halflife of the 0_2^+ state of $t_{1/2} = 41(1)$ ns.

sion curve of the Mini-Orange spectrometer. $1.93(9) \cdot 10^4$ $(2.66(71) \cdot 10^3)$ counts were measured during 66 hours in the K (L) line, respectively, which are shown in more detail in Fig. 3b). During the measurement the deadtime of the data acquisition system amounted to $\sim 30\%$. Therefore the detected E0 yield from the singles data amounts to $2.75(13) \cdot 10^4$ counts in the K line. This can be compared with the expected yield derived from the ^{90}Y source intensity (in 4π) of 120 kBq, which corresponds to a number of $1.54 \cdot 10^{10}$ decaying ^{90}Y nuclei within the measurement time of 66 hours (starting 26 hours after the production of the source). Together with the transmission efficiency of the MO spectrometer ($\epsilon_{MOS} = 0.018(2)$) and a K conversion probability of 66.6%, $2.12(24) \cdot 10^4$ electrons are expected in the K line of the electron singles spectrum, in reasonable agreement with the experimental finding.

Finally panel c) of Fig. 3 displays the electron spectrum measured in coincidence with β decay electrons, achieving a peak-to-background ratio of 10:1.

In order to select events satisfying the β – E0 coincidence condition, a TDC (Caen V775) was used to measure the time difference between the signals of the two electron detectors. This measurement allowed to determine the halflife of the 0_2^+ state.

Fig. 4 displays the background-subtracted decay time spectrum of the K- line at 1743 keV. Since the transmission function is linear in a small range around the K line, the background was determined setting two windows with half of the K line width below and above the K line in the electron singles spectrum. In order to determine the halflife of the 0_2^+ state in ^{90}Zr, the histogram in Fig. 4 was fitted using an exponential function. The decay constant λ was determined as $\lambda = 0.0169(5)$/ns, which results in a halflife of the 0_2^+ state of $t_{1/2} = 41(1)$ ns. This value is significantly smaller than the only published value of 61.3(25) ns [5], which dates back to a measure-

ment published in 1972. The published value was determined via the ^{90}Zr(p,p'e) reaction using an 8.16 MeV proton beam. In this reaction the isomeric 8^+ (5^-) state at 3589.4 keV (2319.0 keV) with a halflife of 131(4) ns [4] (809.2(20) ms [6] discovered in the same year) may have been populated. Both states have transitions feeding the 0_2^+ state (see Fig. 1) affecting the lifetime measurement. In our experiment the isomeric 8^+ or 5^- state could not be populated, because the Q value of the ^{90}Y β decay is smaller than the excitation energy of this state, thus avoiding feeding contributions to the 0_2^+ state. So our new measurement leads to the correct halflife of the 0_2^+ state of $t_{1/2} = 41(1)$ ns. The monopole strength ρ^2(E0) can be calculated using Eq. (2) from Ref. [1]

$$\rho^2(\text{E0}) = \frac{1}{(\Omega_\text{K} + \Omega_\text{L} + \ldots + \Omega_\text{IP}) \cdot \tau}. \quad (1)$$

With the revised lifetime $\tau = 59(1)$ ns of the 0_2^+ state and the electronic factors Ω_i ($\sum \Omega_i = 3.24 \cdot 10^9$/s), which can be calculated with Ref. [7], a corrected value for the E0 strength of ρ^2(E0) $= 5.2(1) \cdot 10^{-3}$ is obtained, significantly increasing the previous value. Nevertheless this new value of ρ^2(E0) does not qualitatively change the systematics of the electrical monopole strength within the isotopic chain of the Zr isotopes $^{90-96}$Zr as presented in Ref. [1].

[1] J.L. Wood, E.F. Zganjar, C. De Coster and K. Heyde, Nucl. Phys. A651 (1999) 323.

[2] J. van Klinken and K. Wisshak, Nucl. Instr. Meth. 98 (1972) 1.

[3] W. Schwerdtfeger et al., submitted to Phys. Rev. Lett. (2008); W. Schwerdtfeger, PhD thesis, LMU Munich (2008), unpublished.

[4] ENSDF (2007), http://www.nndc.bnl.gov/ensdf

[5] D. Burch, P. Russo, H. Swanson and E.G. Adelberger, Phys. Lett. B40 (1972) 357.

[6] O. Brandstädter, F. Girsig, F. Grass and R. Klenk, Nucl. Inst. and Meth. 104 (1972) 45.

[7] J. Kantele, *Handbook of Nuclear Spectrometry* (Academic Press, 1995)

Bibliography

[AND00] A. N. Andreyev et al., *Nature* **405** (2000) 430.

[AUD03] G. Audi, A. Wapstra and C. Thibault, *Nucl. Phys. A* **729** (2003) 337.

[AUD06] G. Audi, A. Wapstra and C. Thibault, *Nucl. Phys. A* **766** (2006) 52.

[BAX93] A. Baxter et al., *Phys. Rev. C* **48** (1993) R2140.

[BEC08] S. Becker and D.Habs, private communication (2008).

[BEL70] D. A. Bell et al., *Canadian Journal of Physics* **48** (1970) 2542.

[BEN06] M. Bender, P. Bonche and P. Heenen, *Phys. Rev. C* **74** (2006) 024312.

[BER84] J. Berger, M. Girod and D. Gogny, *Nucl. Phys. A* **428** (1984) 23c.

[BER92] Bergmann and Schaefer, *Lehrbuch der Experimentalphysik, Band 4: Teilchen* (W. de Gruyter, 1992).

[BOH69] A. Bohr and B. Mottelson, *Nuclear Structure, Vol. 1* (Benjamin, Reading, 1969).

[BOH75] A. Bohr and B. Mottelson, *Nuclear Structure, Vol. 2* (Benjamin, Reading, 1975).

[BOU03] E. Bouchez et al., *Phys. Rev. Lett.* **90** (2003) 082502.

[BRA72] O. Brandstädter, F. Girsig, F. Grass and R. Klenk, *Nucl. Inst. and Meth.* **104** (1972) 45.

[BUR72] D. Burch, P. Russo, H. Swanson and E. G. Adelberger, *Phys. Lett. B* **40** (1972) 357.

[BÜR02] T. Bürvenich, D. Madland, J. Maruhn and P. Reinhard, *Phys. Rev. C* **65** (2002) 044308.

[CAM75] X. Campi, H. Flocard, A. Kerman and S. Koonin, *Nucl. Phys. A* **251** (1975) 193.

[CAS90] R. Casten, *Nuclear Structure from a Simple Perspective* (Oxford University Press, 1990).

[CAU01] E. Caurier et al., *Nucl. Phys. A* **693** (2001) 374.

[CER] CERN, *European Organization for Nuclear Research.*
`http://user.web.cern.ch/user/Welcome.asp`.

[CHI01] V. Chisté et al., *Phys. Lett. B* **514** (2001) 233.

[CHU56] E. Church and J. Weneser, *Phys. Rev.* **103** (1956) 1035.

[COC98] J. Cocks et al., *Eur. Phys. J. A* **3** (1998) 17.

[COZ99] Y. L. Coz et al., *EPJdirect A* **3** (1999) 1.

[CST] CST EM Studio, *Computer Simulation Technology: EM Studio.*
`http://www.cst.com/Content/Products/EMS/Overview.aspx`.

[CT97] C. Cohen-Tannoudji, B. Diu and F. Laloë, *Quantenmechanik, Vol. 1* (W. de
Gruyter, 1997).

[CT99] C. Cohen-Tannoudji, B. Diu and F. Laloë, *Quantenmechanik, Vol. 2* (W. de
Gruyter, 1999).

[DRA98] G. Dracoulis et al., *Phys. Lett. B* **432** (1998) 37.

[DUP90] P. V. Duppen, M. Huyse and J. Wood, *J. Phys. G: Nucl. Part. Phys.* **16**
(1990) 441.

[EIC07] T. Eichner et al., *Phys. Rev. Special Topics* **10** (2007) 082401.

[ENS07] ENSDF, *Evaluated Nuclear Structure Data File* (2007).
`http://www.nndc.bnl.gov/ensdf/`.

[FAU75] H. Faust, Diploma thesis, MPI Heidelberg (1975).

[FIR96] R. Firestone et al., *Table of Isotopes* (J. Wiley, 1996).

[GAD07] A. Gade et al., *Phys. Rev. Lett.* **99** (2007) 072502.

[GEA] GEANT4, *GEometry ANd Tracking.* `http://geant4.web.cern.ch/geant4/`.

[GM90] D. Guillemaud-Mueller et al., *Phys. Rev. C* **41** (1990) 937.

[HEE93] J. Heese et al., *Phys. Lett. B* **302** (1993) 390.

[HEY91] K. Heyde and J. Wood, *J. Phys. G: Nucl. Part. Phys.* **17** (1991) 135.

[HEY07] K. Heyde, private communication (2007).

[HUN49] F. Hund, 5. Vortrag in: Das Molekül und der Aufbau der Materie (1949).

[ISO] ISOLDE, *ISOLDE CERN, Radioactive Ion Beam Facility.*
`http://isolde.web.cern.ch/ISOLDE/`.

[IWA01] H. Iwasaki et al., *Phys. Lett. B* **522** (2001) 227.

[KAN83] J. Kantele et al., *Phys. Rev. Lett.* **51** (1983) 91.

[KAN84] J. Kantele et al., *Phys. Rev. C* **29** (1984) 1693.

[KAN95] J. Kantele, *Handbook of Nuclear Spectroscopy* (Academic Press, 1995).

[KIB05] T. Kibédi and R. H. Spear, *Atomic Data and Nuclear Data Tables* **89** (2005) 77.

[KLI72] J. van Klinken and K. Wisshak, *Nucl. Inst. and Meth.* **98** (1972) 1.

[KLI75] J. van Klinken, S. J. Feenstra, K. Wisshak and H. Faust, *Nucl. Inst. and Meth.* **130** (1975) 427.

[KLI78] J. van Klinken, S. J. Feenstra and G. Dumond, *Nucl. Inst. and Meth.* **151** (1978) 433.

[KLO93] G. Klotz et al., *Phys. Rev. C* **47** (1993) 2502.

[KÖS08] U. Köster, private communication (2008).

[KRÖ08] T. Kröll, R. Krücken, K. Wimmer et al., CERN-INTC-2008-008 and INTC-P-239 (2008).

[LUT03] R. Lutter, O. Schaile et al., *MAR$_a$B@U Data Acquisition* (2003). `http://www.bl.physik.uni-muenchen.de/marabou/html/`.

[MAC90] H. Mach et al., *Phys. Rev. C* **41** (1990) 226.

[MAC05] H. Mach et al., *Eur. Phys. J. A* **25** (2005) s01 105.

[MAC08] H. Mach, private communication (2008).

[MAT07] C. Mattoon et al., *Phys. Rev. C* **75** (2007) 017302.

[MBS]   MBS, *Multi Branch System.* `http://www-win.gsi.de/daq/`.

[MOT95] T. Motobayashi et al., *Phys. Lett. B* **346** (1995) 9.

[NG74]   W. Ng and B. Castel, *Phys. Rev. C* **10** (1974) 2643.

[NIE05] O. Niedermaier et al., *Phys. Rev. Lett.* **94** (2005) 172501.

[NIK08] T. Nikšić and P. Ring, private communication (2008).

[NIL69] S. Nilsson, C. Tsang, A. Sobiczewski, Z. Symanski, S. Wycech, G. Gustafson, I. Lamm, P. Möller and B. Nilsson, *Nucl. Phys. A* **131** (1969) 1.

[OTS01] T. Otsuka, R. Fujimoto, Y. Utsuno, B. Brown, M. Honma and T. Mizusaki, *Phys. Rev. Lett.* **87** (2001) 0825021.

[OTS02] T. Otsuka, Y. Utsuno, R. Fujimoto, B. Brown, M. Honma and T. Mizusaki, *Eur. Phys. J. A* **15** (2002) 151.

[OTS04] T. Otsuka et al., *Eur. Phys. J. A* **20** (2004) 69.

[PAS86] A. Passoja and T. Salonen, (1986).

[PET00] A. Petrovici et al., *Nucl. Phys. A* **665** (2000) 333.

[PIE01] S. Pieper, V. Pandharipande, R. Wiringa and J. Carlson, *Phys. Rev. C* **64** (2001) 014001.

[PRI99] B. Pritychenko et al., *Phys. Lett. B* **461** (1999) 322.

[RAM01] S. Raman, J. C.W. Nestor and P. Tikkanen, *Atomic Data and Nuclear Data Tables* **78** (2001) 1.

[REI93] P. Reiter, Dissertation, MPI Heidelberg (1993).

[RG02a] R. Rodríguez-Guzmán, J. L. Egido and L. M. Robledo, *Nucl. Phys. A* **709** (2002) 201.

[RG02b] R. Rodríguez-Guzmán, J. L. Egido and L. M. Robledo, **65** (2002) 024304.

[RG03] R. Rodríguez-Guzmán, J. L. Egido and L. M. Robledo, *Phys. J. A* **17** (2003) 37.

[RG04] R. Rodríguez-Guzmán, J. L. Egido and L. M. Robledo, *Phys. Rev. C* **69** (2004) 054319.

[RIN80] P. Ring and P. Schuck, *The Nuclear Many-body Problem* (Springer Verlag, Heidelberg, 1980).

[ROD07] T. Rodríguez and J. Egido, *Phys. Rev. Lett.* **99** (2007) 062501.

[ROD08] T. Rodriguez and J. Egido, private communication (2008).

[ROO07] ROOT, *An Object-Oriented Data Analysis Framework* (2007). `http://root.cern.ch/`.

[SCH05] H. Scheit et al., *Eur. Phys. J. A* **25** (2005) s01 397.

[SER01] M. Serra, Dissertation, Technische Universität München (2001).

[SIN76] P. Singer, Diploma thesis, MPI Heidelberg (1976).

[SKY56] T. Skyrme et al., *Phil. Mag.* **1** (1956) 1043.

[SKY59] T. Skyrme et al., *Nuc. Phys.* **9** (1959) 615.

[THI75] C. Thibault, R. Klapisch, C. Rigaud, A. Poskanzer, R. Prieels, L. Lessard and W. Reisdorf, *Phys. Rev. C* **12** (1975) 644.

[THI02] P. Thirolf and D. Habs, *Prog. Part. Nucl. Phys.* **49** (2002) 325.

[UTS99] Y. Utsuno, T. Otsuka, T. Mizusaki and M. Honma, *Phys. Rev. C* **60** (1999) 054315.

[UTS04] Y. Utsuno, T. Otsuka, T. Glasmacher, T. Mizusaki and M. Honma, *Phys. Rev. C* **70** (2004) 044307.

[VAR88] D. Varshalovich, A. Moskalev and V. Khersonskii, (1988).

[VRE05] D. Vretenar, A. Afanasjev, G. Lalazissis and P. Ring, *Phys. Rep.* **409** (2005) 101.

[WAL68] M. Waldschmidt and S. Wittig, *Nucl. Inst. and Meth.* **64** (1968) 189.

[WAL95] J. Walecka, *Theoretical Nuclear and Subnuclear Physics* (Oxford University Press, Oxford, 1995).

[WAR90] E. Warburton, J. Becker and B. Brown, *Phys. Rev. C* **41** (1990) 1147.

[WIM07] K. Wimmer, Diploma thesis, LMU München (2007).

[WOO96] J. Wood, E. Zganja and K. Heyde, *Z. Phys. A* **353** (1996) 355.

[WOO99] J. Wood, E. Zganja, C. de Coster and K. Heyde, *Nucl. Phys. A* **651** (1999) 323.

[YAM04] M. Yamagami et al., *Phys. Rev. C* **69** (2004) 034301.

[YAN03] Y. Yanagisawa et al., *Phys. Lett. B* **566** (2003) 84.

Acknowledgements

- U. Friebel, R. Großmann, Dr. H.-J. Maier and Dr. J. Szerypo for their help producing sources and R. Großmann for his support concerning radiation protection questions.

- Dipl.-Phys. K. Wimmer for her great help on mechanical work in the laboratory, setting up data acquisition and analyzing data. Without her help and moral support this project would not have been successful in the end. I would also like to thank her for many hours we spent in the mountains, in beer gardens and drinking Espresso.

- During the course of this thesis I have shared my office with a few coworkers and partners in crime. I would like to thank them for the good atmosphere in the office.

- The members of the engineering office especially M. Schumann for the ideas and support in constructing new setups.

- Many thanks go to R. Öhm and all the members of the mechanical workshop. You have done a great job. I want to apologize for being pressuring on urgent orders and showing up several times a day.

- The members of the electronics workshop helping on building and repairing electronic devices or cabling.

- Many thanks go to R. Satzkowski for save transports of equipment to CERN and back and for contributing to the good atmosphere in the office.

- Our secretary A. Leinthaler for her help concerning administrative things.

- Everybody I may have forgotten.

I want to thank all my friends in Munich and outside. You gave me great help and support during the last years. Especially I want to thank for your moral assistance.

Finally I want to thank my family who gave me the opportunity to make a PhD. Thank you for your support and encouragement.